Behaviour of High- and Ultra-High Performance Fibre Reinforced Concrete Flexural Members

Tianyu Xie

BEng (Architectural Engineering) Hons

M.Phil (Structural Engineering)

Thesis submitted to The University of Adelaide in fulfilment of the requirements for the degree of Doctor of Philosophy

ABSTRACT

Concrete is a quasi-brittle material that increases in brittleness as the compressive strength increases and as such plain high-strength concrete always fails in an explosive manner. Incorporation of randomly distributed discrete non-metallic or metallic fibres into conventional concrete mixes has now been well-recognized as a feasible solution to address the issue of the low material ductility of concrete. The presence of fibres in concrete can prevent wider cracks on the concrete structural elements under instantaneous and sustained loads and an associated refinement of the pore structure and mitigations of micro-cracks also effectively contributes to enhancing the durability-related material properties.

This thesis presents a series of research work investigating the behaviour of various types of high- and ultra-high performance concrete flexural members. The work starts with an investigation to develop mix proportions for ultra-performance concrete with and without fibres to achieve the desired dimensional stability as reported in Chapters 2 and 3 in this thesis. The optimal concrete recipe is then used continuously through the entire experimental program to manufacture the flexural members for investigations, as presented in Chapters 5 to 8, where the behaviour of a series of high- and ultra-high performance concrete flexural members, including fibre-reinforced concrete (FRC) simply-supported beams, ultra-high performance fibre reinforced concrete (UHPFRC) continuous beams, curved beams, skew slabs and also sandwich panels using ultra-high performance concrete (UHPC) face sheets, are experimentally studied.

Having experimentally investigated the performances of these high- and ultra-high performance concrete flexural members, in Chapter 4, a generic analysis technique, (the segmental based moment-rotation approach), is extended to simulate the behaviour of high- and ultra-high fibre reinforced concrete flexural members. This approach is based on the fundamental Euler-Bernoulli postulation that plane remains plane and applies the well-established mechanics of partial interaction (PI) theory to simulate crack formation and crack widening including the influence of the discrete fibre reinforcement. Moreover, in Chapters 6 to 8, analytical approaches, in terms of the fundamental mechanics based closed-form models are also derived using energy theorem to predict the performance of non-orthogonal ultra-high performance fibre-reinforced concrete flexural members.

STATEMENT OF ORIGINALITY

I certify that this work contains no material which has been accepted for the award of any other degree or diploma in my name, in any university or other tertiary institution and, to the best of my knowledge and belief, contains no material previously published or written by another person, except where due reference has been made in the text. In addition, I certify that no part of this work will, in the future, be used in a submission in my name, for any other degree or diploma in any university or other tertiary institution without the prior approval of the University of Adelaide and where applicable, any partner institution responsible for the joint-award of this degree.

I give consent to this copy of my thesis when deposited in the University Library, being made available for loan and photocopying, subject to the provisions of the Copyright Act 1968.

The author acknowledges that copyright of published works contained within this thesis resides with the copyright holder(s) of those works.

I also give permission for the digital version of my thesis to be made available on the web, via the University's digital research repository, the Library Search and also through web search engines, unless permission has been granted by the University to restrict access for a period of time.

_____   _____17/04/2019_____

Tianyu Xie   Date

Declaration

I, **Tianyu Xie**, certify that this work contains no material which has been accepted for the award of any other degree or diploma in my name, in any university or other tertiary institution and, to the best of my knowledge and belief, contains no material previously published or written by another person, except where due reference has been made in the text. In addition, I certify that no part of this work will, in the future, be used in a submission in my name, for any other degree or diploma in any university or other tertiary institution without the prior approval of the University of Adelaide and where applicable, any partner institution responsible for the joint-award of this degree.

I acknowledge that copyright of published works contained within this thesis resides with the copyright holder(s) of those works.

I also give permission for the digital version of my thesis to be made available on the web, via the University's digital research repository, the Library Search and also through web search engines, unless permission has been granted by the University to restrict access for a period of time.

_____   _____17/04/2019_____

Tianyu Xie   Date

iii

ACKNOWLEDGEMENTS

THIS PAGE HAS BEEN LEFT INTENTIONALLY BLANK

Table of Contents

THIS PAGE HAS BEEN LEFT INTENTIONALLY BLANK

CHAPTER 1

INTRODUCTION

Concrete is by far the most important and commonly used construction material in the world and demand for concrete is rapidly growing because of the increase in world population and improved standards of living in emerging economies. Concrete is a type of quasi-brittle material in which the brittleness of the material generally increases with an increase in its compressive strength. Plain high-strength concrete always fails in an explosive way due to its inherent brittle nature. Incorporation of randomly distributed, discrete non-metallic or metallic fibres into the conventional concrete mixes has now been well-recognized as a feasible solution for the problem associated with the lower ductility of concrete.

In the year 1972, a type of high-strength and low porosity cement based composite, namely ultra-high performance concrete/composite (UHPC) was firstly reported in the literature. This material is characterized by a very high compressive strength and superior durability. These characteristics are typically achieved using mix designs with high quantities of binder (cement and silica fume) and low water to cement ratios (in the order of 0.2 or less). The superior structural engineering properties of UHPC over conventional concrete provides a great potential of using such a material for the construction of high-performance structures.

Of late years, incorporations of a small amount discrete non-mantellic and metallic fibre (i.e. at a volume faction from 1 to 3%) with UHPC yields a novel concrete that not only has superior mechanical properties (i.e. over 150 MPa compressive strength and good

ductility under tension) but also exceptional durability-related properties. This hence leads to the creation of a novel hybrid composite material, namely ultra-high performance fibre reinforced concrete/composite (UHPFRC), which is a particular type of fibre reinforced concrete (FRC). The presence of the internal fibers in UHPFRC not only prevents wider cracks but also effectively acts as reinforcement to resist shear and torsion seen on structures with non-orthogonal shapes. Further, the denser matrix of UHPFRC creates a feasible solution for the problem associated with concrete deterioration caused by inner steel reinforcement corrosion. Moreover, the use of UHPFRC materials in buildings and infrastructure can also effectively address the shortcomings of conventional construction work which is rather labor-intensive and time-consuming.

Despite these benefits, the application of UHPFRC has been hindered by: 1) the high cost of material development; 2) a lack of design standards which directly incorporate the beneficial properties of FRC and UHPFRC, thereby limiting the potential to realize the benefits of FRC and UHPFRC material properties at a structural level; and 3) together (1) and (2) place the risks involved in applying innovative materials in practice on traditionally risk adverse infrastructure owners. Therefore, aiming at facilitating the wider adaption and application of this high- (i.e. FRC) and ultra-high- performance material (i.e. UHPC and UHPFRC) in field of structural engineering, it is necessary to economize the mix design procedure involving commercial ingredients to reduce the cost, and it also urgently required that we establish the better understandings on the structural behaviour of this material experimentally, as well as developing analytical procedure. To this end, it leads to the basic theme of this Ph.D. research and the major objectives of this project are:

At material level:

1. To further refine the mix proportions of a low-cost and high-strength UHPC and UHPFRC using only conventional concrete manufacturing materials, casting and curing methods and on the most appropriate means for achieving the desired reduction in shrinkage.

2. To find feasible solutions to mitigate the impact of shrinkage on the mechanical properties of UHPC mortar, which can be significantly higher than in conventional concrete due to the high binder content in UHPC.

3. To explore the effects of fibres on shrinkage characterizations of UHPFRC and also to understand the underlying mechanisms of the actions.

At structural level:

1. To study the behaviour of UHPC or UHPFRC structural members subjected to flexure or combined flexure and torsion and;

2. To develop numerical and analytical tools to simulate the fundamental mechanics governing the behaviour of high- and ultra-high- performance FRC structural members subjected to pure bending or combined flexure and torsion.

Thesis overview

This thesis consists of 9 chapters in publication format. **Chapter 1** presents a general introduction of research. Each of Chapters 2 to 8 is a manuscript that has been published or submitted for publication as a journal article [1-7]. Table 1 presents detailed information of each manuscript. The breakdown of tasks are also introduced briefly as follows:

Chapters 2 and 3 present systematic research on shrinkage properties of UHPC and UHPFRC materials. Techniques to mitigate the impacts of shrinkage on the materials are experimentally studied and the underlying mechanisms of the actions are characterized.

Chapter 4 presents a numerical study to modify the existing numerical method using partial interaction (PI) mechanisms; the interface slip between reinforcement and concrete (tension stiffening) and the interface slip between concrete sliding planes once softening wedges have formed (shear friction) to simulate the flexural behavior of a novel type FRC beam with GFRP bars. The results of a pilot experiential study are used to validate the modified approach.

Chapter 5 presents the results of an experimental study of the moment redistribution capacity of four two-span continuous beams constructed from ultra-high performance fibre reinforced concrete (UHPFRC) and with various reinforcement ratios, such that the suitability of extending of exiting empirical design approaches to UHPFRC can be investigated.

Chapter 6 and 7 present experimental, analytical and/or numerical studies on the behaviours of two non-orthogonal structural members made of UHPFRC, namely simply-supported skew slab and fixed end curved beam, where the responses of UHPFRC structures under combined flexure and torsion are examined. In addition to numerical modelling approach presented in Chapter 4

to simulate behaviour of FRC flexural members at the serviceability limit, the moment rotation approach is also further used into the yield-lien method to simulate ultimate strength of the FRC members in Chapter 7.

Chapter 8 presents an investigation on the flexural behaviour of novel forms of light weighted composite sandwich structures comprised of two basalt fibre reinforced polymer (BFRP) mesh reinforced UHPC faces sheets and their core layers were fabricated by combining light-weighted normal strength mortar and expanded Polystyrene (EPS) foam of different configurations. Modified elementary sandwich panel theory (EST) and advanced sandwich theory (AST) were applied to provide feasible approaches to model the behaviours of the sandwich panels at their serviceability limit states.

The above contents in this Ph.D. thesis are summarised in **Chapter 9** where the contributions and outcomes are discussed. Limitations of the research and recommendation to the future work are also presented.

Table 1. Summary of publications, materials/structural elements studied, research area focused, and type of research

Publications	Research area focused	Materials/ Structural elements studied	Type of research
Fang et al. [1]	Shrinkage characterizations	UHPC	Experimental/Chemical
Xie et al. [2]	Shrinkage characterizations	UHPFRC, FRC	Experimental
Xie et al. [3]	Numerical modelling/Flexural behaviour	FRP reinforced FRC simply-supported beams	Experimental/Numeral
Visintin et al. [4]	Moment redistribution	UHPFRC/FRC continuous beams	Experimental
Xie et al. [5]	Combined bending and torsion	Simply-supported UHPFRC/FRC skew slabs	Experimental/Analytical
Xie et al. [6]	Combined bending and torsion	Fixed end UHPFRC/FRC curved beams	Experimental/Numerical/Analytical
Xie et al. [7]	Flexural behaviour/ Composite structures	FRP-UHPC sandwich panel	Experimental/Analytical

LISTS OF PUBLICATIONS

[1] C. Fang, M.S. Mohamed Ali, and P. Visintin, T. Xie. "Effects of Steel Fibres on Shrinkage Characterizations of Ultra-High Performance Fibre Reinforced Concrete." To be submitted to *ACI materials.*

[2] T. Xie, C. Fang, M.S. Mohamad Ali, and P. Visintin. "Characterizations of autogenous and drying shrinkage of ultra-high performance concrete (UHPC): An experimental study." *Cement and Concrete Composites* 91 (2018): 156-173.

[3] T. Xie, M.S. Mohamed Ali, P. Visintin, D. J. Oehlers, and A. H. Sheikh. "Partial Interaction Model of Flexural Behavior of PVA Fiber–Reinforced Concrete Beams with GFRP Bars." *Journal of Composites for Construction* 22, no. 5 (2018): 04018043.

[4] Visintin, P., M.S. Mohamed Ali, T. Xie, and A. B. Sturm. "Experimental investigation of moment redistribution in ultra-high performance fibre reinforced concrete beams." *Construction and Building Materials* 166 (2018): 433-444.

[5] T. Xie, M.S. Mohamed Ali, M. Elchalakani, M. David. "An Experimental and Analytical Study of Ultra-High Performance Fibre Reinforced Concrete Curved Beams." Submitted to ASCE Journal of Structural Engineering (under review).

[6] T. Xie, C. Fang, M.S. Mohamed Ali, and P. Visintin. "Behaviour and Analysis of Ultra High Performance Fibre Reinforced Concrete (UHPFRC) Skew Slabs." Submitted to *Engineering Structures* (under review).

[7] T. Xie, M.S. Mohamed Ali, M. Elchalakani, C. Fang. "An Innovative Insulated Sandwich Panel with FRP Reinforced Ultra-high performance Concrete Face Sheets：Concept and Behaviour." Submitted *Composite Part B: Engineering* (under review).

CHAPTER 2

Characterizations of Autogenous and drying shrinkage of ultra-high performance concrete (UHPC): An experimental study

[1]Xie, T., [2]Fang, C., [3]Mohamed Ali, M.S., [*4]Visintin, P.

[1]**Mr. Tianyu Xie**

Ph. D Candidate,

School of Civil, Environmental and Mining Engineering

The University of Adelaide

South Australia 5005

AUSTRALIA

[2]**Mr Chenfeng Fang**

Ph. D Candidate,

School of Civil, Environmental and Mining Engineering

The University of Adelaide

South Australia 5005

AUSTRALIA

[3]**Dr. Mohamed Ali, M.S**

Senior Lecturer,

 School of Civil, Environmental and Mining Engineering

The University of Adelaide

 South Australia 5005

AUSTRALIA

[4]**Dr.Phillip Visintin (Corresponding author)**

Associate Professor,

School of Civil, Environmental and Mining Engineering

The University of Adelaide

South Australia 5005

THIS PAGE HAS BEEN LEFT INTENTIONALLY BLANK

Statement of Authorship

Title of Paper	CHARACTERIZATIONS OF AUTOGENOUS AND DRYING SHRINKAGE OF ULTRA-HIGH PERFORMANCE CONCRETE (UHPC): AN EXPERIMENTAL STUDY
Publication Status	☑ Published ☐ Accepted for Publication ☐ Submitted for Publication ☐ Unpublished and Unsubmitted work written in manuscript style
Publication Details	Xie, T., Fang, C., Ali, M. M., & Visintin, P. (2018). Characterizations of autogenous and drying shrinkage of ultra-high performance concrete (UHPC): An experimental study. *Cement and Concrete Composites*, *91*, 156-173.

Principal Author

Name of Principal Author (Candidate)	Tianyu Xie		
Contribution to the Paper	Designing concept, conducting experiments, analysing of data, drafting manuscript		
Overall percentage (%)	40		
Certification:	This paper reports on original research I conducted during the period of my Higher Degree by Research candidature and is not subject to any obligations or contractual agreements with a third party that would constrain its inclusion in this thesis. I am the primary author of this paper.		
Signature		Date	12/02/2019

Co-Author Contributions

By signing the Statement of Authorship, each author certifies that:

  i.   the candidate's stated contribution to the publication is accurate (as detailed above);
  ii. permission is granted for the candidate in include the publication in the thesis; and
  iii. the sum of all co-author contributions is equal to 100% less the candidate's stated contribution.

Name of Co-Author	Chengfeng Fang		
Contribution to the Paper	Designing concept, conducting experiments, analysing of data, drafting manuscript (20%)		
Signature		Date	12/02/2019

Name of Co-Author	Dr Mohamed Ali Sadakkathulla		
Contribution to the Paper	Designing concept, analysing of data, revising manuscript (20%)		
Signature		Date	12/02/2019

Name of Co-Author	Associate Professor Phillip Visintin		
Contribution to the Paper	Designing concept, analysing of data, revising manuscript (20%)		
Signature		Date	12/02/2019

Please cut and paste additional co-author panels here as required.

ABSTRACT

Due to the high content of binder and low water to cement ratio, ultra-high performance concrete (UHPC), exhibits higher levels of autogenous shrinkage compared to ordinary concrete. This shrinkage has been shown to lead to a reduction in strength over time as a result of the formation of thermal and shrinkage cracks. Aiming to mitigate the negative impacts associated with shrinkage, the efficacy of three different techniques to reduce the impact of shrinkage are investigated, namely: reducing the binder content; incorporating high levels of shrinkage reducing admixture; and using crushed ice to partially replace mixing water. The effects of these techniques are experimentally investigated and the underlying mechanisms of the actions are characterized. It is found that autogenous shrinkage predominates the overall shrinkage of UHPC and that the three techniques can effectively reduce shrinkage without significantly compromising its mechanical strength. The results also suggest, that from the perspective of reducing shrinkage: the optimal binder-to-sand ratio is in the range of 1 - 1.1; the optimal dosage rate of shrinkage reducing admixture is 1%; and replacing of mixing water by crushed ice up to 50% by weight has also induced a significant reduction in shrinkage.

Keywords: Ultra-high performance concrete (UHPC); Autogenous shrinkage; free total shrinkage; compressive strength; microstructure; hydration

2.1 INTRODUCTION

Ultra-high performance concrete (UHPC) is characterized by very high compressive strength and superior durability (Mosaberpanah and Eren 2016; Shi et al. 2015; Singh et al. 2017; Wang et al. 2015; Yoo and Banthia 2016). These characteristics are typically achieved using mix designs with high quantities of binder (cement and silica fume) and low water to cement ratios (in the order of 0.2 or less). As a result, partially hydrated binder is often present within the

mortar resulting in an increase in autogenous shrinkage (Wu et al. 2017; Youssef 2013) up to an order of magnitude greater than that of conventional concrete (Park et al. 2014; Soliman and Nehdi 2011; Soliman and Nehdi 2014; Yalçınkaya and Yazıcı 2017; Yoo et al. 2013; Yoo et al. 2014). Hence total shrinkage strains in UHPC (including both the autogenous- and drying-shrinkage) are expected to be higher than conventional concrete. This is significant as high early age shrinkage strains may result in early age cracking (Şahmaran et al. 2009; Sobuz et al. 2016; Wang et al. 2015; Yoo et al. 2014; Yoo et al. 2014); and if containing fibers, a reduction in strength over time due to the restraint provided by fibers (Soliman and Nehdi 2014; Yoo et al. 2017; Yoo et al. 2014; Yoo et al. 2014).

The importance of quantifying shrinkage strains has led to a number of recent studies aimed at understanding the underlying mechanisms governing autogenous shrinkage of UHPC and its impact on performance. For example, experimental programs conducted by Yoo et al. (Yoo et al. 2018; Yoo et al. 2018; Yoo et al. 2014) and Şahmaran et al. (Şahmaran et al. 2015; Şahmaran et al. 2009; Sahmaran et al. 2009) systematically examined the effects of mixing proportion, curing condition, geometry and specimen restraint on autogenous shrinkage of UHPC specimens. Research has also identified several means for reducing both the magnitude of shrinkage strains, as well as the time over which they develop. For example, Rößler et al. (Rößler et al. 2014) have shown that by curing at a temperature of 20 ℃, a reduction of 85% in autogenous shrinkage strains is possible compared to those obtained under at 90 ℃ heat curing. Alternatively (Dudziak and Mechtcherine 2008; Jensen 2013) have shown that it is possible to reduce drying shrinkage via the inclusion of moisture retaining superabsorbent polymers into the mix. These release water over time, replacing that lost due to hydration and drying, resulting in a reduction of shrinkage strains of up to 75%. The effects of shrinkage

reducing admixtures on the autogenous shrinkage of UHPC have been investigated by (Koh et al. 2011; Soliman and Nehdi 2014; Yoo et al. 2015).

In this paper a standard UHPC mix which has been widely investigated at both the material (Sobuz et al. 2016; Sobuz et al. 2017; Visintin et al. 2018) and member levels (Singh et al. 2017; Sturm et al. 2018; Visintin et al. 2018) is taken as a baseline, and simple means for improving its dimensional stability is investigated. Approaches considered in this study include:

- The use of iced water in the mix design to lower concrete temperature and hence reduce the potential for autogenous shrinkage and temperature induced deformations (Smith 2001).
- Varying mix design proportions to identify the beneficial restraining influence of (fine) aggregate, and the presence of unhydrated binders that may act as a filler providing additional dimensional stability.
- Varying mix design proportions to identify the reduction in autogenous shrinkage due to a reduction in cementitious binder content.
- The use of high dosages of conventional shrinkage reducing admixtures to physically reduce shrinkage by reducing the surface tension in the concrete pore water.

For each approach investigated a range of material and characterization tests are conducted to determine the relative effectiveness of each approach, as well as the underlying mechanism of action. It is envisaged that this work will assist in allowing concrete technologists to decide on the most appropriate means for achieving the desired reduction in shrinkage.

In the remainder of the paper the characteristics and constituents of the UHPC materials investigated are first described. This is followed by a description of the experimental method

and tests conducted; finally, the change in autogenous and drying shrinkage achieved by each approach is presented as well as a discussion of the mechanism of action.

2.2 EXPERIMENTAL PROGRAM

2.2.1 Ingredients used for UHPC mix

Two types of cementitious binder were used, namely sulphate resisting cement and silica fume. The sulphate resisting cement, which contains 3-8% gypsum by weight, has a 28-day compressive strength of 60 MPa and a 28-day mortar shrinkage strain of 650 (microstrain) as determined through the tests performed as per AS 2350. 11 (Australian Standard 2006) and AS 2350. 13 (Australian Standard 2006), respectively. The undensified silica has a bulk density of 635 kg/m^3 and has a silicon dioxide (SiO_2) content over 89.6 %. A natural washed river sand with a maximum nominal grain size of 0.4 mm was used as the fine aggregate for all UHPC mixes. A third generation high range water reducer with an added retarder was added to each UHPC during the mixing. For the purpose of further minimizing shrinkage, a shrinkage reducing admixture (SRA), which meets and exceeds all requirements of Australian Standard 1478.1-2000 (Australian Standard 2000) as special purpose admixture type (SN), was added to the UHPC mix with different dosages. As an alternative to the use of an SRA, aiming to prevent the generation of a large amount of heat and therefore thermally and chemically induced plastic shrinkage cracks, the use of crushed ice to partially replace mixing water is also examined.

A total of ten batches of UHPC mortar were manufactured. The first five batches of UHPCs designated as U- series were prepared using the same water-to-binder (*w/b*) ratio but with different binder-to-sand (*b/s*) ratios. A UHPC mix with a *b/s* ratio of 1.266 and *w/b* ratio of 0.152, which was identified as optimal using the same raw materials in the previous study (Sobuz et al. 2016), was used as the reference mix design. Note that the water content from the chemical admixtures (i.e. 20% in SRA and 70% in SP) has been included in the calculation of

the water-to-binder ratio for each mix. In the first stage of testing, the compressive strengths and total shrinkage strains of five batches of UHPC with varying *b/s* ratio were measured. The mix with the overall best performance was then taken for the second stage of testing. This stage included: the addition of SRA to three mixes in dosages of SRA-to-cement weight ratio of 1, 2 or 3% (designated as SRA series) or the addition of crushed ice (designated as Ice series) was incorporated into the remaining two UHPC mixes as a partial replacement of water by a weight ratio of 25 or 50%. The proportions of all mixes are given in Table 2-1. For manufacturing UHPCs, all the dry materials, including sand and binders were initially mixed in an 80 L capacity rotating pan mixer with fixed blades for approximately 5 minutes. Following the dry mixing, water, crushed ice, superplasticizer and SRA, were subsequently added to the mixer and the mixing was continued until the concrete started to flow.

Table 2-1. Mix proportion of the UHPCs

Mix	Cement (wr)	Silica fume (wr)	Sand (wr)	water (wr)	Crushed ice (wr)	SRA[1] (wr)	SP[2] (wr)	*w/b*	*b/s*	Paste weight fraction	Mixing water weight fraction
U-0.8	0.632	0.168	1.000	0.104			0.024	0.152	0.800	0.480	0.063
U-0.9	0.711	0.189	1.000	0.117			0.027	0.152	0.900	0.509	0.067
U-1.0/SRA-0/Ice-0	0.790	0.210	1.000	0.130			0.030	0.152	1.000	0.535	0.070
U-1.1	0.869	0.231	1.000	0.143			0.033	0.152	1.100	0.559	0.073
U-1.266	1.000	0.266	1.000	0.165			0.038	0.152	1.266	0.593	0.078
SRA-1	0.790	0.210	1.000	0.129		0.008	0.030	0.152	1.000	0.535	0.070
SRA-2	0.790	0.210	1.000	0.127		0.016	0.030	0.152	1.000	0.535	0.070
SRA-3	0.790	0.210	1.000	0.126		0.024	0.030	0.152	1.000	0.535	0.070
Ice-25/75	0.790	0.210	1.000	0.098	0.033		0.030	0.152	1.000	0.535	0.070
Ice-50/50	0.790	0.210	1.000	0.065	0.065		0.030	0.152	1.000	0.535	0.070

1. Containing 20% water; 2. Containing 70% water

2.2.2 Test concepts and methods

To assess the effectiveness of each approach in reducing shrinkage, standard shrinkage tests were performed according to Australian Standard 2350.13 (Australian Standard 2006) over a

period of 180 days when subjected to constant environmental conditions (25°C and humidity < 50%).

To monitor the total shrinkage properties of UHPCs, square prism specimens which were 75 mm wide, and 285 mm long (shown in Fig.2-1 (a)) were regularly monitored to measure the change in length. To provide an indication of the drying shrinkage relative to the total observed shrinkage, autogenous shrinkage was determined from the length change of the prisms in Fig. 2-1(b) which were carefully sealed with water-proof aluminum tape to prevent the moisture loss to the environment.

| (a) | (b) |

Figure 2-1. Shrinkage test specimens: a) sealed prism for autogenous shrinkage measurement; b) unsealed prism for free total shrinkage measurements

It is known that the evolution of autogenous shrinkage of cementitious composite is strongly related to the time when the paste develops a 'stable' solid skeleton to transfer tensile stress, which is defined as 'time-zero' for autogenous shrinkage measurement. In the present study, the final setting time obtained from calorimetry curve was adopted as the 'time-zero' where autogenous shrinkage initiated in according to ASTM C1698-09 (ASTM 2009) and the studies reported previously (Darquennes et al. 2011; Mechtcherine et al. 2014).

To further characterize the materials tested, and in order to identify the mechanisms controlling the change in shrinkage, a series of further material and characterization tests were undertaken as follows:

2.2.2.1 Compressive strength

The compressive strengths (f'_c) of the UHPCs at different concrete ages were obtained through axial compression tests, performed on cylinders (100mm diameter × 200mm height) in accordance with Australian Standard (Standard Australia 2014).

2.2.2.2 Flowability and passing ability

The rheological properties of each mix was assessed through a slump flow test performed in accordance with ASTM standard C143/C143M (ASTM International 2000) and a flow-table test according to ASTM C1621 (ASTM International 2009) including the use of a J-ring to assess passing ability around reinforcement.

2.2.2.3 Exothermic reaction at early curing ages

Heat generated as a result of the exothermic reaction associated with cement hydration accelerates the autogenous shrinkage of the concrete (Kadri and Duval 2009; Langan et al. 2002) and may result in the formation of micro-cracks (Aitcin 1999; Kim et al. 2011; Lura et al. 2003). To examine the exothermic reaction of the UHPCs, a thermal sensor was embedded at the center of a 100 mm cubic specimen. The ambient room temperature and internal concrete temperature was also continuously recorded monitored for a period of three days, after which no significant change in temperature occurred.

2.2.2.4 Unit weight and porosity

The unit weight of the hardened UHPCs was obtained by weighing concrete cylinders (100mm diameter ×200 mm height) 90 days after casting, such that the hydration reaction can be considered to be complete. The porosity of each series of the UHPC was quantified by measuring the volume of pore space voids in disc specimens of 150 mm diameter and 50 mm thickness through tests performed in accordance with ASTM C642-13 (ASTM International 2013) using a hot water bath. Measurements of porosity were taken because porosity of concrete is an essential indicator associated with not only the mechanical strength but also the durability characteristics of the concrete.

2.2.2.5 Scanning electron microscopy (SEM) analysis and Energy-dispersive X-ray spectroscopy (EDS)

Scanning electron microscopy (SEM) characterization was performed to evaluate the microstructure of the UHPC matrix and hence assist in identifying the: unreacted binder component, homogeneity of the matrix, and pores and cracks seen in the microstructure of the matrix. Energy-dispersive X-ray spectroscopy (EDS) analysis was also conducted to identify any change in the hydration products resulting from the shrinkage reduction methods applied.

2.2.2.6 Thermal gravity (TG) analysis

Thermal gravity (TG) analysis was undertaken to estimate the degree of hydration of the UHPC 90-days after casting. The analysis was undertaken to assess both the non-evaporable water content and the calcium hydroxide ($Ca(OH)_2$) content. These approaches have been commonly applied cementitious mortar, for example see (Bentz 2005; Chen and Wu 2013; Maltais and Marchand 1997).

TG analysis was conducted using METTLER TOLEDO TGA testing machine, for each mix a sample weighing 2.5 kg was oven-dried at 105 °C for 24 hours to remove the evaporable water, and the sample was then pulverized to a size of < 45μm. About 20 μg of this sample was placed in a ceramic crucible and heated in the furnace from ambient temperature to 900 °C in a nitrogen atmosphere at a rate of 10 °C/min to determine the weight loss of matrix due to decomposition of the hydration products.

2.2.2.6.1 Non-evaporable water content

The amount of hydration products and the degree of hydration (D_h) of UHPC is obtained by determining the non-evaporable water content (W_{ne}) using loss-on-ignition (LOI) method. Cementitious paste is commonly used for this test as the non-evaporable water content is present due to the reactive cementitious binders only, and the degree of hydration is strongly correlated with the *w/b* ratio of the cementitious paste (Huang et al. 2017; Lam et al. 2000; Yio et al. 2014). The effects of coarse and fine aggregates on hydration are usually ignored due to their inertness. It is worth noting that in this study cement mortar was used instead of cement paste as the: pore diameter, paste-to aggregate interfacial transition zone (ITZ), distribution of aggregate and the mixing efficiency are all affected by the aggregate content, and hence their effects on hydration cannot be neglected. The LOIs of the UHPC mortar were estimated using the LOIs of cementitious powder without moisture damage and considering the LOIs of the sand (Bentz 2005; Chen and Wu 2013; Maltais and Marchand 1997).

Previous studies by Lam et al. and Wong et al. (Lam et al. 2000; Wong and Buenfeld 2009) have shown that absolute hydration of 1g anhydrous cement can produce approximately 0.23g of non-evaporable water and this non-evaporable water content-to-cement ratio (W_{ne0}/C_0) of

0.23g/g was applied as the reference value to determine the degree of hydration of the UHPCs in the following calculations for D_h.

To calculate D_h, the LOI_{raw} of the raw cementitious powder, silica fume and sand are firstly calculated using:

$$LOI_{raw} = \frac{(W_{d-raw} - W_{i-raw})}{W_{i-raw}} \tag{2-1}$$

where W_{d-raw} is the dry weight of the as-received raw material, and W_{i-raw} is the ignited weight of the as-received raw material after TG test. These LOI_{raw} values are required to correct the calculations of non-evaporable water content (W_{ne}) as follows:

$$W_{ne} = [W_{d-U} - W_{i-U} * (1 + \sum LOI_{raw})] \tag{2-2}$$

where W_{d-u} is the dry weight of the UHPC mortar sample, W_{i-u} is the ignited weight of the UHPC mortar sample after TG test and $\sum LOI_{raw}$ is the total ignited weight of the as-received raw materials, including sand cement and silica fume. The effective residual cementitious binder content (C_{eff}) is calculated by

$$C_{eff} = \left[W_{i-U} * (1 - \frac{\sum LOI_{raw}}{W_{ne0}/C_0})\right] \tag{2-3}$$

Finally, the degree of hydration of UHPC (D_h) is defined as the function of W_{ne}, effective residual cementitious binder content (C_{eff}) and the reference value of the non-evaporable water content-to-cement ratio (W_{ne0}/C_0), as given in Eq. (2-4):

$$D_h(\%) = \frac{W_{ne}/C_{eff}}{W_{ne0}/C_0} \times 100 \tag{2-4}$$

The loss of the non-evaporable water that is chemically bonded in hydration products can be determined by calculating the difference in weights between at 100^0C and $700\,^{\circ}C$ from TG. This temperature interval is selected to avoid the interference due to the water evaporation at $100\,^{\circ}C$ and de-carbonation of calcium carbonate ($CaCO_3$) of the composite when the temperature overs $700\,^{\circ}C$ (Vedalakshmi et al. 2003).

2.2.2.6.2 Calcium hydroxide (Ca(OH)$_2$) content

A fully hydrated cementitious-silica fume material usually consists of dicalcium silicate (C$_2$S) and tricalcium silicates (C$_3$S) (Brunauer and Kantro 1964; Hasanzadeh et al. 2016; Newman et al. 2005). The formations of these calcium silicates (C$_n$S) consume around 20-25 % by weight of the water in the mix and produce 20-25 % by weight of the calcium hydroxide (Ca(OH)$_2$). Therefore, the degree of hydration of the UHPC can also be assessed by the Ca(OH)$_2$ content in the concrete. The amount of Ca(OH)$_2$ products can be determined by calculating the drop in weight of the sample within 400 to 450 °C during TG tests (Dweck et al. 2000; Vedalakshmi et al. 2003), which indicates the decomposition of Ca(OH)$_2$ in the hydration products.

In the remainder of the paper the effectiveness of each shrinkage reduction approach including 1) reducing binder usage; 2) using SRA; 3) partially reducing mixing water with crushed ice will be presented and the mechanism of their action explored using the characterization tests above.

2.3 EFFECT OF BINDER-TO-SAND RATIO ON THE PROPERTIES OF THE UHPCS

2.3.1 Flowability of concrete

Table 2-2 presents the results of slump flow and flow-table tests of the UHPC specimens, from which it can be inferred that the flow- and passing ability of the UHPC generally increased with an increase in the *b/s* ratio. This can be attributed to the fact that the increased *b/s* ratio in the UHPC mix resulted in an increased volume of paste that covered the surface of the fine aggregates leading to the reduction in friction between the sand particles in the fresh UHPC (Hermida et al. 2009).

Table 2-2. Influence of binder-to-sand ratio on rheological properties of fresh UHPCs

Specimen	*b/s* ratio	Slump (mm)	Flow table (mm)	J-ring (mm)
U-0.8	0.8	165	375	412
U-0.9	0.9	240	440	451
U-1.0	1	235	425	443
U-1.1	1.1	250	430	455
U-1.266	1.266	250	470	506

2.3.2 Autogenous shrinkage

The autogenous shrinkage strains (ε_a) plotted in Fig. 2-2 for each mix with a different *b/s* ratio, were measured using the sealed prisms shown in Fig. 2-1(b). These values can be seen to decrease with an increase in *b/s* ratio. Further it is also observed that for all mixes, regardless of the variation in *b/s,* the autogenous shrinkage began to plateau 42 days after casting, indicating the completion of hydration. At the concrete age of 42 days, the ε_a of U-1.266 was up to 35% lower than those of the companion specimens. Furthermore, the UHPC prepared using a higher *b/s* ratio (i.e. U-1.1 and -1.266 series) exhibited a lower rate of autogenous shrinkage gain which can be inferred by the reduced slope of the curves.
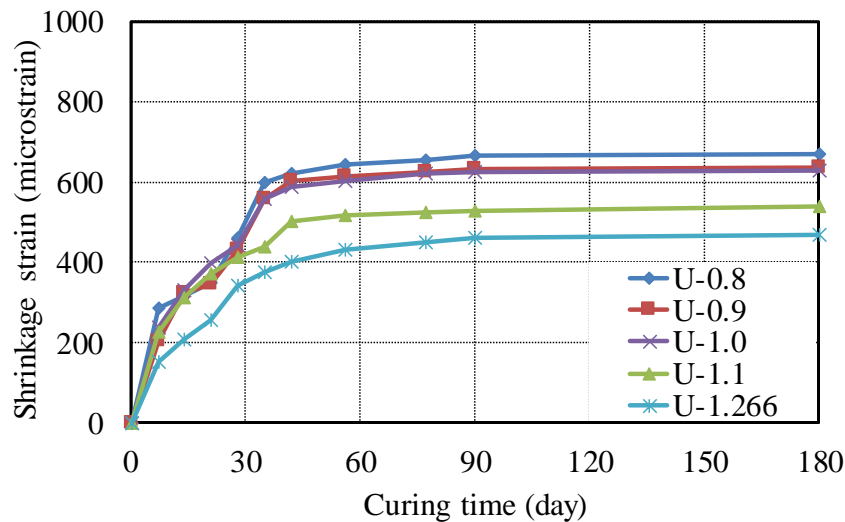

Figure 2-2. Effect of binder-to-sand ratio on autogenous shrinkage

Moreover, when comparing the autogenous shrinkage strains in Fig. 2-2 with those expected from conventional concrete (e.g. (Bentur et al. 2001; Zhang et al. 2003)) for a given age (i.e.

concrete age of 28 days), the autogenous shrinkage of UHPCs (>400 macrostrain) are significantly higher than those of the conventional normal- and high- strength concrete (< 150 macrostrain). This difference is because the increased binder and reduced mixing water in UHPC means it tends to undergo a more rapid self-desiccation than conventional concrete and potentially to form more micro-cracks as further shown and discussed in Section 2.3.9.

2.3.3 Free total shrinkage

Figure 2-3 illustrates the effect of *b/s* ratio on free total shrinkage measured using the unsealed prisms shown in Figure 2-2(a). Similar to the results of the autogenous shrinkage tests, the free total shrinkage strains (ε_t) of the UHPC specimens generally decreased with an increase in *b/s* ratio for a given concrete age. Unlike the autogenous shrinkage tests, where the shrinkage deformations stabilized at 42 days, it is observed that the free total shrinkage increased in all five mixes continued up to the concrete age of 90 days. This is due to the continuous drying of the UHPCs, which is associated with loss of moisture from the concrete to the environment and is in contrast to the significant slowing of autogenous shrinkage after 42 days as a result of the decreased rate of hydration.
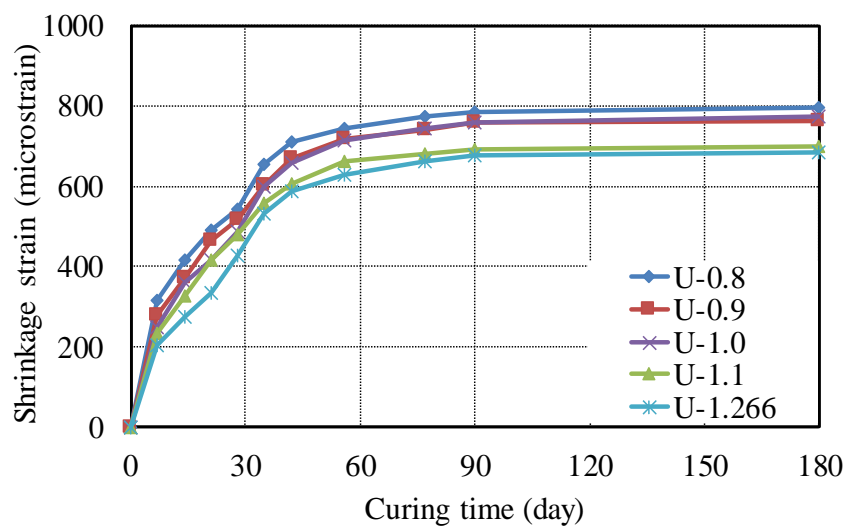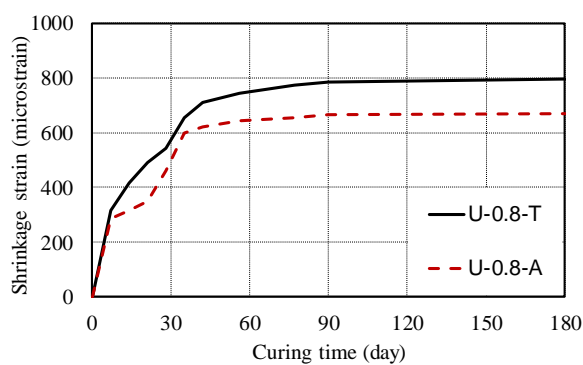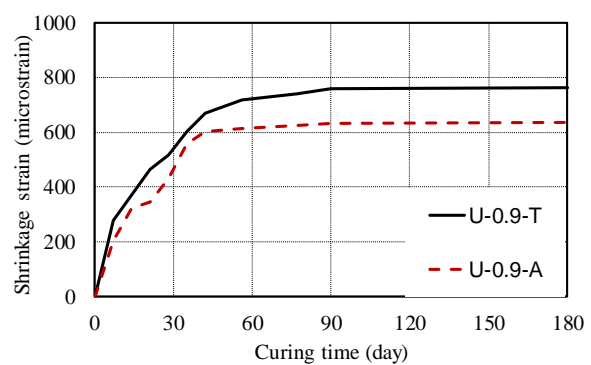

Figure 2-3. Effect of binder-to-sand ratio on free total shrinkage

2.3.4 Assessment of free drying component

The free drying shrinkage component of the UHPCs can be estimated and assessed by the difference between the free total (solid line) and autogenous (dashed line) shrinkage properties shown in Fig. 2-4 (a) to (e). It is evident from the Fig. 2-4 that at the early curing ages (i.e. before the concrete age of 7 days), the difference between the free total and autogenous shrinkage of each UHPC series was negligible. The difference between the ε_a and ε_t of each series increased up to 110% with an increase in the *b/s* ratio from 0.8 to 1.266 at the concrete age of 180 days. Note that although the *w/b* ratio for a UHPC mix is low, with adequate mixing energy the moisture (including water and superplasticizer) can be evenly distributed to form a high paste volume (Russell and Graybeal 2013; Schießl et al. 2007). This suggests that more moisture was able to diffuse from the UHPC for mixes with a higher paste volume owing to the higher *b/s* ratio, as reported in Table 2-1, and the observation is in consistent with previous research (Ma et al. 2004; Shen et al. 2016; Soliman and Nehdi 2013). In addition, as illustrated in Fig. 2-4 (a) and (b), the drying shrinkage component of each specimen was significantly lower than the corresponding autogenous shrinkage at each given concrete age, indicating that the autogenous shrinkage predominates the overall free total shrinkage of UHPCs.
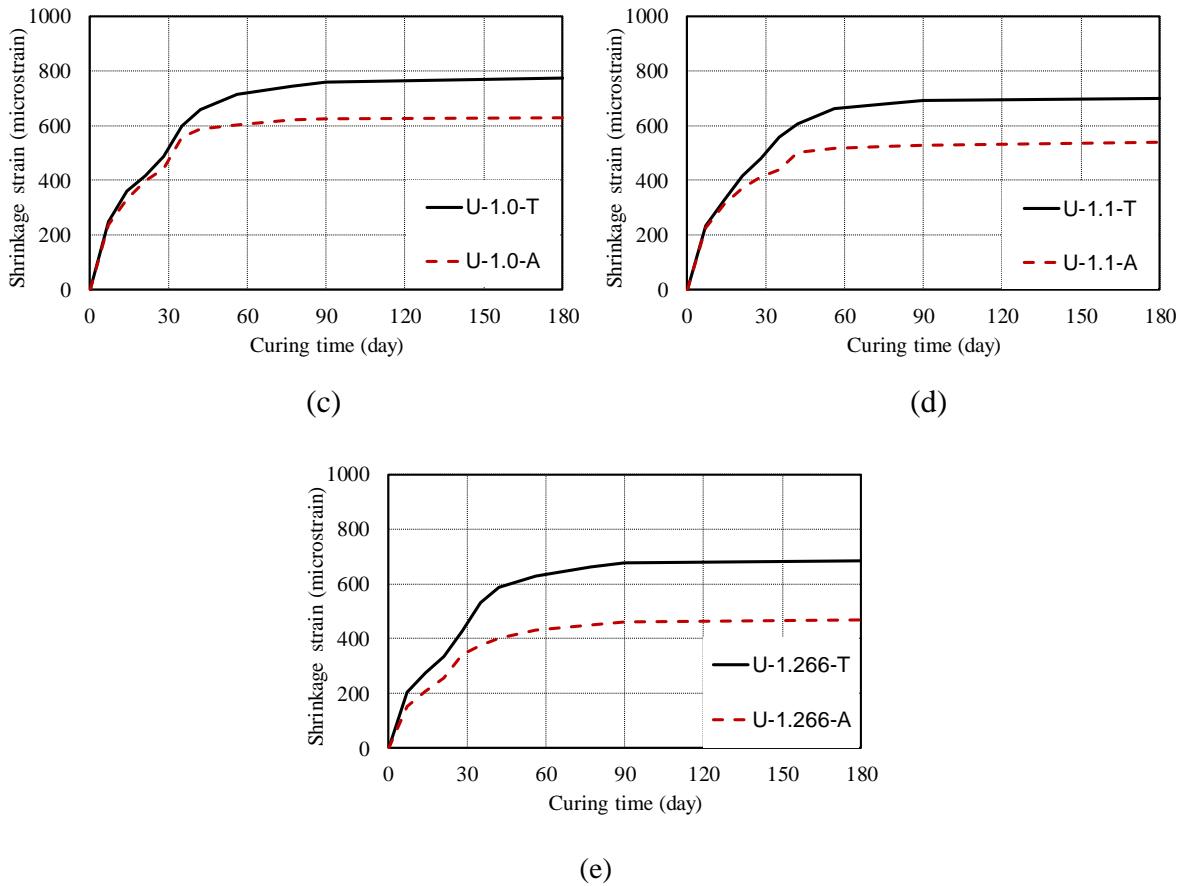

(a)　　　　　　　　　　　　　　　　(b)

Figure 2-4. Effect of binder-to-sand ratio on free drying component: a) U-0.8; b) U-0.9; c) U-1.0; d) U-1.1; (e) U-1.266

2.3.5 Assessment of free drying component

The free drying shrinkage component of the UHPCs can be estimated and assessed by the difference between the free total (solid line) and autogenous (dashed line) shrinkage properties shown in Fig. 2-4 (a) to (e). It is evident from the Fig. 2-4 that at the early curing ages (i.e. before the concrete age of 7 days), the difference between the free total and autogenous shrinkage of each UHPC series was negligible. The difference between the ε_a and ε_t of each series increased up to 110% with an increase in the *b/s* ratio from 0.8 to 1.266 at the concrete age of 180 days. Note that although the *w/b* ratio for a UHPC mix is low, with adequate mixing energy the moisture (including water and superplasticizer) can be evenly distributed to form a high paste volume (Russell and Graybeal 2013; Schießl et al. 2007). This suggests that more

moisture was able to diffuse from the UHPC for mixes with a higher paste volume owing to the higher *b/s* ratio, as reported in Table 2-1, and the observation is in consistent with previous research (Ma et al. 2004; Shen et al. 2016; Soliman and Nehdi 2013). In addition, as illustrated in Fig. 2-4 (a) and (b), the drying shrinkage component of each specimen was significantly lower than the corresponding autogenous shrinkage at each given concrete age, indicating that the autogenous shrinkage predominates the overall free total shrinkage of UHPCs.

2.3.6 Compressive strength

The effect of *b/s* ratio on f'_c is shown in Fig. 2-5. It is observed that the U-1.266 series developed a lower compressive strength than the other four companion mixes for a given age. The reduction in strength associated with the reduction in fine aggregate could be a result of the mechanism of stress transfer within the concrete as per the well-known theory for conventional mortars (Reddy and Gupta 2008). That is the transfer of normal force in a mortar is largely due to the interaction of sand to sand interfaces. For the UHPC with a lower *w/b* ratio, its compressive strength is not predominated by failures of cementitious paste but by adhesive failures between aggregates and cementitious materials (Jun et al. 2004; Park et al. 2008). The presence of excessive unhydrated cementitious materials in the UHPC series with higher binder content weakened the interfacial transition zones (ITZs) between the fine aggregate and binder, which led to the observed reduction in compressive strength. It is also worth noting in Fig. 2-5 that, all these five UHPC series experienced reduction (up to 5.3%) in their compressive strengths within the curing age from 90 to 180 days, as shown in Fig. 2-5. This reduction in the f'_c was caused by the formation of internal micro cracks (discussed further in section 2.3.9) as a consequence of the increased shrinkage of the concrete (Sobuz et al. 2016). The above observations indicate that the most appropriate *b/s* ratio for UHPC should be within 1 to 1.1 to achieve adequate aggregate interaction without compromising the f'_c.
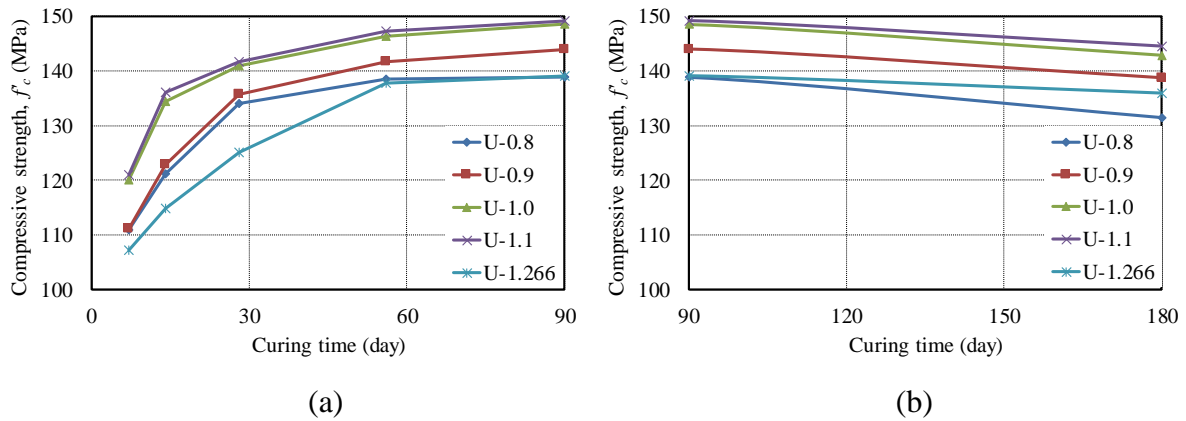
Figure 2-5. Effect of binder-to-sand ratio on compressive strength: (a) curing time from 0 to 90 day; (b) curing time from 90 to 180 day

2.3.7 Unit weight and porosity of the UHPCs

Figure 2-6 shows the effect of *b/s ratio* on the unit weight and porosity of the hardened UHPCs measured at the concrete age of 28 days. It is observed that the unit weight of the UHPC increased with an increase in *b/s* ratio due to the higher unit weight of the cementitious materials (approximate 3500 kg/m^3) compared to that of the sand (approximate 2000 kg/m^3). The porosity of the UHPC also decreased approximately 10 % with an increase in *b/s* ratio from 0.8 to 1.266. This reduction in porosity may be attributed to the increased amount of residual unhydrated binder which fills the pore spaces. The reduction in binder also reduces the total amount of porous ITZs around the sand particles (Brough and Atkinson 2000; Scrivener et al. 2004).
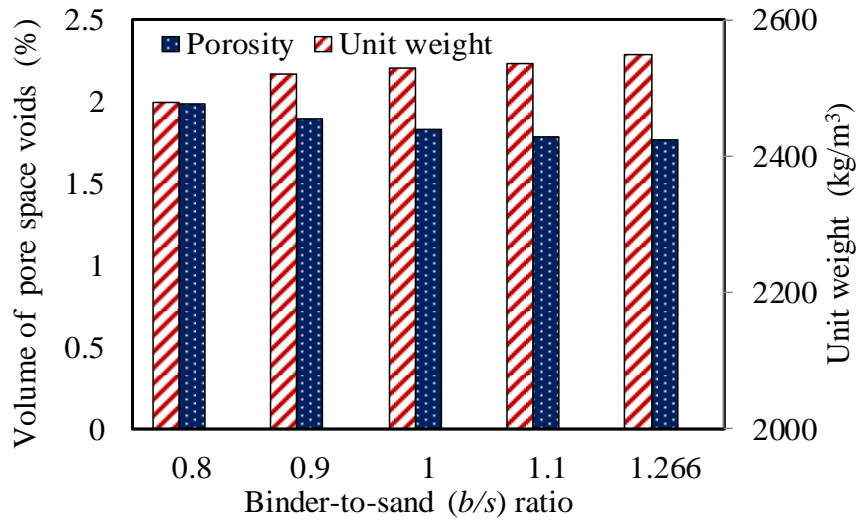
Figure 2-6. Effects of binder-to-sand ratio on unit weight and porosity of hardened UHPCs

2.3.8 Exothermic reaction at early curing period

Figure 2-7 illustrates the variations of internal temperature of the five different specimens with the curing time. It is worth noting that the temperature measured at the center of each UHPC series was normalized by the corresponding ambient temperature in order to remove its influence. From the calorimetry curves in Fig. 2-7, it can be observed that a decrease in *b/s* ratio led to an increase in the magnitude of the peak temperature measured at the center of the sample, with the maximum magnitude of change being approximately 10%. The increase in temperature with a reduction in *b/s* indicates that the UHPC with a lower *b/s* ratio had a higher degree of exothermic reaction and generated more heat as the consequence of a higher degree of reaction. This is due to the residual unhydrated binders in the UHPC with a higher *b/s* which act to fill the pores and voids and absorbed water to their surface, which hindered the level and rate of hydration in the concrete (Yu et al. 2014). These facts can be further verified using the TG analysis and SEM characterizations presented in the following sections. The above observation indicates that the UHPC prepared using a lower *b/s* ratio underwent a more significant chemical reaction process, which consumed more raw materials and achieved a higher degree of hydration. Therefore, UHPC prepared using a lower *b/s* ratio tended to have

a more significant autogenous shrinkage at the early curing stage, which can be inferred from the curves in Fig. 2-2.
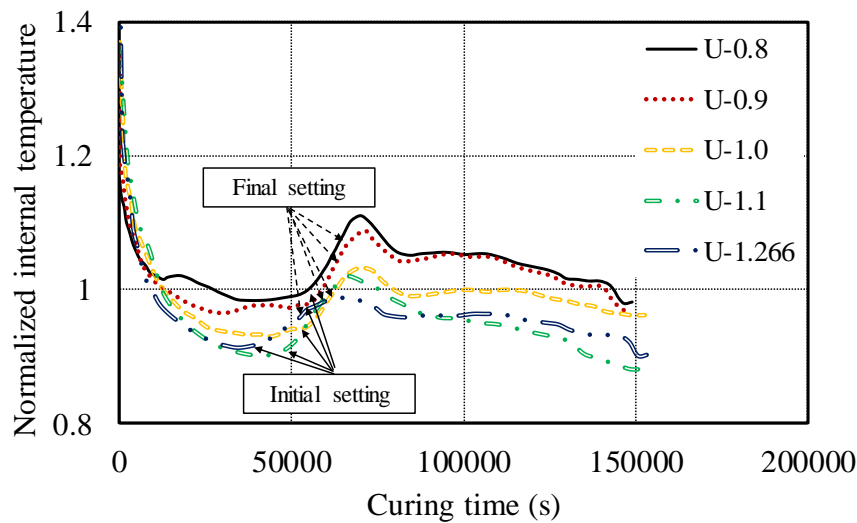

Figure 2-7. Effect of binder-to-sand ratio on variations of the internal temperature with curing time

The initial and final setting times of each mix can be identified as the first trough and the end point of the linear ascending branch on the calorimetry curves in Fig. 2-7. These points were also affected by the *b/s* ratio, in which the initial and final setting time of the UHPC were delayed by approximately 4 hours when the highest quantity of aggregate was considered. This could be explained by the fact that the increased amount of aggregates hindered the contact between water and binder which led to a longer induction period (referred to the initial gentle trough stage) and resulted in this later setting of the concrete (Jennings and Pratt 1979; Odler 1998).

2.3.9 Morphological characterization by scanning electron microscopy (SEM) and Energy-dispersive X-ray spectroscopy (EDX)

The scanning electron microscopy (SEM) micrographs were evaluated to investigate the effect of *b/s* ratio on the microstructure of the UHPCs, as depicted in Figs. 2-8 and 2-9 at different

magnifications. It is evident from the SEM micrographs at 1000× magnification that the increased volume of cementitious paste (at higher *b/s* ratio) led to a much denser microstructure as a result of the reduction in volume fraction of the porous aggregate-paste ITZs. This fact also caused by the micro-filler effect offered by unreacted cementitious binders. Moreover, as shown on the SEM micrographs at 10000× magnification, a large amount of ettringite ($3CaO \cdot Al_2O_3 \cdot 3CaSO_4 \cdot 32H_2O$) and calcium hydroxide (C-H) were observed and characterized using EDX spectroscopy in the microstructure of the UHPC prepared using the lower *b/s* ratio (i.e. U-0.8, and -0.9). This is because the increased porosity in the concrete provided the space for the growth of ettringite and C-H crystals owing to their expansive nature (Mehta 1973). For the UHPC prepared using a relatively higher *b/s* ratio (i.e. U-1.0, -1.1 and -1.266), a larger amount of unreacted cementitious materials were detected, as indicated in Fig. 2-9. Ettringite and C-H crystals were rarely observed in the matrix of U-1.0, -1.1 and -1.266 series owing to the increased denseness and reduced pore space in their matrix shown in Fig. 2-8. The presence of these unreacted binders may restrain the shrinkage of the matrix contributing to the reduction in autogenous- and drying- shrinkage shown in Figs. 2-2 and 2-3. The presence of the unreacted binder is also a clear indication of the decreased degree of hydration in the UHPC prepared using a higher *b/s* ratio. It is worth mentioning that the observed increased pore space in UHPC adversely affected the drying shrinkage of the concrete, which seemingly contradicts to the observations reported in the literature (Han and Lytton 1995). The possible explanation is that the expansion resulting from the abundance of crystalline ettringite and C-H in the pores and cracks was more significant than the drying shrinkage of the concrete (Mehta 1973; Yan et al. 2004). To verify the deduction on the decrease in mechanical strength of UHPC after a long-term curing, Fig. 2-10 illustrates a representative SEM micrograph of U-1.1 series with the indications of the micro-cracks that were induced by thermal and autogenous shrinkage.
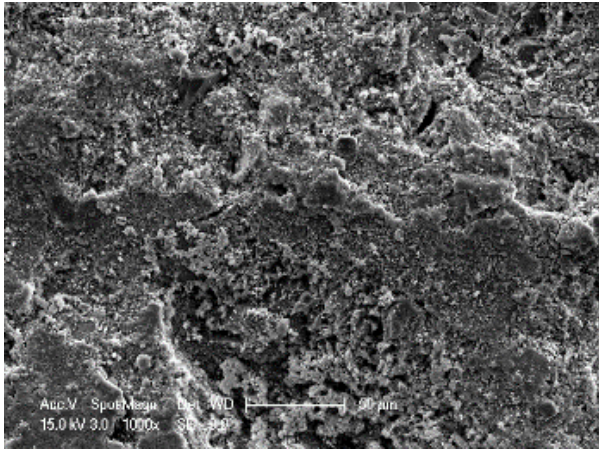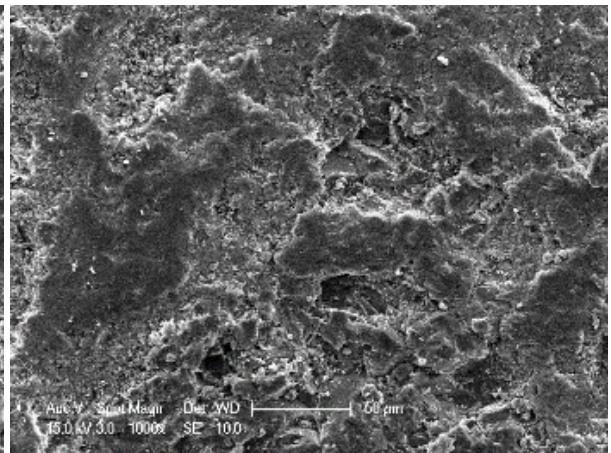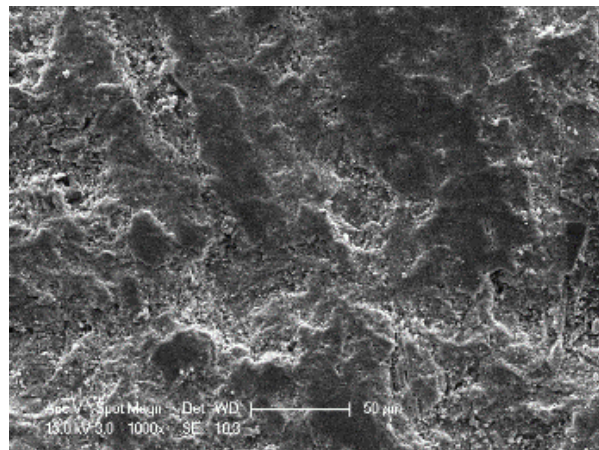
(a)
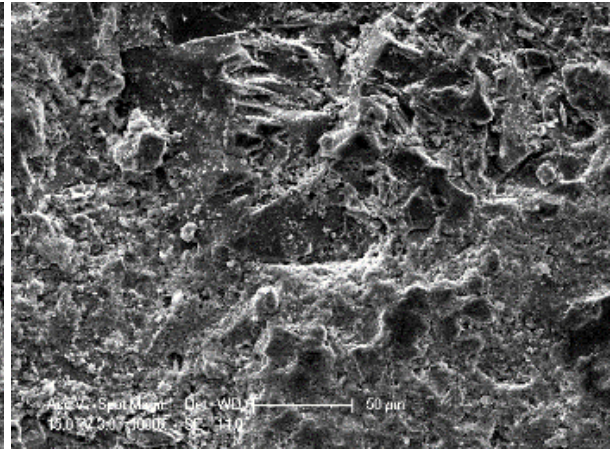
(b)
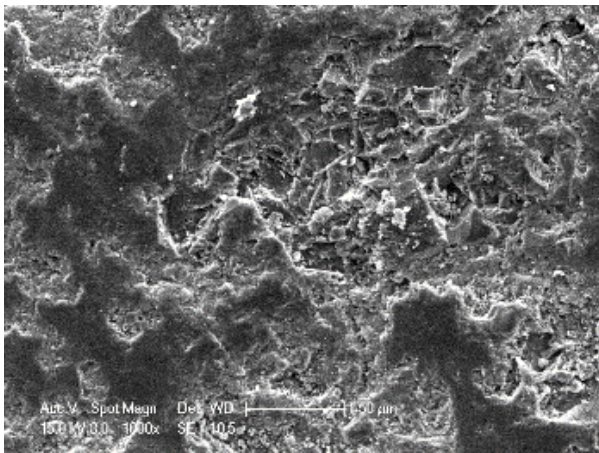
(c)

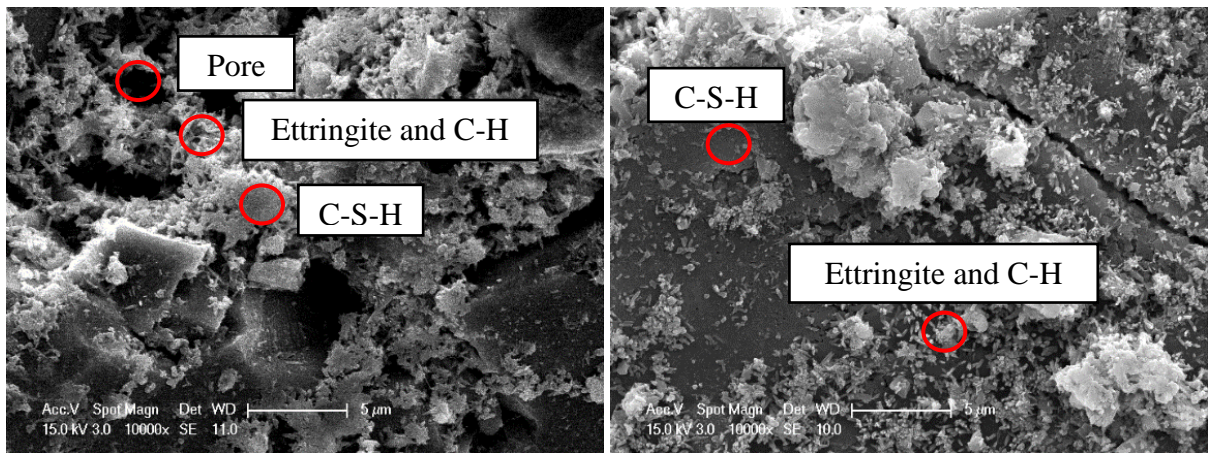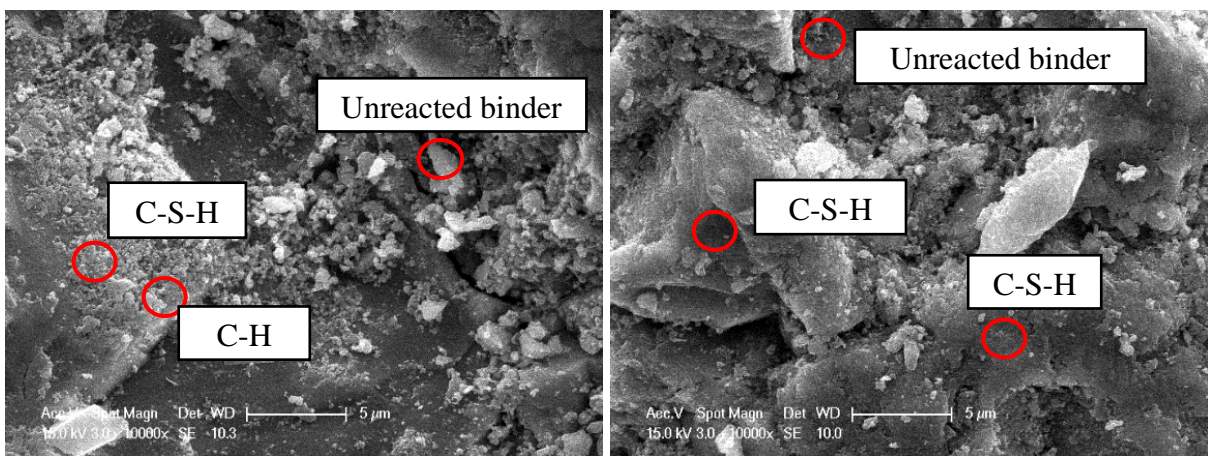(d)

(e)

Figure 2-8. SEM images of the fracture surface of the UHPCs (1000× magnification): a) U-0.8; b) U-0.9; c) U-1.0; d) U-1.1; e) U-1.266
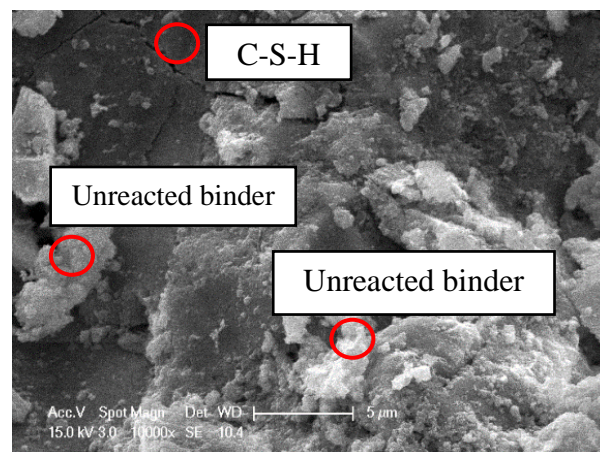
Figure 9. SEM images of the fracture surface of the UHPCs (10000× magnification): a) U-0.8; b) U-0.9; c) U-1.0; d) U-1.1; e) U-1.266
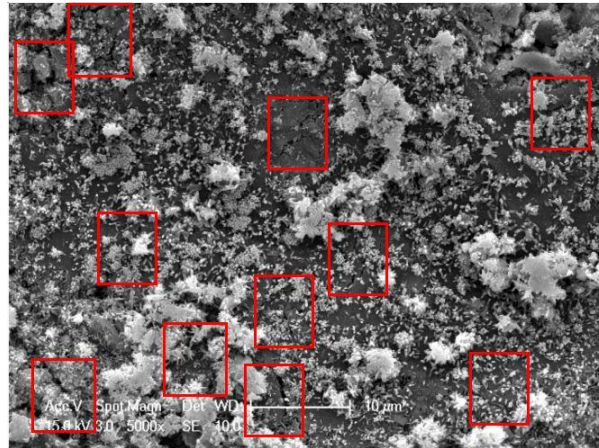
Figure 2-10. Observed shrinkage induced micro-cracks in the micro-structure of the UHPC

2.3.10 Results of thermal gravity (TG) analysis

The TGA curves of the comparing UHPCs are shown in Fig. 2-11 and the effect of binder to sand ratio on the degree of hydration and C-H content are shown in Fig. 2-12. It should be noted that the paste weight fraction factor for each specimen series, as given in Table 2-1, was considered in the calculations of the chemically bonded water and C-H content of the paste that is the actual materials for hydration. In general, except for U-0.8 series, the calculated degree of hydration and the C-H content decreased with an increase in the *b/s* ratio (i.e. up to approximately 18% lower). While the *w/b* ratio remained the same for the mixes being compared, the UHPC prepared using a higher *b/s* underwent a lower degree of hydration and hence contained less hydration products. This further confirmed the previously observed less significant autogenous shrinkage for the UHPC prepared using a lower *b/s* ratio.
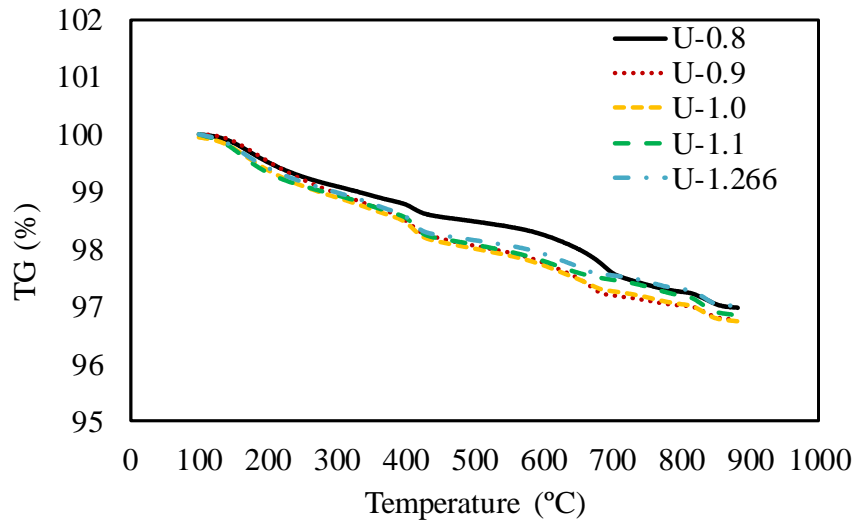
Figure 2-11. TG analysis for U-0.8, -0.9, -1.0, -1.1, and -1.266 UHPC series
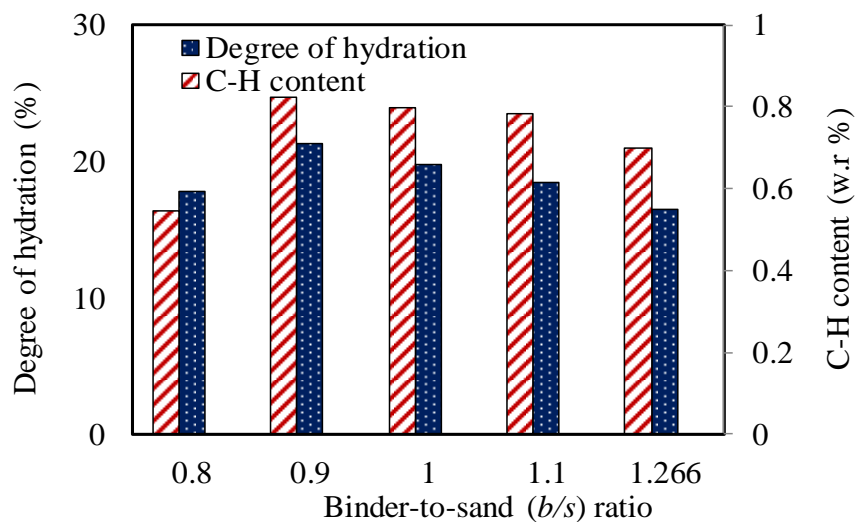
Figure 2-12. Effect of binder-to-sand ratio on degree of hydration and C-H content

2.3.11 Selection of the mix for further investigations to migrate autogenous shrinkage

A comprehensive study of the experimental results of among U-0.8,-0.9, -1.0 -1.1 and -1.266 UHPC series led to the selection of the mix design of U-1.0 as the mix for further investigation. These investigations include: the incorporation of shrinkage reducing admixture (SRA) and the used crushed ice to partially replace mixing water. Mix designs for the second stage of this work are shown in Table 2-3.

Table 2-3. Effect of SRA content on rheological properties of fresh UHPCs

Specimen	*b/s* ratio	SRA content (%)	Slump (mm)	Flow table (mm)	J-ring (mm)
SRA-0	1	0	235	425	443
SRA-1	1	1	280	512	529
SRA-2	1	2	Full	579	568
SRA-3	1	3	Full	560	585

2.4 EFFECTS OF APPLIED TECHNIQUES ON THE PROPERTIES OF THE UHPCS

2.4.1 Flowability

2.4.1.1 Effect of shrinkage reducing admixture (SRA) content

For the flow test results reported in Table 2-3, it can be seen that the UHPC series prepared with a higher SRA content exhibited better flowability and passing ability. This is due to the higher liquid content (i.e. 80% of the organic liquid component in SRA) in the UHPC mix with a higher SRA content that provides better lubrication, resulting in a better rheology of the UHPC.

2.4.1.2 Effect of crushed ice dosage

The flow test results presented in Table 2-4 indicate that that the replacement of water with crushed ice had negligible impact on the flowability and passing ability of the UHPC as the added crush ice completely melted after sufficient mixing. The temperature of the mixing water was recorded immediately prior to adding to the mixer. For mixes without using crushed ice the water temperature was found to be the same as the ambient temperature (i.e. 25 °C) while for water with crushed ice the temperature was found to be 2.6°C and 1.2°C at 25% and 50% replacement ratio (by weight) respectively. The incorporations of crushed ice in a UHPC mix are expected to reduce the internal temperature of the specimens and hence lessen the potential formations of thermal cracks.

Table 2-4. Effect of crushed ice dosage on rheological properties of fresh UHPCs

Specimen	*b/s* ratio	Crushed ice dosage (%)	Slump (mm)	flow table (mm)	J-ring (mm)
Ice-0	1	0	235	425	443
Ice-25/75	1	25	240	418	456
Ice-50/50	1	50	235	431	462

2.4.2 Autogenous shrinkage

2.4.2.1 Effect of shrinkage reducing admixture (SRA) content

Figure 2-13 shows the effects of SRA contents on the autogenous shrinkage of the UHPC. It can be seen that the ε_a of the UHPC decreased significantly with an increasing SRA content (up to approximately 69% for UHPC at age of 90 days). It is also observed that the SRA started reducing the autogenous shrinkage right after the initial casting of the UHPC. As stated by Collepardi et al., Folliard et al. (Collepardi et al. 2005; Folliard and Berke 1997) and Lura et al. (Lura et al. 2003), SRA incorporation eases the surface tension in the capillary pores of the concrete and subsequently reduces the drying- and autogenous- shrinkage of the concrete. The reduction in autogenous shrinkage with incorporation of SRA seen in the present study is also in reasonable agreement with those reported by studies on UHPC mortar. For example, Su et al. (Anshuang et al. 2017) reported an up to 95% reduction in autogenous shrinkage with 2% SRA dosage at 7 days (compared to 65.6 % as reported in the present study) and an approximated 61% reduction in autogenous shrinkage with 2% SRA dosage at 160 days was observed by Soliman and Nehdi (Soliman and Nehdi 2014) (compared to 57.8% as reported in the present study). In addition, the comparison of the efficacy of using SRA on autogenous shrinkage between UHPC and conventional cementitious mortar (i.e. as reported in (Bentz et al. 2001)) suggests the nearly the same performance of SRA to reduce autogenous shrinkage at a given dosage of SRA.
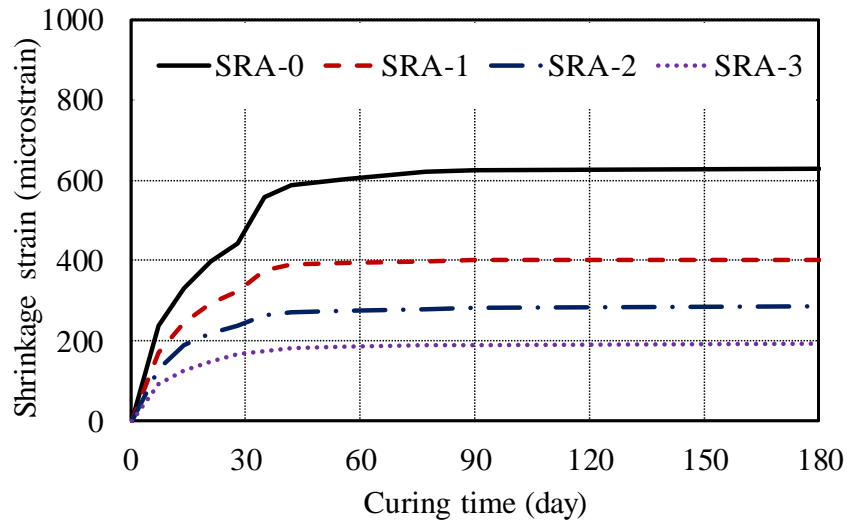
Figure 2-13. Effect of SRA content on autogenous shrinkage properties

2.4.2.2 Effect of crushed ice dosage

The effect of crushed ice on the autogenous shrinkage of the UHPCs is depicted in Fig. 2-14.

At each given curing age, the UHPC manufactured using a higher crushed ice exhibited a lower

ε_a (up to approximately 19 % at concrete age of 180 days). This observation is expected as the

internal temperature of UHPC decreased with the incorporation of crushed ice, which led to

the deceleration of the rate of hydration of the concrete and hence reduced autogenous
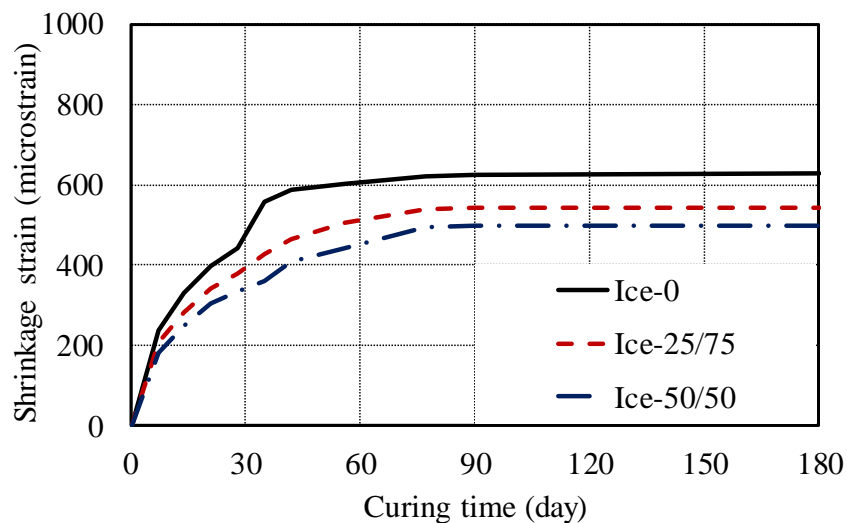
shrinkage.

Figure 2-14. Effect of crushed ice dosage on autogenous shrinkage properties

2.4.3 Free total shrinkage and assessment of free drying component

2.4.3.1 Effect of shrinkage reducing admixture (SRA) content

The effect of SRA content on the free total shrinkage of the UHPC is illustrated in Fig. 2-15, where it can be seen that the UHPC prepared using a higher content of SRA exhibited a lower ε_t. Fig. 2-16 (a) to (c) illustrate the comparisons between the free total shrinkage and the autogenous shrinkage at all curing ages of each of the four comparing UHPC series, in which the difference between the free total shrinkage and the autogenous shrinkage of each UHPC series yields approximately the free drying shrinkage component of the concrete. It is observed that the UHPC prepared using a higher SRA content developed a lower drying shrinkage than their counterparts with lower SRA contents. This observation is consistent with the findings of previous studies by Yoo et al. (Yoo et al. 2013; Yoo et al. 2014) and suggests that the SRA is particularly effective to mitigate the free drying shrinkage of the UHPC through reducing the surface tension in the capillary pores of the concrete during the drying process.
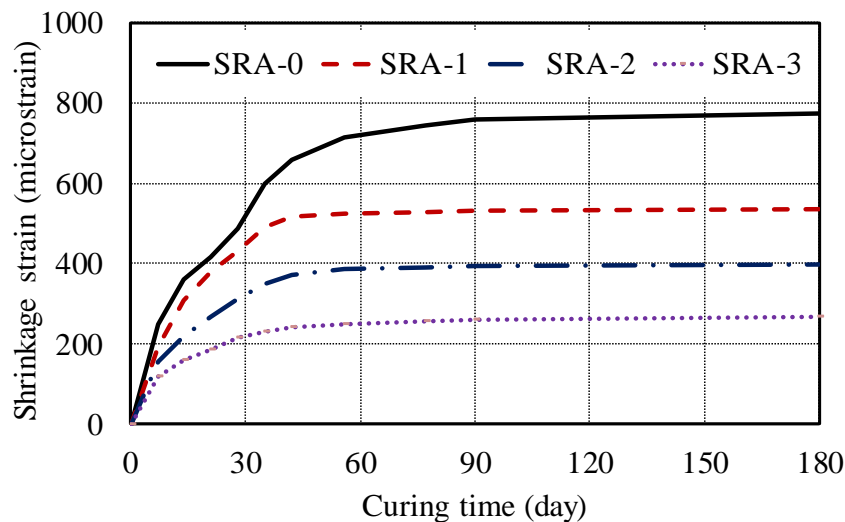
Figure 2-15. Effect of SRA content on total shrinkage
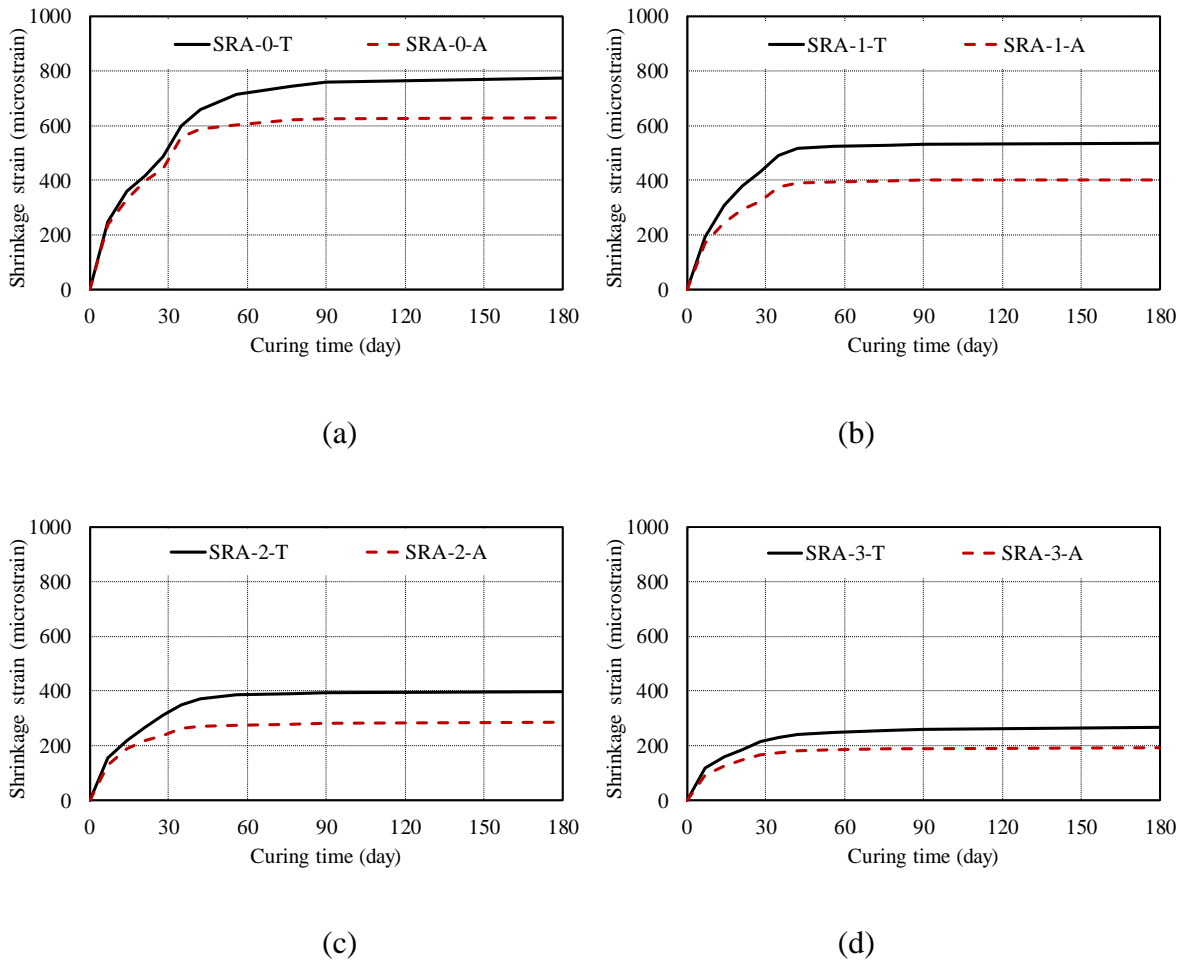
Figure 2-16. Effect of SRA content on free drying component: (a) SRA=0%; (b) SRA=1%; (c) SRA=2%; (d) SRA=3%

2.4.3.2 Effect of crushed ice

The ε_t of the UHPC series with different crushed ice dosages were also periodically measured up to the concrete age of 180 days and illustrated in Fig. 2-17 as the corresponding values of the ε_r and ε_a are also shown in Fig. 2-18. It is observed that the ε_t of the UHPC decreased with an increase in crushed ice dosage whereas the replacement of mixing water with crushed ice led to no impact on the free drying shrinkage property of the concrete. This is observed because the drying shrinkage only depends on the moisture movement out of the concrete.
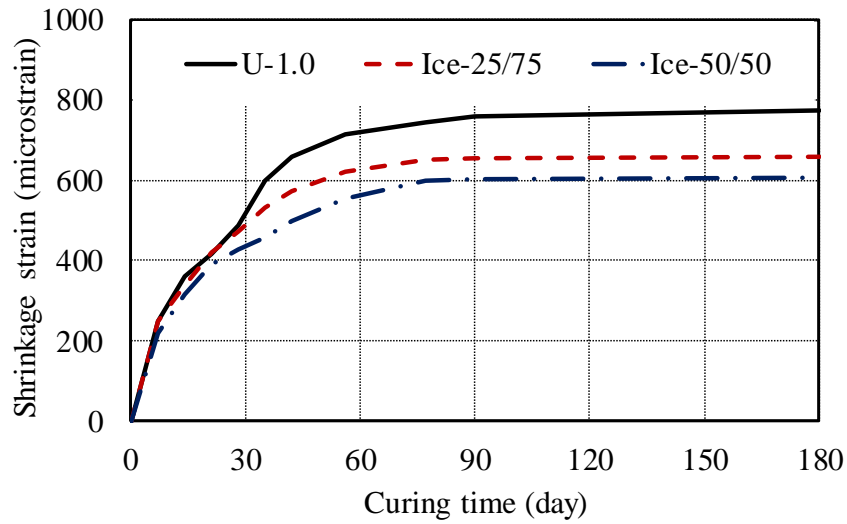
Figure 2-17. Effect of crushed ice dosage on total shrinkage

(a)

(b)

(c)
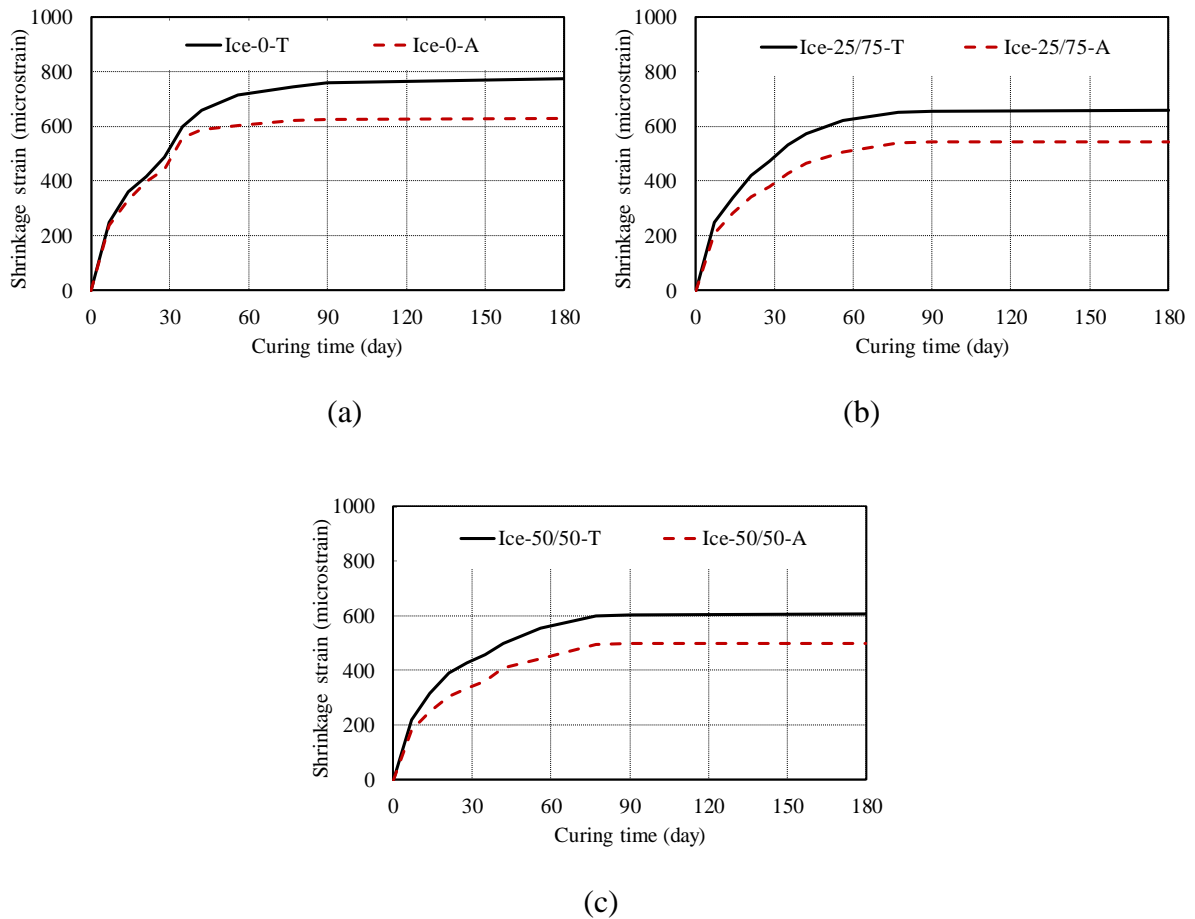
Figure 2-18. Effect of ice replaced water ratio on free drying shrinkage: (a) Ice = 0%; (b) Ice = 25%; (c) Ice = 50%

2.4.4 Compressive strength

2.4.4.1 Effect of shrinkage reducing admixture (SRA) content

The effect of SRA content on f'_c at all curing time are illustrated in Fig. 2-19. For each given concrete age, f'_c decreased significantly with an increase in the SRA dosage (up to 21.5 % decrease in f'_c at 90 days with SRA content of 3%), which is in agreement with those reported in the previous studies on UHPCs (Soliman and Nehdi 2011; Yoo et al. 2013). It is also worth noting that the mixes incorporating SRA exhibited no compressive strength losses ($\Delta f'_c$) for the concrete age ranging between 90 to 180 days. This finding further validates the hypothesis of Sobuz et al. (Sobuz et al. 2016) that the reduction in strength of UHPC over time is due to the formation of micro-shrinkage cracks.
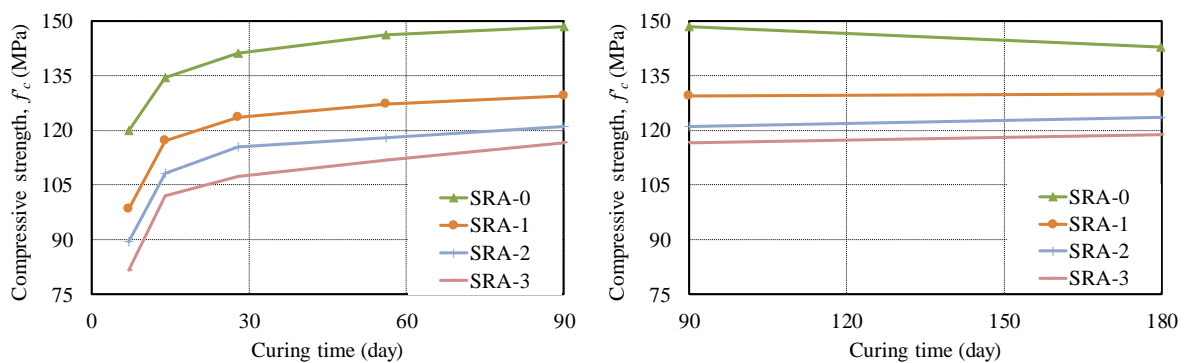
Figure 2-19. Effect of SRA content on compressive strength: (a) curing time from 0 to 90 day; (b) curing time from 90 to 180 day

2.4.4.2 Effect of crushed ice dosage

Figure 2-20 illustrates the variations of f'_c with curing time of the UHPCs manufactured using different crushed ice replacement ratios. For a given concrete age, the U-25/75 and -50/50 series, which were prepared with crushed ice, developed a lower f'_c than the corresponding UHPC without crushed ice (up to 8 % reduction when replacing 50% of water by crushed ice), whereas there was only a slight difference in f'_c between U-25/75 and -50/50 series. This is likely due to the small difference in temperature between mix U-25/75 and -50/50 compared

to the control without ice. Moreover, as shown in Fig. 2-20, U-25/75 and -50/50 UHPC series all exhibited insignificant strength losses (< 1%) between concrete age between 90 and 180 days compared to that seen in U-1.0. This can be explained by the fact that less thermal and plastic shrinkage cracks formed during the exothermic reaction stage, due to the reduction in the heat generation by the incorporation of crushed ice at the early curing stage (i.e. within 72 hours after casting). This will be shown in the calorimetry curves of these UHPC series are presented and their effects are discussed in the following sections. This finding indicates that the simple replacement of a proportion of the mixing water with ice may be all that is required to mitigate the excessive shrinkage strains which causes a reduction in strength of UHPC over time.

(a)   (b)
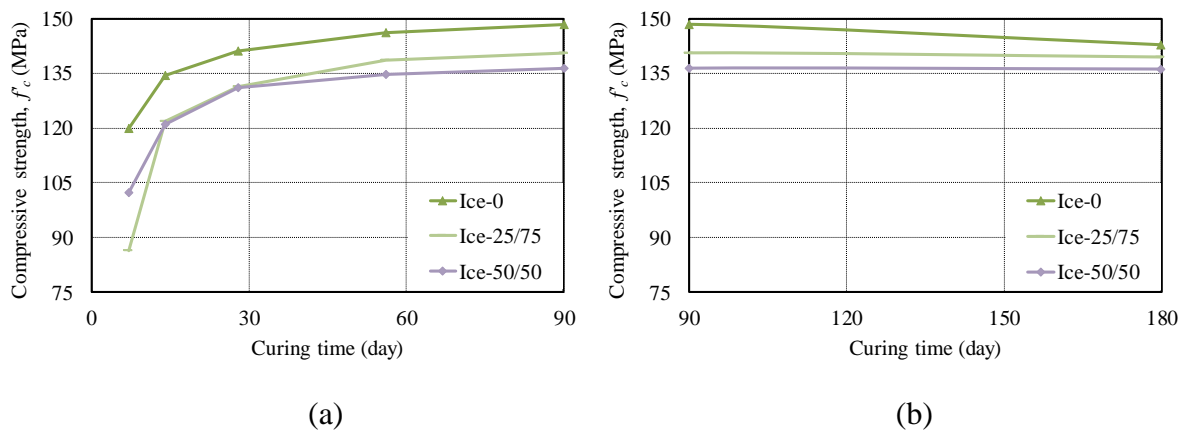
Figure 2-20. Effect of ice replaced water ratio on compressive strength: (a) curing time from 0 to 90 day; (b) curing time from 90 to 180 day

2.4.5 Exothermic reaction at early curing ages: effects of SRA and crushed ice dosage

The effects of SRA content and crushed ice dosage on the internal temperature of the UHPC are depicted in Figs. 2-21 and 2-22, respectively. As can be seen from both figures, the incorporation of SRA or replaced mixing water by crushed ice in the UHPC mix can significantly delay the initial and final setting time and reduce the magnitude of peak temperature, which indicates a lower degree of hydration. It is also observed that the strength

development period (referred to the width of the hump of the temperature history curve) was increased by using SRA or replacing mixing water with crushed ice. This indicates that the UHPC mixed with SRA or crushed ice could experience a slightly slower strength gain within the very early age (i.e. 72 hours) due to the decelerated reaction rate.
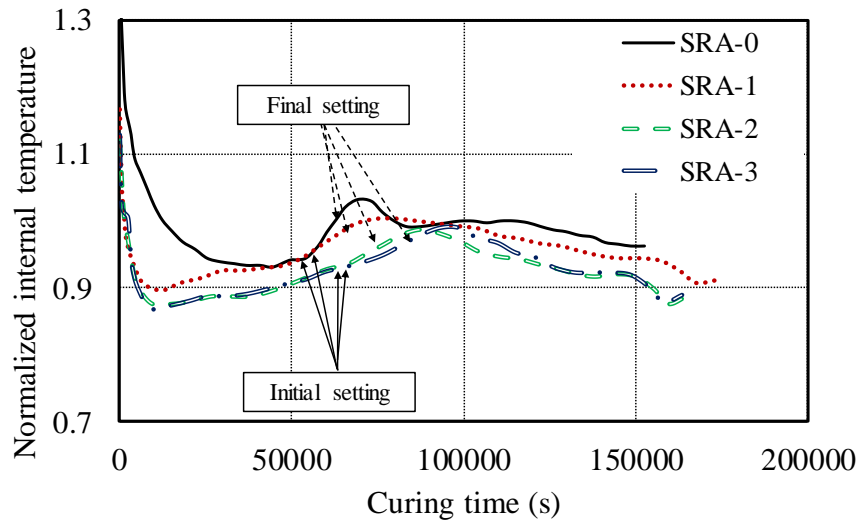
Figure 2-21. Effect of SRA content on variations of the internal temperature with curing time
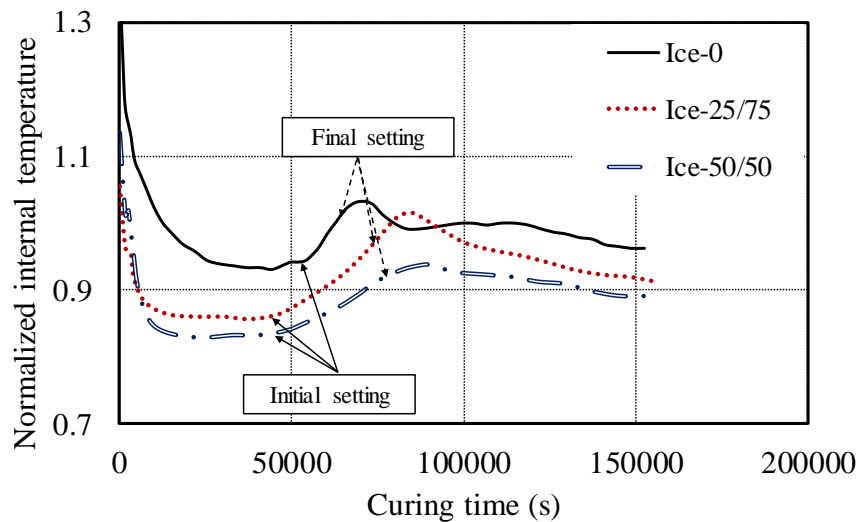
Figure 2-22. Effect of ice replaced mixing water ratio on variations of the internal temperature with curing time

2.4.6 Unit weight and porosity of the hardened UHPCs

As illustrated in Fig. 2-23, it is observed that the SRA content has marginal effect on the unit weight of the hardened UHPC, however it did lead to an increase in the volume of pore space. This was as expected as SRA, which is a type of organic substance (mainly chemically stable ethanol derivatives) (Shlonimskaya et al. 2014), is inert to during hydration and thus causes formation of additional pores in the UHPCs.
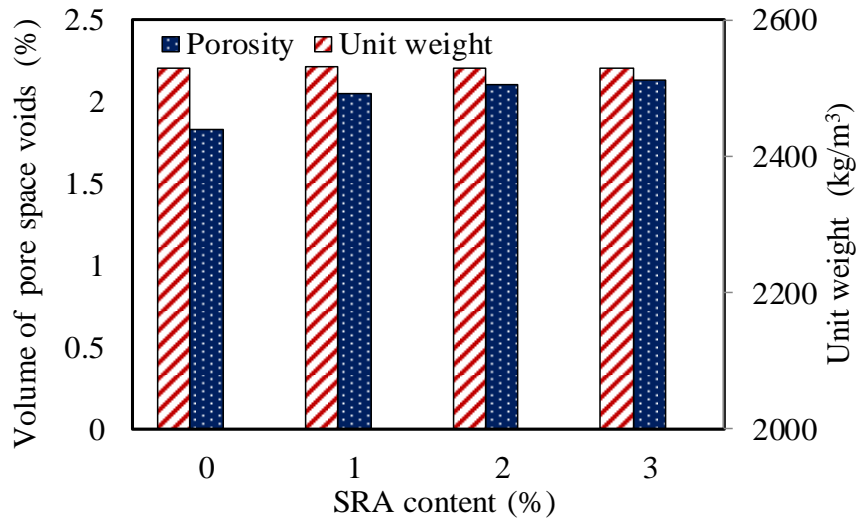
Figure 2-23. Effects of ice replaced water ratio on unit weight and porosity of hardened UHPCs

The test results of the unit weight and porosity of the hardened UHPCs shown in Fig. 2-24 suggest that partially replacing the mixing water by crushed ice resulted had no significant effect on the unit weight of the concrete. However, a slight increase in the porosity of the UHPC with an increase in the crushed ice dosage was observed due to the decreased reaction rate. This is because the lower temperature caused amount of unreacted raw materials (i.e. water and binder) to remain in the structure of the matrix. The gradual evaporation of the residual water subsequently led to the increased porosity of the concrete.
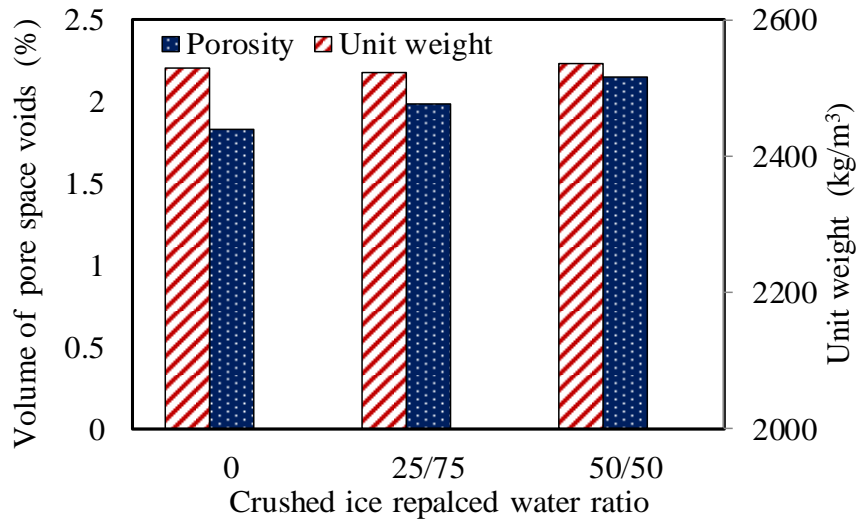
Figure 2-24. Effects of SRA content on unit weight and porosity of hardened UHPCs

2.4.7 Morphological characterization of the UHPCs

2.4.7.1 Effect of SRA content

Figures. 2-25 and 2-26 illustrated the SEM micrographs of the fracture surface of SRA -0, -1, -2 and -3 UHPCs with different magnifications. The comparisons among these micrographs at the lower magnification (i.e. 1000×) suggest that the increased SRA content in the UHPC mix led to increased porosity of the concrete, which is in agreement with the findings from the porosity test mentioned earlier. For the SEM micrographs at the higher magnification (i.e. 10000×), an increased amount of unhydrated binder and ettringite were observed, which indicated lower degree of hydration and increased pore space in the concrete. As discussed previously, this arises because the SRA does not participate in the hydration process but rather acts to slow the hydration process by reducing the contact between the water and binder. In addition, based on the porosity tests results and SEM micrograph, the increased porosity of the UHPC with SRA incorporation might be another potential explanation for the reduction in the autogenous shrinkage of the concrete, where the presence of pores limited the space for the autogenous shrinkage of the matrix for a given content of aggregate in the mix.

<center>(a)</center> <center>(b)</center>

<center>(c)</center> <center>(d)</center>

Figure 2-25. SEM images of the fracture surface of the UHPCs (1000× magnification): a) SRA-0; b) SRA-1; c) SRA-2; d) SRA-3

(a)   (b)

(c)   (d)
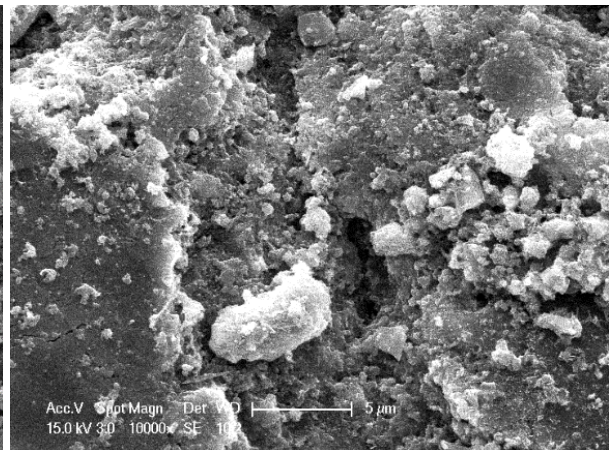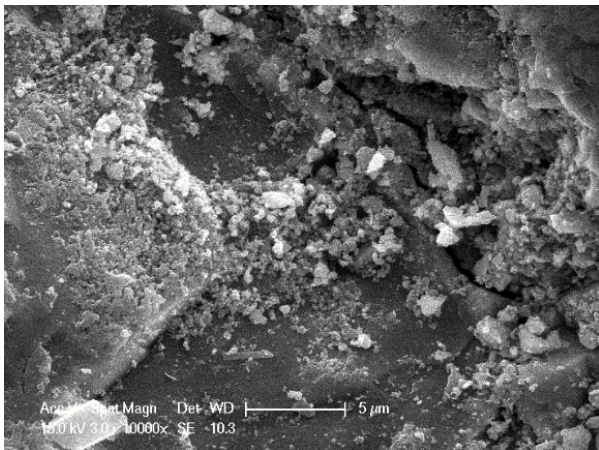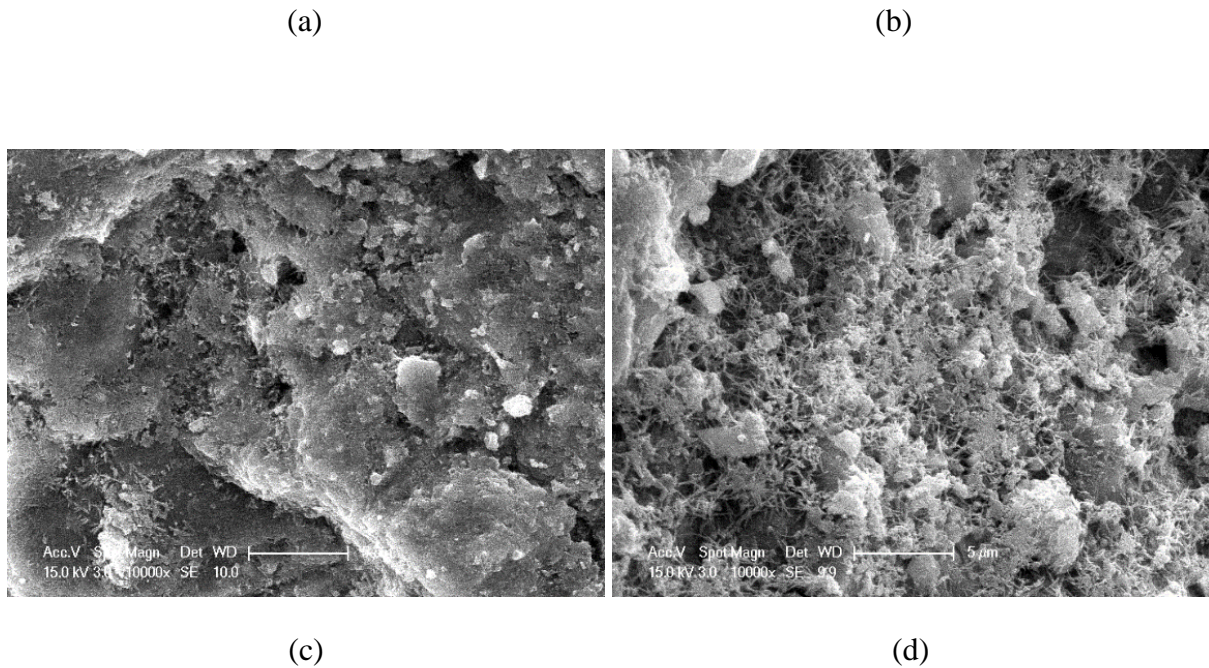
Figure 2-26. SEM images of the fracture surface of the UHPCs (10000× magnification): a) SRA-0; b) SRA-1; c) SRA-2; d) SRA-3

2.4.7.2 Effect of crushed ice dosage

Figures. 2-27 and 2-28 show SEM micrographs of the fracture surface of Ice -0, -25/75, and -50/50 UHPCs at the different magnifications. From SEM micrographs of these UHPC series at the lower magnification (i.e. 1000×), the denseness of the UHPC is observed to decrease with an increase in the crushed ice dosage, indicating an increase in porosity. The comparisons of the SEM micrographs at the higher magnification (i.e. 10000×) show the increased amount of unhydrated binder and ettringite, which suggest the lower degree of hydration and increased pore space for the UHPC prepared using a higher crushed ice replaced water ratio. The increased porosity, formation of ettringite in the concrete and the reduced heat of hydration together explain the mechanism by which the replacement of mixing water with crushed ice reduces self-desiccation.

(a)

(b)

(c)

Figure 2-27. SEM images of the fracture surface of the UHPCs (1000× magnification): (a) Ice = 0%; (b) Ice = 25%; (c) Ice = 50%
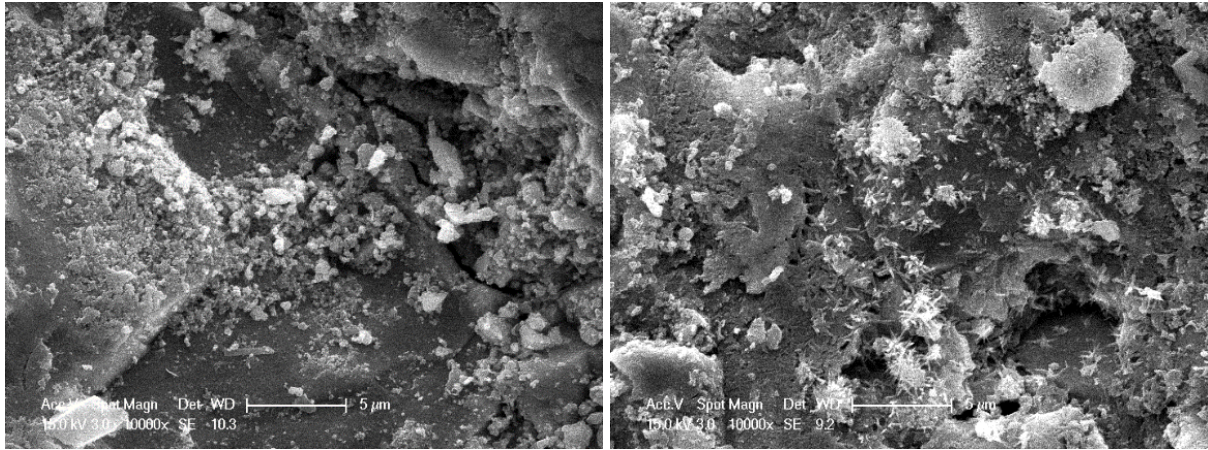
(a)   (b)
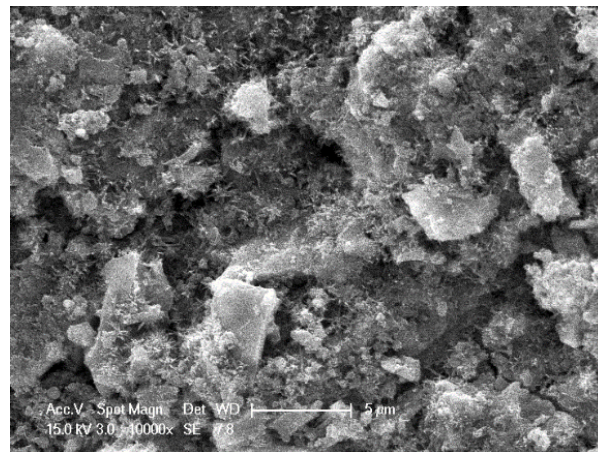
(c)

Figure 2-28. SEM images of the fracture surface of the UHPCs (10000× magnification): (a)

Ice = 0%; (b) Ice = 25%; (c) Ice = 50%

2.4.8 Thermal gravity (TG) analysis

The TGA curves of SRA -0,-1, -2 and -3 UHPC series and Ice -0, -25/75, and -50/50 UHPC

series are shown in Figs. 2-29 and 2-30 respectively and the degree of hydration of these

UHPCs at their hardened stage are shown in Figs. 2-31 and 2-32 in conjunction with the

calculated C-H contents. It is evident from Fig. 2-31 that the increased SRA content generally

lowered the degree of hydration of the UHPCs (i.e. up to around 20%). An even more

pronounced reduction in the degree of hydration (i.e. up to approximately 95%) was observed for the UHPC using a higher crushed ice replaced dosage. These characterizations further confirm that using SRA or replacing mixing water by crushed ice can efficiently reduce the shrinkage of UHPC due to chemical reaction.
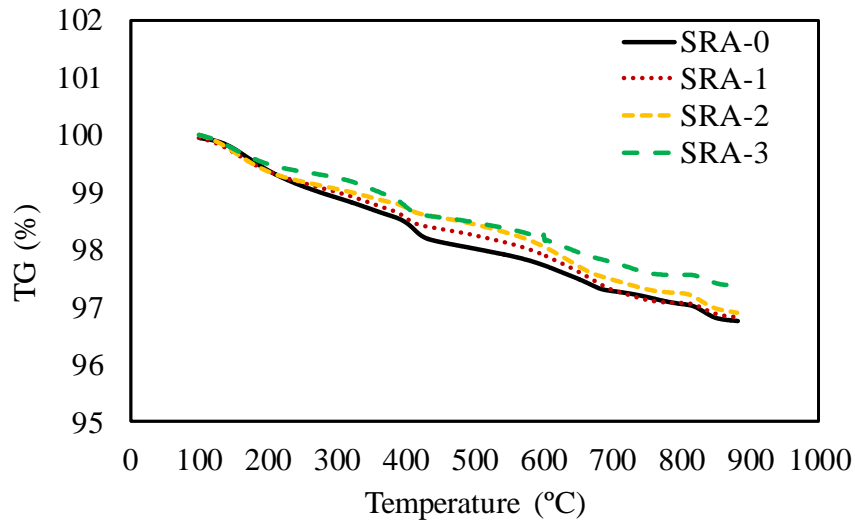
Figure 2-29. TG analysis for SRA -0,-1, -2 and -3 UHPC series.
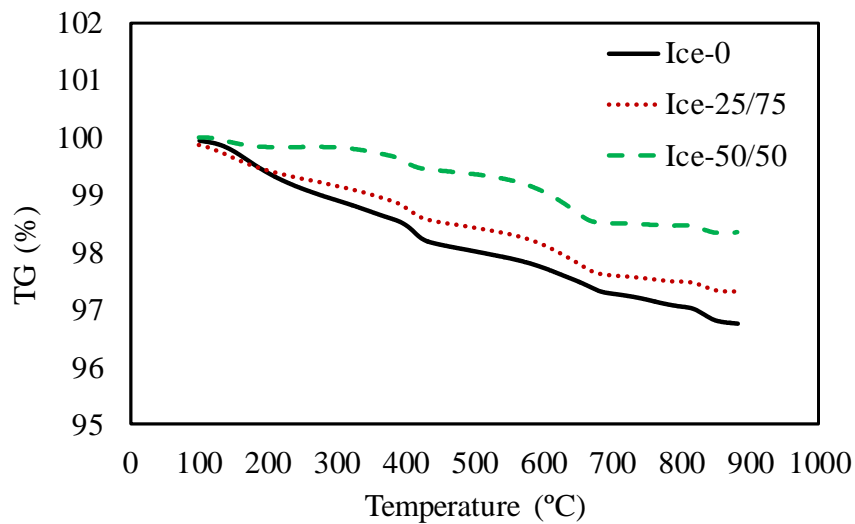
Figure 2-30. TG analysis Ice = 0%, Ice = 25% and Ice = 50% UHPC series
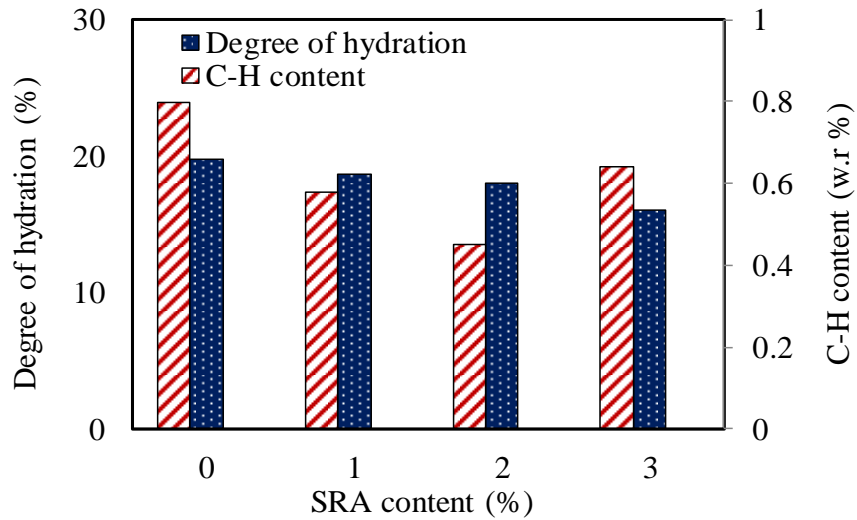
Figure 2-31. Effect of SRA content on degree of hydration and C-H content
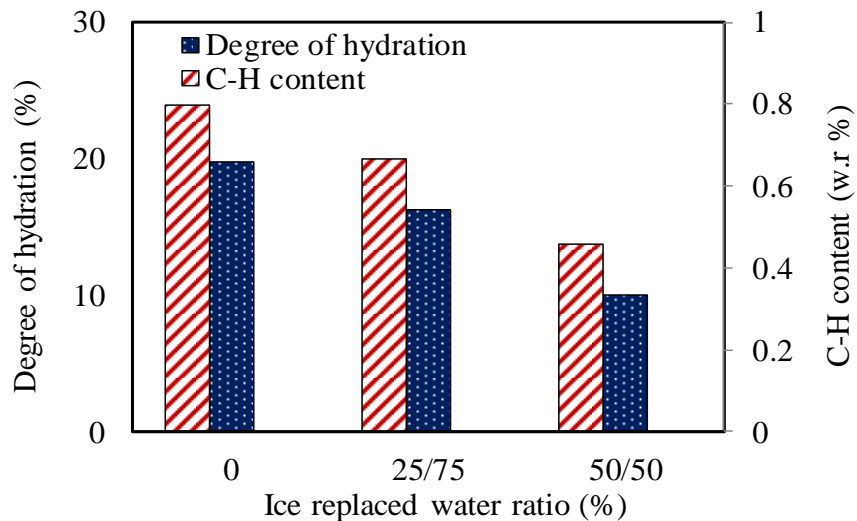
Figure 2-32. Effect of ice replaced water ratio on degree of hydration and C-H content

2.5 COMPARISONS AMONG THE THREE TECHNIQUES AND FURTHER SUGGESTIONS FOR UHPC MIX

To compare the effectiveness of the three techniques used in the present study to mitigate shrinkage of the UHPCs, the key findings of each test are summarized in Table 2-5. To make a valid comparison, the test results of each UHPC series are compared with the reference mix, U-1.0 series. It can be seen from Table 2-5 that compared to U-1 series, both U-1.1 and 1.266 had significantly lower 90-day autogenous- and total- shrinkage strains and a marked $\Delta f'_c$ at

90 days. All five U-series of UHPCs experienced strength drop after 90 days. Incorporation of SRA and partially replaced of mixing water in UHPC mix by crushed ice can both led to the reduction in autogenous- and total- shrinkage of the concrete, hence minimizing the compressive strength loss ($\Delta f'_c$) after long term. While the use of SRA is more efficient in reducing shrinkage and the associated reduction in strength over time than replaced mixing water by ice, the low cost and simplicity of using ice has significant benefits. However, it is also noted that the application of either of the technique causes a reduction the maximum compressive strength achieved. Therefore, from this study, it can be concluded that the best mix for reducing the impact of shrinkage without significant $\Delta f'_c$ in the long-term will be 1) SRA-1 using 1% SRA dosage and 2) Ice-50/50 prepared using crushed ice dosage of 50%.

Table 2-5. Effects of nominated techniques on shrinkage and other properties of the UHPCs

Specimen	Change in autogenous shrinkage strain at 90 days	Change in total shrinkage strain at 90 days	Change in f'_c at 90 days	$\Delta f'_c$ between 90 and 180 days
U-0.8	6.4%	3.3%	-6.5%	-5.3%
U-0.9	0.8%	-0.2%	-3.0%	-3.6%
U-1.0/SRA-0/Ice-0	0.0%	0.0%	0.0%	-3.8%
U-1.1	-15.7%	-8.6%	0.5%	-3.9%
U-1.266	-26.3%	-10.9%	-6.3%	-2.3%
SRA-1	-36.1%	-30.0%	-12.9%	0.6%
SRA-2	-69.6%	-47.9%	-18.5%	2.0%
SRA-3	-55.0%	-65.7%	-21.5%	1.8%
Ice-25/75	-13.5%	-13.7%	-5.3%	-0.8%
Ice-50/50	-20.7%	-20.4%	-8.1%	-0.2%

2.6 CONCLUSIONS

The following major inferences can be made from the results of the present study to investigate the effects of *b/s* ratio, SRA content and crushed ice dosage on the shrinkage properties of the UHPC：

1. Autogenous shrinkage of the UHPC decreases with an increase in the *b/s* ratio due to the more significant shrinkage restraint provided by the residual binders in the UHPC prepared with a higher *b/s* ratio.

2. An increase in the *b/s* ratio in the UHPC mix leads to a decrease in the porosity of the concrete. For UHPC prepared using a lower *b/s* ratio, the abundance of crystalline ettringite and C-H seen in the pores and cracks in the concrete minimized the drying shrinkage of the concrete

3. An optimal *b/s* ratio will be 1 - 1.1 for a typical UHPC mix to minimize the shrinkage effect without significantly comprising f'_c.

4. The autogenous shrinkage has more significant effect than the drying shrinkage on total shrinkage of the UHPCs.

5. The porosity and the amount of unreacted binder, which are related to the degree of hydration of the concrete, are the two influential factors on the shrinkage properties of UHPCs.

6. SRA is not only able to reduce the drying shrinkage but also the autogenous shrinkage (i.e. up to 55% at 90 days with 3% of SRA dosage) of UHPCs

7. The replacement of half of the mixing water by crushed ice in a UHPC mix can reduce the autogenous shrinkage of the UHPC up to 22% and has nearly no effect on the drying shrinkage properties of the UHPCs. This technique is cost-effective and relatively practical to apply in any cast in-situ or pre-casting scenarios.

2.7 REFERENCES

Aitcin, P. "17 AUTOGENOUS SHRINKAGE MEASUREMENT." *Proc., Autogenous shrinkage of concrete: proceedings of the international workshop, organised by JCI (Japan Concrete Institute), Hiroshima, June 13-14, 1998*, Taylor & Francis, 257.

Anshuang, S., Ling, Q., Shoujie, Z., Jiayang, Z., and Zhaoyu, L. (2017). "Effects of Shrinkage Reducing Agent and Expansive Admixture on the Volume Deformation of Ultrahigh Performance Concrete." *Advances in Materials Science and Engineering*, 2017.

ASTM, A. (2009). "C1698-09 Standard test method for autogenous strain of cement paste and mortar." *ASTM International, West Conshohocken, PA*.

ASTM International (2000). "ASTM C143 / C143M - 00, Standard Test Method for Slump of Hydraulic Cement Concrete." *ASTM International, West Conshohocken*.

ASTM International (2009). "ASTM C1621/C1621M–09 Standard Test Method for Passing Ability of Self-Consolidating Concrete by J-Ring." *ASTM International, West Conshohocken*.

ASTM International (2013). "ASTM C642 - 13. Standard Test Method for Density, Absorption, and Voids in Hardened Concrete." *ASTM International, West Conshohocken*.

Australian Standard (2000). "AS 1478.1-2000. Chemical admixtures for concrete, mortar and grout Admixtures for concrete." *Standards Australia, Sydeny*.

Australian Standard (2006). "AS/NZS 2350.11. Methods for testing Portland, blended and masonry cements." *Standards Australia, Sydeny*.

Australian Standard (2006). " AS/NZS 2350.13. Methods for testing Portland, blended and masonry cements – determination of drying shrinkage of cement mortars." *Standards Australia, Sydney*.

Bentur, A., Igarashi, S.-i., and Kovler, K. (2001). "Prevention of autogenous shrinkage in high-strength concrete by internal curing using wet lightweight aggregates." *Cement and concrete research*, 31(11), 1587-1591.

Bentz, D., Geiker, M. R., and Hansen, K. K. (2001). "Shrinkage-reducing admixtures and early-age desiccation in cement pastes and mortars." *Cement and concrete research*, 31(7), 1075-1085.

Bentz, D. P. "Capitalizing on self-desiccation for autogenous distribution of chemical admixtures." *Proc., Lund University*, Citeseer.

Brough, A., and Atkinson, A. (2000). "Automated identification of the aggregate–paste interfacial transition zone in mortars of silica sand with Portland or alkali-activated slag cement paste." *Cement and Concrete Research*, 30(6), 849-854.

Brunauer, S., and Kantro, D. (1964). "The Hydration of Tricalcium Silicate and β Dicalcium Silicate from 5 C to 50 C." *The Chemistry of Cement*, 1, 287.

Chen, X., and Wu, S. (2013). "Influence of water-to-cement ratio and curing period on pore structure of cement mortar." *Construction and Building Materials*, 38, 804-812.

Collepardi, M., Borsoi, A., Collepardi, S., Olagot, J. J. O., and Troli, R. (2005). "Effects of shrinkage reducing admixture in shrinkage compensating concrete under non-wet curing conditions." *Cement and Concrete Composites*, 27(6), 704-708.

Darquennes, A., Staquet, S., and Espion, B. (2011). "Determination of time-zero and its effect on autogenous deformation evolution." *European journal of environmental and civil engineering*, 15(7), 1017-1029.

Dudziak, L., and Mechtcherine, V. "Mitigation of volume changes of ultra-high performance concrete (UHPC) by using super absorbent polymers." *Proc., Proceedings of the 2nd international symposium on ultra high performance concrete. Kassel University Press, Kassel*, 425-432.

Dweck, J., Buchler, P. M., Coelho, A. C. V., and Cartledge, F. K. (2000). "Hydration of a Portland cement blended with calcium carbonate." *Thermochimica Acta*, 346(1), 105-113.

Folliard, K. J., and Berke, N. S. (1997). "Properties of high-performance concrete containing shrinkage-reducing admixture." *Cement and Concrete Research*, 27(9), 1357-1364.

Han, M. Y., and Lytton, R. L. (1995). "Theoretical prediction of drying shrinkage of concrete." *Journal of materials in civil engineering*, 7(4), 204-207.

Hasanzadeh, B., Liu, F., and Sun, Z. (2016). "Monitoring hydration of UHPC and conventional paste by quantitative analysis on Raman patterns." *Construction and Building Materials*, 114, 208-214.

Hermida, G., Moranville, M., and Flatt, R. (2009). "The Role of Paste Volume on Performance of Concrete." *Special Publication*, 261, 201-214.

Huang, W., Kazemi-Kamyab, H., Sun, W., and Scrivener, K. (2017). "Effect of cement substitution by limestone on the hydration and microstructural development of ultra-high performance concrete (UHPC)." *Cement and Concrete Composites*, 77, 86-101.

Jennings, H., and Pratt, P. (1979). "An experimental argument for the existence of a protective membrane surrounding Portland cement during the induction period." *Cement and Concrete Research*, 9(4), 501-506.

Jensen, O. M. (2013). "Use of superabsorbent polymers in concrete." *Concrete international*, 35(1), 48-52.

Jun, P. J., Tae, K. S., Sung, R. G., Wook, K. S., and Hwa, L. J. "The effect of material factors on the compressive strength of ultra-high strength Steel Fiber Reinforced Cementitious Composites." *Proc., Proceedings of the Korea Concrete Institute Conference*, Korea Concrete Institute.

Kadri, E.-H., and Duval, R. (2009). "Hydration heat kinetics of concrete with silica fume." *Construction and Building Materials*, 23(11), 3388-3392.

Kim, G.-Y., Lee, E.-B., Nam, J.-S., and Koo, K.-M. (2011). "Analysis of hydration heat and autogenous shrinkage of high-strength mass concrete." *Magazine of Concrete Research*, 63(5), 377-389.

Koh, K., Ryu, G., Kang, S., Park, J., and Kim, S. (2011). "Shrinkage properties of ultra-high performance concrete (UHPC)." *Advanced Science Letters*, 4(3), 948-952.

Lam, L., Wong, Y., and Poon, C. (2000). "Degree of hydration and gel/space ratio of high-volume fly ash/cement systems." *Cement and Concrete Research*, 30(5), 747-756.

Langan, B., Weng, K., and Ward, M. (2002). "Effect of silica fume and fly ash on heat of hydration of Portland cement." *Cement and Concrete research*, 32(7), 1045-1051.

Lura, P., Jensen, O. M., and van Breugel, K. (2003). "Autogenous shrinkage in high-performance cement paste: an evaluation of basic mechanisms." *Cement and Concrete Research*, 33(2), 223-232.

Ma, J., Orgass, M., Dehn, F., Schmidt, D., and Tue, N. "Comparative investigations on ultra-high performance concrete with and without coarse aggregates." *Proc., Proceedings of international symposium on ultra high performance concrete, Germany*, 205-212.

Maltais, Y., and Marchand, J. (1997). "Influence of curing temperature on cement hydration and mechanical strength development of fly ash mortars." *Cement and concrete research*, 27(7), 1009-1020.

Mechtcherine, V., Gorges, M., Schroefl, C., Assmann, A., Brameshuber, W., Ribeiro, A. n. B., Cusson, D., Custˇdio, J., da Silva, E. F., and Ichimiya, K. (2014). "Effect of internal curing by using superabsorbent polymers (SAP) on autogenous shrinkage and other properties of a high-performance fine-grained concrete: results of a RILEM round-robin test." *Materials and structures*, 47(3), 541-562.

Mehta, P. K. (1973). "Mechanism of expansion associated with ettringite formation." *Cement and Concrete Research*, 3(1), 1-6.

Mosaberpanah, M. A., and Eren, O. (2016). "Relationship between 28-days Compressive Strength and Compression Toughness Factor of Ultra High Performance Concrete Using Design of Experiments." *Procedia Engineering*, 145, 1565-1571.

Newman, S. P., Clifford, S. J., Coveney, P. V., Gupta, V., Blanchard, J. D., Serafin, F., Ben-Amotz, D., and Diamond, S. (2005). "Anomalous fluorescence in near-infrared Raman spectroscopy of cementitious materials." *Cement and concrete research*, 35(8), 1620-1628.

Odler, I. (1998). "Hydration, setting and hardening of Portland cement." *Lea's chemistry of cement and concrete*, 4, 241-297.

Park, J.-J., Yoo, D.-Y., Kim, S.-W., and Yoon, Y.-S. (2014). "Benefits of using expansive and shrinkage-reducing agents in UHPC for volume stability." *Magazine of Concrete Research*, 66(14), 745-750.

Park, J. J., Kang, S. T., Koh, K. T., and Kim, S. W. "Influence of the ingredients on the compressive strength of UHPC as a fundamental study to optimize the mixing proportion." *Proc., Proceedings of the international symposium on ultra-high performance concrete, structural materials and engineering series*, 105-112.

Reddy, B. V., and Gupta, A. (2008). "Influence of sand grading on the characteristics of mortars and soil–cement block masonry." *Construction and Building Materials*, 22(8), 1614-1623.

Rößler, C., Bui, D.-D., and Ludwig, H.-M. (2014). "Rice husk ash as both pozzolanic admixture and internal curing agent in ultra-high performance concrete." *Cement and Concrete Composites*, 53, 270-278.

Russell, H. G., and Graybeal, B. A. (2013). "Ultra-high performance concrete: A state-of-the-art report for the bridge community."

Şahmaran, M., Al-Emam, M., Yıldırım, G., Şimşek, Y. E., Erdem, T. K., and Lachemi, M. (2015). "High-early-strength ductile cementitious composites with characteristics of low early-age shrinkage for repair of infrastructures." *Materials and Structures*, 48(5), 1389-1403.

Şahmaran, M., Lachemi, M., Hossain, K. M., and Li, V. C. (2009). "Internal curing of engineered cementitious composites for prevention of early age autogenous shrinkage cracking." *Cement and Concrete Research*, 39(10), 893-901.

Sahmaran, M., Lachemi, M., Hossain, K. M., Ranade, R., and Li, V. C. (2009). "Influence of aggregate type and size on ductility and mechanical properties of engineered cementitious composites." *Materials Journal*, 106(3), 308-316.

Schießl, P., Mazanec, O., and Lowke, D. (2007). "SCC and UHPC—effect of mixing technology on fresh concrete properties." *Advances in Construction Materials 2007*, Springer, 513-522.

Scrivener, K. L., Crumbie, A. K., and Laugesen, P. (2004). "The interfacial transition zone (ITZ) between cement paste and aggregate in concrete." *Interface Science*, 12(4), 411-421.

Shen, W., Li, X., Gan, G., Cao, L., Li, C., and Bai, J. (2016). "Experimental investigation on shrinkage and water desorption of the paste in high performance concrete." *Construction and Building Materials*, 114, 618-624.

Shi, C., Wu, Z., Xiao, J., Wang, D., Huang, Z., and Fang, Z. (2015). "A review on ultra high performance concrete: Part I. Raw materials and mixture design." *Construction and Building Materials*, 101, 741-751.

Shlonimskaya, N., Biernacki, J. J., Kayello, H. M., and Visco, D. P. (2014). "An Application of Computer-Aided Molecular Design (CAMD) Using the Signature Molecular Descriptor–Part 2. Evaluating Newly Identified Surface Tension-Reducing Substances for Potential Use as Shrinkage-Reducing Admixtures." *Journal of the American Ceramic Society*, 97(2), 378-385.

Singh, M., Sheikh, A., Ali, M. M., Visintin, P., and Griffith, M. (2017). "Experimental and numerical study of the flexural behaviour of ultra-high performance fibre reinforced concrete beams." *Construction and Building Materials*, 138, 12-25.

Smith, B. G. (2001). "Durability of silica fume concrete exposed to chloride in hot climates." *Journal of materials in civil engineering*, 13(1), 41-48.

Sobuz, H., Visintin, P., Ali, M. M., Singh, M., Griffith, M., and Sheikh, A. (2016). "Manufacturing ultra-high performance concrete utilising conventional materials and production methods." *Construction and Building Materials*, 111, 251-261.

Sobuz, H. R., Oehlers, D. J., Visintin, P., Hasan, N. M. S., Hoque, M. I., and Akid, A. S. M. (2017). "Flow and Strength Characteristics of Ultra-high Performance Fiber Reinforced Concrete: Influence of Fiber Type and Volume-fraction." *Journal of Civil Engineering and Construction*, 6(1), 15.

Soliman, A., and Nehdi, M. (2011). "Effect of drying conditions on autogenous shrinkage in ultra-high performance concrete at early-age." *Materials and structures*, 44(5), 879-899.

Soliman, A., and Nehdi, M. (2013). "Effect of partially hydrated cementitious materials and superabsorbent polymer on early-age shrinkage of UHPC." *Construction and Building Materials*, 41, 270-275.

Soliman, A., and Nehdi, M. (2014). "Effects of shrinkage reducing admixture and wollastonite microfiber on early-age behavior of ultra-high performance concrete." *Cement and Concrete Composites*, 46, 81-89.

Standard Australia (2014). "AS 1012.9:2014. Methods of testing concrete Compressive strength tests - Concrete, mortar and grout specimens. ." *Standards Australia, Sydeny*.

Sturm, A. B., Visintin, P., Ferris, K., and Oehlers, D. J. (2018). "A new testing approach for extracting the shear friction material properties of ultra-high performance fibre reinforced concrete." *ASCE Journal of Materials in Civil Engineering*.

Vedalakshmi, R., Raj, A. S., Srinivasan, S., and Babu, K. G. (2003). "Quantification of hydrated cement products of blended cements in low and medium strength concrete using TG and DTA technique." *Thermochimica Acta*, 407(1), 49-60.

Visintin, P., Ali, M. M., Xie, T., and Sturm, A. B. (2018). "Experimental investigation of moment redistribution in ultra-high performance fibre reinforced concrete beams." *Construction and Building Materials*, 166, 433-444.

Visintin, P., Sturm, A. B., Ali, M. M., and Oehlers, D. J. (2018). "Blending Macro and Micro Fibres to Enhance the Serviceability Behaviour of UHPFRC." *Australian Journal of Civil Engineering*.

Wang, D., Shi, C., Wu, Z., Xiao, J., Huang, Z., and Fang, Z. (2015). "A review on ultra high performance concrete: Part II. Hydration, microstructure and properties." *Construction and Building Materials*, 96, 368-377.

Wong, H., and Buenfeld, N. (2009). "Determining the water–cement ratio, cement content, water content and degree of hydration of hardened cement paste: Method development and validation on paste samples." *Cement and Concrete Research*, 39(10), 957-965.

Wu, L., Farzadnia, N., Shi, C., Zhang, Z., and Wang, H. (2017). "Autogenous shrinkage of high performance concrete: a review." *Construction and Building Materials*, 149, 62-75.

Yalçınkaya, Ç., and Yazıcı, H. (2017). "Effects of ambient temperature and relative humidity on early-age shrinkage of UHPC with high-volume mineral admixtures." *Construction and Building Materials*, 144, 252-259.

Yan, P., Zheng, F., Peng, J., and Qin, X. (2004). "Relationship between delayed ettringite formation and delayed expansion in massive shrinkage-compensating concrete." *Cement and Concrete Composites*, 26(6), 687-693.

Yio, M., Phelan, J., Wong, H., and Buenfeld, N. (2014). "Determining the slag fraction, water/binder ratio and degree of hydration in hardened cement pastes." *Cement and Concrete Research*, 56, 171-181.

Yoo, D.-Y., and Banthia, N. (2016). "Mechanical properties of ultra-high-performance fiber-reinforced concrete: A review." *Cement and Concrete Composites*, 73, 267-280.

Yoo, D.-Y., Banthia, N., and Yoon, Y.-S. (2015). "Effectiveness of shrinkage-reducing admixture in reducing autogenous shrinkage stress of ultra-high-performance fiber-reinforced concrete." *Cement and Concrete Composites*, 64, 27-36.

Yoo, D.-Y., Banthia, N., and Yoon, Y.-S. (2017). "Ultra-High-Performance Fiber-Reinforced Concrete: Shrinkage Strain Development at Early Ages and Potential for Cracking." *Journal of Testing and Evaluation*, 45(6), 2061-2070.

Yoo, D.-Y., Banthia, N., and Yoon, Y.-S. (2018). "Geometrical and boundary condition effects on restrained shrinkage behavior of UHPFRC slabs." *KSCE Journal of Civil Engineering*, 22(1), 185-195.

Yoo, D.-Y., Kang, S.-T., Lee, J.-H., and Yoon, Y.-S. (2013). "Effect of shrinkage reducing admixture on tensile and flexural behaviors of UHPFRC considering fiber distribution characteristics." *Cement and Concrete Research*, 54, 180-190.

Yoo, D.-Y., Kim, M.-J., Kim, S., Ryu, G.-S., and Koh, K.-T. (2018). "Effects of mix proportion and curing condition on shrinkage behavior of HPFRCCs with silica fume and blast furnace slag." *CONSTRUCTION AND BUILDING MATERIALS*, 166(1), 241-256.

Yoo, D.-Y., Min, K.-H., Lee, J.-H., and Yoon, Y.-S. (2014). "Shrinkage and cracking of restrained ultra-high-performance fiber-reinforced concrete slabs at early age." *Construction and Building Materials*, 73, 357-365.

Yoo, D.-Y., Park, J.-J., Kim, S.-W., and Yoon, Y.-S. (2014). "Influence of reinforcing bar type on autogenous shrinkage stress and bond behavior of ultra high performance fiber reinforced concrete." *Cement and Concrete Composites*, 48, 150-161.

Yoo, D.-Y., Park, J.-J., Kim, S.-W., and Yoon, Y.-S. (2014). "Influence of ring size on the restrained shrinkage behavior of ultra high performance fiber reinforced concrete." *Materials and structures*, 47(7), 1161-1174.

Youssef, D. (2013). "The Use of Lightweight Sand for Internal Curing and Its Effect on Performance of HPC Used for Concrete Infrastructures." Université de Sherbrooke.

Yu, R., Spiesz, P., and Brouwers, H. (2014). "Effect of nano-silica on the hydration and microstructure development of Ultra-High Performance Concrete (UHPC) with a low binder amount." *Construction and Building Materials*, 65, 140-150.

Zhang, M., Tam, C., and Leow, M. (2003). "Effect of water-to-cementitious materials ratio and silica fume on the autogenous shrinkage of concrete." *Cement and Concrete Research*, 33(10), 1687-1694.

CHAPTER 3

The Influence of Steel Fibre Properties on the Shrinkage of Ultra-High Performance Fibre Reinforced Concrete

[1]Fang, C., [2]Mohamed Ali, M.S., [*3]Xie, T., [**4]Visintin, P.

[1] **Mr Chenfeng Fang**

Ph. D Candidate,

School of Civil, Environmental and Mining Engineering

The University of Adelaide

South Australia 5005

AUSTRALIA

[2]**Dr. Mohamed Ali, M.S**

Senior Lecturer,

 School of Civil, Environmental and Mining Engineering

The University of Adelaide

 South Australia 5005

AUSTRALIA

[3]**Mr. Tianyu Xie (Corresponding author)**

Ph. D Candidate,

School of Civil, Environmental and Mining Engineering

The University of Adelaide

South Australia 5005

AUSTRALIA

[4]**Dr.Phillip Visintin (Corresponding author)**

Associate Professor,

School of Civil, Environmental and Mining Engineering

The University of Adelaide

South Australia 5005

THIS PAGE HAS BEEN LEFT INTENTIONALLY BLANK

Statement of Authorship

Title of Paper	THE INFLUENCE OF STEEL FIBRE PROPERTIES ON THE SHRINKAGE OF ULTRA-HIGH PERFORMANCE FIBRE REINFORCED CONCRETE
Publication Status	☐ Published ☐ Accepted for Publication ☑ Submitted for Publication ☐ Unpublished and Unsubmitted work written in manuscript style
Publication Details	Fang, C., Ali, M. M., Xie, T., & Visintin, P. (2018). The influence of steel fibre properties on the shrinkage of ultra-high performance fibre reinforced concrete. Submitted to *ACI materials*.

Principal Author

Name of Principal Author	Chengfeng Fang		
Contribution to the Paper	Designing concept, conducting experiments, analysing of data, drafting manuscript		
Overall percentage (%)	30		
Certification:	This paper reports on original research I conducted during the period of my Higher Degree by Research candidature and is not subject to any obligations or contractual agreements with a third party that would constrain its inclusion in this thesis. I am the primary author of this paper.		
Signature		Date	12/02/2019

Co-Author Contributions1

By signing the Statement of Authorship, each author certifies that:

    i.   the candidate's stated contribution to the publication is accurate (as detailed above);

    ii.   permission is granted for the candidate in include the publication in the thesis; and

    iii.   the sum of all co-author contributions is equal to 100% less the candidate's stated contribution.

Name of Co-Author	Dr Mohamed Ali Sadakkathulla		
Contribution to the Paper	Designing concept, analysing of data, revising manuscript (20%)		
Signature		Date	12/02/2019

Name of Co-Author (Candidate)	Tianyu Xie
Contribution to the Paper	Designing concept, conducting experiments, analysing of data, drafting manuscript (20%)

Signature			Date	12/02/2019

Name of Co-Author	Associate Professor Phillip Visintin
Contribution to the Paper	Designing concept, analysing of data, revising manuscript (20%)

Signature			Date	12/02/2019

Name of Co-Author	Associate Professor Abdul H. Sheikh
Contribution to the Paper	Designing concept (10%)

Signature			Date	12/02/2019

Please cut and paste additional co-author panels here as required.

ABSTRACT

The effects of fibre content, shape, aspect ratio and the blending of micro- and macro-fibres on the total and autogenous shrinkage of the ultra-high performance fibre reinforced concretes (UHPFRCs) is experimentally investigated. The results of single-fibre pull-out tests are used to describe the underlying mechanisms that influences both autogenous and drying shrinkage. It is found that the incorporation of randomly distributed steel fibre reinforcement into an ultra-high performance concrete (UHPC) matrix can significantly reduce the total and autogenous shrinkage of the concrete. It is also found that the UHPFRC prepared using fibres at a higher volume fraction, with a higher aspect ratio, and with improved bond lowers total and autogenous shrinkage.

Keywords: ultra-high performance fibre reinforced concrete (UHPFRC); steel fibres; autogenous shrinkage; free total shrinkage; fibre pull-out load-slip relationship.

3.1 INTRODUCTION

The exceptional durability of ultra-high performance fibre-reinforced concrete (UHPFRC) will bring about a step-change in the way structures and infrastructure are planned, managed, and maintained, while its exceptional mechanical properties will fundamentally change how structural engineers approach reinforced concrete design. The great potential of UHPFRC has largely been demonstrated by instantaneous load testing, in which structural elements are tested within weeks or months of manufacture. The exceptional structural performance of these tests highlights the efficiency of using UHPFRC with a reduced amount of the traditional reinforcement (Parra-

Montesinos 2005; Parra-Montesinos et al. 2005), and rely instead on randomly distributed steel fibres to transfer stresses across a crack.

Although showing excellent performance under instantaneous loading, the very high binder volumes of binder and very low water to binder ratios cause ultra-high performance concrete (UHPC) to undergo severe shrinkage (predominately from sustained autogenous shrinkage due to hydration of concrete) (Koh et al. 2011; Shi et al. 2015; Wang et al. 2015; Xie et al. 2018). Investigations of the short- and long-term shrinkage of UHPFRCs, including autogenous shrinkage (Yoo et al. 2015; Yoo et al. 2014), drying shrinkage (i.e. (Park et al. 2013)) and restrained shrinkage (Yoo et al. 2014; Yoo et al. 2014) have mostly been conducted by Yoo and his colleagues, with other studies also by (Garas et al. 2009; Meng and Khayat 2018; Soliman and Nehdi 2014). The majority of these studies incorporated fibres into a ultra-high performance concrete (UHPC) matrix at a signal dosage (2% fibre volume fraction as reported in Yoo et al. (Yoo et al. 2013) and Garas et al. (Garas et al. 2009) for autogenous- and drying- shrinkage, respectively), and with a single fibre shape. The only research program found in the literature that studied the variation in autogenous shrinkage of UHPFRCs with different fibre configurations (shape, dosage and the effect of blending fibres), was recently reported in a study (Meng and Khayat 2018). In this study it was found that autogenous shrinkage of the UHPC mix was decreased by more than 60% with an increase in fibre content of straight fibres from 0% to 5%. Furthermore, the inclusion of 0.5% PVA fibres as well as maximum 1% of hook-end steel fibres significantly reduced the autogenous shrinkage and also enhanced the tensile strength as well as tensile dissipated energy of specimens with fibre content (V_f) of 2%. A further increase in fibre content of hooked-end fibre resulted in reductions in flexural and tensile properties of UHPFRC, and this mainly contributed by the fibre agglomeration.

Based on the above literature review, it is evident that there is a lack of studies that directly consider variations in fibre volume and fibre types on a single binder, and therefore it is difficult to extract the influence of fibre properties on the shrinkage behaviour which is necessary for both the development of mix design procedures and codifiable design standards. Hence in this paper the effects of various fibres parameters on the shrinkage characterizations and mechanical properties of UHPFRCs are experimentally studied. The specific aims of the work are to experimentally quantify the effects of fibres' geometry and content, and using blended micro and macro-fibres on the shrinkage properties of UHPFRCs by investigating both shrinkage and fibre matrix interactions.

In the following, the constituents and mix proportions of the UHPFRCs investigated are first described. This is followed by a description of the experimental method and tests conducted. Finally, the effects of specific fibre parameters on autogenous and drying shrinkage is presented as well as a discussion of the mechanism of action.

3.2 EXPERIMENTAL PROGRAM

3.2.1 Materials and Concrete mixes

3.2.1.1 Ingredients used for the UHPC matrix

A single UHPC mix design based on the work of Sobuz et al. (2016) was used to prepare the mortar matrix of the UHPFRCs (the detailed mix proportions summarized in Table 2-1). The blended

binder consists of sulphate resisting cement and undensified silica fume and a detail description of the chemical composition of both binders can be found in Sobuz et al. (2016), in which idnetical materials were utilised. A well-graded natural washed river sand with a nominal maximum size of 4 mm and a fineness modulus of 2.34 was used as the only aggregate in all mixes. To enhance the workability, a third generation superplasticizer (SP) with an added retarder (which meets the requirements of AS1478.1-2000 (Australian Standard 2000)), was used as the chemical admixture for all mixes at a rate of 6% of the SP-to-binder weight.

| 1 | | | | | | | | | | | | | | |

Table. 2-1 Mix proportion, physical-and mechanical-properties of the UHPFRCs.

| Mix No. | Designation | Mix proportion (kg/m³) | | | | | | Fibre volume fraction | Discriptions of fibre incorporations | Fibre reinforcing index (RI) | Slump (mm) | 28-d f_{st} (MPa) | 28-d f'_c (MPa) | 180-d f'_c (MPa) |
		Sulfate resisting cement	Silica fume	Sand	Water	SP	Fibre							
M1	Ref						0	0.0%	-	0.00	255	6.1	128.3	126.8
M2	H1-0.015						0.155	1.5%	Dramix 3D-45/35 BL	0.68	230	14.1	129.1	134.9
M3	H2-0.015						0.155	1.5%	Dramix 3D-65/35 BG	0.98	210	14.4	133.7	137.1
M4	H3-0.015						0.155	1.5%	Dramix 3D-80/60 BG	1.20	195	14.8	141.8	144.4
M5	S-0.02						0.207	2.0%	Micro straight fibres	1.30	215	13.6	122.6	126.8
M6	H1-0.02						0.207	2.0%	Dramix 3D-45/35 BL	0.90	205	12.4	147.2	151.4
M7	H2-0.02						0.207	2.0%	Dramix 3D-65/35 BG	1.30	210	11.8	133.7	138.2
M8	H3-0.02	0.79	0.21	1.00	0.12	0.06	0.207	2.0%	Dramix 3D-80/60 BG	1.60	170	13.9	137.3	139.7
M9	50H2/50S-0.02						0.207	2.0%	Blended fibres (50% & 50%) (Straight & Dramix 3D- 65/35 BG)	1.30	205	12.0	133.9	137.9
M10	H1-0.025						0.259	2.5%	Dramix 3D-45/35 BL	1.13	155	10.7	139.8	142.6
M11	H2-0.025						0.259	2.5%	Dramix 3D-65/35 BG	1.63	125	11.9	125.8	130.3
M12	H3-0.025						0.259	2.5%	Dramix 3D-80/60 BG	2.00	145	13.0	127.6	131.0

2

Table. 3-2 Manufacturer-reported details of steel fibres

Fibre type	Designation	Diameter, d_f (mm)	Length, l_f (mm)	Aspect ratio, (l_f/d_f)	Yield tensile strength, f_t (MPa)	Young's modulus, E_c (MPa)	Fibre shape
Micro fibres	S	0.2	13	65	2850	210000	Straight
Dramix 3D-45/35 BL	H1	0.75	35	45	1225	210000	Hooked end
Dramix 3D-65/35 BG	H2	0.55	36	65	1345	210000	Hooked end
Dramix 3D-80/60 BG	H3	0.75	60	80	1225	210000	Hooked end

4

5

3.2.1.2 Steel Fibres

Four different types of steel fibres, as illustrated in Fig. 3-1 were added to the concrete mixes. The manufacturer reported properties of each fibre are reported in Table 3-2. Three of these four fibres (type H1, H2 and H3) are macro-fibres of hooked end shape and with different nominal diameters and lengths, the last (type S) is a straight micro-fibre. Each type of fibre was added to the UHPC mortar at volume fractions of 0%, 1.5%, 2% and 2.5%. In addition to mixes with a single type of fibre, micro- (S) and macro- (H2) fibres were added at a volumetric ratio of 50/50 to investigate the effects of blending fibres. Note that S and H2 fibres were selected for blending because they have the same aspect ratio. Table 3-1 also presents the reinforcing index (RI) of each mix as this is commonly used as a measure of the influence of fibres (Ou et al. 2011; Xie and Ozbakkaloglu 2015). The *RI* is defined as

$$RI = V_f\% \times \frac{l_f}{d_f} \tag{1}$$

in which V_f % is the total fibre volume fraction as a percentage, and l_f and d_f are the length and nominal diameter of the fibre, respectively. For the UHPFRC containing blended fibres the *RI* is determined by calculating the volumetric average *RI* of each fibre.
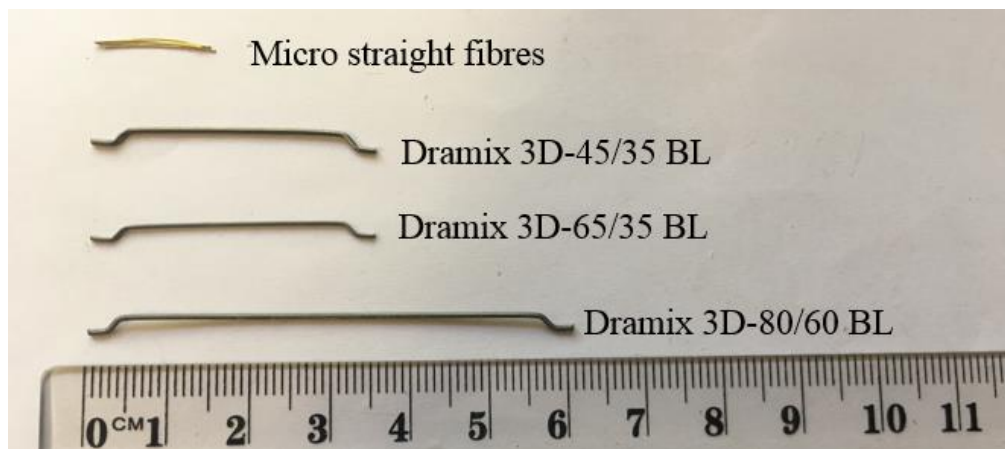
Figure. 3-1 Steel fibres used in the UHPFRCs.

3.2.1.3 Mixing procedure of UHPFRCs

A total of 12 UHPFRC mixes were prepared to investigate the effects of fibre type, fibre volume fraction and the ratio of macro-to-micro fibre on the mechanical and shrinkage properties of UHPFRCs. The detailed proportion of all mixes and their designations are given in Table 3-1. In the preparation of UHPFRC mixes, all the dry components, including binder materials and sand were mixed in a rotating pan mixer with 80 L capacity for five minutes. Following this, the liquid constituents (water and superplasticizer) were added and mixing was continued until the desirable slump flow of the mortar was achieved. Finally, the discrete steel fibres were added before mixing for a further ten minutes to ensure a uniformly-distribution of the fibres.

3.2.2 Test methods

3.2.2.1 Measurements total- and autogenous- shrinkage

The total- and autogenous- shrinkage was determined using prismatic specimens which were 75 mm x 75 mm in cross section and 285 mm long (Fig 3-2(a)). Specimens used to establish autogenous shrinkage were carefully sealed with waterproofed aluminium tape to prevent diffusion of moisture from the concrete into the surrounding environment (Fig 3-2(b)). The change in length of each specimen was regularly monitored up to the concrete age of 180 days with the 'time-zero' for autogenous shrinkage measurement taken as the final setting time of the matrix in according to ASTM C1698-09 (ASTM 2009) and previously reported studies (Darquennes et al. 2011;

Mechtcherine et al. 2014). All the total- and autogenous- shrinkage specimens were stored in an environmental chamber set at a constant 25 °C temperature and 50% relative humidity for the duration of testing.

(a)   (b)

Figure. 3-2 Shrinkage test specimens: a) sealed prism for autogenous shrinkage measurement; b) unsealed prism for free total shrinkage measurements

3.2.2.2 Fibre pulled-out for the UHPC matrix

To explore the underlying mechanism governing the effect of fibres on the shrinkage UHPFRC, the interaction between the steel fibres and the UHPC matrix was studied by considering the pull-out load-slip relationship established using single fibre pull out tests. Semi-dog bone shaped specimens were used, in which the fibre was embedded in the matrix with an embedded length equal to half the length of the fibre perpendicular to the concrete face. Three identical specimens were used for each test series. Details of test specimens and set-up are illustrated in Fig. 3-3 (a) and (b). All the pull-out test were done under a displacement-control with the rate of 1 mm/min.
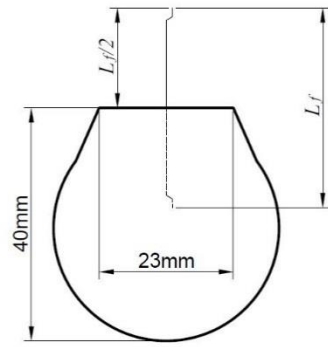
Figure. 3-3 Single fibre pull-out test: a) specimen details; b) set-up.

3.2.2.3. Compressive and splitting tensile strength

To obtain the compressive strength (f'_c) of the UHPFRCs at concrete age of 28 days and 180 days, compression tests were conducted on cylinder specimens with a 100 mm diameter and 200 mm as per ASTM standard C39/C39 M-05 (ASTM International 2005). The splitting tensile strength (f_{st}) tests were performed on cylinder specimens with a 100 mm diameter and 200 mm height according to ASTM standard C496/C496 M-04 (ASTM International 2004) at a concrete age of 28 days only.

3.3 RESULTS AND DISCUSSIONS

3.3.1 Fibre pulled-out test results

The typical failure mode of fibre pull-out is illustrated in Fig. 3-4 with the corresponding representative load-slip relationship shown in Fig. 3-5. Note that due to the limitations of testing facilities, the pull-out tests of type S fibres from the matrix were not successfully conducted.

Therefore, the pull-out load–slip behaviour of this type of fibre has been approximated as that tested by Qi et al. (Qi et al. 2018) on exactly same type of straight micro-fibre (from the same supplier with l_f=13 mm, d_f =0.2 mm) which was pulled-out from a UHPC matrix of cubic strength f'_c =151.5 MPa, which is similar to that reported in this study.

Figure. 3-4 Typical failure mode of fibre pull-out test.
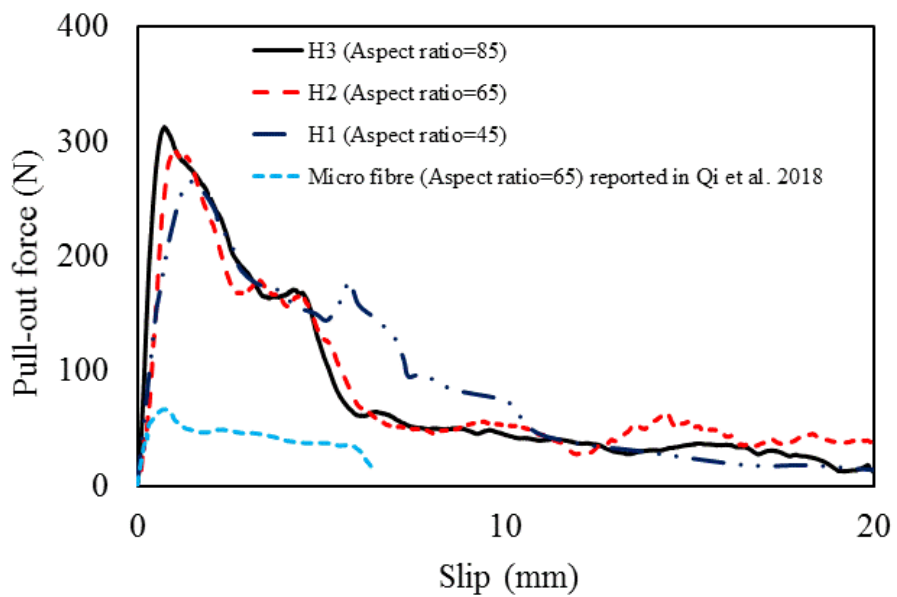
Figure. 3-5 Fibre pull-out force- slip relationships.

It is observed from Fig. 3-5 that the pull-out load-slip curve of the straight fibre from the matrix is comprised of three distinct phases: the initial linear ascending proportion (elastic behaviour with physical adhesion and static friction), a small transition region between the end of elastic stage and the peak load (debonding with physical adhesion and static friction) and finally the nearly monotonically descending branch (pull-out with kinetic friction) (Qi et al. 2018). Unlike the behaviour of the straight micro-fibre, the pull-out load-slip curves of all the three hooked end fibres exhibit five major parts: the initial linear ascending proportion (debonding and elastic behaviour with physical adhesion and static friction), a small proportion of transition region between the end of elastic stage and the peak load (deformed pull-out with kinetic friction and mechanical anchorage); stress relaxation at the beginning of the descending region (deformed pull-out stage with kinetic friction and mechanical anchorage), a strain hardening stage (deformed pull-out with kinetic friction and mechanical anchorage), and finally the gradually descending branch (straight pull-out with kinetic friction). To investigate the underlying mechanism governing the effects of fibres on the shrinkage properties of the UHPFRCs, only the static friction proportion on the pull-out load-slip curve is considered as the shrinkage induced strain caused by a single fibre is negligible.

As shown in Fig. 3-5, for a given pull-out force within the static friction region, fibre type H3, which has the highest aspect ratio developed a slightly lower slip compared to those developed by the hooked end fibres with lower aspect ratios. This indicates the fibre with a higher aspect ratio

is more effective to resist the tensile stress exerted on the matrix. Moreover, it is also observed that due to the anchorage offered by their hooked ends, each of the H series of fibres induced a lower slip than the straight fibre for a given pull-out force within the static friction region.

3.3.2 Shrinkage characterizations

3.3.2.1 General observations

Figure 3-6 (a) to (l) shows the shrinkage characterizations, including the total shrinkage strain, autogenous shrinkage stain and the calculated free drying shrinkage component of all test series. Note that the free drying shrinkage component of each of the UHPCs was estimated by subtracting the autogenous (red dashed line) shrinkage strain from the free total (black solid line) shrinkage strain at each given concrete age for each specimen series. It can be seen from Fig. 3-6 that for all mixes, the shrinkage strain increases over time in a similar way but with the magnitude of shrinkage varying significantly depending on the fibre inclusion.
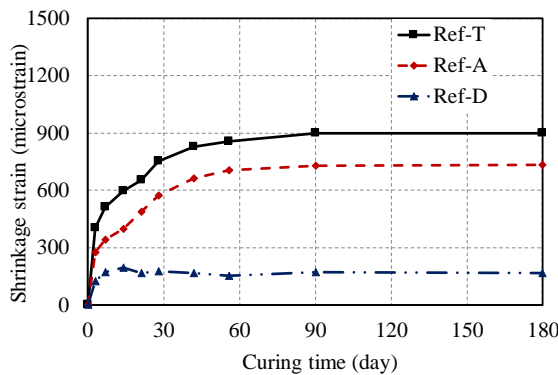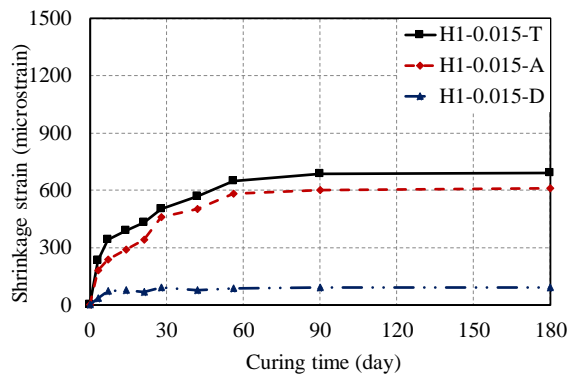
(a)   (b)
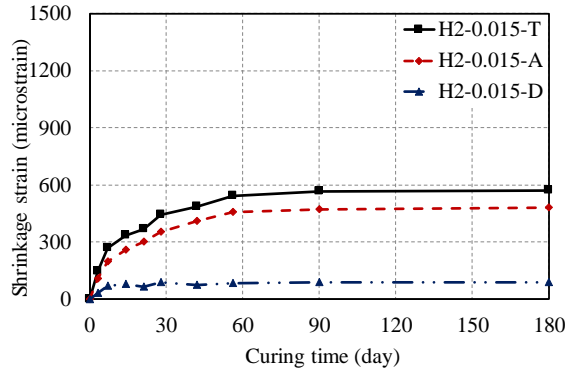
(c)
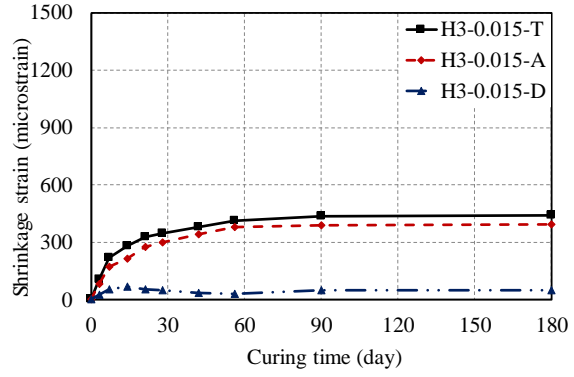
(d)
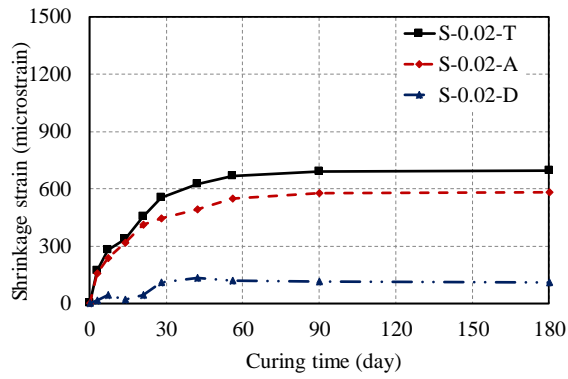
(e)
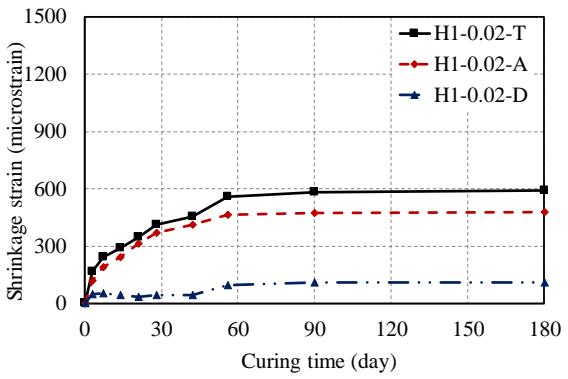
(f)
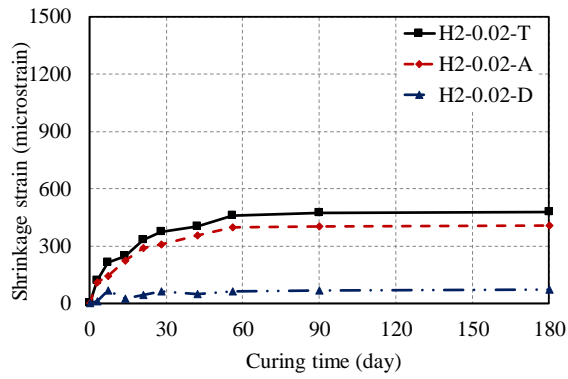
(g)
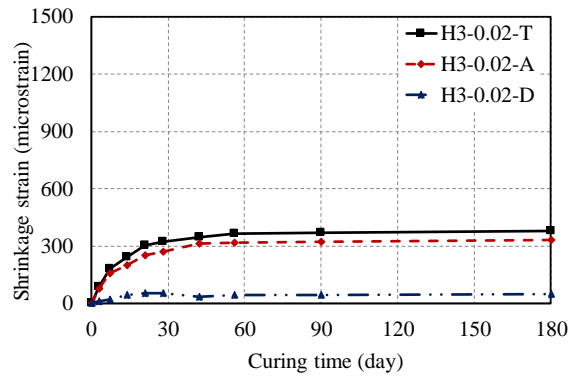
(h)
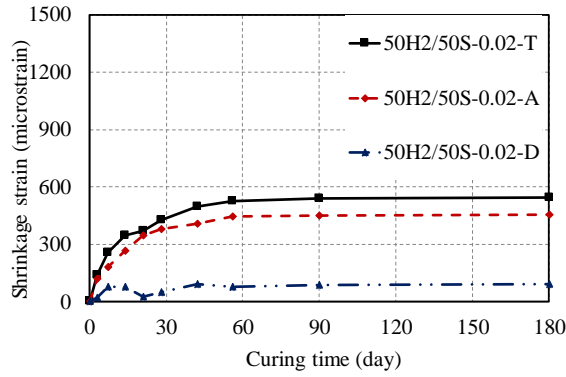
(i)
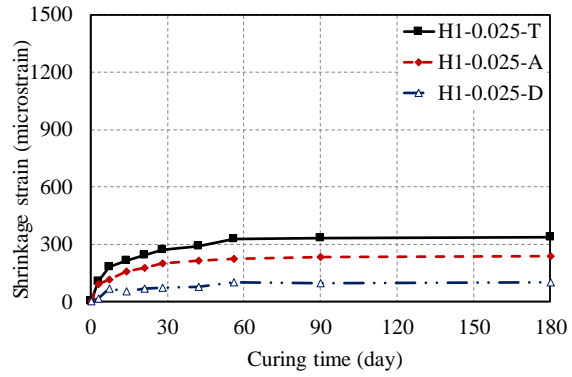
(j)
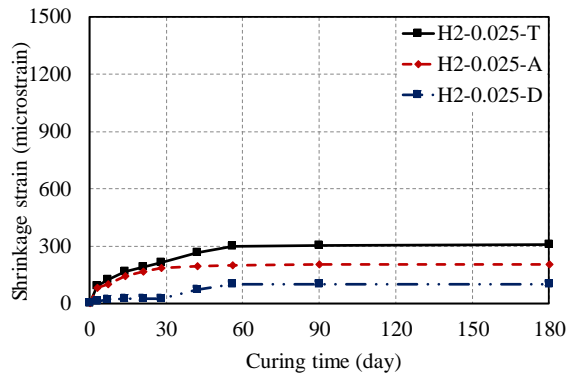
(k)
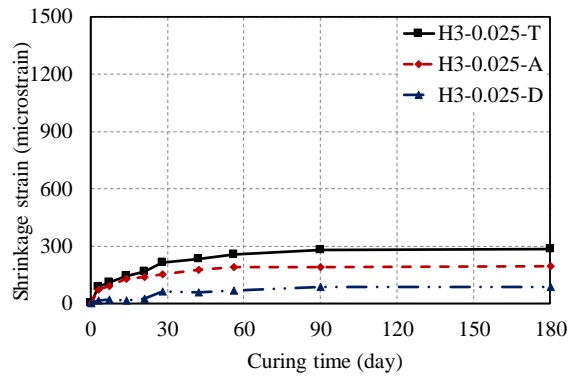
(l)

Figure. 3-6 Shrinkage characterization of the UHPFRCs: a) Ref series; b) H1-0.015 series; c) H2-0.015 series; d) H3-0.015 series; e) S-0.02 series; f) H1-0.02 series; g) H2-0.02 series; h) H3-0.02 series; i) 50H2/50S-0.02 series; j) H1-0.025 series; k) H2-0.025 series; l) H3-0.025 series.

Comparing the three shrinkage components of each mix type indicates that due to the high binder content and low volume of mixing water, only a small proportion in the total shrinkage was drying shrinkage caused by the moisture diffused from the matrix of the concrete (Xie et al. 2018), with the majority of shrinkage arising from self-desiccation caused by chemical reactions (hydration of

cement and pozzolanic reaction of silica fume) (Xie et al. 2018). As can also be seen from Fig. 3-6 that, in general, the incorporation of steel fibres in the UHPC matrix can reduce both autogenous- and drying- shrinkage of the concrete. This observation is in general agreement with those reported in the studies on UHPFRCs or FRCs in that the presence of discrete, rigid metallic fibres in the concrete is shown to reduce drying- and autogenous- shrinkage (Lei and Cao 2011; Mangat and Azari 1984; Meng and Khayat 2018; Ullah 2017). For drying shrinkage the reduction is caused by a disruption of the interconnection of pores, reducing the amount of water existed in the capillary pores (Lei and Cao 2011). For autogenous shrinkage, the steel fibres restrain shrinkage due to the bond between the fibres and matrix (Mangat and Azari 1984). The effects of the specific fibre parameters on the shrinkage characterizations are discussed in the following sections.

3.3.2.2 Effect of fibre volume fraction

The effect of fibre volume fraction on shrinkage can be studied by comparing the shrinkage measurements at a given concrete curing age of the companion concrete series produced using the same type of fibre and at different fibre concentrations (illustrated in Fig. 3-7 (a) to (f)). It is evident from the figure that, for a given type of steel fibre, the increase in fibre volume fraction in a UHPFRC reduced both the total- and autogenous- shrinkage strain of the UHPFRC at each given curing age. It is observed that the inclusions of 2.5% of steel fibres by volume in the UHPC matrix resulted in an approximately 67% reduction in total shrinkage and over 70% reduction in autogenous shrinkage. Further, inspections of the effect of fibre volume fraction on the free drying components by comparing concretes in Fig. 3-6 shows that, in general, an increase in fibre volume slightly reduces drying shrinkage. These observations were expected and can be explained by the fact that the steel fibres in the UHPC matrix acted as a skeleton in addition to the fine aggregate to

provide increased dimensional stability. Moreover, the reduction in all kinds of shrinkage with increased fibre content can also be attributed to the high elastic modulus of fibres being compared to that of the matrix, as well as the higher strength-to-size ratio of the fibres (Ullah 2017).
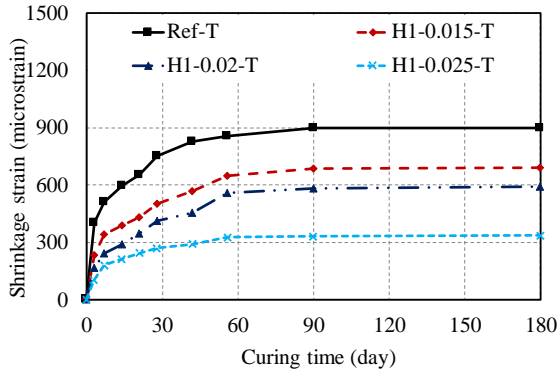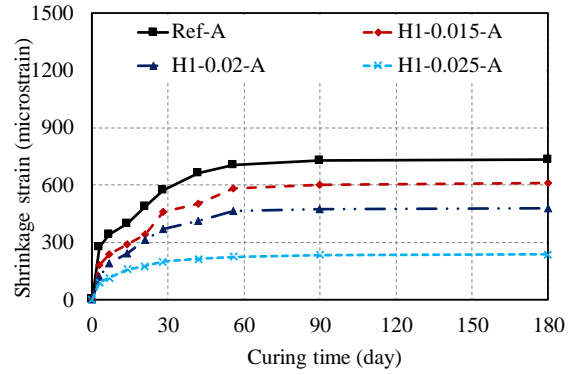
(a)   (b)
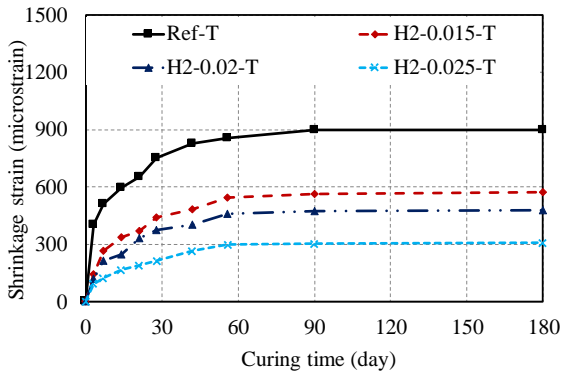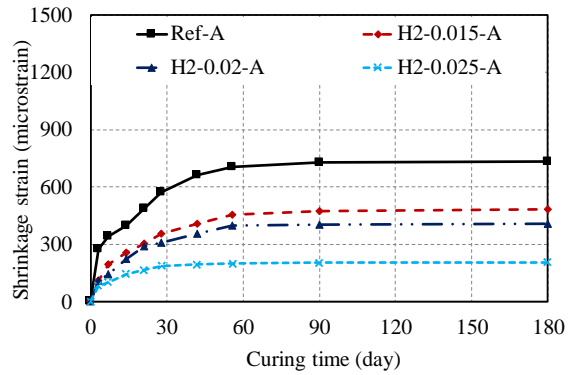
(c)   (d)
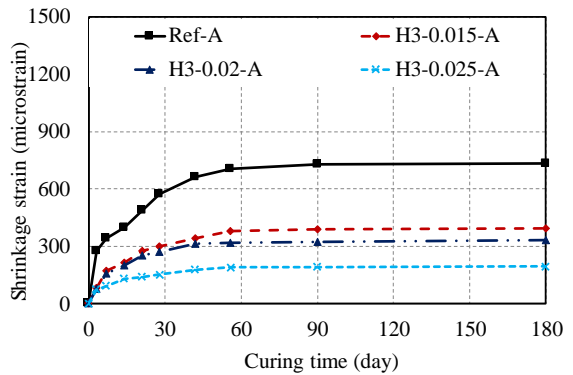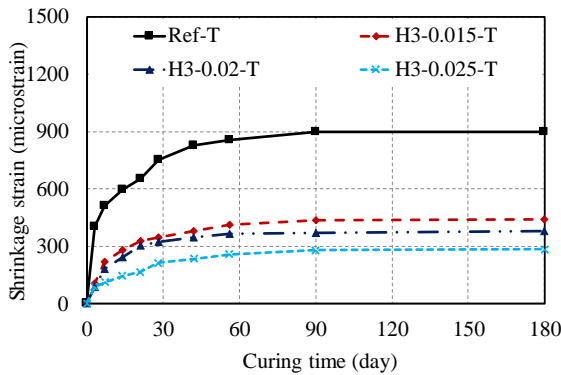
(e)   (f)

Figure. 3-7 Effect of fibre volume fraction on: a) total shrinkage-H1 series; b) autogenous shrinkage-H1 series; c) total shrinkage-H2 series; d) autogenous shrinkage-H2 series; e) total shrinkage-H2 series; f) autogenous shrinkage-H2 series.

3.3.2.3 Effect of fibre shape

Figure 3-8(a) and (b) shows the effect of fibre shape on the total and autogenous shrinkage of the UHPSFCs. It is worth mentioning that the comparisons were conducted among the shrinkage properties of concrete produced using the fibres with the same aspect ratio (i.e. S and H2 both have an aspect ratio of 65), at the same volume fraction (i.e. $V_f\% = 2.0$), and with different shapes (i.e. straight, hooked end or blended straight and hooked end). The comparisons shown in the figure suggest that the hooked fibres were more effective than the straight fibres to reduce both the total- and autogenous- shrinkage of the UHPFRCs. For instance, the incorporations of S series of fibres reduced the total shrinkage by around 23% and the autogenous shrinkage by 35%, while the addition of H2 hooked end fibres resulted in a 47% reduction in total shrinkage and 55% reduction in autogenous shrinkage. Although the straight micro-fibres may be more evenly distributed than the hooked-end fibres in the matrix, the larger reduction in shrinkage with the addition of a hooded end is attributed to a bond between the fibres and matrix (see Fig. 3-5).
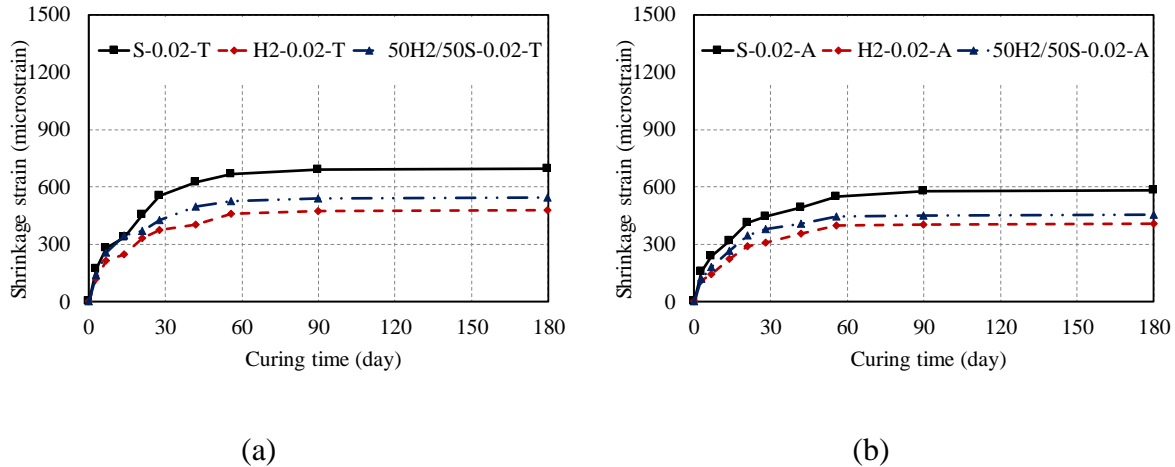
Figure. 3-8 Effect of fibre shape on: a) total shrinkage; b) autogenous shrinkage.

As can also be seen from Fig. 3-6 (e) to (h), the effect of fibre shape on the drying shrinkage component was in a similar manner to those on the total and autogenous shrinkage, where hooked end fibres performed better than the straight- and the blended fibres in reducing the drying shrinkage strain of the concrete. Compared with using only a single type of fibre, the blending of fibres resulted in a moderate reduction in the shrinkage of the UHPFRCs, including their total, autogenous (49% lower) and drying shrinkage (39% lower).

3.3.2.4 Effect of fibre aspect ratio

Figure 3-9 (a) to (f) presents the effect of fibre aspect ratio on the shrinkage characterizations at different fibre volume fractions (i.e. V_f %= 1.5, 2, or 2.5). It is evident from the that at the same fibre dosage, the use of H3 type of fibre, which has the highest aspect ratio among all the three types of hooked end fibres, resulted in a lower total- and autogenous- shrinkage of the UHPFRCs. In addition, it is shown in Fig. 3-6 that the drying shrinkage component of the UHPFRCs were

also influenced by the fibre aspect ratio, where in general, at a given fibre volume and for a given age, the calculated drying shrinkage strain of the UHPFRCs decreased with an increase in the fibre aspect ratio. As is also confirmed by the fibre pull-out test results, this observation is attributed to a higher interfacial bond force for fibres with a higher aspect (Qi et al. 2018). Note that H1 and H2 types of fibres have the same length but different diameters; H1 and H3 type of fibres are identical in their diameters but different in their lengths. The findings reported in this section therefore also suggest that longer fibres are more beneficial in preventing the shrinkage, whereas the fibres with larger diameters are less effective in restraining the shrinkage of the matrix. This finding might be explained by the fact that the build-up stress due to bond between the fibres and matrix occurred mostly along the length of fibres. Note that within the current rage of the aspect ratios of the selected fibres (i.e. 45 to 85), the aspect ratio of the fibre is not as influential as the volume fraction and the shape of fibre on the shrinkage properties of the UHPFRCs.
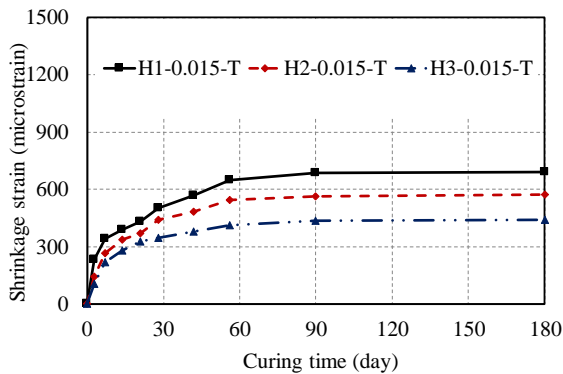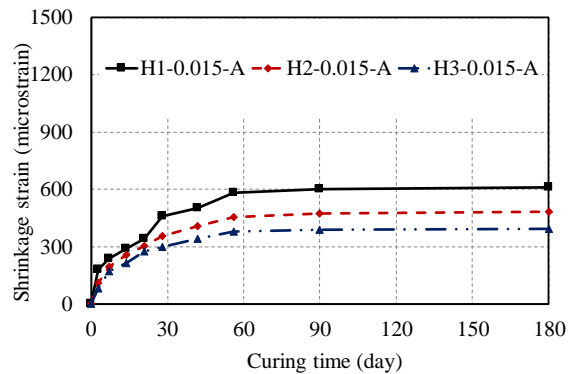
(a)   (b)
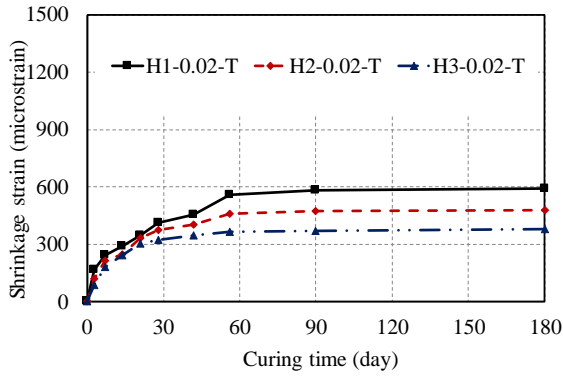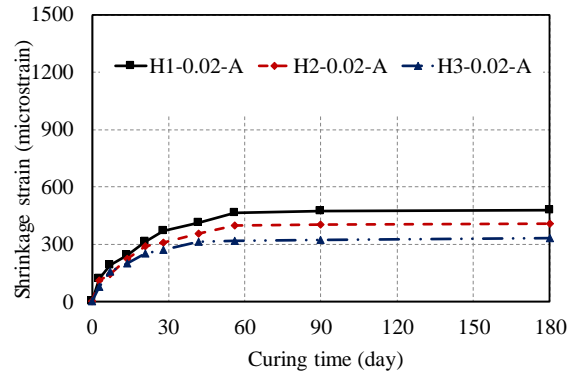
(c)   (d)
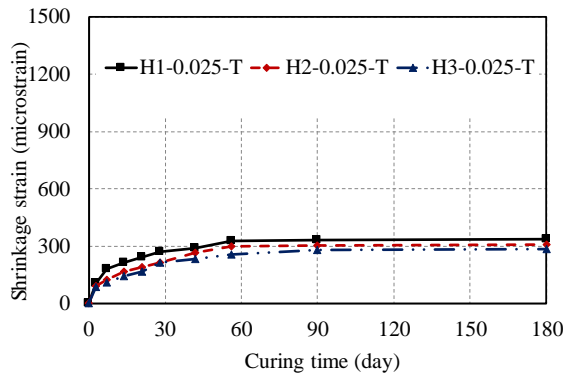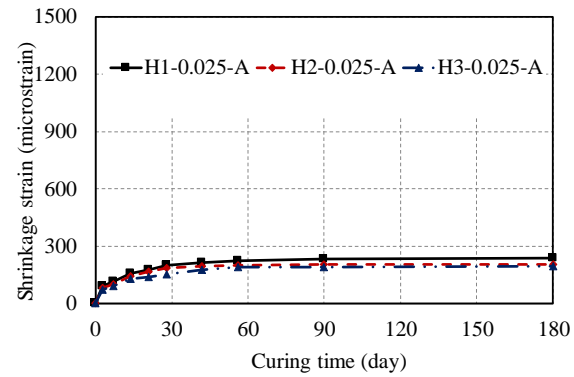
(e)   (f)

Figure. 3-9 Effect of fibre aspect ratio on: a) total shrinkage ($V_f\%$ =1.5); b) autogenous shrinkage ($V_f\%$ =1.5); c) total shrinkage ($V_f\%$ =2.0); d) autogenous shrinkage ($V_f\%$ =2.0); e) total shrinkage ($V_f\%$ =2.5); c) autogenous shrinkage ($V_f\%$ =2.5).

3.3.3 Mechanical properties of the UHPFRCs

Figure. 3-10 (a) and (b) shows graphically the compressive and splitting tensile strength of the UHPFRCs at specific testing ages and these mechanical properties are also reported in Table 3-1. As can be seen from Fig. 3-10 (a), the incorporations of steel fibres into the UHPC matrix generally

87

resulted in insignificant changes in their compressive strength at each given concrete age. This observation is in agreements with the findings reported in the previous studies on FRCs (Bhargava et al. 2006; Nataraja et al. 1999). It is observed a slight reduction in compressive strength between the curing age of 28 and 180 days of the Ref series that contained no fibres. As explained in the previous studies on UHPCs and UHPFRCs (Sobuz et al. 2016; Xie et al. 2018), this reduction in mechanical strength was caused by the shrinkage induced cracks in the specimens. For the UHPFRC series with steel fibres, their compressive strength all increased slightly between the concrete curing age of 28 and 180 days and no drops in their compressive strength were observed owing to the fibres inclusion which prevents the formations of the shrinkage induced micro-cracks.
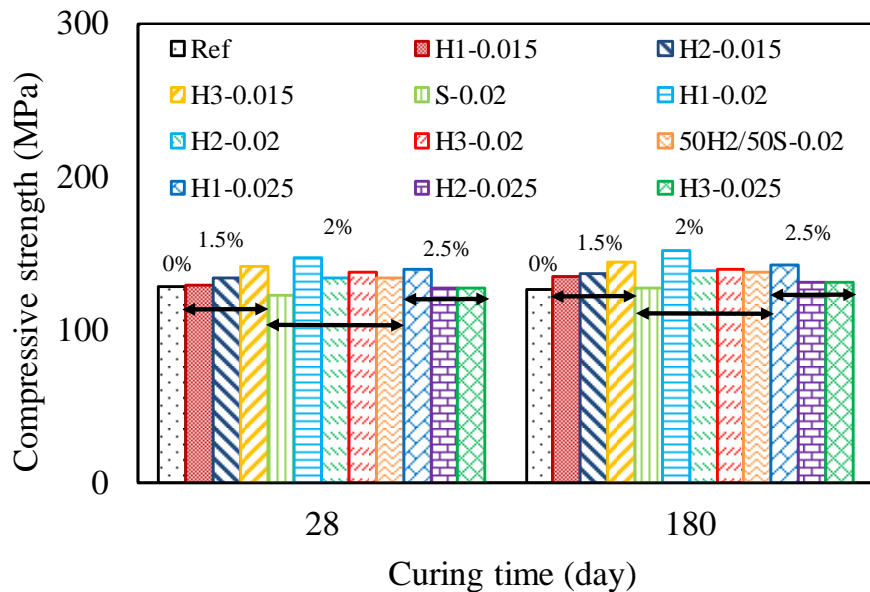
(a)
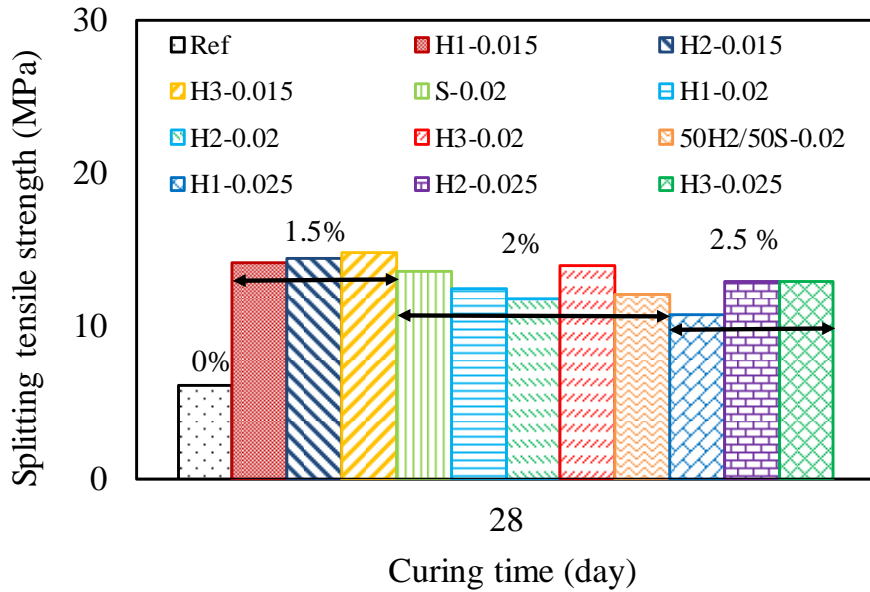
(b)

Figure. 3-10 Mechanical properties of the UHPFRCs: a) compressive strength; b) splitting tensile strength.

For the splitting tensile strength of the concretes measured at 28 days, it can be seen from Fig. 3-10 (b) that the inclusion of discrete steel fibres in UHPC matrix significantly improves the tensile properties of the concrete because the fibres provide an internal confining effect by bridging the tensile cracks (Visintin and Oehlers 2018; Visintin et al. 2018). It can be seen from Fig. 3-10 (b) that, regardless of the geometry of the fibres, the UHPFRC contained 1.5 % of fibres (by volume fraction) exhibited a higher splitting tensile strength compared to those of its companion produced using fibres at a higher volume fraction (i.e. 2% or 2.5%) and the UHPFRCs with 2 and 2.5% had nearly comparable f_{st}. This observation might be explained by the fact that at the fibre volume fraction of 1.5%, the fibres could be more evenly distributed in the matrix, which more effectively enhanced the splitting tensile strength compared to those of its counterparts with higher fibre

concentrations. It can also be seen from Table 3-1 and Fig. 3-10 (b), that for a given fibre volume fraction, the UHPFRC series with a higher fibre reinforcing index (which indicates a higher internal confining effect offered by the steel fibres) generally exhibited a slightly higher f_{st}.

3.4 CONCLUSIONS

The following major conclusions can be drawn based on the results of the present study to investigate the steel fibre on the shrinkage properties of the UHPFRCs:

1. At the initial static friction stage, the pull-out test results of a single fibre from a UHPC matrix suggests that the fibre with hooked-ends and a higher aspect ratio leads to higher pull-out force at a given slip.

2. Incorporations of discrete steel fibres into a UHPC matrix can significantly reduce the total- and autogenous- shrinkage of the concrete which are the consequences of reducing pore water in the matrix as well as reducing the tensile stress induced by the self-desiccation of the matrix through the bond between the fibre and the matrix.

3. An increase in fibre volume fraction contributes to reducing both the total and autogenous shrinkage.

4. For a given aspect ratio, steel fibres with hooked ends are more efficient than straight micro-fibres in reducing the total and autogenous shrinkage of the UHPFRCs. The use of blended hooked end and straight fibres leads to an only moderate effect on reducing the shrinkage of a UHPFRCs.

5. The use of fibres with a higher aspect ratio in a UHPFRC mix can effectively reduce the total- and autogenous shrinkage of the UHPFRCs. However, the fibre aspect ratio only slightly affects the shrinkage properties of UHPFRC.

6. The fibres inclusion in a UHPC matrix significantly improves its splitting tensile strength, whereas only a minor increase in the compressive strength of the concrete is seen. In addition, it is found that the fibre inclusion at the volume fraction of 1.5% is optimal to improve the tensile strength of the concrete.

3.5 REFERENCES

ASTM, A. (2009). "C1698-09 Standard test method for autogenous strain of cement paste and mortar." *ASTM International, West Conshohocken, PA*.

ASTM International (2004). "ASTM C496/C496M-04. Standard Test Method for Splitting Tensile Strength of Cylindrical Concrete Specimens." *ASTM International, West Conshohocken*.

ASTM International (2005). "ASTM C39/C39M-05. tandard Test Method for Compressive Strength of Cylindrical Concrete Specimens." *ASTM International, West Conshohocken*.

Australian Standard (2000). "AS 1478.1-2000. Chemical admixtures for concrete, mortar and grout Admixtures for concrete." *Standards Australia, Sydeny*.

Bhargava, P., Sharma, U. K., and Kaushik, S. K. (2006). "Compressive stress-strain behavior of small scale steel fibre reinforced high strength concrete cylinders." *Journal of advanced concrete technology*, 4(1), 109-121.

Darquennes, A., Staquet, S., and Espion, B. (2011). "Determination of time-zero and its effect on autogenous deformation evolution." *European journal of environmental and civil engineering*, 15(7), 1017-1029.

Garas, V. Y., Kahn, L. F., and Kurtis, K. E. (2009). "Short-term tensile creep and shrinkage of ultra-high performance concrete." *Cement and Concrete Composites*, 31(3), 147-152.

Koh, K., Ryu, G., Kang, S., Park, J., and Kim, S. (2011). "Shrinkage properties of ultra-high performance concrete (UHPC)." *Advanced Science Letters*, 4(3), 948-952.

Lei, Y. B., and Cao, X. J. "Study on thermal dilation coefficient of fiber concrete at early stage." *Proc., Applied Mechanics and Materials*, Trans Tech Publ, 777-781.

Mangat, P., and Azari, M. M. (1984). "A theory for the free shrinkage of steel fibre reinforced cement matrices." *Journal of materials science*, 19(7), 2183-2194.

Mechtcherine, V., Gorges, M., Schroefl, C., Assmann, A., Brameshuber, W., Ribeiro, A. n. B., Cusson, D., Cust˘dio, J., da Silva, E. F., and Ichimiya, K. (2014). "Effect of internal curing by using superabsorbent polymers (SAP) on autogenous shrinkage and other properties of a high-performance fine-grained concrete: results of a RILEM round-robin test." *Materials and structures*, 47(3), 541-562.

Meng, W., and Khayat, K. H. (2018). "Effect of hybrid fibers on fresh properties, mechanical properties, and autogenous shrinkage of cost-effective UHPC." *Journal of Materials in Civil Engineering*, 30(4), 04018030.

Nataraja, M., Dhang, N., and Gupta, A. (1999). "Stress–strain curves for steel-fiber reinforced concrete under compression." *Cement and concrete composites*, 21(5-6), 383-390.

Ou, Y.-C., Tsai, M.-S., Liu, K.-Y., and Chang, K.-C. (2011). "Compressive behavior of steel-fiber-reinforced concrete with a high reinforcing index." *Journal of Materials in Civil Engineering*, 24(2), 207-215.

Park, J.-J., Yoo, D.-Y., Kim, S.-W., and Yoon, Y.-S. (2013). "Drying shrinkage cracking characteristics of ultra-high-performance fibre reinforced concrete with expansive and shrinkage reducing agents." *Magazine of concrete research*, 65(4), 248-256.

Parra-Montesinos, G. J. (2005). "High-performance fiber-reinforced cement composites: an alternative for seismic design of structures." *ACI Structural Journal*, 102(5), 668.

Parra-Montesinos, G. J., Peterfreund, S. W., and Shih-Ho, C. (2005). "Highly damage-tolerant beam-column joints through use of high-performance fiber-reinforced cement composites." *ACI Structural Journal*, 102(3), 487.

Qi, J., Wu, Z., Ma, Z. J., and Wang, J. (2018). "Pullout behavior of straight and hooked-end steel fibers in UHPC matrix with various embedded angles." *Construction and Building Materials*, 191, 764-774.

Shi, C., Wu, Z., Xiao, J., Wang, D., Huang, Z., and Fang, Z. (2015). "A review on ultra high performance concrete: Part I. Raw materials and mixture design." *Construction and Building Materials*, 101, 741-751.

Sobuz, H., Visintin, P., Ali, M. M., Singh, M., Griffith, M., and Sheikh, A. (2016). "Manufacturing ultra-high performance concrete utilising conventional materials and production methods." *Construction and Building Materials*, 111, 251-261.

Soliman, A., and Nehdi, M. (2014). "Effects of shrinkage reducing admixture and wollastonite microfiber on early-age behavior of ultra-high performance concrete." *Cement and Concrete Composites*, 46, 81-89.

Ullah, F. (2017). "Early age autogenous shrinkage and long-term drying shrinkage of fibre reinforced concrete."

Visintin, P., and Oehlers, D. J. (2018). "Fundamental mechanics that govern the flexural behaviour of reinforced concrete beams with fibre-reinforced concrete." *Advances in Structural Engineering*, 21(7), 1088-1102.

Visintin, P., Sturm, A. B., Ali, M. M., and Oehlers, D. J. (2018). "Blending Macro and Micro Fibres to Enhance the Serviceability Behaviour of UHPFRC." *Australian Journal of Civil Engineering*.

Wang, D., Shi, C., Wu, Z., Xiao, J., Huang, Z., and Fang, Z. (2015). "A review on ultra high performance concrete: Part II. Hydration, microstructure and properties." *Construction and Building Materials*, 96, 368-377.

Xie, T., Fang, C., Ali, M. M., and Visintin, P. (2018). "Characterizations of autogenous and drying shrinkage of ultra-high performance concrete (UHPC): An experimental study." *Cement and Concrete Composites*, 91, 156-173.

Xie, T., and Ozbakkaloglu, T. (2015). "Behavior of steel fiber-reinforced high-strength concrete-filled FRP tube columns under axial compression." *Engineering Structures*, 90, 158-171.

Yoo, D.-Y., Banthia, N., and Yoon, Y.-S. (2015). "Effectiveness of shrinkage-reducing admixture in reducing autogenous shrinkage stress of ultra-high-performance fiber-reinforced concrete." *Cement and Concrete Composites*, 64, 27-36.

Yoo, D.-Y., Min, K.-H., Lee, J.-H., and Yoon, Y.-S. (2014). "Shrinkage and cracking of restrained ultra-high-performance fiber-reinforced concrete slabs at early age." *Construction and Building Materials*, 73, 357-365.

Yoo, D.-Y., Park, J.-J., Kim, S.-W., and Yoon, Y.-S. (2013). "Early age setting, shrinkage and tensile characteristics of ultra high performance fiber reinforced concrete." *Construction and Building Materials*, 41, 427-438.

Yoo, D.-Y., Park, J.-J., Kim, S.-W., and Yoon, Y.-S. (2014). "Influence of reinforcing bar type on autogenous shrinkage stress and bond behavior of ultra high performance fiber reinforced concrete." *Cement and Concrete Composites*, 48, 150-161.

Yoo, D.-Y., Park, J.-J., Kim, S.-W., and Yoon, Y.-S. (2014). "Influence of ring size on the restrained shrinkage behavior of ultra high performance fiber reinforced concrete." *Materials and structures*, 47(7), 1161-1174.

CHAPTER 4

Partial Interaction Model of Flexural Behaviour of PVA Fibre Reinforced Concrete Beams with GFRP Bars

[1]Xie, T., [2]Mohamed Ali, M.S., [3]Visintin, P., [4]Oehlers, D.J., [5]Sheikh, A.H

[1]**Mr. Tianyu Xie (Corresponding author)**

Ph. D Candidate,

School of Civil, Environmental and Mining Engineering

The University of Adelaide

South Australia 5005

AUSTRALIA

[2]**Dr. Mohamed Ali, M.S**

Senior Lecturer,

 School of Civil, Environmental and Mining Engineering

The University of Adelaide

 South Australia 5005

AUSTRALIA

[3]**Dr.Phillip Visintin**

Associate Professor,

School of Civil, Environmental and Mining Engineering

The University of Adelaide

 South Australia 5005

AUSTRALIA

[4]Emeritus Professor Deric J. Oehlers

School of Civil, Environmental and Mining Engineering

The University of Adelaide

South Australia 5005

AUSTRALIA

[5]Associate Professor Abdul H. Sheikh

School of Civil, Environmental and Mining Engineering

The University of Adelaide

South Australia 5005

AUSTRALIA

Publication: T. Xie, M.S. Mohamed Ali, P. Visintin, D. J. Oehlers, and A. H. Sheikh. "Partial Interaction Model of Flexural Behavior of PVA Fiber–Reinforced Concrete Beams with GFRP Bars." *Journal of Composites for Construction* 22, no. 5 (2018): 04018043.

THIS PAGE HAS BEEN LEFT INTENTIONALLY BLANK

Statement of Authorship

Title of Paper	PARTIAL INTERACTION MODEL OF FLEXURAL BEHAVIOUR OF PVA FIBRE REINFORCED CONCRETE BEAMS WITH GFRP BARS
Publication Status	☑ Published ☐ Accepted for Publication ☐ Submitted for Publication ☐ Unpublished and Unsubmitted work written in manuscript style
Publication Details	Xie, T., Mohamed Ali, M. S., Visintin, P., Oehlers, D. J., & Sheikh, A. H. (2018). Partial Interaction Model of Flexural Behavior of PVA Fiber–Reinforced Concrete Beams with GFRP Bars. Journal of Composites for Construction, 22(5), 04018043.

Principal Author

Name of Principal Author (Candidate)	Tianyu Xie		
Contribution to the Paper	Developing model, analysing of data, drafting manuscript		
Overall percentage (%)	40		
Certification:	This paper reports on original research I conducted during the period of my Higher Degree by Research candidature and is not subject to any obligations or contractual agreements with a third party that would constrain its inclusion in this thesis. I am the primary author of this paper.		
Signature		Date	12/02/2019

Co-Author Contributions

By signing the Statement of Authorship, each author certifies that:

i.   the candidate's stated contribution to the publication is accurate (as detailed above);

ii.   permission is granted for the candidate in include the publication in the thesis; and

iii.   the sum of all co-author contributions is equal to 100% less the candidate's stated contribution.

Name of Co-Author	Dr Mohamed Ali Sadakkathulla		
Contribution to the Paper	Designing concept, supervising experiments, revising manuscript (15%)		
Signature		Date	12/02/2019

Name of Co-Author	Associate Professor Phillip Visintin		
Contribution to the Paper	Designing concept, developing model, revising manuscript (15%)		
Signature		Date	12/02/2019

Name of Co-Author	Emeritus Professor Deric J. Oehlers		
Contribution to the Paper	Designing concept, supervising experiments, analysing of data (15%)		
Signature		Date	7/2/19

Name of Co-Author	Associate Professor Abdul H. Sheikh		
Contribution to the Paper	Designing concept, supervising experiments (15%)		
Signature		Date	12/02/2019

Please cut and paste additional co-author panels here as required.

ABSTRACT

This paper describes experimental and analytical investigations on a highly durable composite structural system comprising of polyvinyl alcohol (PVA) fibre-reinforced concrete (PVA-FRC) reinforced with glass-FRP (GFRP) bars. To aid in the development of a design guideline for this novel composite beam system, a generic, analytical approach which is equally applicable to both conventional concrete and FRC beams reinforced with steel or FRP rebars is applied. Predicted load-deflection and load crack width responses are compared to the experimental results, showing very good correlation for the flexural behaviour of PVA fibre reinforced concrete members.

Keywords: Polyvinyl alcohol (PVA) fibres; Glass-FRP (GFRP) bars, Partial interaction analysis (PI); Flexural behaviour; Fibre reinforced concrete (FRC)

4.1 INTRODUCTION

Degradation of steel reinforced concrete (RC) infrastructure due to reinforcement corrosion results in significant damage and economic loss (Almusallam 2001; Feng et al. 2015). In the past three decades, glass fibre-reinforced polymer (GFRP) reinforcement has been used as a corrosion resistant alternative to conventional steel reinforcement (Alsayed 1998; Barris et al. 2009; Goldston et al. 2017; Jakubovskis et al. 2014; Mazaheripour et al. 2016). Due to the elastic brittle nature of GFRP, the design of glass fibre reinforced polymer reinforced concrete (GFRPRC) at the ultimate limit is generally restricted to over reinforced sections in which member ductility arises from concrete crushing (Kachlakev and McCurry 2000; Qu et al. 2009). Moreover, due to the low elastic modulus of GFRP and the weaker bond between GFRP and

the surrounding concrete, deflections and crack widths in GFRPRC beams at the serviceability limit may be greater than that of conventional steel RC beams (Toutanji and Deng 2003).

A recent focus of concrete technology has been the incorporation of randomly distributed fibres to form fibre reinforced concretes (FRC). These materials have been shown to improve the flexural ductility of members by restraining post-peak sliding of concrete wedges (Matthys 2017; Visintin and Oehlers 2017) and to reduce deflections and crack widths due to the ability to transfer stresses across tensile cracks (Altun et al. 2007; Schumacher 2006; Visintin and Oehlers 2017; Yoo et al. 2015). Hence the incorporation of fibres into GFRPRC may provide a means for compensating for the lower ductility and larger deflections and crack widths seen in this form of construction.

In this paper, a highly durable structural system is proposed by combining the durability of GFRP reinforcement with polyvinyl alcohol (PVA) FRC. The paper first describes an experimental program to establish the fundamental material properties that control the behaviour of GFRP reinforced PVA-FRC; namely the compressive and tensile stress-strain relationships of the PVA-FRC and the local bond stress-slip relationship between the PVA-FRC are determined. Having quantified the fundamental material properties the results of four tests on PVA-FRC beams with GFRP bars are reported. It is then shown how an existing mechanics based analysis technique for predicting the load-deflection and load-crack width behaviours of conventional concrete beams can be extended for the analysis of FRC beams.

The application of a generic approach is considered important as an increasingly large number of design options are becoming available to practitioners and hence for widespread application of new materials to occur, standardised analysis procedures, which can be applied to a range

of material types, are required. It should be noted that the segmental approach proposed here has already been widely applied to a wide range of materials and loading scenarios including: the short and long term performance of steel and FRP reinforced concrete (Feng et al. 2015; Knight et al. 2014; Visintin et al. 2013) and prestressed concrete (Knight et al. 2014; Knight et al. 2013) beams, and it will be shown here that it can be further applied to GFRP reinforced FRC. Significantly, in applying the analytical approach to this novel system, it is shown how very few experimental inputs are required in order to adequately predict the load-deflection and load-crack width behaviour of the member. Hence the analysis approach proposed should allow for a more rapid development of novel materials, as well as a faster transition from the lab technologies to real world applications.

4.2 EXPERIMENTAL PROGRAM

Aiming to apply the segmental analytical approach (Visintin et al. 2012; Visintin and Oehlers 2017; Visintin et al. 2016) to the prediction of the load-deflection and load-crack width behaviour of the FRC-FRP system, an experimental program was formulated to establish to obtain the fundamental material properties required for the analysis. The required material properties include: the compressive and direct tensile behaviour of the PVA-FRC and the bond between the GFRP reinforcement and PVA-FRC. To then show the predictive capability of the segmental approach, four beam tests were conducted to obtain the load-deflection and load-crack width behaviour.

4.2.1 Materials

4.2.1.1 PVA fibre-reinforced concrete (PVA-FRC)

Test specimens used in the experimental program were manufactured using two different PVA fibre-reinforced normal-strength concretes. These two mixes were both prepared using a water-

to-cement ratio (*w/c*) of 0.5, and to investigate the influence of fibre content, the fibre weight fraction was either 6 kg/m^3 (designated as FRC-6), or 12 kg/m^3 (designated as FRC-12). The PVA fibre had a length of 30 mm and a nominal diameter of 0.75 mm (with the aspect ratio of 40). The manufacturer reported tensile strength and density of the fibre is1620 MPa and 1.3 g/cm^3 respectively. The full mix proportions of the FRCs are given in Table 3-1.

Table 3-1. Mix proportions of concrete

Components	FRC-6	FRC-12
Fibre content (kg/m^3)	6	12
Water (kg/m^3)	166	166
Cement (kg/m^3)	332	332
Water-to-cement ratio	0.5	0.5
Sand (kg/m^3)	875	830
Aggregate-10 mm (kg/m^3)	330	330
Aggregate-20 mm (kg/m^3)	700	700
Density (kg/m^3)	2409	2370

4.2.1.2 GFRP bar

The GFRP bars were sand-coated with a nominal diameter of 12 mm. For analysis, the GFRP bars were assumed to behave in a linear elastic-brittle manner where the ultimate tensile strength and elastic modulus of GFRP bar are 1186 MPa and 66.3 GPa respectively. These properties were obtained from the manufacturer of the GFRP and were determined by averaging the results of 12 direct tension tests.

4.2.2 Test methods

4.2.2.1 Material tests

4.2.2.1.1 Compressive stress-strain relationship

To quantify the axial compressive stress-strain relationship of the PVA-FRC compression tests according to Australian standard 1012.9 (Standard Australia 2014) were conducted on standard cylindrical specimens with 100 mm diameter and 200 mm height. Axial deformations were recorded using two 10 mm LVDTs installed along the full-height of the specimens.

4.2.2.1.2 Tensile stress-strain relationship

The pre-cracking stress-strain and post-cracking stress-crack width behaviour of the FRC was determined in accordance with the RILEM TC 162-TDF standard (Rilem 2002). In these tests cylindrical specimens with 150 mm diameter and 150 mm height were tested under uniaxial tension by applying a force to steel plates adhesively bonded to the ends of the specimens (Fig. 4-1). During testing, a tensile force was applied to maintain a displacement rate of 0.1 mm per minute and to obtain the stress crack width behaviour, the deformation across a circumferential notch with a depth of 15 mm and width of 2.5 mm was recorded using two LVDTs.
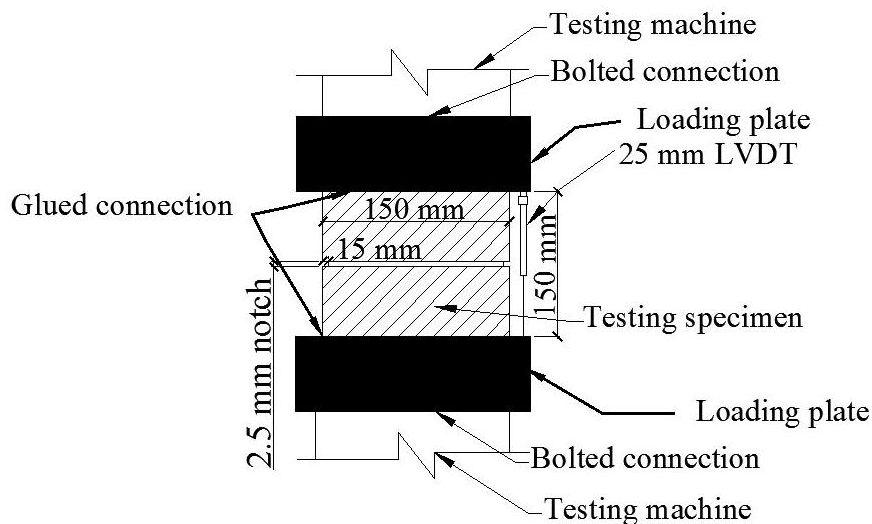
Figure 4-1. Details of direct tension test specimen and set up

4.2.2.1.3 Pull-out tests

To obtain the local bond stress-slip behaviour of the FRC-FRP bar interface, pull-out tests were conducted using the specimens shown in Fig. 4-2. These specimens consisted of a 200 mm x 200 mm square prism with a height of 350 mm into which a 12 mm GFRP bar with a bonded length of 60 or 300 mm was embedded. The short embedment length tests (60 mm) were used to assess the local bond-slip response for the subsequent modelling of tension stiffening and crack opening in the beams. In these tests a 60 mm bonded length was chosen to ensure the bond stresses along the bar are approximately evenly distributed, this ensures that the average bond stress at failure is close to the actual local bond stress (Feng et al. 2015; Haskett et al. 2008).

Additionally, in order to ensure the reinforcement was fully anchored in the beam tests, specimens with a longer embedment length (300 mm) and different fibre contents (i.e. 0 or 6 kg/m^3) were also prepared and tested.

(a)   (b)
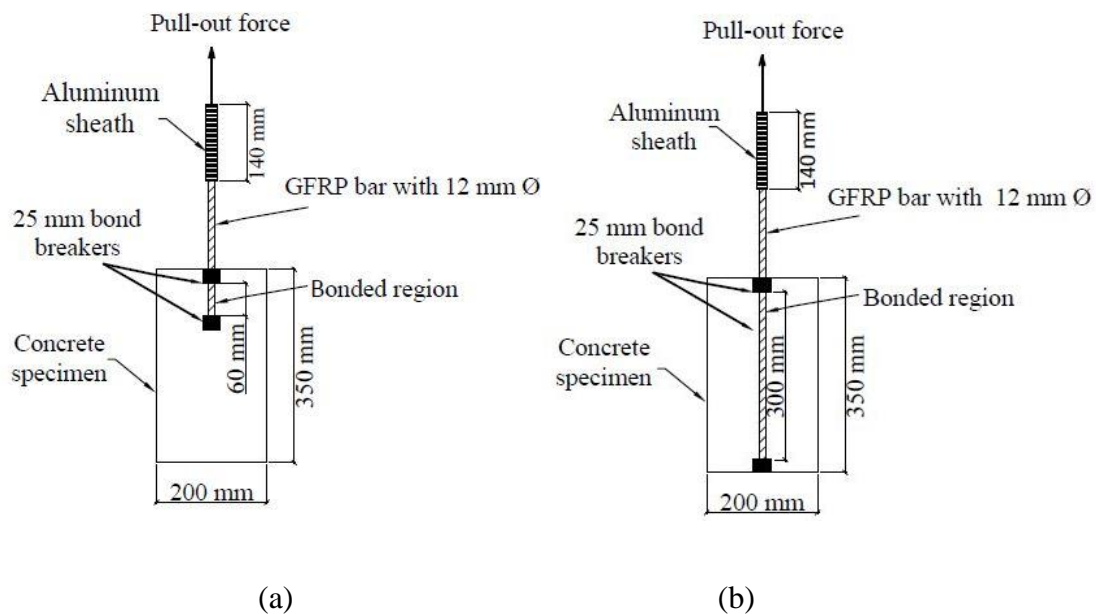
(c)

Figure 4-2. Details of pull-out test: a) test specimen with a shorter embedment length (60 mm); b) test specimen with a longer embedment length (300 mm); c) pull-out test setup

For all bond tests, in order to avoid concrete conical pull-out failure the bond was broken over the first 25 mm of the embedded length using a PVC tube as a bond breaker. During testing the bar was pulled from the concrete block at a rate of 6 kN/min and the slip of the bar relative to the top of the concrete block was measured using an LVDT as shown in Fig. 4-2. For the purpose of examining the effects of the fibre content on the bond-slip behaviour, a series of reference specimens without fibres were also tested. It should be noted that although the concrete surrounding the reinforcement in pull tests is in a state of compression, that the bond properties derived from this form of test is commonly used to simulate behaviour where the concrete surrounding the reinforcement is in tension. For example bond properties have been used to simulate crack formation and crack widening in (Achillides and Pilakoutas 2004; Mo et al. 2016; Visintin et al. 2018; Visintin et al. 2016; Zhang et al. 2016). While this is a generally accepted approach, the use of bond properties extracted from half-beam tests more closely matches the state of stress experience in the tensile region of a beam (Ashtiani et al. 2013; Jakubovskis et al. 2014).

4.2.2.2 Beam tests

In order to experimentally establish the flexural behaviour of PVA fibre reinforced members with GFRP bars, and for validations of the proposed model, two series of beams prepared using FRC with different fibre weight fractions were manufactured and tested. Two nominally identical specimens were tested for each beam series in order to establish any variation in behaviour due to differences in the distribution of fibre density or orientation which may occur during casting.

Each beam was designed to be over reinforced and had a cross-section of 200 mm × 200 mm and was reinforced with four 12 mm GFRP bars at an effective depth of 170 mm. To prevent shear failure, adequate shear reinforcements were also provided which consisted of 7 mm diameter stirrups spaced at 120 mm centres. It should be noted that no shear reinforcement was provided in the constant moment region (the central 600 mm) in order to avoid any confining effect which may occur. The details of the cross-section of test beams are shown in Fig. 4-3 (a). To hang the stirrups, two steel bars with a 7 mm diameter, located at an effective depth of 30 mm were included in the compression region.

Figures 4-3 (b) and (c) schematically illustrate the details of the beam test set-up. All members were tested as simply-supported under four-point bending. The first beam was tested with a span of 1600 mm between the two supports and with the concentrated loads positioned at a spacing of 600 mm. However, this arrangement resulted in unexpected shear failure. To avoid such a shear failure in subsequent tests, length of the constant moment region was reduced to 500 mm. Throughout testing, the deflection of the beam was measured by 50 mm LVDTs positioned at the location of each loading point and at the mid-span of the beam. To record

crack width, a lateral LVDT was placed in the centre of the beam at the level of the tensile reinforcement.

(a)

(b)

(c)
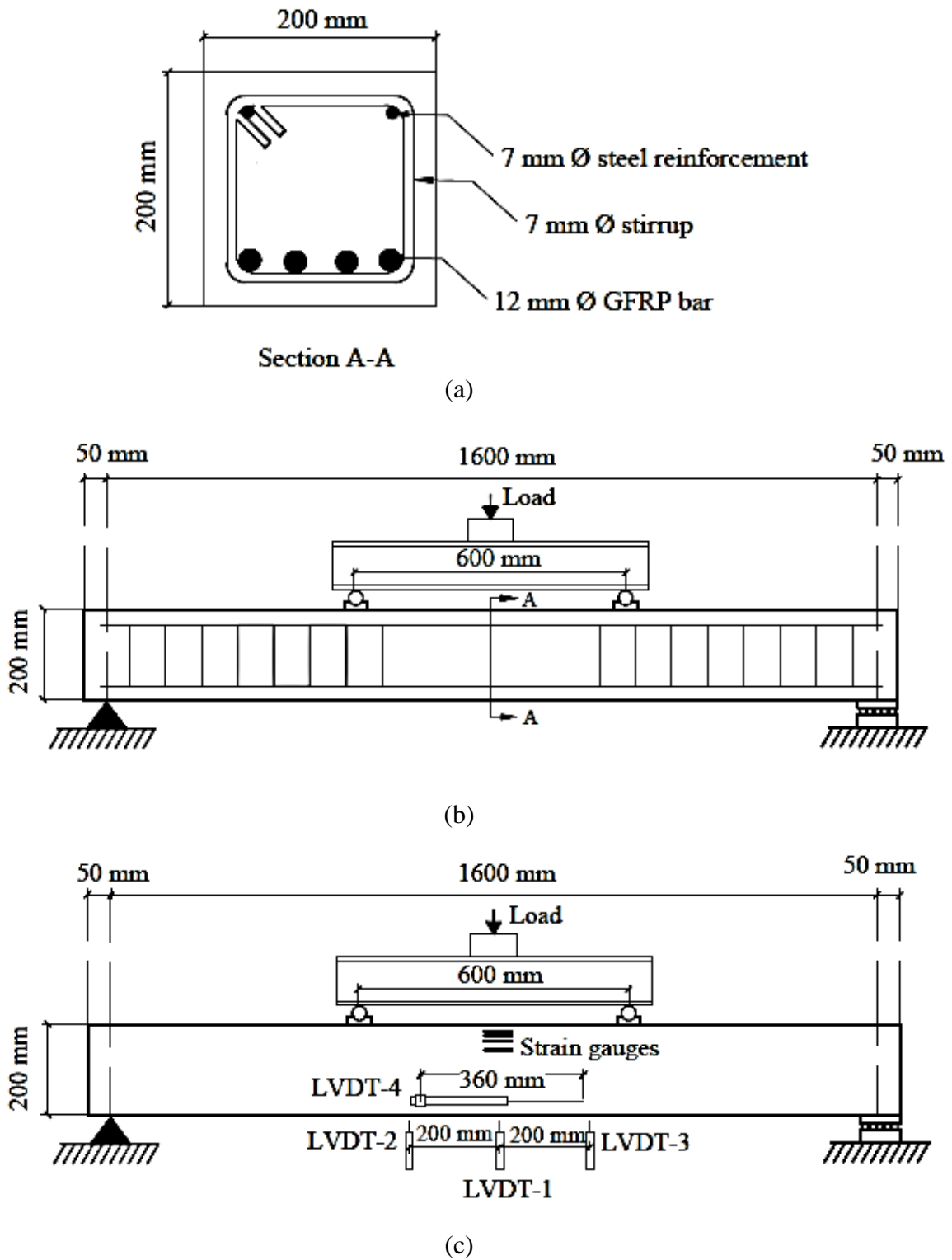
Figure 4-3. Details of beam specimen and test set up: a) details of beam cross-section; b) details of the beam specimen; c) test set up

4.3 RESULTS AND DISCUSSIONS

4.3.1 Materials properties

4.3.1.1 Compressive strength and stress-strain behaviour

Figure 4-4 illustrates the axial compressive stress-strain relationship for each FRC, from which it can be seen that, regardless of fibre content the axial stress-strain relationship of the concrete are nearly identical until that the peak stress is reached. After the peak stress, an increase in ductility with the increase in fibre content increased is observed. These observations are in close agreement with those reported in previous studies on the compressive stress-strain behaviour of FRCs (Bhargava et al. 2006; Ezeldin and Balaguru 1992; Olivito and Zuccarello 2010; Wang et al. 2012) where the increase in ductility can be attributed to the additional confining effect provided by the internal fibres. To model the compressive stress-strain behaviour of the PVA-FRC, Hognestad's (Hognestad et al. 1955) model for conventional concrete was modified to induce a linear descending branch. A general expression that can describe the compressive stress-strain behaviour of FRC with different PVA fibres is given in Eq. (3-1)

$$\sigma_c = \begin{cases} f_c' \left(\frac{2\varepsilon_c}{\varepsilon_o} - \left(\frac{\varepsilon_c}{\varepsilon_o} \right)^2 \right) & if \ \varepsilon_c \leq \varepsilon_o \\ f_c' \left(1 - \alpha(\varepsilon_c - \varepsilon_o) \right) & if \ \varepsilon_c > \varepsilon_o \end{cases} \tag{3-1}$$

where ε_o is the concrete strain corresponding to the peak stress, and α is the shape factor for the descending branch of the compressive stress-strain curves of FRC with different content fibers. In the present study, α was taken as 200 for mixes with 6 kg/m^3 of fibres, and 100 for mixes with 12 kg/m^3 of fibres. Fig. 4-4 shows that the proposed expressions for $\sigma - \varepsilon$ relationship well reproduces the test results.
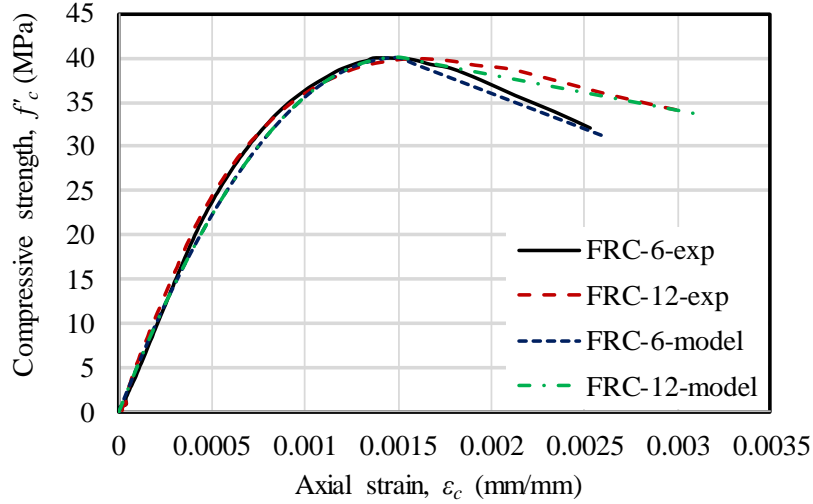
Figure 4-4. Compressive stress-strain relationship of FRCs

4.3.1.2 Tensile strength and stress-strain behaviour

The tensile behaviour of the FRC-6 and FRC-12 is shown in Fig. 4-5. Note that prior to cracking of the FRC, its tensile stress-strain relationship is shown in Fig. 4-5 (a) and in the post-cracking stage, its tensile stress-crack width relationship is shown in Fig. 4-5 (b). Comparing the behaviour with different fibre contents, it can be seen that the mix with a higher fibre content (FRC-12) exhibited a higher tensile strength prior to cracking and required a higher tensile strength to attain the same crack width as that of FRC-6 at the post-cracking stage. This improvement in the tensile behaviour of FRC can be attributed to the increase in the number of fibres crossing the crack as the fibre content increases (Olivito and Zuccarello 2010; Xu et al. 1998). From this experimental data, the general expression in Eq. (3-2) is proposed to represent the tensile characterisation of the FRCs with different PVA fibres content.

$$\sigma_t = \begin{cases} E_{ct}\varepsilon_t & prior\ mircocracking \\ f_{t1} + E_{t1}(\varepsilon_t - \varepsilon_{t1}) & crack\ straining\ stage \\ f_t - \beta W_{cr} & crack\ opening\ stage \\ 0.035 f_t & residual\ tensile\ stress \end{cases} \tag{3-2}$$

Where, in Eq. 3-2 E_{ct} is the modules of the FRC prior cracking, f_{t1} and ε_{t1} are the tensile

stress and the strain corresponding to the initiation of the crack, E_{t1} is the modulus for the

crack straining stage f_t is the peak tensile stress of the FRC, W_{cr} is the crack width of the FRC

in mm, β is the slope of the descending branch of the stress crack width curve of the FRC.

Figs. 4-5 (a) and (b) show that the proposed model provided a close match to the experimental
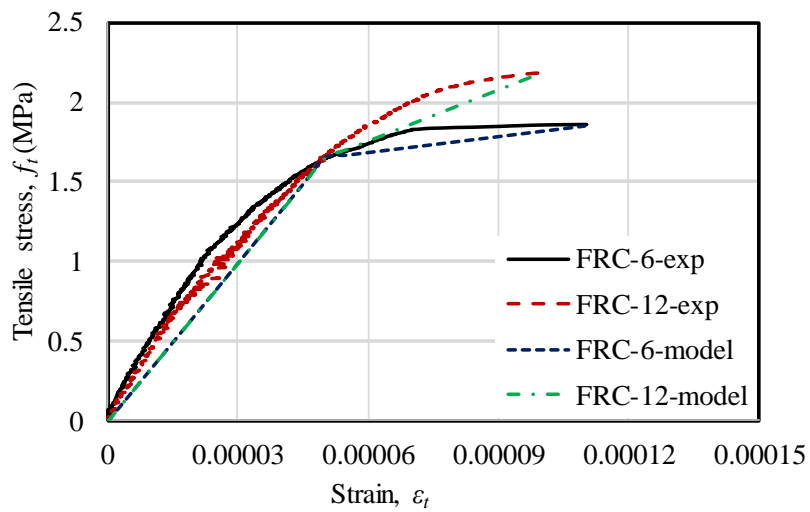
results.

(a)
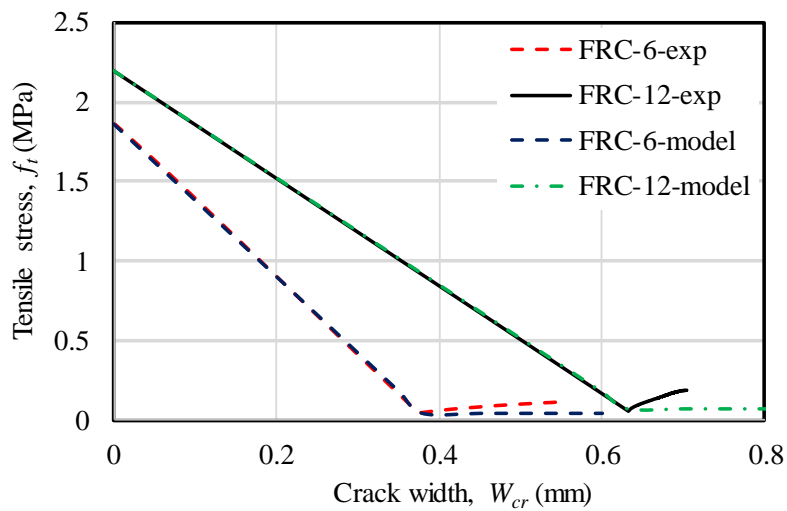
(b)

Figure 4-5. Tensile response of FRCs

4.3.1.3 Pull-out test results

4.3.1.3.1 Global load-slip (P/Δ) relationship

Key values used for defining the global load-slip (*P/Δ*) relationship are presented in Table 3-2. In all but two cases, the specimens failed by pull-out of the reinforcing bar. A typical bar following pull-out is shown in Fig. 4-6. Pull-out failure occurred once the shear strength of the bond between the rebar and concrete was exceeded. At this point, the bar began to pull out at a gradually decreasing load and all that remained was the residual strength due to friction between the bar and adjacent concrete, which simulated the process of the intermediate crack (IC) debonding of the FRP bar. The typical local load-slip relationship of each concrete series is illustrated in Fig. 4-7. Regardless of the fibre content used in the tests, a similar ascending branch was observed. However, when compared with the plain concrete mix, the FRC mix showed a slight increase in the peak load and a steeper ascending branch as a stronger bond was present for smaller slips. These observations are in agreement with those studies reported previously on bond-slip response of FRP bars in FRCs (Mazaheripour et al. 2013) and could be explained by two factors; the fibres providing more friction as the bars pull-out, or more likely, the passive confinement exerted by increasing fibre content as the concrete starts failing in tension locally. It is worth noting that the fracture failure of the FRP in each test series, which is different to those IC debonding cases, indicates that 300 mm is nearly sufficient to fully anchor the FRP bar in either plain concrete of 40 MPa strength of PVA FRC with 6 kg/m^3 fibre content.

Table 3-2. Pull Test Results

Specimen	Embedment Length (mm)	Bar diameter (mm)	Fibre Content (kg/m^3)	P_{max} (kN)	Ave. (kN)	τ_{av} (MPa)	Ave. (MPa)	Failure Mode
FRC-0-L-1	300	12	0	136		12.0		Pull-out
FRC-0-L-2	300	12	0	164*	141	14.5	12.5	FRP bar rupture
FRC-0-L-3	300	12	0	146		12.9		Pull-out
FRC-6-L-1	300	12	6	154		13.6		Pull-out
FRC-6-L-2	300	12	6	145	150	12.9	13.3	Pull-out
FRC-6-L-3	300	12	6	164*		14.5		FRP bar rupture
FRC-0-S-1	60	12	0	26.6		11.7		Pull-out
FRC-0-S-2	60	12	0	27.9	28.3	12.4	12.5	Pull-out
FRC-0-S-3	60	12	0	30.4		13.4		Pull-out
FRC-6-S-1	60	12	6	30.3		13.4		Pull-out
FRC-6-S-2	60	12	6	31.4	29.8	13.9	13.2	Pull-out
FRC-6-S-3	60	12	6	27.5		12.2		Pull-out
FRC-12-S-1	60	12	12	33.7		14.9		Pull-out
FRC-12-S-2	60	12	12	34.3	34.7	15.2	15.3	Pull-out
FRC-12-S-3	60	12	12	36.0		15.9		Pull-out

* Excluded for calculating the average value
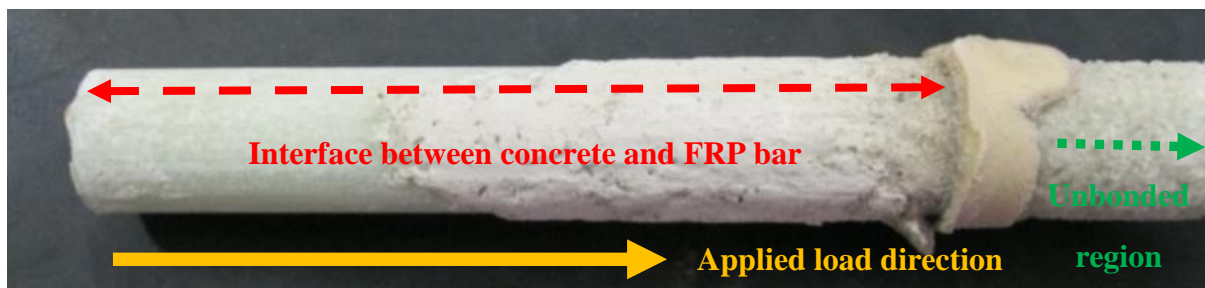
Figure 4-6. FRP bar pull-out failure
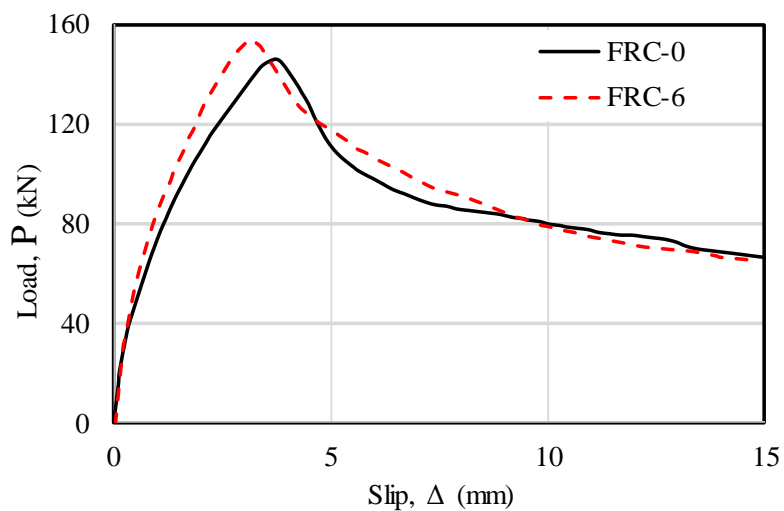
Figure 4-7. Global load-slip relationship response for each fibre content

4.3.1.3.2 Local bond stress-slip (τ/δ) relationship

In order to model the tension stiffening behaviour of the fibre reinforced concrete beams reinforced with GFRP bars used in this research, the local bond-slip (τ/δ) relationship needs to be extracted from the experimental global load-slip (P/Δ) relationship obtained from the pull-out tests. Based on typical pull-out test results obtained for specimens with 60 mm bond length as shown in Fig. 4-8, it was decided that a tri-linear local τ/δ relationship as shown in the same figure would be suitable to simulate the results obtained. Based on the experimental data, the general expressions in Eqs. (3-3) − (3-5) are developed to represent the local bond stress-slip relationship of the FRCs.

$$\tau_{max} = \gamma_1 \sqrt{f_c'} \tag{3-3}$$

$$\tau = \tau_{max}(\delta/\delta_1)^{\gamma_2} \tag{3-4}$$

$$\tau_{resd} = \gamma_3 \tau_{max} \tag{3-5}$$

Where in Eqs. (3) − (5), τ_{max} is the maximum bond stress in MPa, δ_1 (in mm) is the slip corresponding to the maximum bond stress, and γ_1, γ_2, γ_3 are the empirical coefficients depended on different fibre contents in FRC, in which $\gamma_1 = 2.0$, $\gamma_2 = 0.30$, $\gamma_3 = 0.45$ for the FRC-6 series, and $\gamma_1 = 2.4$, $\gamma_2 = 0.15$, $\gamma_3 = 0.33$ for the FRC-12 series. Figs. 4-8 (a) and (b) present the comparison between the experimental and modelled local bond stress-slip relationship of each concrete series.

(a)   (b)
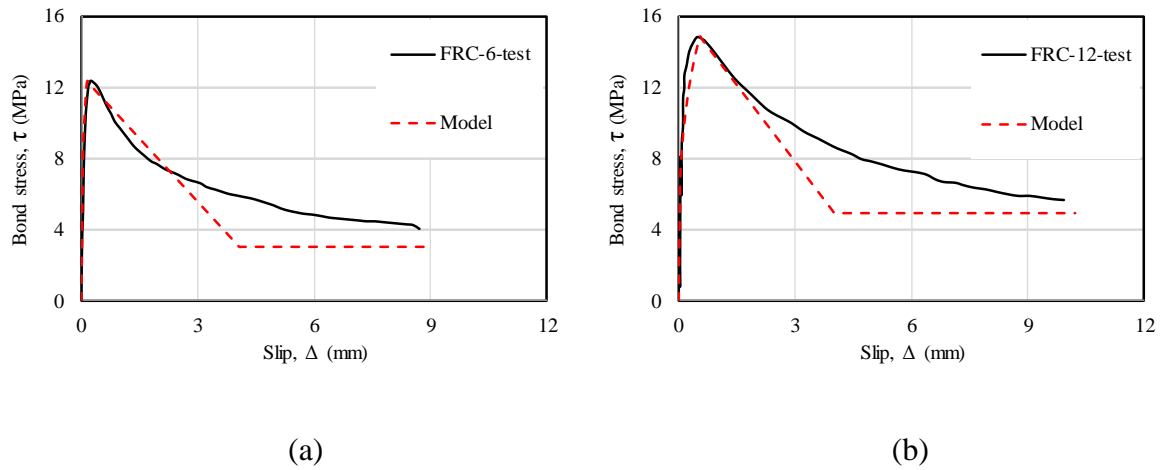
Figure 4-8. Local bond stress-slip relationship of FRCs

4.3.2 Structural behaviours

4.3.2.1 General observations of the beam tests

The failure modes of all beam specimens are presented in Figs. 4-9 (a) – (d). The observed

failure modes of all the beams are typical flexural failure modes, except the first of the two

FRC beams with 6 kg/m^3 fibres (FRC-6-1) which experienced a premature failure due to web

shear cracking (shown in Fig. 4-9 (a)). The test result of FRC-6-1 beam is reported but it is not

used in any further comparisons and model validations. To ensure the subsequent beams failed

in typical flexural failure mode, the locations of loading points and supports of the rest of the

beams were adjusted to increase the length of the constant bending moment region. In the

beams that experienced flexural failure, it was observed that the flexural cracks initially formed

within the constant moment area and propagated upwards to the neutral axis position. This in

turn led to a series of flexural cracks in the constant bending moment region. Compression

wedges then gradually formed, accompanied with the buckling of compression bars.

Consequently, the specimen failed with the concrete crushing. As can be seen from Fig. 4-9 (b)

− (d), the change of fibres content in the beams lead to no distinct change in the failure mode

of the specimen under flexure. The failure mode of all the beam tests and the critical data, including the peak load and the corresponding mid-span deflection are summarized in Table 3-3.

Table 3-3. Summary of beam test results

Specimen	Peak load (kN)		deflection at peak load (mm)		Failure mode
	Exp.	Model.	Exp.	Model.	
FRC-6-1	159	162	21.1	29.5	Shear*
FRC-6-2	164		24.4		FRP bar rupture
FRC-12-1	168	170	26.0	31.1	FRP bar rupture
FRC-12-2	180		26.9		FRP bar rupture

* Premature failure, will be excluded for further analysis and model validation
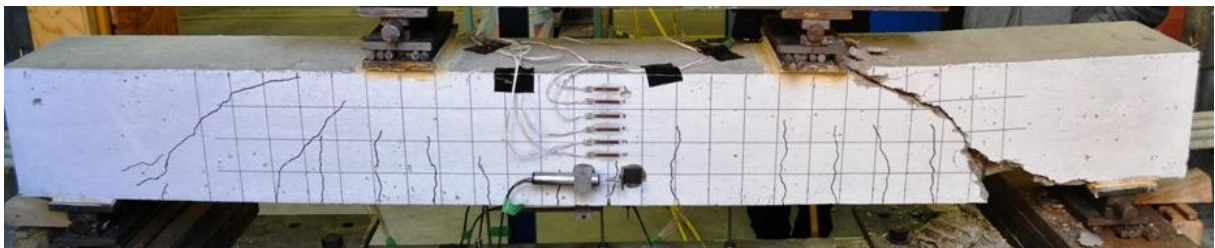
(a)

(b)

(c)

(d)

Figure 4-9. Failure modes of beam specimens: a) FRC-6-1; b) FRC-6-2; c) FRC-12-1; d) FRC-12-2

4.3.2.2 Load-deflection relationship: experimental results

The experimentally recorded load-deflection relationship of each beam series is illustrated in Fig. 4-10, where it can be seen that the load-deflection relationship of all the beams followed a similar trend. It should be noted that beam FRC-6-1 was loaded with a longer constant moment region and hence has a higher stiffness in Fig. 4-10. For each set of the identical beams, their load-deflection curves initially exhibit similar stiffness and load prior the first flexural cracks formed. Following this, a nearly linear ascending load-deflection relationship is observed up to the peak point of the load-deflection curves of all the beams. At the peak load point, all the beams exhibited sudden drops in their load carrying capacities in their load-deflection relationship, which is referred to the concrete wedge failure. Once the steel reinforcement at the top yielded, the steel compressive force did not compensate for the reduction in the strength of the softening concrete and the beam consequently failure due to concrete crushing. Fig. 4-10 shows the comparison of the load-deflection curve between the FRC-6 and FRC-12 series of specimens. As the comparisons illustrated in this figure, FRC-12 series of beam exhibited a slightly improved flexural behaviour, including the increases in the peak load and ultimate deflection, compared to that of its companion FRC-6 series of beam. This observation suggests that the load-deflection properties of PVA-FRC beam are improved by using an increased content of fibres in the concrete owing to the additional internal confining effect by the fibres.

116
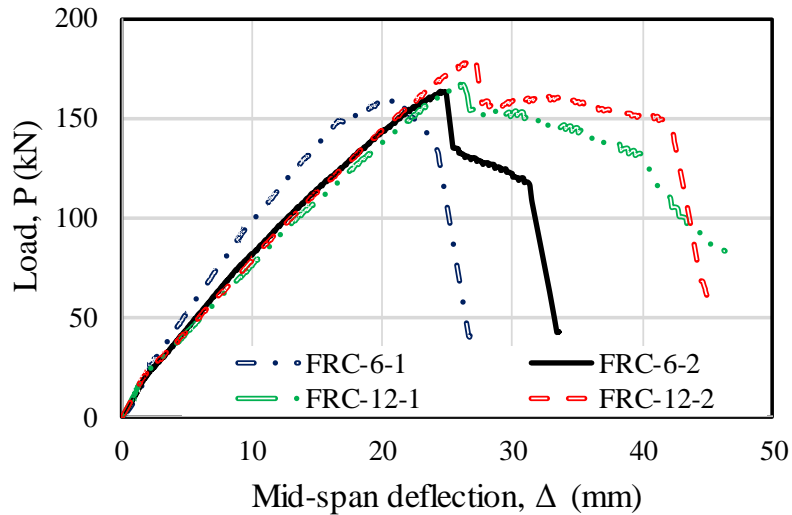
Figure 4-10. Load-deflection relationship of test beams: experimental results

4.3.3 Simulations of Flexural Behaviour of PVA Fibre Reinforced Concrete Beams with GFRP Bars

4.3.3.1 The segmental approach

This section presents the application of a displacement-based analysis technique previously developed by the authors. The approach, which has been widely validated for the flexural and shear analysis of both conventional and prestressed concrete with either steel or FRP reinforcement (Knight et al. 2014; Knight et al. 2015; Knight et al. 2014; Oehlers et al. 2016)and which has recently been extended to allow for the analysis of steel fibre reinforced concrete (Visintin and Oehlers 2017) is based on the direct simulation of localized partial interaction behaviour. The basic mechanics of the approach will now be summarised, and the reader referred to an extensive list of publications in which the development of the approach is covered in greater depth. It may be worth noting here that the approach is a direct application of the Euler-Bernoulli theorem of plane section remain plane without the corollary of a linear strain profile. Hence a similar solution technique to that which is followed when undertaking a moment-curvature analysis is applied, with the major difference being the starting point is the

imposition of a deformation rather than strain profile. This change is significant as it allows for the direct application of partial interaction theory to simulate localized behaviours such as crack formation, widening and tension stiffening in the tension region and concrete softening in the compression region. Consider the segment of a fibre reinforced concrete beam in Fig. 4-11 which has been extracted from a beam. The segment is of length equal to a crack spacing S_{cr} and is subjected a Euler-Bernoulli deformation causing an end rotation θ.
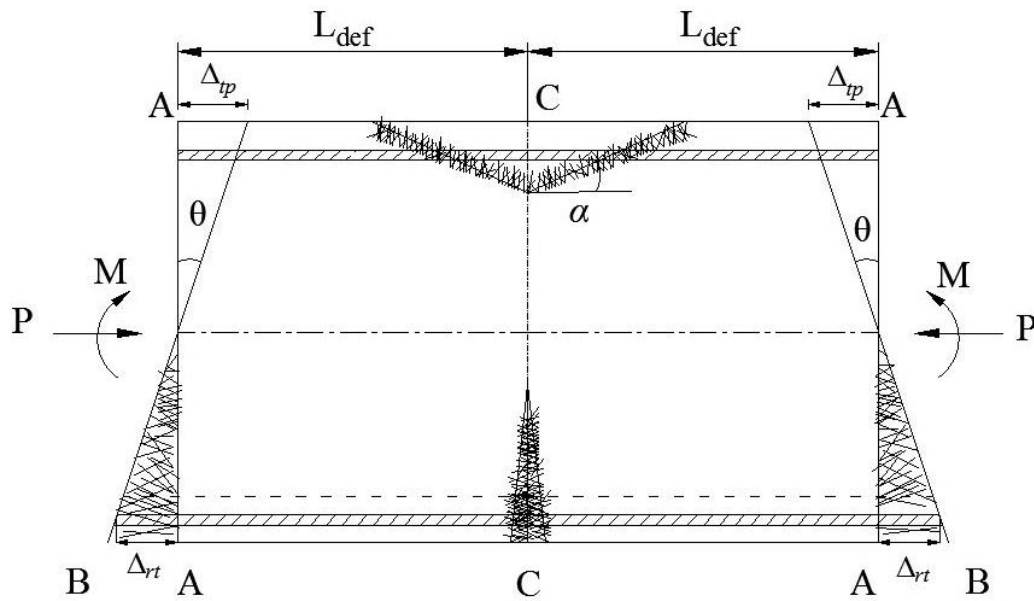
Figure 4-11. Segment of fibre reinforced concrete beam

For analysis, it is considered that a constant moment is applied to the segment and hence due to symmetry about the centre point only a single side of the segment A-A C-C in Fig. 4-10 needs to be considered. The application of a rotation θ causes a deformation of the segment end δ in Fig. 4-12 (a). The deformation can be divided into two categories: the full interaction deformations which occur in regions in which the concrete is not softening in compression or cracked in tension and; partial interaction deformations in which result in localized relative displacements or slips. These local behaviours include concrete to concrete sliding which results in concrete softening or the slip between the reinforcement and the surrounding concrete which results in tension stiffening and crack widening. It should be noted here that in the case

of fibre reinforced concrete the behaviour of cracked concrete in tension is considered to be adequately modelled using the results of a direct tension test to obtain a stress crack-width relationship as in Fig. 4-5 (b). An alternative to this approach is to use micromechanics to simulate the load-slip behaviour of each fibre such as in (Naaman et al. 1991; Naaman et al. 1991; Sumitro and Tsubaki 1998).

In the full interaction regions dividing the deformation from A-A to B-B by the deformation length L_{def} which is equal to half the crack spacing gives the strain profile C-C in Fig. 4-12 (b). Based on the distribution of strain and knowledge of the stress-strain relationships the distribution of stress in Fig. 4-12 (c) and force in Fig. 4-12 (d) can be determined. For cracked concrete in which the fibres have not pulled out the material stress crack-width relationship in Fig. 4-5 (b) may be directly applied to determine the force in the cracked concrete.
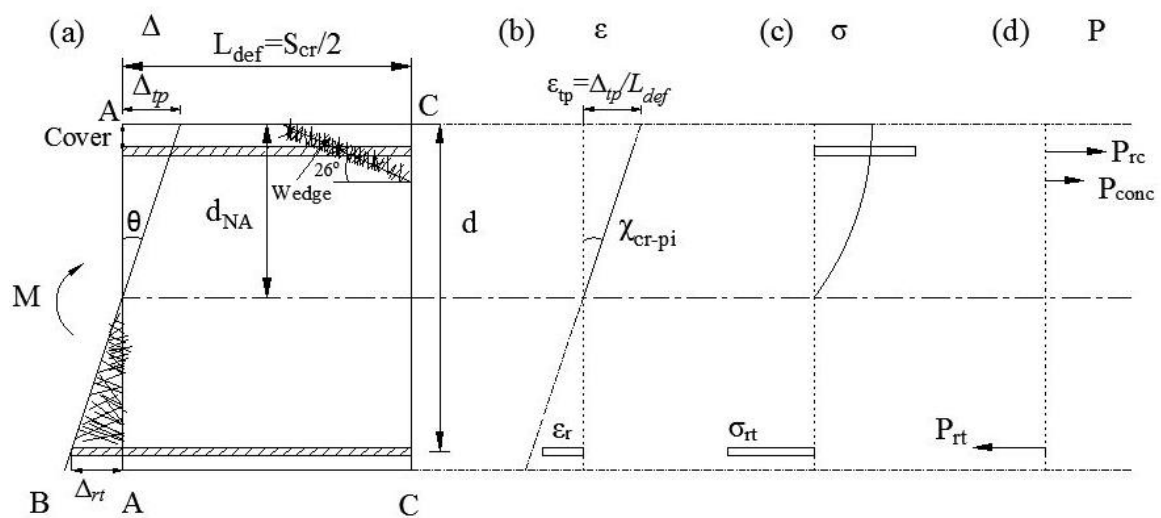
Figure 4-12. Segment for analysis

4.3.3.2 Partial interaction (PI) tension stiffening region

Slip between the reinforcement and the surrounding concrete results in the formation and widening of cracks as well as the phenomena of tension stiffening (Muhamad et al. 2012; Zhang et al. 2016). In order to describe the relationship between the slip of the reinforcement from the

crack face and the force developed in the reinforcement partial interaction tension stiffening mechanics are considered. That is for a given slip form the crack face $\varDelta$, which is equal to half the total crack width, the transfer of stresses from the reinforcement to the concrete through bond is determined to directly give the force in the reinforcing P_{rt} in Fig. 4-12 (d).

After the formation of an initial crack, the force resisted in the prism in Fig. 4-13 is resisted by a combination of the fibres at the crack face P_{fib} and the reinforcing bar force P_{rt}. The reinforcing bar force P_{rt} induces a slip of the reinforcement in Fig. 4-11 which has a maximum at the crack face and results in a transfer of stress from the reinforcement to the concrete which is controlled by the local bond stress-slip relationship in Fig. 4-8. For analysis, a shooting method can be applied to determine the variation in reinforcement slip and the distribution of strain in the reinforcement and the concrete (Haskett et al. 2008; Zhang et al. 2016). By considering the full interaction boundary conditions to this partial interaction problem it is possible to determine not only the crack spacing but also the load slip tension stiffening behaviour of the reinforcement both of which are required for the above analysis (Haskett et al. 2008; Zhang et al. 2016). A full description of the partial interaction tension stiffening model is widely available for example see (Muhamad et al. 2011; Muhamad et al. 2012; Oehlers et al. 2014; Oehlers et al. 2014; Sturm 2018).
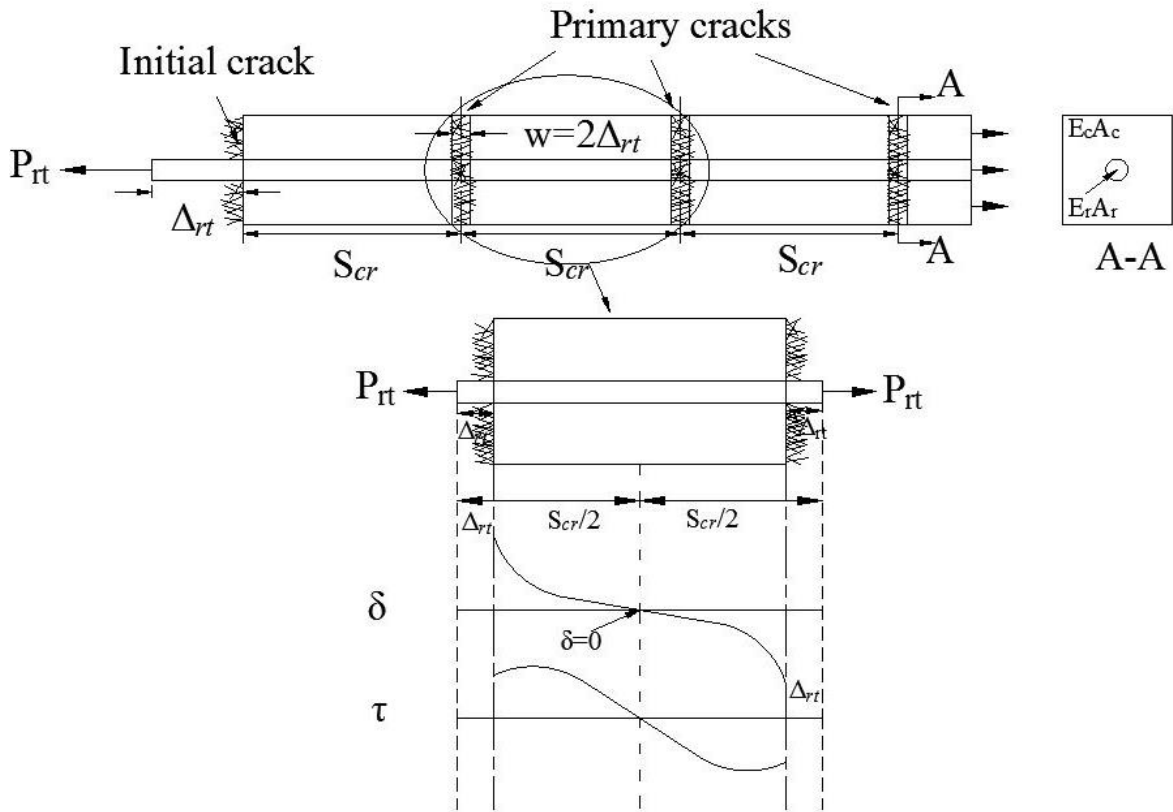
Figure 4-13. Partial interaction tension stiffening prism

4.3.3.3 PI concrete softening

Similarly, in the PI compression region concrete softening of the concrete is associated with partial interaction sliding along the concrete to concrete interface of the softening wedge (Chen et al. 2013; Haskett et al. 2011). According to Chen et al. (Chen et al. 2013) a size-dependent stress-strain relationship can be developed from the results of standard cylinder tests by breaking the total deformation of a cylinder into its material component which is dependent on the length of the test specimen and a PI sliding component which is controlled by the mechanics of shear friction theory which occurs along the sliding wedge. This approach which has been successfully applied to conventional concrete in (Chen et al. 2013)and has been further extended to steel fibre FRCs by Visintin and Oehlers (Visintin and Oehlers 2017), is therefore applied here. That is for analysis the stress-strain relationship obtained from a standard cylinder

test in Fig. 4-14 is made size-dependent such that the height of the cylinder would be $2L_{def}$ in Fig. 4-12 (a), where the stress-strain relationship of the cylinder with the length of $2L_{def}$ can be obtained by applying the expression given in Eq. (3-6) to convert the stress-strain behaviour extracted empirically from a standard compressive test specimen with the length of 200 mm.

$$\varepsilon_{Ldef} = \varepsilon_{mat} + (\varepsilon_{test} - \varepsilon_{mat})\frac{200}{L_{def}} \qquad (3\text{-}6)$$

where ε_{mat} is the material strain, ε_{test} is the total strain from the standard compression test and L_{def} is deformation length in M/θ analysis in mm. Having now determined all forces in Fig. 4-12 (d) it is simply a matter of shifting the neutral axis in Fig. 4-12 (a) until equilibrium of forces is obtained after which the moment corresponding to the rotation θ can be determined.
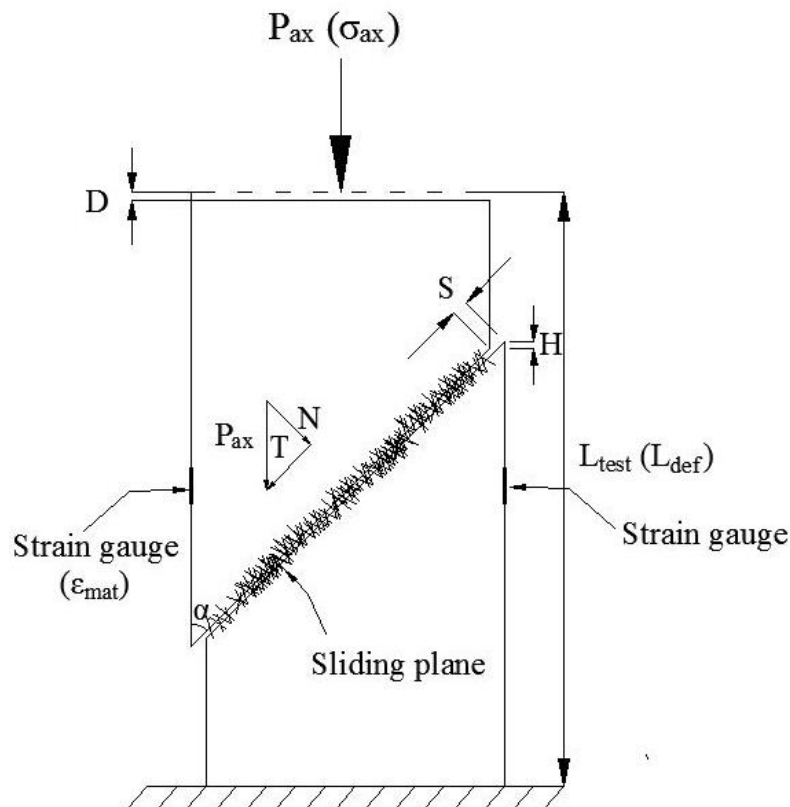
Figure 4-14. Compression test

Having obtained the moment-rotation for each of the concrete sections in Fig. 4-15, the load-deflection and load-crack width behaviour of the beam can be determined using a standard analytical procedure. That is by dividing the rotation in Fig. 4-15 (a) by the deformation length L_{def}, the moment-curvature behaviour of a cross-section shown in Fig. 4-15 (b) is obtained. It is important to note that this is not the same as that which would be obtained from a standard moment-curvature analysis as the partial interaction behaviours associated with concrete cracking and softening have been directly simulated using partial interaction approaches. Having obtained the moment-curvature relationship of the cross-section it is simply a matter of integrating the distribution of curvature along the beam twice in order to determine deflection as in standard analysis. In addition, it should be noted that the change in the curvature following the commencement of concrete softening is associated with the formation of the hinge in which the hinge length is defined in terms of the length of the softening wedge. It is also worth noting that, in the modelling process, the rotation due to the multiple discrete cracks with the variations in the moment within the hinge region were incorporated when calculating the load and deflection of the beam.
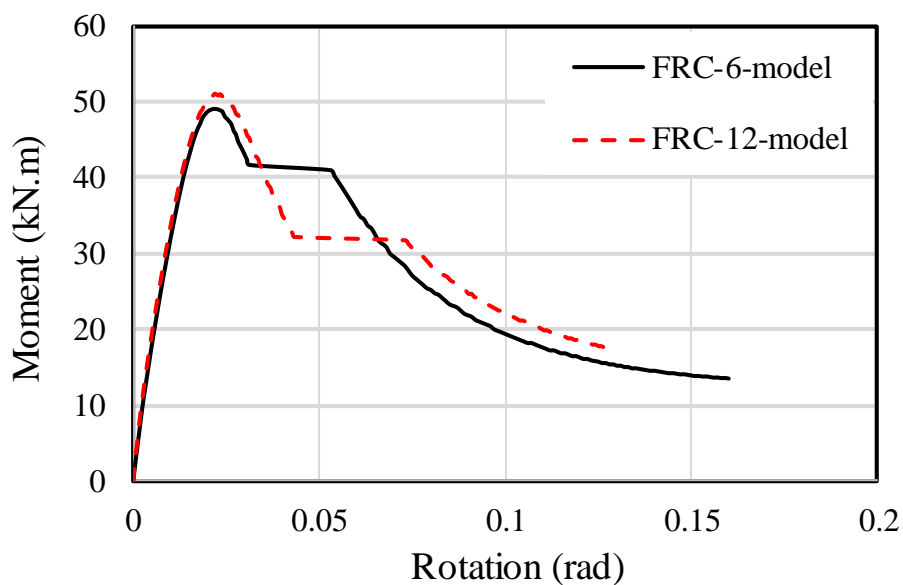
(a)
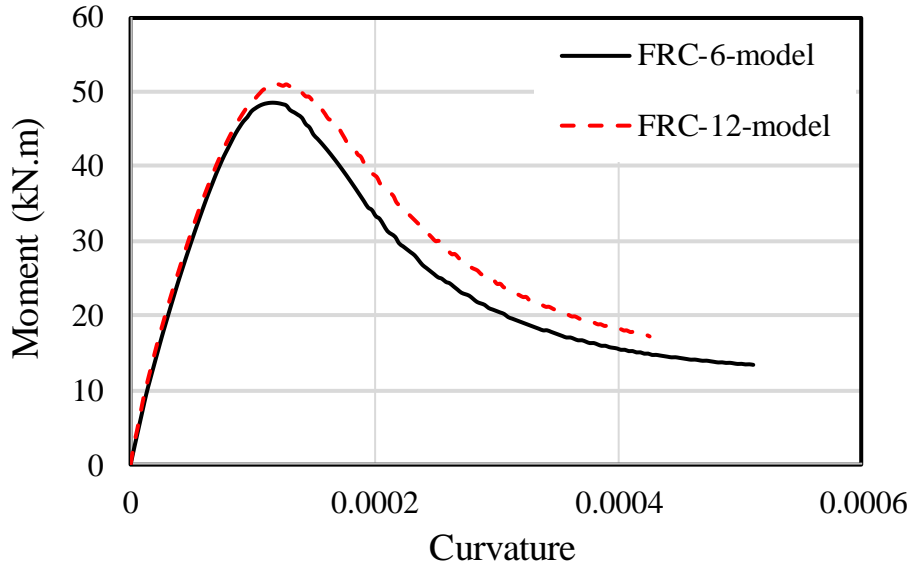
(b)

Figure 4-15. Simulated moment-rotation and moment-curvature relationship of each beam cross-section: a) moment-rotation relationship; b) moment-curvature relationship

Similarly, to determine the load crack width behaviour the moment-crack width relationship in Fig. 4-16 is a direct consequence of the segmental analysis technique, for any given moment distribution applied to the beam the distribution of crack width is known, where the crack width (W_{cr}) is the sum of the slip of the reinforcement relative to each crack face, that is $2\Delta_{rt.}$
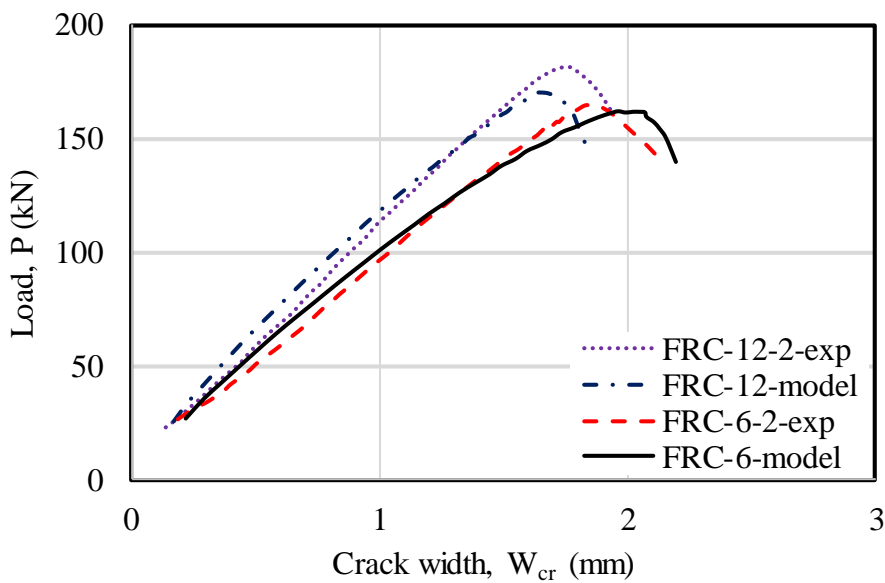
Figure 4-16. Load-crack width relationship for each beam series

4.3.3.4 Cracking behaviour

In the present study, the crack widths (W_{cr}) at all load levels of each beam was measured using LVDTs mounted at the GFRP position of the FRC beams along the longitudinal direction. Fig. 4-15 provides the experimentally-recorded and the simulated load-crack width relationships of FRC-6 and 12 beam series, respectively. It should be noted that the numerically generated crack width was established using the relative slip between the tensile reinforcement (i.e. the GFRP bar) and surrounding FRC, in which the magnitude of the crack width for a given load is twice of the relative slip between the FRC and GFRP bar. As illustrated in Fig. 4-15, respectively, the experimental and theoretical load-crack width relationships are matched closely. Fig. 4-15 provides the comparison between the load-crack width relationships of the FRC-6 and the companion FRC-12 series. It is evident from the figure that, in general, for a given load, the beam prepared using FRC with higher fibre content had a smaller crack width. This observation is similar to the aforementioned observation on the crack spacing of FRC beams and can be explained the delayed formation of cracks as the result of the increased fibre content.

4.3.3.5 Simulated load-deflection behaviours

The comparisons in Fig. 4-17 (a) and (b) indicate that the simulated load-deflection relationships of the FRCs are in good agreements with the experimental results. Whilst the model well-simulates the flexural behaviour of the PVA FRC beam with GFRP bars, it slightly overestimates the mid-span deflection, as shown in Fig. 4-17 (a) and (b). This might be attributed to the fact that fibre distributions in material test specimens are different to those in the beam specimens which may be due to the difference in casting direction of the cylinders and beams or due to more significant edge effects in cylinders which may results in a change

in fibre orientation. Another potential explanation of the variations between the numerical and experimental results is the early failure of the individual GFRP fibres due to the anisotropy and inhomogeneity of the bar (Rizkalla et al. 2003). This leads to a type of premature failure of the FRP bars and hence results in a less ductile behaviour of the beams seen in the experiments.
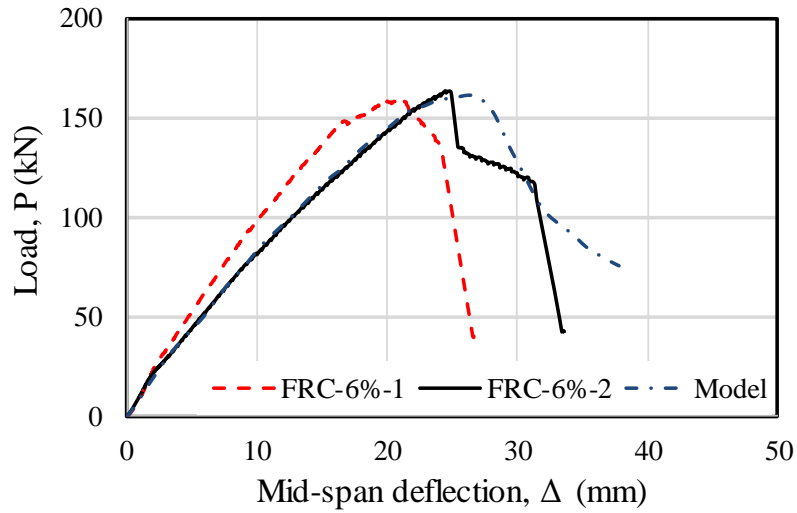
(a)
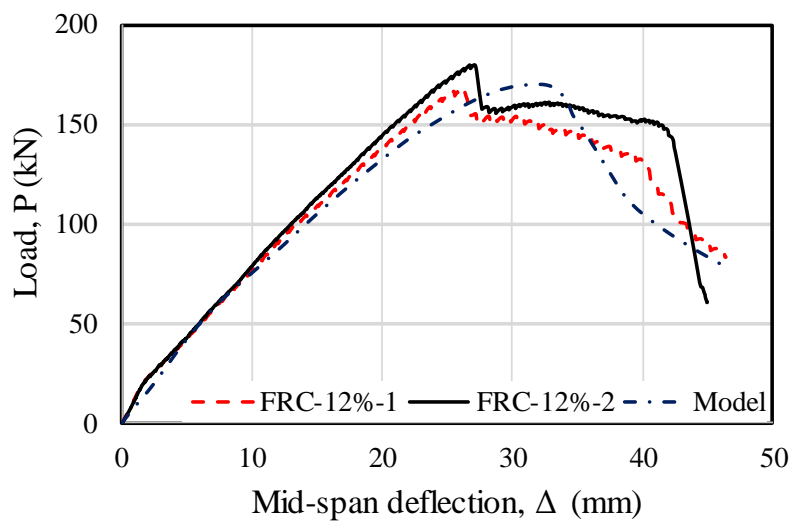
(b)

Figure 4-17. Load-deflection relationship of test beams: comparison between simulated and experimental results: a) FRC-6 series; b) FRC-12 series

4.4 CONCLUSIONS

Based on the experimental investigations and the numerical analysis to simulate the flexural behaviour of PVA-FRC beam with GFRP bars, the following conclusions can be drawn:

PVA fibre content is an influential parameter to affect the material properties of the FRC. The peak and post-peak behaviours of the FRC under axial compression and tension are improved with the increased PVA fibre content. The results from a series of pull-out tests performed to establish the bond properties between GFRP bars and fibre concrete showed the ascending slope of the bond stress-slip relationship was steeper for specimens containing fibres when compared to specimens with no fibres, indicating that FRP bars embedded in fibre concrete will experience smaller slips for a given load.

Based on the beam test results, FRC content had nearly no effect on the stiffness of the PVA-FRC-GFRP beam at the service region, whereas the beam with a higher FRC content exhibited a slightly more improved flexural behaviour, including the increases in the peak load and ultimate deflection. The crack response of GFRP-PVA FRC beams has a strong correlation with the fibre content in FRC, in which an increase FRC content results in smaller crack width for a given load. The displacement based moment-rotation numerical model is able to predict the behaviour well and this approach for beam analysis is applicable to simulate the flexural behaviour of any types of FRC beams or beams with any types of FRP bars as tension reinforcements.

4.5 REFERENCES

Achillides, Z., and Pilakoutas, K. (2004). "Bond behavior of fiber reinforced polymer bars under direct pullout conditions." *Journal of Composites for construction*, 8(2), 173-181.

Almusallam, A. A. (2001). "Effect of degree of corrosion on the properties of reinforcing steel bars." *Construction and Building Materials*, 15(8), 361-368.

Alsayed, S. H. (1998). "Flexural behaviour of concrete beams reinforced with GFRP bars." *Cement and Concrete Composites*, 20(1), 1-11.

Altun, F., Haktanir, T., and Ari, K. (2007). "Effects of steel fiber addition on mechanical properties of concrete and RC beams." *Construction and Building Materials*, 21(3), 654-661.

Ashtiani, M. S., Dhakal, R., Scott, A., and Bull, D. (2013). "Cyclic beam bending test for assessment of bond–slip behaviour." *Engineering Structures*, 56, 1684-1697.

Barris, C., Torres, L., Turon, A., Baena, M., and Catalan, A. (2009). "An experimental study of the flexural behaviour of GFRP RC beams and comparison with prediction models." *Composite Structures*, 91(3), 286-295.

Bhargava, P., Sharma, U. K., and Kaushik, S. K. (2006). "Compressive stress-strain behavior of small scale steel fibre reinforced high strength concrete cylinders." *Journal of advanced concrete technology*, 4(1), 109-121.

Chen, Y., Visintin, P., Oehlers, D., and Alengaram, U. (2013). "Size-dependent stress-strain model for unconfined concrete." *Journal of Structural Engineering*, 140(4), 04013088.

Ezeldin, A. S., and Balaguru, P. N. (1992). "Normal-and high-strength fiber-reinforced concrete under compression." *Journal of materials in civil engineering*, 4(4), 415-429.

Feng, Q., Visintin, P., and Oehlers, D. J. (2015). "Deterioration of bond–slip due to corrosion of steel reinforcement in reinforced concrete." *Magazine of Concrete Research*, 68(15), 768-781.

Goldston, M., Remennikov, A., and Sheikh, M. N. (2017). "Flexural behaviour of GFRP reinforced high strength and ultra high strength concrete beams." *Construction and Building Materials*, 131, 606-617.

Haskett, M., Oehlers, D. J., and Ali, M. M. (2008). "Local and global bond characteristics of steel reinforcing bars." *Engineering Structures*, 30(2), 376-383.

Haskett, M., Oehlers, D. J., Ali, M. M., and Sharma, S. K. (2011). "Evaluating the shear-friction resistance across sliding planes in concrete." *Engineering Structures*, 33(4), 1357-1364.

Hognestad, E., Hanson, N. W., and McHenry, D. "Concrete stress distribution in ultimate strength design." *Proc., Journal Proceedings*, 455-480.

Jakubovskis, R., Kaklauskas, G., Gribniak, V., Weber, A., and Juknys, M. (2014). "Serviceability analysis of concrete beams with different arrangements of GFRP bars in the tensile zone." *Journal of Composites for Construction*, 18(5), 04014005.

Kachlakev, D., and McCurry, D. (2000). "Behavior of full-scale reinforced concrete beams retrofitted for shear and flexural with FRP laminates." *Composites Part B: Engineering*, 31(6), 445-452.

Knight, D., Visintin, P., Oehlers, D., and Ali, M. M. (2014). "Simulating RC beams with unbonded FRP and steel prestressing tendons." *Composites Part B: Engineering*, 60, 392-399.

Knight, D., Visintin, P., Oehlers, D., and Mohamed Ali, M. (2013). "Short-term partial-interaction behavior of RC beams with prestressed FRP and steel." *Journal of Composites for Construction*, 18(1), 04013029.

Knight, D., Visintin, P., and Oehlers, D. J. (2015). "Displacement‐based simulation of time‐dependent behaviour of RC beams with prestressed FRP or steel tendons." *Structural Concrete*, 16(3), 406-417.

Knight, D., Visintin, P., Oehlers, D. J., and Ali, M. M. (2014). "Simulation of RC beams with mechanically fastened FRP strips." *Composite Structures*, 114, 99-106.

Matthys, T. S. S. (2017). "Shear-stress transfer across a crack in steel fibre-reinforced concrete." *Cement and Concrete Composites*.

Mazaheripour, H., Barros, J. A., Sena-Cruz, J., and Soltanzadeh, F. (2013). "Analytical bond model for GFRP bars to steel fiber reinforced self-compacting concrete." *Journal of Composites for Construction*, 17(6), 04013009.

Mazaheripour, H., Barros, J. A., Soltanzadeh, F., and Sena-Cruz, J. (2016). "Deflection and cracking behavior of SFRSCC beams reinforced with hybrid prestressed GFRP and steel reinforcements." *Engineering Structures*, 125, 546-565.

Mo, K. H., Visintin, P., Alengaram, U. J., and Jumaat, M. Z. (2016). "Bond stress-slip relationship of oil palm shell lightweight concrete." *Engineering Structures*, 127, 319-330.

Muhamad, R., Ali, M. M., Oehlers, D., and Sheikh, A. H. (2011). "Load-slip relationship of tension reinforcement in reinforced concrete members." *Engineering Structures*, 33(4), 1098-1106.

Muhamad, R., Ali, M. M., Oehlers, D. J., and Griffith, M. (2012). "The tension stiffening mechanism in reinforced concrete prisms." *Advances in Structural Engineering*, 15(12), 2053-2069.

Naaman, A. E., Namur, G. G., Alwan, J. M., and Najm, H. S. (1991). "Fiber pullout and bond slip. I: Analytical study." *Journal of Structural Engineering*, 117(9), 2769-2790.

Naaman, A. E., Namur, G. G., Alwan, J. M., and Najm, H. S. (1991). "Fiber pullout and bond slip. II: Experimental validation." *Journal of Structural Engineering*, 117(9), 2791-2800.

Oehlers, D., Visintin, P., and Lucas, W. (2016). "Fundamental Mechanics Governing FRP-Retrofitted RC Beams with Anchored and Prestressed FRP Plates." *Journal of Composites for Construction*, 20(6), 04016047.

Oehlers, D. J., Visintin, P., Chen, J. F., and Ibell, T. J. (2014). "Simulating reinforced concrete members. Part 1: partial interaction properties." *Proceedings of the Institution of Civil Engineers: Structures and Buildings*, 167(11), 646-653.

Oehlers, D. J., Visintin, P., Chen, J. F., and Ibell, T. J. (2014). "Simulating reinforced concrete members. Part 2: Displacement-based analyses." *Proceedings of the Institution of Civil Engineers-Structures and Buildings*, 167(12), 718-727.

Olivito, R., and Zuccarello, F. (2010). "An experimental study on the tensile strength of steel fiber reinforced concrete." *Composites Part B: Engineering*, 41(3), 246-255.

Qu, W., Zhang, X., and Huang, H. (2009). "Flexural behavior of concrete beams reinforced with hybrid (GFRP and steel) bars." *Journal of Composites for construction*, 13(5), 350-359.

Rilem, T. (2002). "162-TDF. Test and design methods for steel fibre reinforced concrete." *Materials and structures*, 35, 579-582.

Rizkalla, S., Hassan, T., and Hassan, N. (2003). "Design recommendations for the use of FRP for reinforcement and strengthening of concrete structures." *Progress in Structural Engineering and Materials*, 5(1), 16-28.

Schumacher, P. (2006). "Rotation capacity of self-compacting steel fiber reinforced concrete." TU Delft, Delft University of Technology.

Standard Australia (2014). "AS 1012.9:2014. Methods of testing concrete Compressive strength tests - Concrete, mortar and grout specimens. ." *Standards Australia, Sydeny*.

Sturm, A. B., Visintin, P., Oehlers, D.J., Seracino, R (2018). "Time dependent tension stiffening mechanics of fibre reinforced and ultra-high performance fibre reinforced concrete." *ASCE Journal of Structural Engineering*.

Sumitro, S., and Tsubaki, T. (1998). "Micromechanical fiber pullout model for steel fiber reinforced concrete." *Doboku Gakkai Ronbunshu*, 1998(599), 155-163.

Toutanji, H., and Deng, Y. (2003). "Deflection and crack-width prediction of concrete beams reinforced with glass FRP rods." *Construction and Building Materials*, 17(1), 69-74.

Visintin, P., Ali, M. M., Xie, T., and Sturm, A. B. (2018). "Experimental investigation of moment redistribution in ultra-high performance fibre reinforced concrete beams." *Construction and Building Materials*, 166, 433-444.

Visintin, P., Oehlers, D., Muhamad, R., and Wu, C. (2013). "Partial-interaction short term serviceability deflection of RC beams." *Engineering Structures*, 56, 993-1006.

Visintin, P., Oehlers, D., Wu, C., and Haskett, M. (2012). "A mechanics solution for hinges in RC beams with multiple cracks." *Engineering Structures*, 36, 61-69.

Visintin, P., and Oehlers, D. J. (2017). "Fundamental mechanics that govern the flexural behaviour of reinforced concrete beams with fibre-reinforced concrete." *Advances in Structural Engineering*, 1369433217739705.

Visintin, P., Oehlers, D. J., and Sturm, A. B. (2016). "Mechanics solutions for deflection and cracking in concrete." *Proceedings of the Institution of Civil Engineers-Structures and Buildings*, 1-13.

Wang, S., Zhang, M.-H., and Quek, S. T. (2012). "Mechanical behavior of fiber-reinforced high-strength concrete subjected to high strain-rate compressive loading." *Construction and Building Materials*, 31, 1-11.

Xu, G., Magnani, S., and Hannant, D. J. (1998). "Tensile behavior of fiber-cement hybrid composites containing polyvinyl alcohol fiber yarns." *Materials Journal*, 95(6), 667-674.

Yoo, D.-Y., Yoon, Y.-S., and Banthia, N. (2015). "Flexural response of steel-fiber-reinforced concrete beams: effects of strength, fiber content, and strain-rate." *Cement and Concrete Composites*, 64, 84-92.

Zhang, T., Visintin, P., and Oehlers, D. J. (2016). "Partial-interaction tension-stiffening properties for numerical simulations." *Advances in Structural Engineering*, 1369433216660654.

CHAPTER 5

Experimental Investigation of Moment Redistribution in Ultra-High Performance Fibre Reinforced Concrete Beams

[*1]Visintin, P., [2]Mohamed Ali, M.S., [3]Xie, T., [4]Sturm, A.B.

[1]**Dr.Phillip Visintin (Corresponding author)**

Associate Professor,

School of Civil, Environmental and Mining Engineering

The University of Adelaide

 South Australia 5005

AUSTRALIA

[2]**Dr. Mohamed Ali, M.S**

Senior Lecturer,

 School of Civil, Environmental and Mining Engineering

The University of Adelaide

 South Australia 5005

AUSTRALIA

[3]**Mr. Tianyu Xie**

Ph. D Candidate,

School of Civil, Environmental and Mining Engineering

The University of Adelaide

South Australia 5005

AUSTRALIA

[4]Alexander B. Sturm   132

Ph. D Candidate,

School of Civil, Environmental and Mining Engineering

The University of Adelaide

South Australia 5005
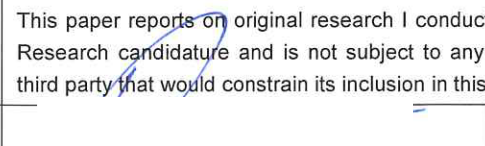
AUSTRALIA

Statement of Authorship

Title of Paper	EXPERIMENTAL INVESTIGATION OF MOMENT REDISTRIBUTION IN ULTRA-HIGH PERFORMANCE FIBRE REINFORCED CONCRETE BEAMS
Publication Status	☑ Published ☐ Accepted for Publication ☐ Submitted for Publication ☐ Unpublished and Unsubmitted work written in manuscript style
Publication Details	Visintin, P., Ali, M., Xie, T., & Sturm, A. B. (2018). Experimental investigation of moment redistribution in ultra-high performance fibre reinforced concrete beams. Construction and Building Materials, 166, 433-444.
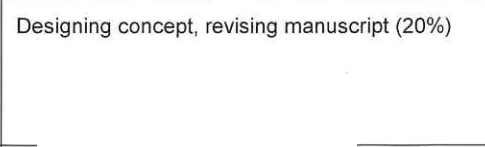
Principal Author
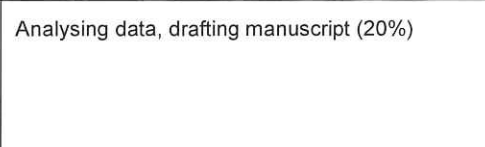
Name of Principal Author	Associate Professor Phillip Visintin
Contribution to the Paper	Designing concept, supervising experiments, analysing data, drafting manuscript (15%)
Overall percentage (%)	40
Certification:	This paper reports on original research I conducted during the period of my Higher Degree by Research candidature and is not subject to any obligations or contractual agreements with a third party that would constrain its inclusion in this thesis. I am the primary author of this paper.
Signature	Date 12/02/2019

Co-Author Contributions

By signing the Statement of Authorship, each author certifies that:

    i.   the candidate's stated contribution to the publication is accurate (as detailed above);

    ii.   permission is granted for the candidate in include the publication in the thesis; and

    iii.   the sum of all co-author contributions is equal to 100% less the candidate's stated contribution.

Name of Co-Author	Dr Mohamed Ali Sadakkathulla
Contribution to the Paper	Designing concept, revising manuscript (20%)
Signature	Date 12/02/2019

Name of Co-Author (Candidate)	Tianyu Xie
Contribution to the Paper	Analysing data, drafting manuscript (20%)
Signature	Date 12/02/2019

Name of Co-Author	Alex B. Sturm		
Contribution to the Paper	Analysing data, drafting manuscript (15%)		
Signature		Date	12/02/2019

Please cut and paste additional co-author panels here as required.

THIS PAGE HAS BEEN LEFT INTENTIONALLY BLANK

ABSTRACT

In the design of statically indeterminate structures the concept of moment redistribution is used to reduce the absolute magnitudes of moments in critical regions, to fully utilise the capacity of non-critical cross sections, and to simplify detailing by enabling a reduction in reinforcement ratios. Due to the complex mechanisms which control the formation and rotation of plastic hinges, moment redistribution capacities are commonly empirically based, and hence not necessarily applicable outside of the bounds of the testing regime from which they were derived. This paper presents the results of an experimental study of the moment redistribution capacity of four two-span continuous beams constructed from ultra-high performance fibre reinforced concrete (UHPFRC) and with various reinforcement ratios, such that the suitability of extending of exiting empirical design approaches to UHPFRC can be investigated. The results of the experimental investigation show that for beams where the hinge formed at the support, the observed moment redistribution was greater than the code predictions. However for the beam where the hinge formed under the load points, observed moment redistribution was significantly less than codes predictions. Hence, the results of this study show current design guidelines do not always provide a conservative prediction of moment redistribution in UHPFRC beams.

Keywords: moment redistribution; ultra-high performance fibre reinforced concrete (UHPFRC); ductility

5.1 INTRODUCTION

The recent expansion in research directed towards high performance materials has seen the development of a number of reliable mix designs for ultra-high performance fibre reinforced concretes (UHPFRC), including a number of commercially available products (Benson and Karihaloo 2005; Chanvillard and Rigaud 2003; Sobuz et al. 2016). These materials which are characterised by a very high compressive strength, a non-negligible tensile strength, high material ductility and enhanced durability have the potential to revolutionise the design of structures allowing for longer spans, reduced member sizes and increased design lives. To date numerous studies have focused on developing mix designs and characterising material performance, and in a more limited way structural tests have been performed on simple beam elements (Graybeal 2008; Singh et al. 2017; Yang et al. 2011; Yang et al. 2010). This research has culminated in the development of initial design guidelines for the use of UHPFRC (AFGC (Association Francaise de Genie Civil) 2013; Japanese Society of Civil Engineers 2008). While these guidelines present methodologies for the design of simple structural members the behaviour of indeterminate UHPC members has not yet been considered.

In statically indeterminate beams, a redistribution of internal forces arises due to the inelastic nature of reinforced concrete. The phenomenon of moment redistribution occurs at all limit states due to a difference in the relative stiffness of individual cross sections (Scott and Whittle 2005), but is typically utilised by designers at the ultimate limit. Moment redistribution allows the designer to reduce both the maximum hogging and sagging elastic moments, thereby reducing the overall moment demanded across a span, enabling a reduction in reinforcement requirements. Additionally, the ability to shift moments away from less efficient cross sections towards other more efficient cross sections may allow for savings in reinforcement costs and the easing reinforcement congestion (Paulay 1976). These factors may be particularly important for UHPFRC which has higher material costs than conventional concrete and has the

potential to perform poorly in regions of congested reinforcement if fibres cannot be uniformly distributed around reinforcement.

At the ultimate limit, moment redistribution occurs due to the formation and gradual rotation of plastic hinge regions, and has also been shown to be highly dependent on the stiffness or flexural rigidity of the non-hinge regions (Oehlers et al. 2010; Scott and Whittle 2005; Visintin and Oehlers 2016). Hence the mechanics of moment redistribution is incredibly complex as it is defined by the localised mechanism which control crack widening and tension stiffening as well as the formation and sliding of concrete softening wedges (Visintin and Oehlers 2016). Due to the complexity of the problem an empirical approach is often adopted to quantify hinge rotation and moment redistribution, and a review of approaches by (Panagiotakos and Fardis 2001) has shown that these typically perform poorly outside of the bounds of the test results from which they were derived.

To date the majority of experimental investigations into moment redistribution have been performed on members constructed from normal strength concrete, with few studies considering the influence of high-strength concrete (HSC). In these studies (Do Carmo and Lopes 2005; do Carmo and Lopes 2008; Scott and Whittle 2005), it has been suggested that the brittle nature of HSC may influence hinge rotation and that the increased bond between the reinforcement and concrete may lead to a higher tension stiffening effect in cracked regions and therefore a significant deviation away from the behaviour expected from conventional concrete members. To allow for the change in behaviour which occurs with increased concrete strengths, national codes of practice often set different limits for moment redistribution in HPC

(International Federation for Structural Concrete (fib) 2010), it is however unknown if these expressions can be further extended to UHPFRC beams.

Previous studies into the material performance of UHPFRC have shown that the addition of fibres to concrete improves the bond between reinforcement and concrete and restrains sliding along concrete to concrete interfaces, thereby improving shear-friction material properties and compressive ductility (Sobuz et al. 2016; Visintin and Oehlers 2018). It can therefore be expected that the addition of fibres to concrete will change the magnitude of hinge rotation and therefore moment redistribution in statically indeterminate beams. Although the addition of fibres can be expected to influence moment redistribution, little experimental work has been undertaken to date, with that available limited to members without reinforcement (Moallem 2010; Mohr 2012).

In this paper the moment redistribution behaviour of two span continuous beams manufactured from UHPFRC is investigated on beams with a range of reinforcing ratios. Existing methods for predicting moment redistribution prescribed by various national codes of practice are then applied to determine if they can be extended for application to UHPFRC.

5.2. EXPERIMENTAL PROGRAM

The experimental program has been devised to provide both an experimental investigation of the moment redistribution behaviour of UHPFRC beams and also to provide a range of material properties such that the results may be of use in the future validation of novel analytical procedures. As such in addition to four continuous beam tests, material tests were undertaken to quantify the compressive and tensile stress-strain and stress-crack width behaviour of the UHPFRC and the stress-strain characteristics of the reinforcement.

5.2.1 Mix design

All beams were cast using a mix design developed at the University of Adelaide as part of a project to develop ultra-high performance fibre reinforced concretes which require only conventional concrete manufacturing materials and equipment, and which do not require special curing regimes (Sobuz et al. 2016). It may also be worth noting that these mixes have also been used for extensive material and member level testing reported elsewhere (Singh et al. 2017; Sobuz et al. 2016).

The full mix design is given in Table 5-1, in which the sulphate resisting cement had a fineness modulus of $365m^2$/kg, a 28 day compressive strength as determined in accordance with AS 2350.11 (Australian Standard 2006) of 60MPa and a 28 day mortar shrinkage strain determined in accordance with AS 2350.13 (Australian Standard 2006) of 650 microstrain. The silica fume was undensified with a bulk density of $625kg/m^3$. The steel fibres were cold drawn hooked end wire fibres with a total length of 35 mm, an aspect ratio of 64 and a minimum yield strength of 1100MPa. The superplasticiser was a third generation high range water reducer with an added retarder.

The concrete was manufactured by first mixing the cement, silica fume and sand for 1 minute in a 750 L pan mixer until well blended. The water and superplasticiser were then added and the concrete mixed until visibly flowable; this took approximately 35 minutes. After the concrete started to flow, the fibres were added and mixed for a further 5 minutes. All specimens were cast in 4 batches on different days with each batch consisting of one beam as well as cylinders to determine the compressive and tensile strengths of the concrete. All dog-bone

specimens were cast along with beam 3. Note that to achieve a uniform distribution of fibres, sufficient mixing time was applied to ensure that the fibres were evenly mixed with the matrix. When placing the concrete, to avoid settlement of fibres, all beams were cast horizontally by pouring the concrete into the form in layers which were individually compacted.

5.2.2 Beam test specimens

To investigate the moment redistribution capacity of UHPFRC, four two-span continuous beams were tested. Note that a rectangular section was chosen in order to simplify analysis and because it is the most common beam cross section tested. It may however be useful to investigate T-sections in the future. As shown in Fig. 5-1 these beams had a total length of 5500 mm and were tested with point loads located at the mid-point of each span of length 2500 mm. To investigate the influence cross sectional ductility on the moment redistribution capacity each beam had a different tensile reinforcement ratio ranging from 1.48% to 1.94% in the sagging region and 1.28% to 1.94% in the hogging region. The reinforcement arrangement was chosen for the first three beams to investigate the relationship between reinforcement ratio and moment redistribution, and in the final beam to investigate the behaviour when moment redistribution occurs from the sagging to the hogging region. To prevent shear failure, 6 mm diameter stirrups were placed at 100 mm centres. Full details of the reinforcement are given in Table 5-2.

Figure 5-1. Beam specimens

Table 5-1: UHPFRC mix design

Material	kg/m^3
Sulphate resisting cement	937.5
Washed river sand	937.5
Silica fume	250
Steel fibres	165
Water	160
High range water reducing agent	52.5

Table 5-2: reinforcement details

		Hogging region					Sagging region		
beam	top	bottom	Tensile reinf. ratio (ρ) (%)	Compressive reinf. ratio (ρ_c) (%)	top	bottom	Tensile reinf. ratio (ρ) (%)	Compressive reinf. ratio (ρ_c) (%)
1	2N12 + 2N16	2N12	1.94	0.673	2N12	2N12 + 2N16	1.94	0.673
2	2N12 + 1N16	2N12	1.48	0.673	2N12	2N12 + 2N16	1.94	0.673
3	2N12 + 1N12	2N12	1.28	0.673	2N12	2N12 + 2N16	1.94	0.673
4	2N12 + 2N16	2N12	1.94	0.673	2N12	2N12 + 1N16	1.48	0.673

5.2.3 Instrumentation and testing

To capture the deformation of the hinge region a series of five linear variable displacement transducers (LVDTs) were placed at the expected location of the plastic hinge in the sagging region. The location of each of the LVDTs is shown in Fig. 5-2.
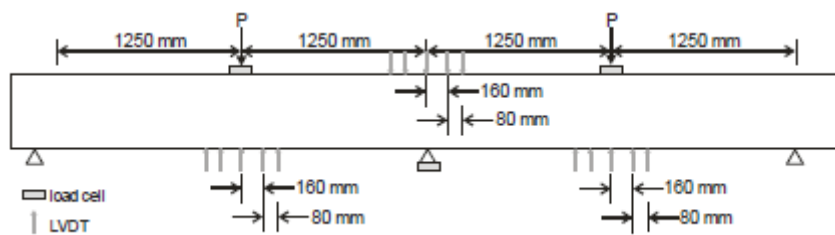
Figure 5-2. Instrumentation for beam tests

During testing a hydraulic ram applied a load to displace the mid-span of the beam at a rate of 0.8 mm/min. To experimentally record the reactions 225kN load cells were located at each loading point and a 1000kN load cell at the centre support as shown in Fig. 5-2. Note that in this study LVDTs were used in preference to strain gauges as they can capture the deformations

associated with localised deformations such as crack opening and concrete to concrete sliding along the softening wedge. It can also be noted that LVDTs were also used by (Schumacher 2006) to directly measure hinge rotation.

5.2.4 Material tests

5.2.4.1 Concrete in compression

To determine the compressive stress-strain behaviour of the UHPFRC, three cylinders of 100 mm diameter and 200 mm height were cast with each batch of concrete. During testing, specimens were loaded at a rate of 50kN/min until an estimated 90% of their peak load and then at a displacement rate of 0.1 mm/min until failure. To determine the full stress-strain relationship of the concrete, each specimen was instrumented with a pair of 30 mm axial strain gauges, additionally, 4 LVDTs recorded to total deformation of the specimen between loading platens throughout testing.

The average stress-strain relationship obtained from each set of three cylinder tests manufactured from concrete cast with each beam are shown in Fig. 5-3. It should be noted that the cylinder tests were conducted on the day of beam testing and hence the time since casting of the specimens ranged from 24 to 67 days.
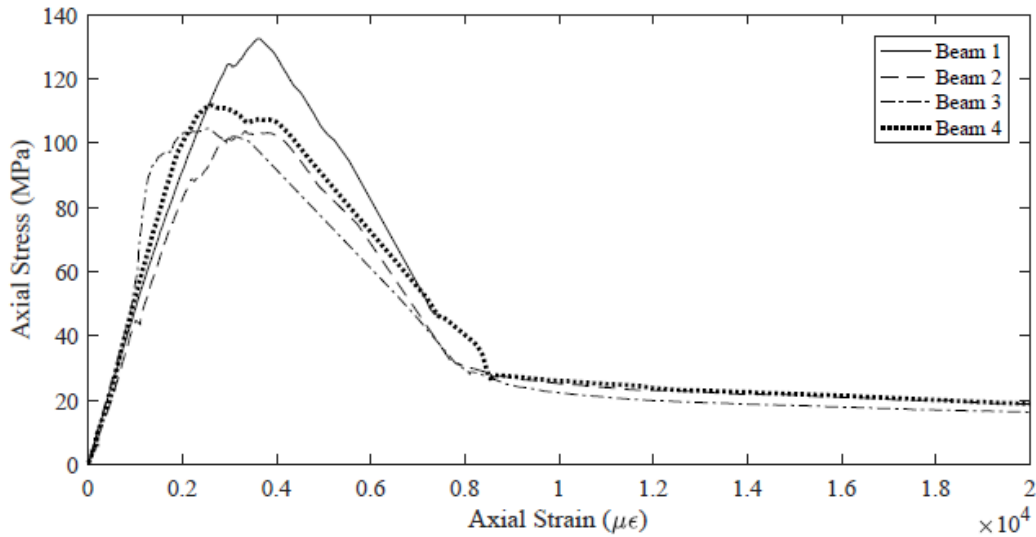
Figure 5-3. Compressive stress strain relationship

5.2.4.2 Concrete in tension

To determine the stress strain behaviour of UHPFRC prior to cracking, as well as the stress-crack-width behaviour following cracking, direct tensile tests were conducted two dog-bone shaped specimens shown in Fig. 5-4. The design of these dog-bone specimens and test set-up has been described in detail elsewhere (Singh et al. 2017) and hence will only be summarised here.
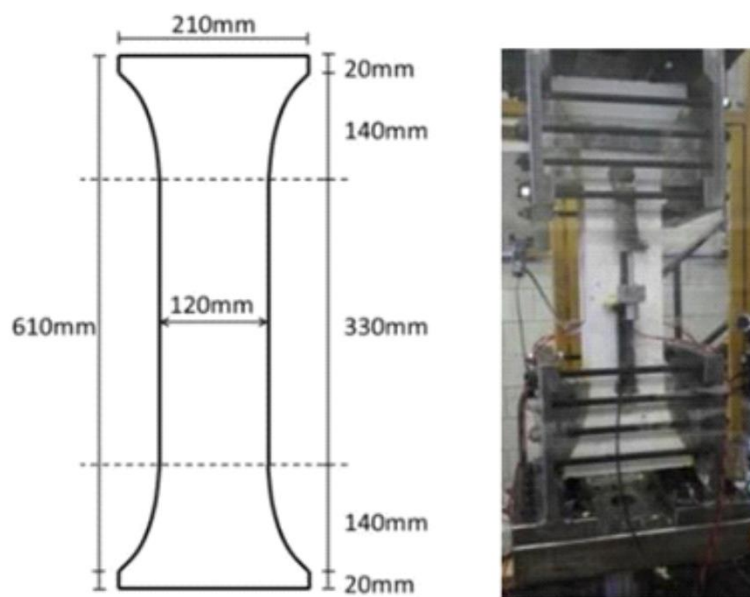
Fig. 5-4. Dog-bone specimens

The specimens in Fig. 5-4 (a) have an overall height 610 mm and a thickness of 120 mm. The width of the specimen tapers from 210 mm at the top to a shank of 120 mm breadth and 330 mm height. During testing the dog-bone shaped specimens were gripped with a steel loading plate having the same radius as the tapered concrete region. These loading plates were bolted to the loading frame which was mounted into the universal testing machine which applied a load such that a displacement rate of 0.05 mm/min was observed throughout the test. Axial strain in the concrete was measured using a pair of 30 mm strain gauges glued to the concrete surface, additionally the total deformation of the shank having a reduced area is measured with 2 LVDTs located on opposite faces.

The tensile stress-strain behaviour of the UHPFRC prior to cracking in Fig. 5-4(a) was determined based on the strain gauge readings and found to be in good agreement with that determined from the deformation recorded by the LVDTs. As only a single major crack was observed post cracking, the stress-crack width behaviour in Fig. 5-5(b) was extracted from the total deformation readings by subtracting the elastic deformation from the total recorded deformation. It should be noted that at the time of testing of the dog bones the corresponding compressive strength of the concrete was 156 MPa.
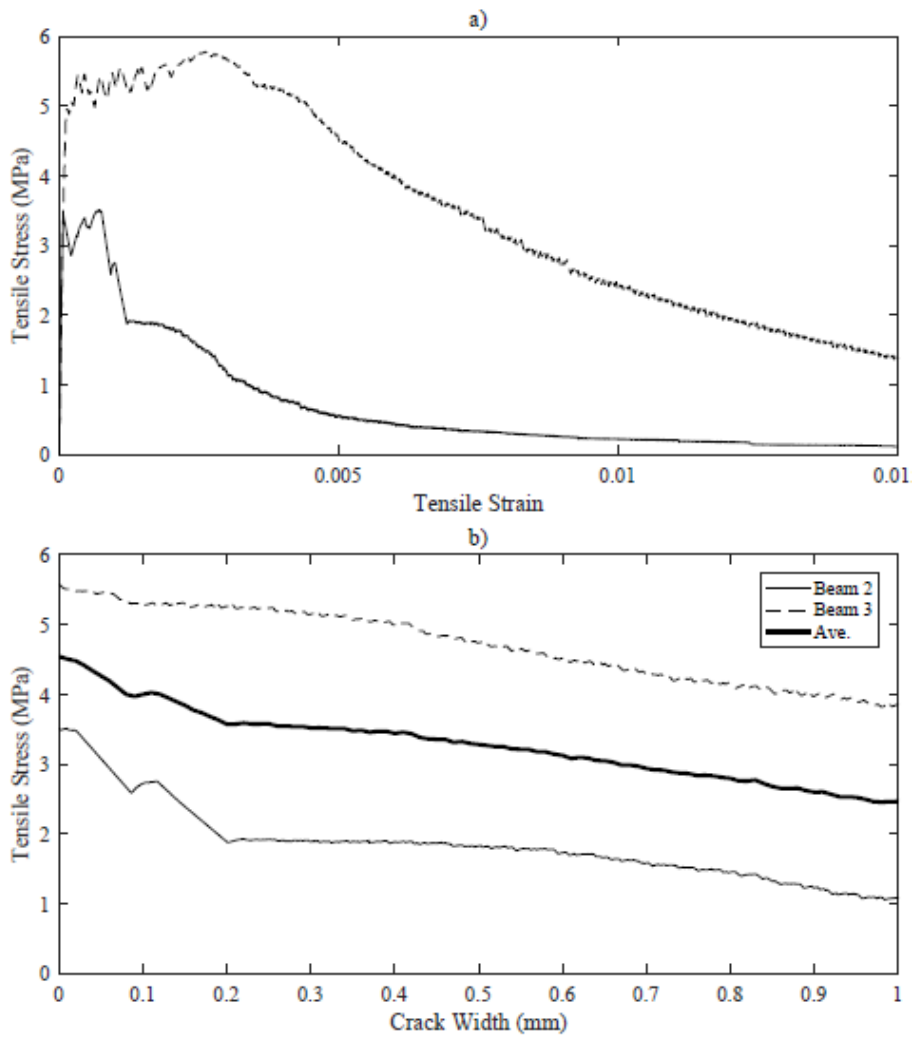
Fig. 5-5. Axial stress strain and stress crack width relationship

5.4.2.3 Reinforcement

The experimental stress-strain relationships for the longitudinal reinforcement is illustrated in Fig. 5-6. This was obtained from Fig. 5-4(a) direct tension test on the 12 mm and 16 mm longitudinal reinforcing bars in which the measured strain obtained from extensometer readings.
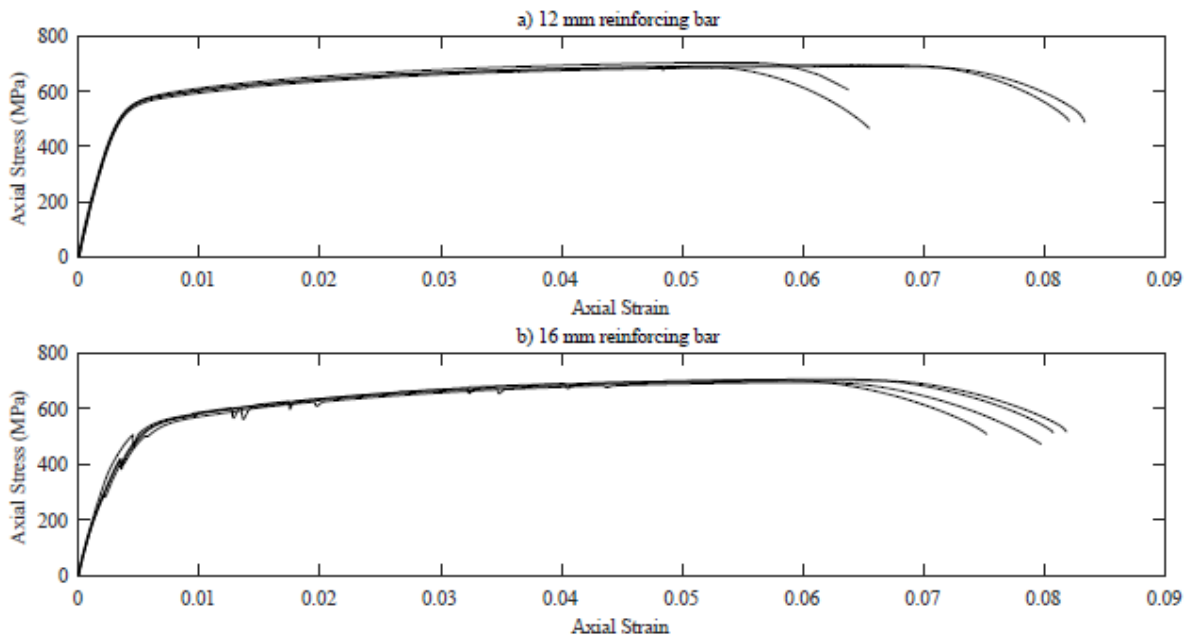
Figure 5-6. Stress-strain relationship of steel reinforcement

5.4.3 Beam test results

The load-deflection response of both spans of each of the beams tested are shown in Fig. 5-7 and a photograph of a typical failed beams in Fig. 5-8. In Fig. 5-7 key points have been identified as follows: the yield point is indicated by a cross, the peak load by a circle and the first rupture of the tensile reinforcement by a triangle. In the load deflection responses it can be observed that each beam exhibited typical approximately bi-linear behaviour, in which a significant increase in deformation occurred after the yielding of the tensile reinforcement. In each case ultimate failure of the member occurred due to rupture of the 12 mm tensile reinforcing bars, and upon inspection it could be observed that significant necking of the 16 mm bars had also occurred. As failure of the beam was due to reinforcement rupture, beams with the greatest reinforcement ratio exhibited the largest deformation and ductility. This

suggests that in order to make use of the full potential of UHPFRC the use of high strength reinforcement may be required.

Fig. 5-7. Load deflection response of beams

Figure 5-8. Typical beam after failure

The experimentally derived moment-rotation relationship of each hinge region is shown in Fig. 5-9. The rotation of the hinge was determined by considering the relative difference in beam deformation recorded by the LVDT readings concentrated about the location of the applied load and central support in Fig. 5-2. The end of the hinge region was identified from the step change in the rotation derived from adjacent LVDTs. The deformation readings outside of the hinge region were ignored. It should be noted that this measurement follows the work of (Visintin et al. 2012) who suggest that the hinge region must capture the deformations

associated with the sliding of the softening wedge as well as the opening of all cracks beneath and immediately adjacent to the softening wedge as shown in Fig. 5-10.
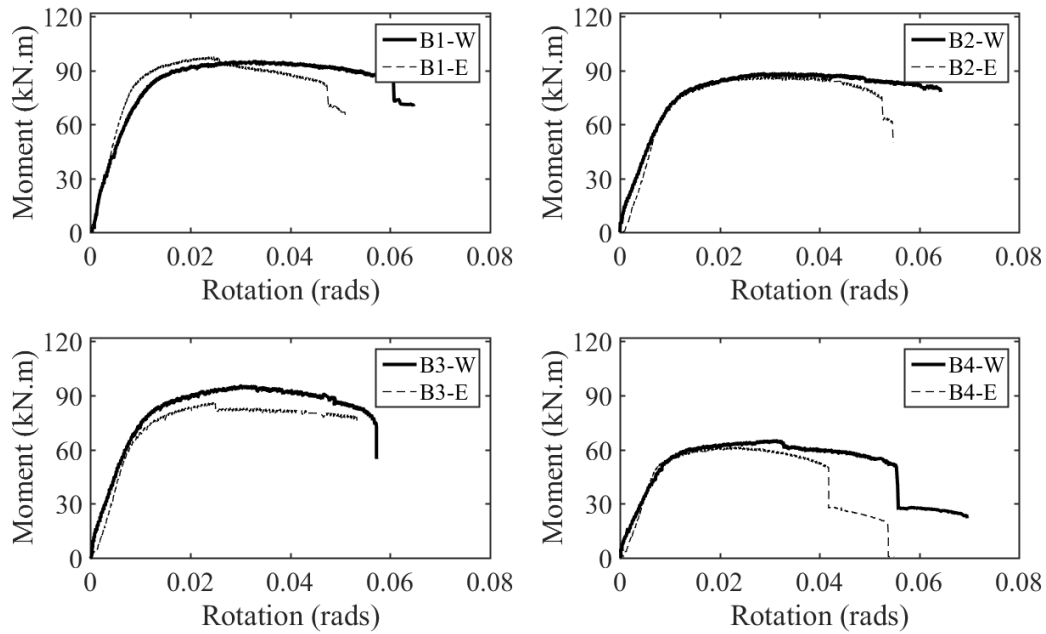
Figure 5-9. Moment rotation relationships
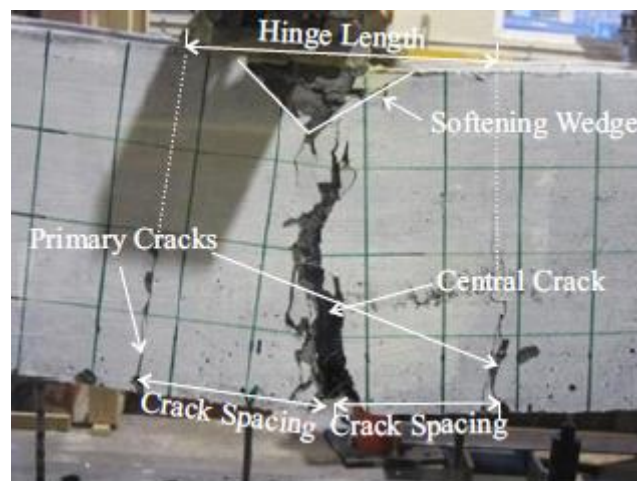
Figure 5-10. Typical hinge region at failure

From the photograph of a typical hinge region in Fig. 5-10 it is observed that the depth of the softening region is shallow despite the high reinforcing ratio of the beams. In normal strength

reinforced concrete beams, Visintin and Oehlers (Visintin and Oehlers 2016) postulated that compressive failure and moment redistribution is controlled by shear-friction sliding of the softening wedge identified in Fig. 5-10. Hence as a comparison to conventional concrete the angle at which shear friction sliding occurs along the softening wedge in the UHPFRC beams was measured and found to vary between 23 and 53 degrees with an average of 37 degrees. This is, in contrast to that of conventional concrete where the softening wedge typically forms at 26 degrees and increases with increased confinement (Chen et al. 2015). This implies that significant confinement of the concrete is provided by the fibre reinforcement, and the scatter within results is likely due to local variation in fibre quantity and orientation.

5.4.3.1 Moment redistribution

Figure 5-11 shows the degree of moment redistribution at each hinge location (mid span of each beam and central support) as a function of the total applied load P_{total}. In Fig. 5-11 percentage of moment redistribution calculated as

$$K_{MR} = \frac{M_{el} - M_{exp}}{M_{el}} \tag{5-1}$$

where M_{el} is the theoretical elastic moment and M_{exp} is the experimental moment which includes the effect of the plastic behaviour.
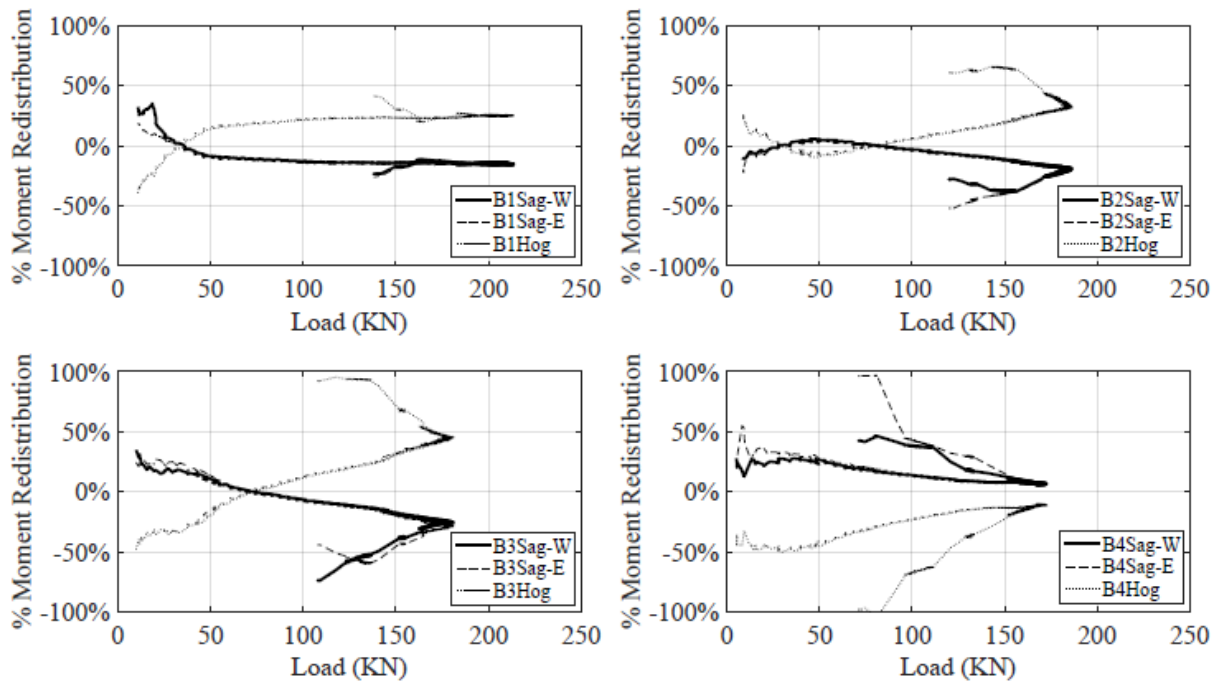
Figure 5-11. Moment redistribution at each span

It can be observed in Fig. 5-11 that moment redistribution begins at first loading. This behaviour can be attributed to variation in stiffness along the span due to the difference in reinforcement ratio in the hogging and sagging region, and due to the presence of flexural cracks which may arise either due to shrinkage or loading of the beam (Scott and Whittle 2005).

After the initial spike in redistribution with occurs around the point of first cracking, moment redistribution becomes more strongly dependent on the reinforcement ratio where for beams 1–3 redistribution occurs from the hogging to the sagging region and for beam 4 from the sagging to the hogging region.

In Fig. 5-12 the bending moment diagrams at corresponding the load at maximum moment redistribution in Fig. 5-11 are compared to the elastic bending moment diagrams. These demonstrates the effect of moment redistribution in equalising the moment between the load

152

point and the central support. In Fig. 5-13 the reaction at the centres support versus the applied

load is also shown.
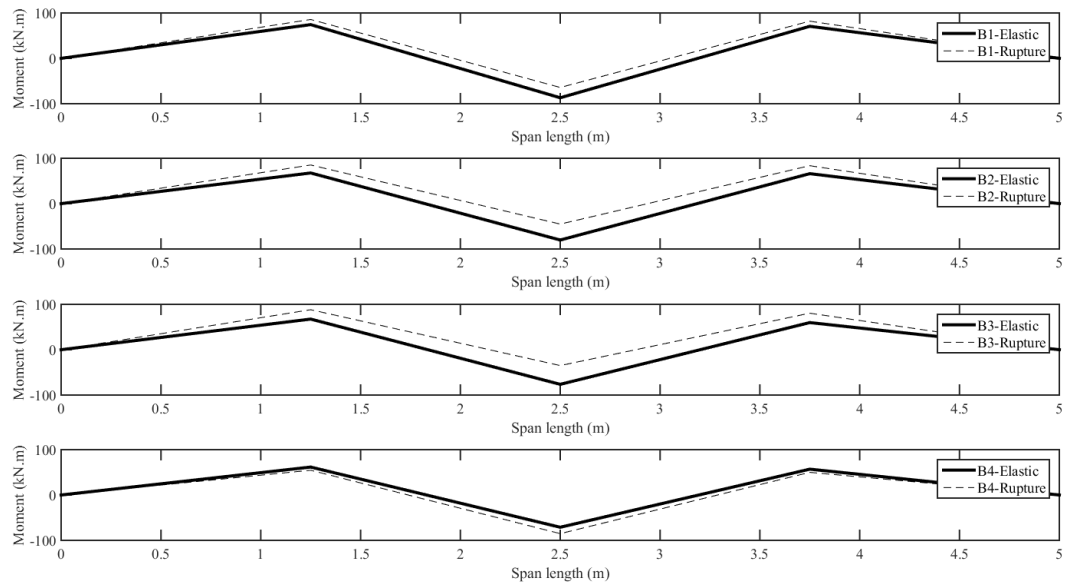
Figure 5-12. Comparison of elastic and experimental bending moment diagrams
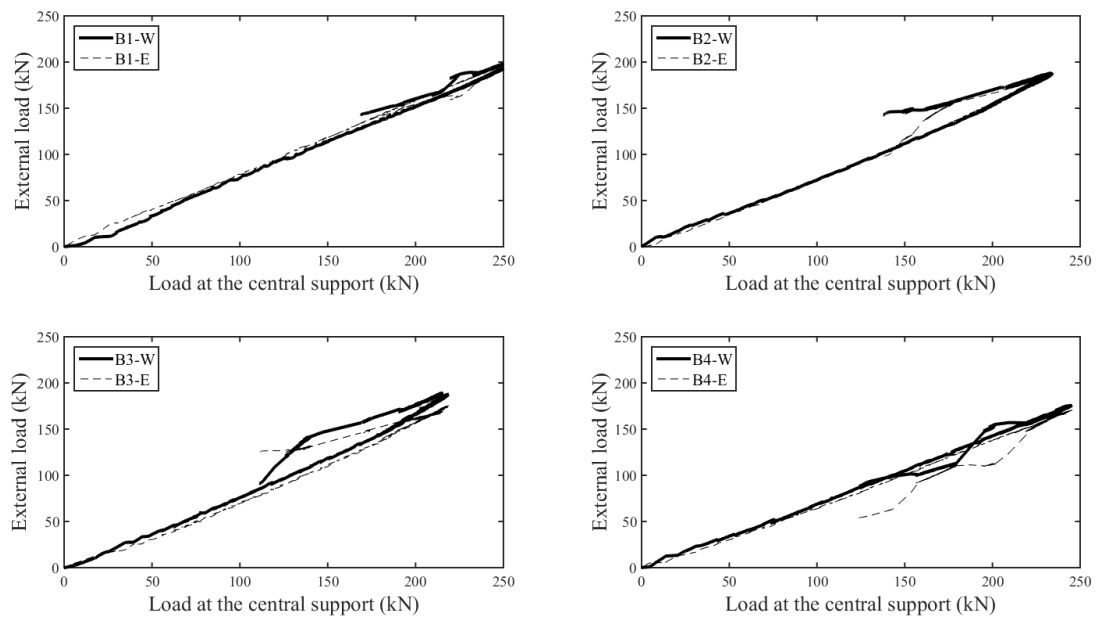
Figure 5-13. Comparison of load at central support to the applied external load

5.4.3.2 Ductility Factor

The ratio of the ultimate to yield deflection, also known as the ductility factor, is often used as a simple measure of energy absorption (Do Carmo and Lopes 2005) and is provided for each beam in Table 5-3. Unlike the behaviour seen in conventional concrete, here it is observed that the ductility factor does vary significantly with the reinforcement ratio. The quantity of the moment redistribution (KMR in Table 5-3) can also be seen not to be a function of the ductility factor. This contrary to the behaviour observed by do Carmo and Lopes (Do Carmo and Lopes 2005), and is likely due to the UHPFRC beams failing by rupture of the tensile reinforcement rather than by compression failure of the softening wedge.

Table 5-3. Ductility Factors for each beam

Beam	West			East			Exp. KMR
	Δ_{yield}	$\Delta_{ultimate}$	$\Delta_{ultimate}/\Delta_{yield}$	Δ_{yield}	$\Delta_{ultimate}$	$\Delta_{ultimate}/\Delta_{yield}$	
1	14.5	74	5.11	14.6	73	4.99	25
2	12.7	60.6	4.79	14	60.9	4.37	31.8
3	11	58	5.29	10.9	58.1	5.34	45.3
4	11.8	63.9	5.41	11.7	74.2	6.32	6.7

5.4.4 Comparison to codes of practice

To investigate the potential to extend existing codified limits on moment redistribution to UHPFRC the experimentally observed moment redistribution is compared to that predicted by the design equations in AS3600-2009 (Australian Standard 2009), fib Model Code 2010 (International Federation for Structural Concrete (fib) 2010) and ACI 318-11 (ACI 318-11 2011).

In AS3600-2009 permissible moment redistribution, K_{MR} is given by

$$K_{MR} = 0.3; k_u < 0.2 \qquad (5\text{-}2)$$

$$K_{MR} = 0.75(0.4 - k_u); 0.2 \leq k_u < 0.4 \qquad (5\text{-}3)$$

$$K_{MR} = 0; k_u \geq 0.4 \qquad (5\text{-}4)$$

and in which the neutral axis parameter k_u is a measure of the ductility of the cross section and is given by

$$k_u = \frac{d_{NA}}{d} \qquad (5\text{-}5)$$

where d_{NA} is the neutral axis depth and d is the effective depth of the cross section.

In the fib Model Code 2010 the permissible moment redistribution for concretes with a characteristic compressive strength of greater than 50 MPa is

$$K_{MR} = \min(0.46 - 1.25(0.6 + 0.0014\varepsilon_{cu2})k_u, 0.3) \qquad (5\text{-}6)$$

in which ε_{cu2} is the ultimate strain of the concrete.

Finally according to ACI 318-14, the maximum permissible moment redistribution is

$$K_{MR} = \min(1000\varepsilon_t, 0.2) \qquad (5\text{-}7)$$

where ε_t is the tensile strain in the reinforcement at the section redistributing moment.

A standard moment curvature analysis was undertaken as this form of analysis has been assumed to be applicable to fibre reinforced concrete at the ultimate limit (AFGC (Association Francaise de Genie Civil) 2013) and it is an analysis approach most commonly applied in practice.

For analysis, in Fig. 5-14 (a) curvature χ was applied to the cross section and a corresponding neutral axis d_{NA} assumed such that the strain profile is known. From this strain profile the concrete was divided into a series of layers and from the strain the stress was determined using the experimental derived stress-strain curves. Note that the tensile stress-crack width was converted to a stress-strain relationship by assuming a characteristic length equal to the length of the fibres (Jungwirth and Muttoni 2004). Applying the assumption of full interaction between the reinforcement and the surrounding concrete and taking the elastic modulus of the reinforcement to be 200 GPa and the yield stress to be 500 MPa the forces in the reinforcement, P_{rt} and P_{rc} can be determined. Having determined the internal forces the neutral axis is then shifted until equilibrium is achieved. The approach is then repeated for each curvature to generate the full moment curvature relationship for each cross section in Fig. 5-15, where significant points of interest have been highlighted. These include the curvature at: (i) yielding of the tensile reinforcement; (ii) commencement of crushing of the concrete when the maximum strain in the corresponds to the strain at peak stress in Fig. 5-3; (iii) an approximation of the end of concrete crushing when the maximum strain in the concrete reaches 0.008 which corresponds to the beginning of the residual stress in Fig. 5-3; and (iv) rupture of the reinforcement. An additional point corresponding to the curvature when the maximum strain in the concrete is 0.003 has been included as this strain condition is commonly used to indicate concrete crushing failure (ACI 318-11 2011; Australian Standard 2009; International Federation for Structural Concrete (fib) 2010).
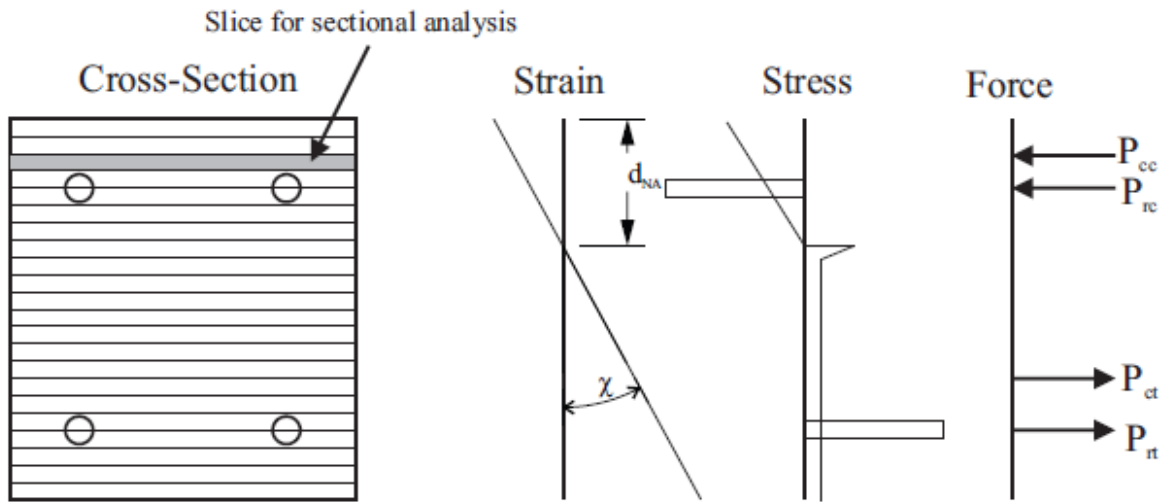
Figure 5-14. Illustration of forces and deformations in sectional analysis
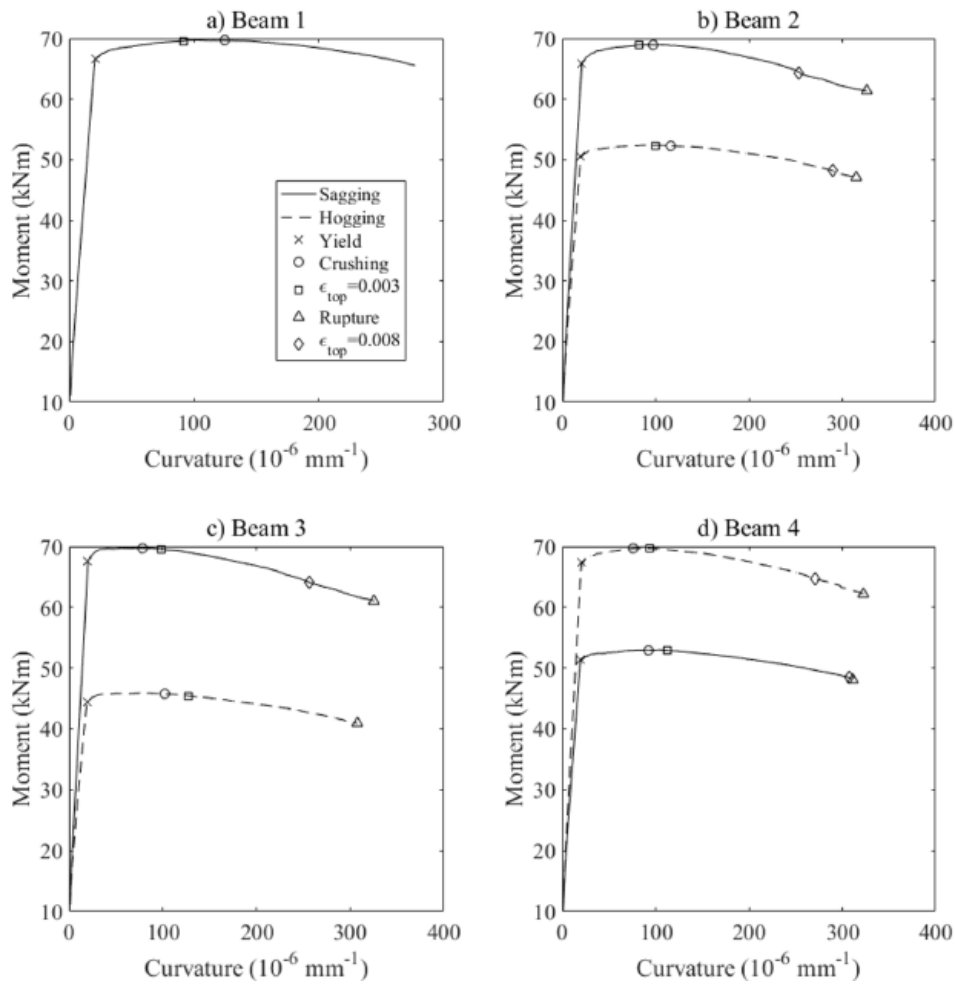
Figure 5-15. Moment curvature relationships of cross sections in each beam

Based on the results of the moment-curvature analysis the strain in the tensile reinforcement ε_t and the neutral axis depth parameter k_u were determined for each key point and used in conjunction with the code approaches to predict the percentage moment redistribution at the failure; and the results are summarised numerically in Table 5-4. This approach was taken as it can be seen in Fig. 5-3 that the assumption that concrete fails at a strain of 0.003 is not valid for the UHPFRC used in the present study.

From Table 5-4 it can be seen that for beam 1 AS3600-2009 stipulations yield conservative results, overestimate moment redistribution. ACI 318-2014 and fib Model Code 2010 is conservative for the first three beams which experience moment redistribution from the hogging and sagging regions as are AS3600-2009 for beams 2 and 3. For Beam 4 which experiences moment redistribution from the sagging to the hogging region all three code approaches are very unconservative which suggests that the code approaches can only predict moment redistribution if the moment is distributing away from a support. Further the code approaches did not show the trend observed experimentally of an increase in moment redistribution as the reinforcement in the hogging region is reduced. It can also be observed that the magnitude of the concrete stain at failure did not significantly influence the predicted moment redistribution, this is because the reinforcement yielded before the concrete reached its peak stress and hence for all strains investigated the neutral axis and hence k_u remained relatively constant.

Table 5-4. Comparison of code approaches to experimental moment redistribution

Beam	Position of Hinge	Exp. KMR	AS3600-2009								ACI 318-14								fib Model Code 2010							
			Crushing		$\varepsilon_t= 0.003$		Rupture		$\varepsilon_t= 0.008$		Crushing		$\varepsilon_t= 0.003$		Rupture		0.008		Crushing		$\varepsilon_t= 0.003$		Rupture		0.008	
			Pred.	Pred./Exp.	Pred.	Pred./Exp.	Pred.	Pred./Exp.	Pred.	Pred./Exp.	Pred.	Pred./Exp.	Pred.	Pred./Exp.	Pred.	Pred./Exp.	Pred.	Pred./Exp.	Pred.	Pred./Exp.	Pred.	Pred./Exp.	Pred.	Pred./Exp.	Pred.	Pred./Exp.
1	Hogging	25	30	1.199	30	1.2	(a)		(a)		19.7	0.789	14.2	0.568	(a)		(a)		24.2	0.966	21.6	0.862	(a)		(a)	
2	Hogging	31.8	30	0.944	30	0.94	30	0.944	30	0.94	18.4	0.577	15.7	0.493	20	0.629	20	0.629	24.5	0.769	23.4	0.737	24.7	0.776	24.7	25.3
3	Hogging	45.3	30	0.662	30	0.66	30	0.662	(b)		16.6	0.367	20	0.442	20	0.442	(b)		27.5	0.607	28.3	0.625	26.8	0.591	(b)	
4	Sagging	6.7	30	4.448	30	4.45	30	4.448	30	4.45	11.6	1.719	14.6	2.161	20	2.965	20	2.965	24.8	3.671	25.9	3.835	26.2	3.882	26.2	26.5

(a)   The cylinder test for this series was stopped at 0.0075 hence a top strain of 0.008 or rupture of the reinforcement could not be achieved in the simulation

(b)   For this test the sectional analysis suggests rupture occurred before a strain of 0.008 was reached

5.5 CONCLUSIONS

In this research, an experimental program has been conducted in order to investigate the moment redistribution capacity of reinforced UHPFRC continuous beams as well as the suitability of extending existing code approaches for application to UHPFRC.

The results of the experiments indicate that:

(1) The improved compressive ductility of the concrete introduced by the presence of fibres, including the approximately 25 MPa residual strength, shifted the failure mode of the UHPFRC sections tested from concrete crushing to reinforcement rupture.

(2) Significant redistribution of moments occurs in UHPFRC beams prior to the plastic limit being reached in either the reinforcement or the concrete. This elastic redistribution occurs as a result of the variation in flexural rigidity of the section throughout the span either because of a variation in reinforcement layout or due to cracking.

(3) ACI and FIB reproaches are conservative in all cases where redistribution occurs from the hogging to the sagging region

(4) No approaches could adequately simulate moment redistribution from the sagging to hogging regions of a beam.

(5) The increased ductility of the concrete was not a significant factor in the analysis approaches as for all limiting strain conditions investigated the neutral axis depth remained relatively constant.

5.6 REFERENCES

ACI 318-11 (2011). "ACI 318-11. Building Code Requirements for Structural Concrete and Commentary, PCA notes on ACI 318-11: with design applications." *Farmington Hills, Mich: ACI International*.

AFGC (Association Francaise de Genie Civil) (2013). "Betons fibres a ultra-hautes performances- Recommandations [Ultra high performance fibre reinforced-concretes – Recommendations]." *Paris, France*

Australian Standard (2006). "AS/NZS 2350.11. Methods for testing Portland, blended and masonry cements." *Standards Australia, Sydeny*.

Australian Standard (2006). " AS/NZS 2350.13. Methods for testing Portland, blended and masonry cements – determination of drying shrinkage of cement mortars." *Standards Australia, Sydney*.

Australian Standard (2009). "AS3600-2009. Concrete Structures." *Standards Association of Australia, North Sydney*.

Benson, S., and Karihaloo, B. L. (2005). "CARDIFRC-Development and mechanical properties. Part 1: development and workability." *Magazine of Concrete Research*, 57(6), 347-352.

Chanvillard, G., and Rigaud, S. "Complete characterization of tensile properties of Ductal UHPFRC according to the French recommendations." *Proc., Proceedings of the 4th International RILEM workshop High Performance Fiber Reinforced Cementitious Composites*, 21-34.

Chen, Y., Visintin, P., and Oehlers, D. (2015). "Concrete shear-friction material properties: Derivation from actively confined compression cylinder tests." *Advances in Structural Engineering*, 18(8), 1173-1185.

Do Carmo, R. N., and Lopes, S. M. (2005). "Ductility and linear analysis with moment redistribution in reinforced high-strength concrete beams." *Canadian Journal of Civil Engineering*, 32(1), 194-203.

do Carmo, R. N., and Lopes, S. M. (2008). "Available plastic rotation in continuous high-strength concrete beams." *Canadian Journal of Civil Engineering*, 35(10), 1152-1162.

Graybeal, B. A. (2008). "Flexural behavior of an ultrahigh-performance concrete I-girder." *Journal of Bridge Engineering*, 13(6), 602-610.

International Federation for Structural Concrete (fib) (2010). "CEB-FIB Model Code 2010 Final Draft Volume 2." *Thomas Thelford, Lausanne, Switzerland.*

Japanese Society of Civil Engineers (2008). "Concrete Engineering Series 82: Recommendations for design and construction of high performance fibre reinforced cement composites with multiple fine cracks." *JSCE, Tokyo, Japan.*

Jungwirth, J., and Muttoni, A. "Structural behavior of tension members in Ultra High Performance Concrete." *Proc., International symposium on ultra high performance concrete*, International Symposium on Ultra High Performance Concrete.

Moallem, M. R. (2010). "Flexural Redistribution in Ultra-High Performance Concrete Lab Specimens." Ohio University.

Mohr, A. W. (2012). "Moment redistribution behaviour of SFRC members with varying fibre content." Stellenbosch: Stellenbosch University.

Oehlers, D. J., Haskett, M., Mohamed Ali, M., and Griffith, M. C. (2010). "Moment redistribution in reinforced concrete beams." *Accepted Proceedings ICE, Structures and Buildings*.

Panagiotakos, T. B., and Fardis, M. N. (2001). "Deformations of reinforced concrete members at yielding and ultimate." *Structural Journal*, 98(2), 135-148.

Paulay, T. (1976). "Moment Redistribution in Continuous Beam of Earthquake Resistant Multistory Reinforced Concrete Frames." *Bulletin of New Zealand National Society for Engineering*, 9(4), 205-212.

Schumacher, P. (2006). "Rotation capacity of self-compacting steel fiber reinforced concrete." TU Delft, Delft University of Technology.

Scott, R., and Whittle, R. (2005). "Moment redistribution effects in beams." *Magazine of concrete research.*, 57(1), 9-20.

Singh, M., Sheikh, A., Ali, M. M., Visintin, P., and Griffith, M. (2017). "Experimental and numerical study of the flexural behaviour of ultra-high performance fibre reinforced concrete beams." *Construction and Building Materials*, 138, 12-25.

Sobuz, H., Visintin, P., Ali, M. M., Singh, M., Griffith, M., and Sheikh, A. (2016). "Manufacturing ultra-high performance concrete utilising conventional materials and production methods." *Construction and Building Materials*, 111, 251-261.

Visintin, P., Oehlers, D., Wu, C., and Haskett, M. (2012). "A mechanics solution for hinges in RC beams with multiple cracks." *Engineering Structures*, 36, 61-69.

Visintin, P., and Oehlers, D. J. (2016). "Mechanics-based closed-form solutions for moment redistribution in RC beams." *Structural Concrete*, 17(3), 377-389.

Visintin, P., and Oehlers, D. J. (2016). "Mechanics closed form solutions for moment redistribution of RC beams." *Structural Concrete*.

Visintin, P., and Oehlers, D. J. (2018). "Fundamental mechanics that govern the flexural behaviour of reinforced concrete beams with fibre-reinforced concrete." *Advances in Structural Engineering*, 21(7), 1088-1102.

Yang, I.-H., Joh, C., and Kim, B.-S. (2011). "Flexural strength of large-scale ultra high performance concrete prestressed T-beams." *Canadian Journal of Civil Engineering*, 38(11), 1185-1195.

Yang, I. H., Joh, C., and Kim, B.-S. (2010). "Structural behavior of ultra high performance concrete beams subjected to bending." *Engineering Structures*, 32(11), 3478-3487.

CHAPTER 6

An Experimental and Analytical Study of Ultra-High Performance Fibre Reinforced Concrete Curved Beams

[*][1]Xie, T., [2]Mohamed Ali, M. S., [3]Elchalakani, M., [4]Moya, D.

[1]Mr. Tianyu Xie (Corresponding author)

Ph. D Candidate,

School of Civil, Environmental and Mining Engineering

The University of Adelaide

South Australia 5005

AUSTRALIA

[2]Dr M. S. Mohamed Ali

Senior Lecturer,

School of Civil, Environmental and Mining Engineering

The University of Adelaide

South Australia 5005

AUSTRALIA

[3]Dr Mohamed Elchalakani

Senior Lecturer

School of Civil, Environmental and Mining Engineering

The University of Western Australia

Western Australia 6009

AUSTRALIA

[4]**Mr. David Moya**

Graduate Engineering Student

School of Civil, Environmental and Mining Engineering

The University of Adelaide

South Australia 5005

AUSTRALIA

Statement of Authorship

Title of Paper	AN EXPERIMENTAL AND ANALYTICAL STUDY OF ULTRA-HIGH PERFORMANCE FIBRE REINFORCED CONCRETE CURVED BEAMS
Publication Status	☐ Published ☐ Accepted for Publication ☑ Submitted for Publication ☐ Unpublished and Unsubmitted work written in manuscript style
Publication Details	Xie, T., Ali, M. M., Elchalakani, M & Moya, D. (2018). An Experimental and Analytical Study of Ultra-High Performance Fibre Reinforced Concrete Curved Beams. Submitted *to ASCE Journal of Structural Engineering*.

Principal Author

Name of Principal Author (Candidate)	Tianyu Xie
Contribution to the Paper	Designing concept, conducting experiments, analysing of data, drafting manuscript
Overall percentage (%)	40
Certification:	This paper reports on original research I conducted during the period of my Higher Degree by Research candidature and is not subject to any obligations or contractual agreements with a third party that would constrain its inclusion in this thesis. I am the primary author of this paper.
Signature		Date	12/02/2019

Co-Author Contributions

By signing the Statement of Authorship, each author certifies that:

    i.   the candidate's stated contribution to the publication is accurate (as detailed above);

    ii.   permission is granted for the candidate in include the publication in the thesis; and

    iii.   the sum of all co-author contributions is equal to 100% less the candidate's stated contribution.

iv. Name of Co-Author	Dr Mohamed Ali Sadakkathulla
Contribution to the Paper	Designing concept, supervising experiments, analysing of data, proofreading (30%)
Signature		Date	12/02/2019

Name of Co-Author	Dr Mohamed Elchalakani
Contribution to the Paper	Designing concept, analysing of data, proofreading (20%)
Signature		Date	7-2-2019

Please cut and paste additional co-author panels here as required.

Name of Co-Author	Mr David Moya		
Contribution to the Paper	Conducting experiments, analysing of data (20%)		
Signature		Date	07/02/2019

THIS PAGE HAS BEEN LEFT INTENTIONALLY BLANK

ABSTRACT

This paper presents experimental and analytical investigations on the structural behaviour of horizontally curved ultra-high performance fibre reinforced concrete (UHPFRC) beams subjected to concentrated loads applied normal to plane of the beam. Four fixed-ends supported UHPFRC beams with curvatures of 0°, 60°, 90° and 120° were tested. The structural responses, including the deflection, out-of-plane rotation and reaction forces of UHPFRC curved beams under all stages of loadings were experimentally studied. A change in failure mechanism of a UHPFRC beam with the change in its curvature was observed and the load carrying capacity and ductility of a UHPFRC beam decreased slightly with an increase in the curvature of the beam. The experimental results also indicated that due to the strain-hardening behaviour of UHPFRC materials under tension, a UHPFRC curved beam exhibited improved load carrying capacity and ductility over conventional straight reinforced concrete beams, as the ductility index of each of the UHPFRC beam in this study was over 3. In addition, structural mechanics based closed form solutions were developed for horizontally curved UHPFRC beams using Castigliano's second theorem to predict the values of bending moment, shear force, reaction force and torsional moment of the beams under linear elastic material conditions. Influence lines for bending moment, shear force and torsional moment were also generated using the closed-form equations which are validated by test results by considering the effects of curvature, bend-to-twist ratio and loading position on the internal actions of UHPFRC curved beams.

Keywords: horizontally-curved beam; ultra-high performance fibre reinforced concrete (UHPFRC); closed form solutions; elastic tests; structural analysis.

6.1. INTRODUCTION

Rapid urbanization and accelerated industrialization increase transport activity worldwide, and hence lead to a greater demand for developing transport infrastructures to provide sufficient connectivity between businesses, ideas, goods and services. Recent reviews of world transport infrastructure reveal that there exists mutual relationship between road infrastructure and economic growth (Engineers Australia 2010; Ismail and Mahyideen 2015; Pojani and Stead 2017). In Australia, according to current estimates, if the farcically inadequate transport infrastructure was not reformed, around 20% increase in travel time and a corresponding reduction in economic growth of $53 billion would occur for the period from 2015 to 2035 (Infrastructure Australia 2015). Lack of extensive road and rail infrastructural facilities in most cities in developing countries even more seriously hinder both economic growth and poverty reduction (Worldbank 1994). To address these issues, methods for promoting of transport infrastructure in pursuit of higher national socio-economical goals are necessary. To date, within some regions, large governmental and private sector efforts are now dedicated in supporting, designing, constructing and facilitating national transport infrastructure. Considering the limitations of space constraints in urban areas, natural obstructions and manmade obstacles, it is inevitable to design structures with skewed and curved alignments to adapt to the surrounding terrains and ground obstacles.

In this context, curved beams are extensively used in constructing large stadiums, highway intersections and bridges, round corners of a building and circular balconies. A bridge constructed using horizontally curved beams is recognized as a viable bridge form in traffic engineering and since 1960s, a good number of studies have been conducted to understand the behaviour of curved beam manufactured using different materials (Al-Hashimy and Eng 2008; Al-Hassaini 1962; Chavel 2008; Hsu et al. 1978; Lee et al. 2017; Mansur and Rangan 1981; McManus et al. 1969). As reported in these studies, unlike straight beams or girders, a

horizontally curved beam loaded normal to plane is subjected to a complex system of combined effects due to shear, flexure and torsion. These actions on the curved beam cause a complex response of the structure under the applied loads, for instance the warping of structures induced by non-uniform torsion (Fatemi et al. 2016; Petrov and Géradin 1998). For the more reliable design of bridges under the conditions of various topography, it urgently requires to clearly examine the behaviour of the structural elements curved in plan such as bridge girders and beams of buildings.

The applications of Ultra-high performance fibre reinforced concretes (UHPFRC) in the bridge constructions have been undergoing steady growth due to the superior characteristics of the material such as its higher compressive and tensile strengths, ductility and better durability-related properties compared to those of plain conventional concrete materials; some practical examples of UHPFRC bridges are Sherbrooke footbridge in Canada (Blais and Couture 1999), Shepherd's Gully bridge in Australia (Foster 2009), Horikoshi C-ramp bridge in Japan (Tanaka et al. 2011), and Saint Pierre La Cour bridge in France (Resplendino 2008). The presence of the internal fibres in UHPFRC not only prevent wider cracks (Xie et al. 2018) but also effectively act as the reinforcements to resist shear and torsion seen on the bridge structures with skewed and curved alignments; and the denser matrix of UHPFRC creates a feasible solution for the problem associated with concrete deterioration caused by inner steel reinforcement corrosion. Moreover, the use of UHPFRC materials in building bridges can also effectively address the shortcomings of conventional bridge construction work which is rather labour-intensive and time-consuming. Due to these advantages, UHPFRC assists in constructing structural elements with longer spans, reduced member sizes and increased design lives. Recent investigations on UHPFRC (Gu et al. 2015; Joe 2016; Larsen et al. 2017) have also listed the benefits of replacing conventional reinforced concrete and concrete-steel

composite transport infrastructure with UHPFRC structures, such as reducing maintenance liability and increasing the robustness of structures. Recent research and development activities at University of Adelaide focusing on developing UHPFRC mix recipe using conventional materials and manufacturing methods will expedite the adoption of UHPFRC in actual construction due to improved economy (Sobuz et al. 2016; Sturm et al. 2018; Sturm et al. 2018; Visintin et al. 2018; Xie et al. 2018). In this regard, investigations were carried out on structurally evaluating the performance of beams and columns (Singh et al. 2016; Singh et al. 2017; Visintin et al. 2018), In continuation of these research efforts, the current study aims to investigate the performance of curved beams as no systematic analytical and theoretical research on UHPFRC curved beams are reported in the published literature.

An extensive literature review indicates that very good amount of investigations have been carried out on studying the behaviour of horizontally curved beams produced using conventional reinforced concrete (RC) or concrete-steel composites (Al-Hashimy and Eng 2008; Al-Hassaini 1962; Chavel 2008; Lee et al. 2017), this can be used as good basis for understanding the behaviour of UHPFRC curved beams. As reported in these studies, combined bending torsion dominate the failure of curved RC or steel-concrete composite beams and UHPFRC could offer positive effects on the behaviour of the beams as its higher tensile strength and ductility cannot be ignored; also the inner fibres contribute to shear and torsion. It is also noted that the majority of the existing theoretical work on horizontally curved beam were developed numerically using finite element analysis (FEA) (i.e. (Lin and Yoda 2014; Mathiyazhagan and Vasiraja 2013; Noor et al. 1977)), or empirically based on limited experimental data (i.e. (Al-Hashimy and Eng 2008; Al-Hassaini 1962; Hsu et al. 1978)). By the very nature of being numerically or empirically derived, these approaches do not help in fully understanding the very complex and important problems seen on curved beams and would

not be able to provide mathematical expressions to directly contribute to the codes and guidelines for designing curved beams. Only a few existing studies have provided closed-form solutions but mainly for curved beams under simply supported conditions (Fatemi et al. 2016; Fatemi et al. 2015). To achieve the transport infrastructure with higher performance and also to address the aforementioned shortcomings of the existing research on curved beams, the experimental and analytical work presented in this study aims to comprehensively investigate the behaviour of fixed-ends supported curved UHPFRC beams and also examine the effect of curvature on the performance of the curved beams. Monotonically concentrated load is applied at the selected positions along each of the beams. Deflection, rotation profiles, and reaction forces at the supports of each curved beam are experimentally recorded. In addition to the experimental work, closed-form solutions are derived using energy method in fundamental structural mechanics to quantify the elastic behaviour of UHPFRC curved beams. The advantage of this closed-form solution is that it is less demanding on computational effort and therefore may have greater potential to be incorporated into practical design guidelines. Significantly, the work presented in this study has been one of the first attempts to thoroughly examine and to establish a quantitative framework for analysing the behaviour of horizontally UHPFRC curved beams. The findings of this study will also redound to facilitate the development of low-cost UHPFRC using conventional manufacturing method into the applications to transport infrastructure

6.2 EXPERIMENTAL PROGRAM

6.2.1 Materials

Two types of cementitious materials were used as binders for the UHPFRC, namely sulphate resisting cement and silica fume and detailed chemical, physical and mechanical properties of these two cementitious materials are reported elsewhere (Singh et al. 2017; Sobuz et al. 2016).

Well-graded natural washed river sand with a nominal maximum size of 4.75 mm was used as the only aggregate for the UHPFRC. A third generation superplasticizer, namely Sika Viscocrete 10 in aqueous form was used in the UHPFRC to attain the desirable flow. Copper coated micro-steel fibre that had a diameter of 0.2 mm and length 13mm were used for producing the UHPFRC. The fibre volume used was 2.25% of the matrix. Note that the micro-fibres were used due to the constraints posed by the cross-sectional dimensions of the beam specimens. The mix proportion of the UHPFRC is 835 kg/m^3 Sulphate resistant cement, 222 kg/m^3 silica fume, 1057 kg/m^3 sand, 127 kg/m^3 water, 64 kg/m^3 SP and 246 kg/m^3 steel fibres. The 10 mm steel reinforcing bar used had a tensile yield strength of 528 MPa and was used as longitudinal tensile and compressive reinforcements for the beams. The 8 mm stirrup used has a tensile yield strength of 511 MPa.

For producing UHPFRC, fine aggregates and cementitious binders were initially mixed in a planetary concrete mixer with a capacity of 1300 kg for 10 minutes till the dry ingredients evenly mixed and the liquids including water and superplasticizer were subsequently added to the mix. The wet mixing process was continued for approximately another 45 minutes until the UHPC mortar attained a favourable flow. Finally, discrete steel fibres were mixed with the UHPC mortar for 10 minutes to ensure the homogenous distribution of fibres in the body of the matrix. All the slabs and the companion specimens for material property tests were demould after 48 hours ambient curing under laboratory condition and then moved to fog room (i.e. 95±5% relative humidity and 23±2° C temperature) to continue the curing for at least 35 days before testing.

6.2.2 Beam tests

*Specimen details***:** In order to experimentally investigate the response of UHPFRC curved members under applied concentrated loads, and for validating the proposed analytical models, four reinforced UHPFRC beams with different curvatures of 0°, 60°, 90° or 120° (designated as B0, B60, B90 or B120, respectively) were manufactured and tested. Each beam had a cross-section of 150 mm × 150 mm. To prevent shear failure, adequate shear reinforcements were also provided which consisted of 8 mm diameter stirrups spaced at 100 mm centres for the middle portion of each beam, and the stirrups were placed at 50 mm centres within 250 mm region for both ends of each beam, where the maximum shear stress is located. The details of the cross-section of the test beams are shown in Fig. 6.1. To hang the stirrups, two 8 mm diameter steel bars, located at an effective depth of 32 mm were included in the compression region. All the members were tested as fixed end-supported under three-point bending and with a constant effective span of 2400 mm between the two supports.

(a)

174
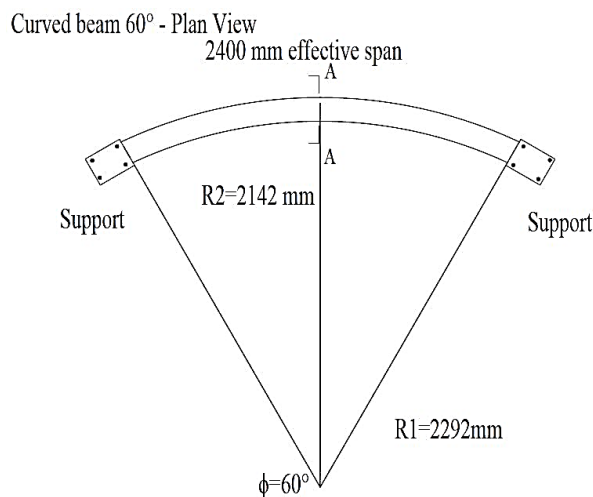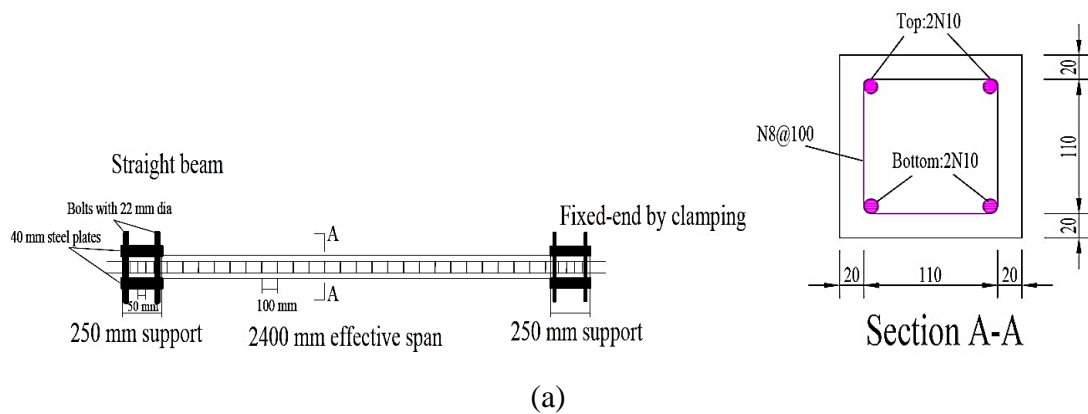
(b)

Curved beam 90°- Plan View

2400 mm effective span

R2=1378 mm

Support   Support

R1=1528mm

φ=90°
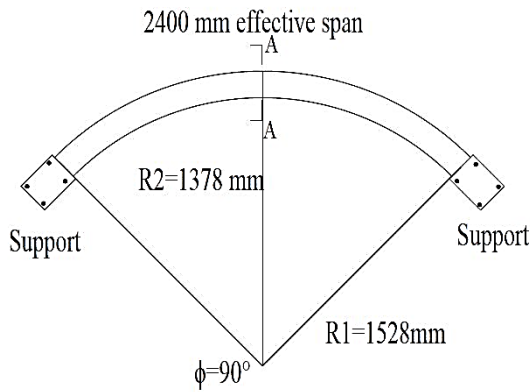
(c)

Curved beam 120°- Plan View

2400 mm effective span

R2=996mm

Support   R1=1146mm Support

φ=120°
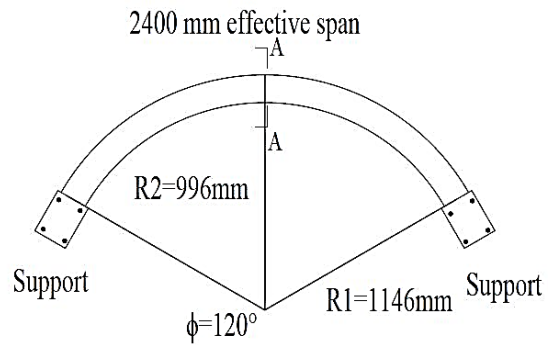
(d)

Figure 6.1. Beam geometries and reinforcement arrangements: a) B0; b) B60; c) B90; d)

B120

Testing procedure: The beams were tested three times by altering the loading position so that the effect of varying combination of shear force (V), bending moment (M) and torsional moment (M) can be studied on the structural behaviour of the curved beams. Fig. 6.2 illustrates the three selected loading points for the beam tests. In the first two instances (i.e. at point P1 orP2), the beams were subjected to a monotonically increasing concentrated load limited to a maximum of 25 kN so that the longitudinal tension steel reinforcements will not yield. Finally in the third test (at point P3), the beam was tested to failure. In this final test scenario, the applied load was continued under loading control at a rate of 5 kN/min until the peak load was attained and the load was continuously applied under displacement control at a displacement rate of 0.1 mm/min until failure to obtain the complete load-defection relationship.

φ/8 φ/8 φ/8 φ/8 φ/8

P1 P2 P3

Support A   Support B

Support A   P1 P2 P3   Support B

L/8 L/8 L/8 L/8
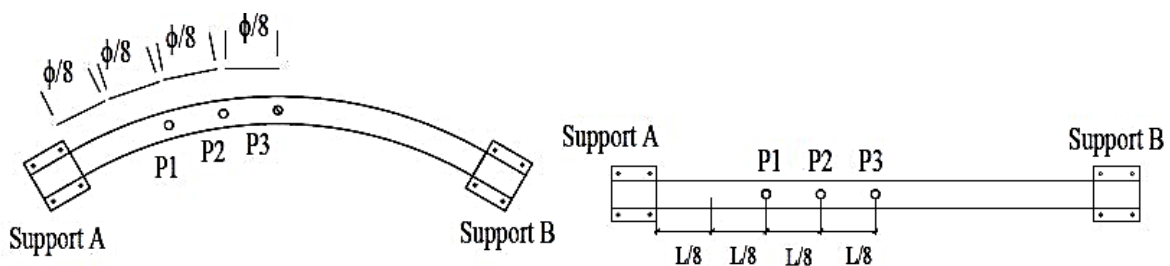
Figure 6.2. Selected loading positions for: a) curved beams; b straight beam

Instrumentations: To generate the deflection profiles of each beam test, a total of 8 LVDTs or laser sensors were used, including 7 positioned at the bottom of each of the beams to measure the vertical deflections, as shown in Figs. 6.3 (a)-(c) and another one mounted on the loading ram to record the displacement of the loading ram. In order to obtain the rotations about the vertical (y-axis) and horizontal (x-axis) directions, five dual-axis tilt sensors, namely accelerometers, were mounted at different locations to the lateral surface of each beam, as shown in Fig. 6.4 (a) to (c). During the test, the rotation was also measured by using the accelerometers, which each can be used to record the changes in accelerations of the structure about two axes (*AX* and *AY*) through a tilt sensor. The measured changes in accelerations at each of the selected locations were further converted into tilts (inclinations) by multiplying a unit of gravitational acceleration ($1g = 9.8$ m/s^2) and consequently, roll (*Rot-X*) and pitch (*Rot-Y*) can be obtained. Moreover, two load cells, each with a capacity to measure a compressive force up to 100 kN and a tensile force up to 1 kN only, were positioned under each of the supports of the beams to record the vertical reaction forces.

(a) (b)
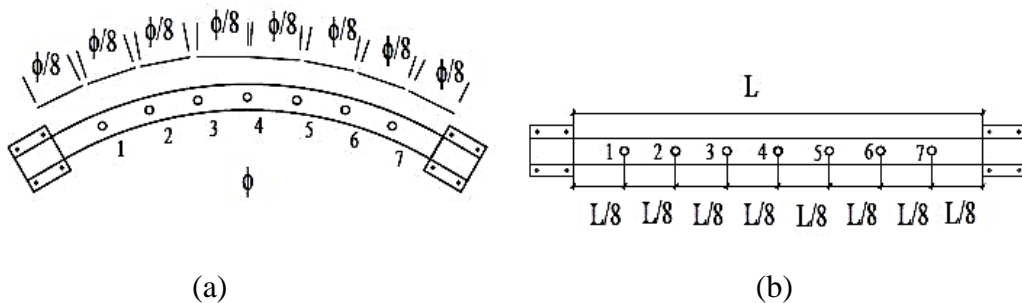
(c)

Figure 6.3. Set-up for displacement measurements: a) LVDT/Laser sensor locations on straight beam; b) LVDT/Laser sensor locations on curved beams; c) instrumentations of LVDTs/Laser sensors

Curved beam: Accelerometer locations-lateral view
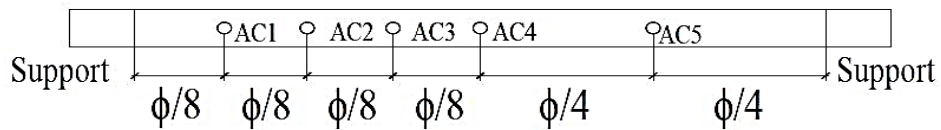
(a)
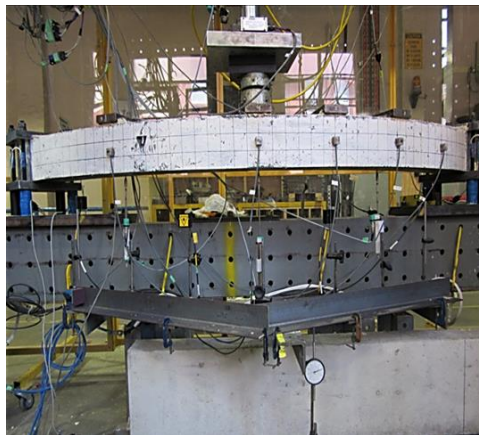
(b)

Figure 6.4. Set-up for rotation measurements: a) accelerometers locations on curved beam; c) instrumentations of accelerometers

6.2.3 Material properties of UHPFRC

Compression tests: The compressive strength (f'_c), elastic modulus (E_c) and the Poisson's ratio of the UHPFRC were determined according to the test methods prescribed by ASTM standard C39/C39M-05 (ASTM International 2005) and ASTM standard C469/C469m-14 (ASTM International 2014) using the cylindrical specimens (100 mm diameter x 200mm height). During the compression tests, load control was applied with the loading rate of 0.3 MPa per second the axial deformation of each specimen was measured with two LVDTs mounted on opposite faces of the specimen. Figure 6.5 (a) illustrates the complete axial compressive stress-strain relationship of the UHPFRC.

Tensile characteristics: To characterize tensile properties of the UHPFRC, direct tension tests were undertaken using dog-bone shaped specimens, as the details of the dog-bone specimens and corresponding set-up of the test can be found in (Singh et al. 2017). In order to record the behaviour of the UHPFRC under direct tension, one 80 mm strain gauge of 80 mm length and one LVDTs with a gauge length of 300 mm were installed on each face of each of the dog-bone specimens. The tensile characterisations of the UHPFRC are shown in Fig. 6.5 (b) and (c). Note that prior to cracking of the UHPFRC, the tensile behaviour of the UHPFRC can be characterized using the stress-strain relationship shown in Fig. 6.5 (b) and the stress-crack width relationship shown in Fig. 6.5 (c) is then used to represent the tensile characterisation of the UHPFRC at the post cracking stage. It is worth highlighting that with incorporation of 2.25% steel fibres by volume into the UHPFRC mix, the stress-strain curve of the UHPCFRC exhibits a strain-hardening branch.
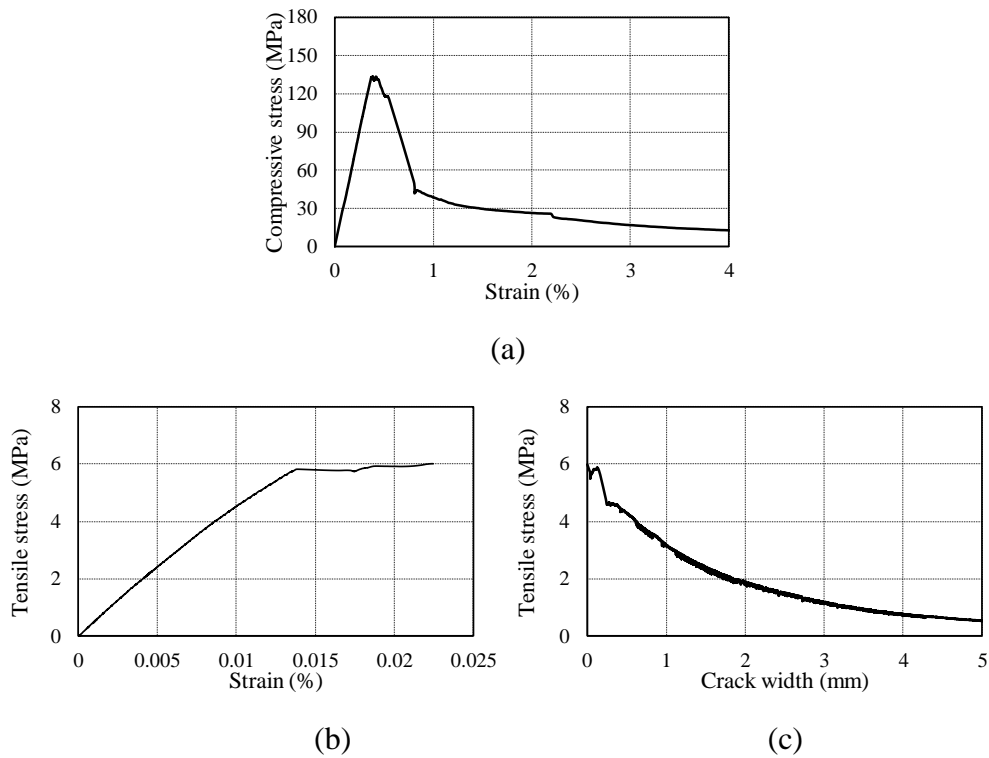
Figure 6.5. Material characterizations: a) compressive stress-strain relationship of UHPFRC;

b) tensile stress-strain relationship of UHPFRC before cracking; c) tensile stress-crack width

relationship of UHPFRC after cracking

6.3 TEST RESULTS AND DISCUSSION

6.3.1 Reaction forces at elastic region

The reaction forces at the supports of each UHPFRC beam within the linear elastic region were

experimentally-recorded using the load cells. Figs. 6.6 and 6.7 display the load applied and the

reaction forces measured for the cases of straight and a representative curved UHPFRC beam

(i.e. curvature $\varphi=120°$) loaded at points P1, P2 or P3. As can be seen from these figures, the

reaction force measured at each support of the beams significantly affected by the loading

position, whereas there was a minimal effect of curvature on the reaction forces. Moreover, the

larger reaction force was measured at the support close to the loading point as can be seen in

Fig. 6.6. It is also worth mentioning that, due to the equilibrium of force at the vertical direction,

for each test, the sum of the reaction forces measured at the two supports was approximately equal to the magnitude of the applied load. This confirms that load cells used in the present study provided valid and reliable measurements of the reaction forces at the supports.

(a) (b) (c)
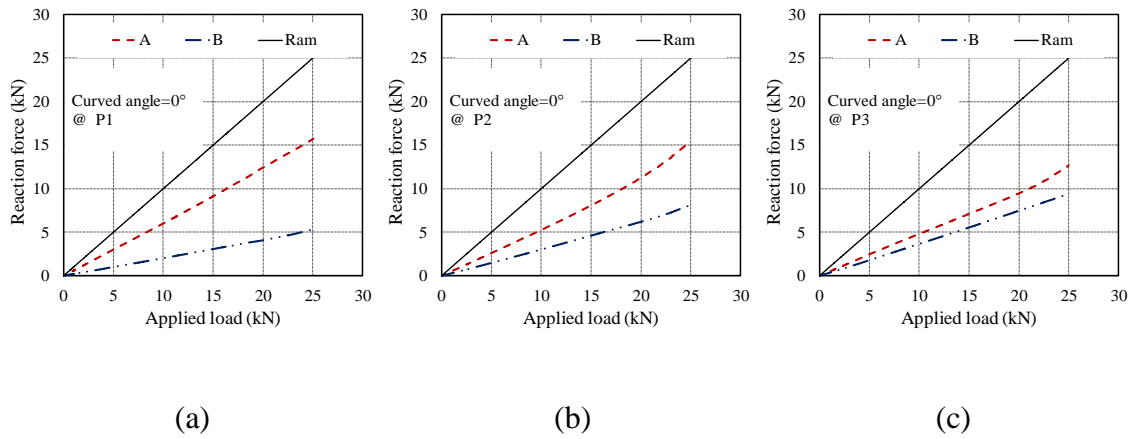
Figure 6.6. Reaction forces of beam-B0 loaded at: a) P1; b) P2; c) P3

(a) (b) (c)
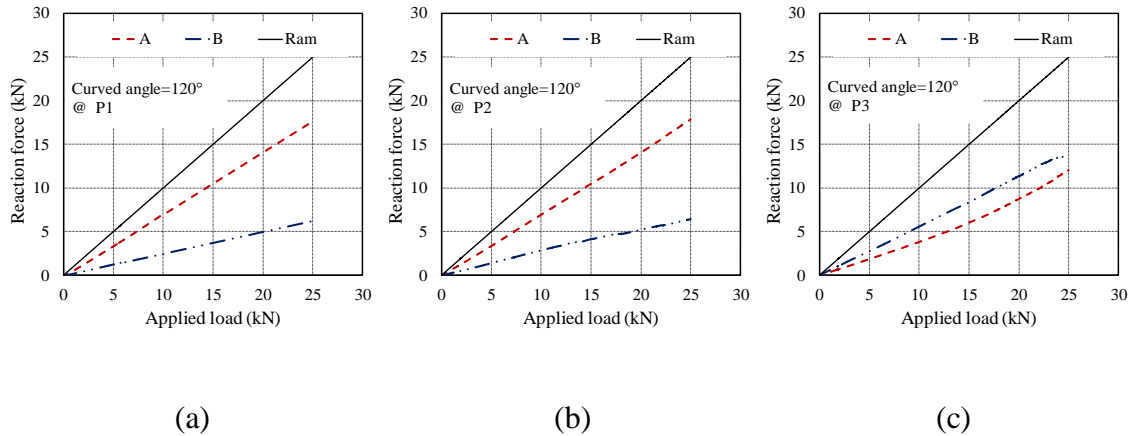
Figure 6.7. Reaction forces of beam B120 loaded at: a) P1; b) P2; c) P3

6.3.2 Deflection profile at linear elastic stage

The deflection profiles of all the UHPFRC beams loaded at 1/4, 3/8 or 1/2 span and with the applied load of 25 kN, are shown in Fig. 6.8 (a) to (d). As introduced in the previous section,

the applied load of 25 kN was selected to ensure all the slabs still under the linear elastic material condition under such a load. For each of the given loading positions, the comparisons among the companion deflection profiles of the UHPFRC beams in the figures show that the deflection of the UHPFRC beam generally decreases with increasing curvature. It can also be seen from the figures that, for each of the curved beams with the applied load at the mid-span (i.e. point P3), the maximum deflection appeared at the region near the mid-span of the beam which is same as that observed from the straight beam test. This is attributed to that, for a curved beam loaded at its mid-span, the maximum bending moment occurs at its mid-span and it predominates the vertical defection, whereas the torsional moment equals to zero. And for the cases of the beams loaded close to one of the supports (i.e. loaded at point P2 or P1), the gradually increasing torsional moment accompanying with the decreasing in bending moment led to a decrease in the magnitude of deflection.
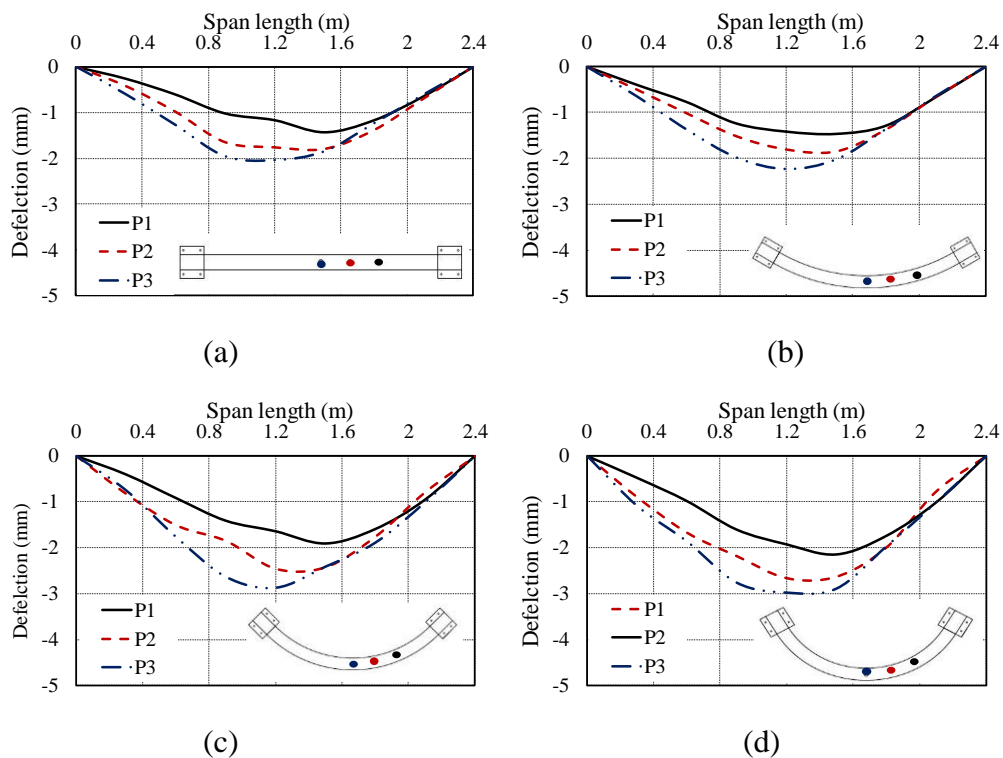
Figure 6.8. Deflection profiles of beams within elastic region: a) B0; b) B60; c) B90; d) B120

6.3.3 Profiles of rotation about the horizontal axis at linear elastic stage

The profiles of rotation about the horizontal axis of all the UHPFRC curved beams loaded at different positions (i.e. at the position of 1/4, 3/8 or 1/2 span from the support) and with the applied load of 25 kN are shown in Fig. 6.9 (a) to (c). It is evident from these figures that, for each of the UHPFRC curved beams subjected to the load of 25 kN, the smaller magnitude of rotation about the horizontal axis was measured at loading position close to the support. This is due to the decrease in the corresponding rotating arm that is defined as the distance between the loading position and the rotation axis. Note that for each test presented in this study, the rotation axis is along the line that connects the two fixed supports. Furthermore, it is also observed that an increase in the beam curvature resulted in an increase in the maximum rotation about the horizontal axis of the curved beam. This observation indicates that a larger torsion generated on a beam with a larger curvature.

(a)   (b)

(c)
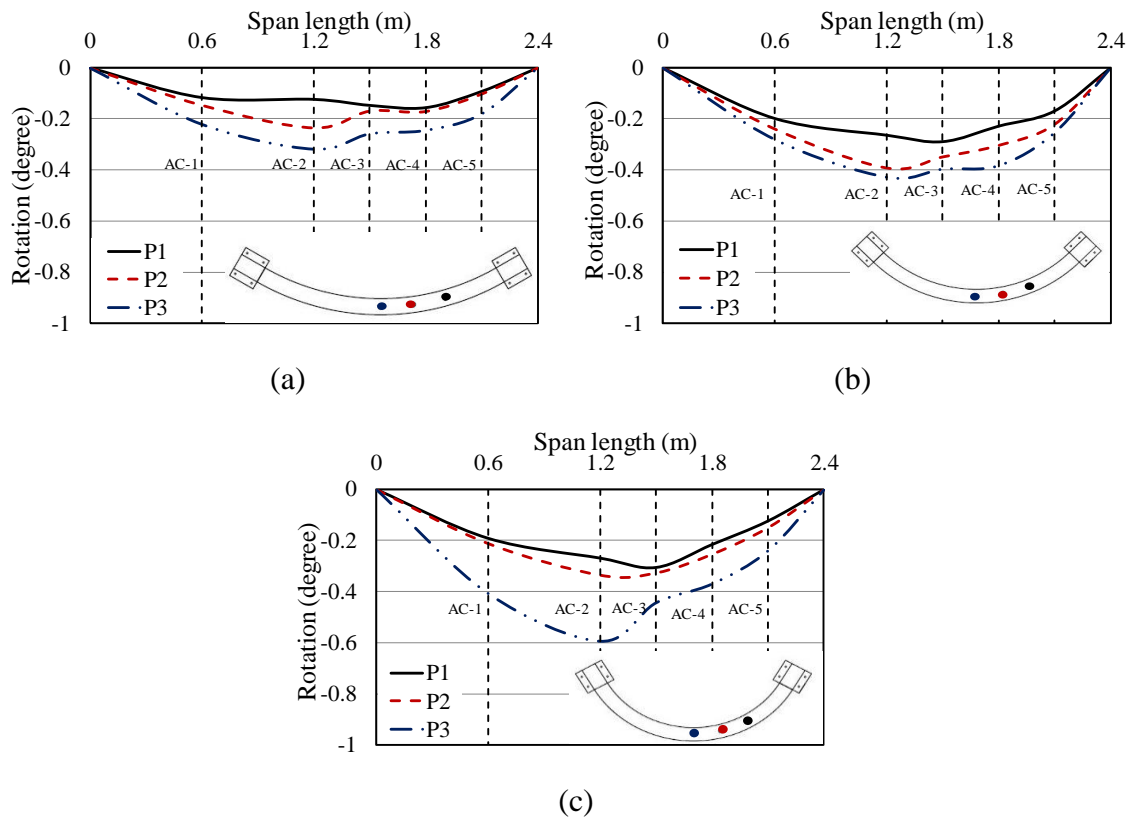
Figure 6.9. Rotation of curved beams within elastic region: a) B60; b) B90; c) B120

182

6.3.4 Failure mode of UHPFRC beams

In the third stage of the test the concentrated point load was applied at the mid-span (point P3 in Fig. 6.2) until it caused the failure of the beam. The straight beam (B0) failed in a classical flexural behaviour as evidenced by the crushing of UHPFRC accompanying with major flexural cracks in both maximum positive and negative moment regions as shown in Fig. 6.10 (a). The representative failure mode of curved beam beams (i.e. using the failure mode of B120) is shown in Fig. 6.10 (b) and all the curved beams were failed due to the rupture of the tensile steel reinforcements within the maximum positive regions under combined flexure and torsion. Note that the locations of the flexural cracks in curved beams were similar to those observed on the straight beam. However, the increased curvature of the beam led to decrease in both the width of the primary flexural cracks and the depth of the concrete softening wedges at the mid-span of the beams where the bending moment is maximum. It is worth highlighting that no concrete softening wedge was observed at the B120 at failure as shown in Fig. 6.10 (b). It is also observed that near the supports where the maximum torsional moment is exerted, a more pronounced twist of the cracked beam section occurred and diagonal torsional cracks developed. These observations suggest that the change in the curvature of a UHPFRC beam leads to the change in failure mechanism of the beam, as that with increasing curvature, the effect of flexure on the failure of a UHPFRC beam becomes less significant and accordingly the effect of torsion generated near the support is more pronounced.

(a)
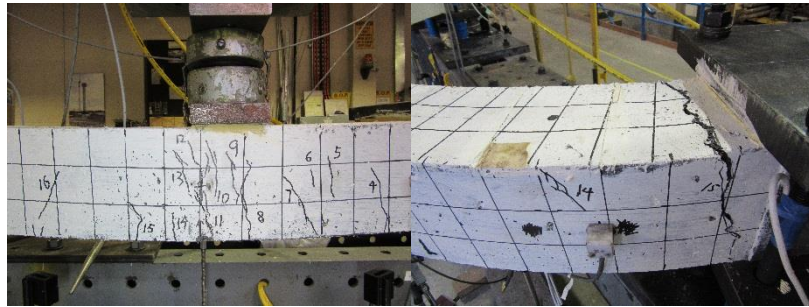
(b)

Figure. 6.10 Failure modes of test UHPFRC beams: a) straight beam (B0); b) curved beam (B120)

6.3.5 Load-displacement and load-torsional rotational relationships

Figure. 6.11 illustrates the experimentally recorded load-deflection relationship of all the UHPFRC beams loaded at their mid-span that were tested to failure. As can be seen from the figure, the load-deflection relationships of all the test beam exhibited a similar ascending branch with a slight reduction in their slopes with increasing curvature up to the peak point of their load-deflection curves. It is evident from the figure that the load carrying capacity of the UHPFRC beam reduced with an increase in the curvature. Over the peak load point, the beams showed gradual reduction in their load carrying capacities. Note that the curvature of the UHPFRC beam also had a pronounced effect on the post-peak load-deflection response of the beams, where the less gradual and shorter descending branch on their load-deflection curves with increasing curvature was observed. The complete load-torsional rotation relationships of the curved beams with the concentrated load applied at the mid-span are shown in Fig. 6.12. It

is evident from the figure that, at all stages of loading, the beam with a larger curvature exhibited a larger mid-span torsional rotation for a given magnitude of the load. Table 6.1 summarizes the salient features indicated on the load-deflection curves for each of the beams, the ductility factors are given in Table 6.1 and it is defined as the ratio of the ultimate to yield deflection (i.e. $\Delta_{ultimate}/\Delta_{yield}$) values which is a simple measure of energy absorption. It can be seen from the table, although there is a slight decrease in the ductility factor with increasing curvature of the beam, due to strain-hardening behaviour of UHPFRC under tension, all the UHPFRC curved beams exhibited a marked improvement in ductility compared to those of the high-strength RC beams with the similar cross-sections and reinforcement arrangements (i.e. normally within the range from 1.5 to 2.5) (Ashour 2000). For further comparisons, Table 6.2 reports the load and the corresponding deflection values of the curved beams at all critical points as a proportion of the corresponding test values of the straight beam. The calculated ratios provided in Table 6.2 shows that there is a gradual reduction in the load carrying capacity and ductility of a UHPRC beam with a larger curvature.
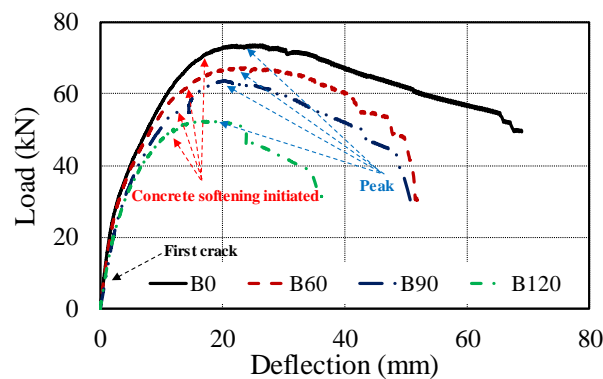
Figure 6.11. Completed load-deflection relationship of test beams
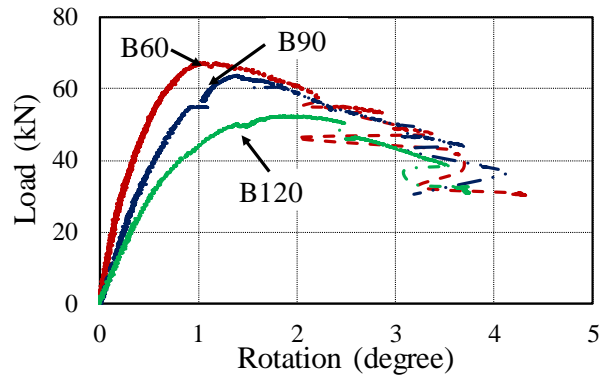
Figure 6.12. Completed load-rotation relationship of curved beams

Table 6.1. Summary of key points on load-deflection curve of the UHPFRC beams

Specimen	P_{yield}	Δ_{yield}	P_{peak}	Δ_{peak}	$P_{ultimate}$	$\Delta_{ultimate}$	$\Delta_{ultimate}/\Delta_{yield}$
B0	70.5	16.7	73.5	24.4	54.3	65.6	3.93
B60	62.7	14.8	67.2	23.1	47.3	53.6	3.62
B90	54.8	12.6	63.4	20.6	44.5	43.1	3.42
B120	49.3	11.3	52.2	18.7	34.7	38.2	3.38

Table 6.2. Comparison of the results between UHPFRC curved and straight beams

Specimen	$P_{yield}/P_{yield-B0}$	$\Delta_{yield}/\Delta_{yield-B0}$	$P_{peak}/P_{peak-B0}$	$\Delta_{peak}/\Delta_{peak-B0}$	$P_{ultimate}/P_{ultimate-B0}$	$\Delta_{ultimate}/\Delta_{ultimate-B0}$
B60/B0	0.89	0.89	0.91	0.95	0.87	0.82
B90/B0	0.78	0.75	0.86	0.84	0.82	0.66
B120/B0	0.70	0.68	0.71	0.77	0.64	0.58

6.4 ANALYTICAL MODEL

6.4.1 Development of closed-form mathematic solutions for a UHPFRC curved beam

In addition to the two commonly-known reactions (i.e. shear force and bending moment) seen at each support of a straight beam with both ends completely built-in, torques appeared at both the supports of a curved beam give a three redundancy problem. Considering that energy methods based on work-energy principles and the work-energy relations give enormous convenience for solutions of complex systems by reducing the difficulty in solving complex partial differential equations, in the present study, Castigliano's second theorem in

186

conjunctions with virtual work, unit-load methods are selected to provide the solutions for the UHPFRC curved beam system. In the modelling process, some assumptions are made based on the conventional elastic mechanics which are: 1) The structure exhibit linear stress-strain relationship to make the principle of superposition valid; 2) The cross-section of the beam is uniform and small compared with the radius of the structure. The sign convention and coordinate systems used for the derivation of the closed-form solutions are shown in Fig. 6.13. It is worth mentioning that two coordinate systems including a conventional Cartesian coordinate system (x-y-z) and a polar coordinate system $(R - \theta)$ are utilized.
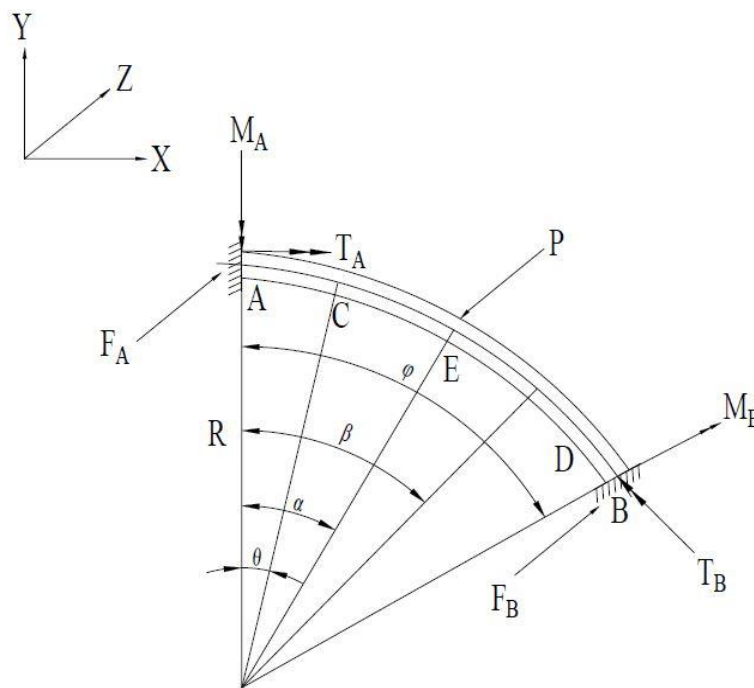
Figure 6.13. Sign convention and coordinate system

Based on the equilibrium of forces acting in the vertical direction (i.e. X-direction), the relationship among the two reaction forces (i.e. F_A and F_B) at the supports and the applied load, P is given by:

$$F_A + F_B = P \qquad (6.1)$$

and the internal shear force, V_θ along the beam is:

187

$$V_\theta = F_A \quad \text{for } 0 \le \theta \le \alpha \tag{6.2}$$

and

$$V_\theta = F_A - P \ \text{ for } \alpha < \theta \le \varphi \tag{6.3}$$

Taking moments or applying rotational equilibrium about X- and Y- axes, respectively, the bending moment, M_θ and torsional moment, T_θ along the beam can be expressed as:

$$M_\theta = M_A \cos\theta + T_A \sin\theta - F_A R \sin\theta \quad \text{for } 0 < \theta \le \alpha \tag{6.4}$$

$$T_\theta = -M_A \sin\theta + T_A \cos\theta + F_A R(1 - \cos\theta) \quad \text{for } 0 < \theta \le \alpha \tag{6.5}$$

and

$$M_\theta = M_A \cos\theta + T_A \sin\theta - F_A R \sin\theta + PR \sin(\theta - \alpha) \quad \text{for } \alpha < \theta \le \varphi \tag{6.6}$$

$$T_\theta = -M_A \sin\theta + T_A \cos\theta + F_A R(1 - \cos\theta) - PR(1 - \cos(\theta - \alpha)) \quad \text{for } \alpha < \theta \le \varphi \tag{6.7}$$

where M_A is the bending moment at support A, T_A is the torsional moment at support A, R is the radius of beam curvature, θ is the angle reflecting the any position along the beam in the $R - \theta$ coordinate system.

Using Castigliano's Second Theorem by neglecting the energy associated with axial and shear deformations, the strain-energy equation can be written as:

$$U = \int \frac{(M_\theta)^2}{2EI} R d\theta + \int \frac{(T_\theta)^2}{2GJ} R d\theta \tag{6.8}$$

where EI is the flexural stiffness and GJ is the torsion rigidity, respectively.

Using the boundary conditions $\omega_A = \psi_A = \Delta_A = 0$ at one of the supports of the curved beam (i.e. support A), where ω is the rotation caused by bending moment, ψ is the rotation caused by torsional moment, and Δ is the vertical deflection, the changes in strain energy due to these actions are:

$$\frac{\partial U}{\partial M_A} = \frac{\partial U}{\partial T_A} = \frac{\partial U}{\partial F_A} = 0 \tag{6.9}$$

By expending Eq. (6.9), the following Eq. (6.10) can be obtained.

$$\frac{1}{\mathrm{EI}} \int \frac{M_\theta M_\theta}{M_A} + \frac{1}{\mathrm{GJ}} \int \frac{T_\theta T_\theta}{M_A} = 0 \tag{6.10}$$

Note that for a rectangular cross section of the curved beam with the width of b and depth of h, torsional constant J is taken as $J = \frac{(h-0.63b)\,b^3}{3}$. And the bend-to-twist ratio is $m = \frac{\mathrm{EI}}{\mathrm{GJ}}$.

By substituting Eqs. (6.1) to (6.8) into Eq. (6.10), the following equations can be obtained:

$$\frac{R}{2\mathrm{EI}}[M_A(\varphi(m+1) - sin\varphi cos\varphi(m-1))] - \frac{R}{2\mathrm{EI}}T_A[\sin^2\varphi(m-1)] + \frac{R^2}{EI}F_A[\sin^2\varphi(m-$$
$$1) + 2m(\cos\varphi - 1)] = \frac{PR^2}{2\mathrm{EI}}[(m-1)cos\alpha(\sin^2\varphi - \sin^2\alpha) + \sin\alpha(\varphi - \alpha)(m+1) -$$
$$\sin\alpha\frac{(m-1)}{2}(sin2\varphi - sin2\alpha) + 2m(cos\varphi - cos\alpha)] \tag{6.11}$$

$$-\frac{R}{\mathrm{EI}}M_A\sin^2\varphi(m+1) + \frac{R}{2\mathrm{EI}}T_A[\varphi(m+1) + \sin\varphi cos\varphi(m-1)] + \frac{R^2}{EI}F_A[(2msin\varphi -$$
$$\varphi(m+1) - \sin\varphi cos\varphi(m-1)] = \frac{PR^2}{2\mathrm{EI}}[-\cos\alpha(\varphi - \alpha)(m+1) - \frac{1}{2}\cos\alpha(m-$$
$$1)(sin2\varphi - sin2\alpha) - (m-1)sin\alpha(\sin^2\varphi - \sin^2\alpha) + 2m(\sin\varphi - sin\alpha)] \tag{6.12}$$

$$\frac{R^2}{2\mathrm{EI}}M_A[\sin^2\varphi(m-1) + 2m(\cos\varphi - 1)] + \frac{R^2}{2\mathrm{EI}}T_A[2\sin\varphi - \varphi(m+1) - sin\varphi cos\varphi(m-$$
$$1)] + \frac{R^3}{2EI}F_A[\varphi(m+1) + sin\varphi cos\varphi(m-1) - 4msin\varphi + 2m\varphi] + \frac{PR^3}{2\mathrm{EI}}[\frac{(m-1)}{2}cos\alpha(sin2\varphi -$$
$$sin2\alpha) = \frac{PR^3}{2\mathrm{EI}}[\frac{(m-1)}{2}cos\alpha(sin2\varphi - sin2\alpha) + 2m(\cos\varphi + 1)(\sin\varphi - sin\alpha) +$$
$$2msin\alpha(cos\varphi - cos\alpha)] \tag{6.13}$$

where φ is the curvature of the beam, α is the angle defining the position of the applied load along the beam in $R - \theta$ coordinate system

The above equations (Eqs. (6.11) to (6.13)) can be further simplified using a set of three generic equations as follows:

$$\delta_{11}M_A - \delta_{12}T_A + \delta_{13}F_A R = \Delta_{1P}PR \tag{6.14}$$

$$-\delta_{12}M_A + \delta_{22}T_A + \delta_{23}F_A R = \Delta_{2P}PR \tag{6.15}$$

$$\delta_{13}M_A + \delta_{23}T_A + \delta_{33}F_A R = \Delta_{3P}PR \tag{6.16}$$

where the coefficients δ_{ij} are defined as follows:

$$\delta_{11} = \varphi(m+1) - sin\varphi cos\varphi(m-1)$$

$$\delta_{12} = \sin^2 \varphi(m-1)$$

$$\delta_{13} = \sin^2 \varphi(m-1) + 2m(\cos\varphi - 1)$$

$$\Delta_{1P} = (m-1)cos\alpha(\sin^2\varphi - \sin^2\alpha) + sin\alpha(\varphi - \alpha)(m+1)$$

$$- \sin\alpha \frac{(m-1)}{2}(sin2\varphi - sin2\alpha) + 2m(cos\varphi - cos\alpha)$$

$$\delta_{21} = \delta_{12} = \sin^2 \varphi(m-1)$$

$$\delta_{22} = \varphi(m+1) + \sin\varphi cos\varphi(m-1)$$

$$\delta_{23} = 2msin\varphi - \varphi(m+1) - \sin\varphi cos\varphi(m-1)$$

$$\Delta_{2P} = -\cos\alpha(\varphi - \alpha)(m+1) - \frac{1}{2}\cos\alpha(m-1)(sin2\varphi - sin2\alpha)$$

$$-(m-1)sin\alpha(\sin^2\varphi - \sin^2\alpha) + 2m(\sin\varphi - sin\alpha)$$

$$\delta_{31} = \delta_{13} = \sin^2 \varphi(m-1) + 2m(\cos\varphi - 1)$$

$$\delta_{32} = \delta_{23} = 2msin\varphi - \varphi(m+1) - \sin\varphi cos\varphi(m-1)$$

$$\delta_{33} = \varphi(m+1) + sin\varphi cos\varphi(m-1) - 4msin\varphi + 2m\varphi$$

$$\Delta_{3P} = \frac{(m-1)}{2}cos\alpha(sin2\varphi - sin2\alpha) + 2m(cos\,\varphi + 1)(sin\,\varphi - sin\alpha)$$

$$+2msin\alpha(cos\varphi - cos\alpha)$$

By solving simultaneously Eqs. (6.14) to (6.16), the three unknowns (i.e. M_A, T_A and F_A), can be obtained and it is as follows:

$$M_A = \frac{-\Delta_{1P}\delta_{22}\delta_{33}PR + \Delta_{1P}\delta_{23}{}^2PR + \delta_{12}\Delta_{3P}\delta_{23}PR - \Delta_{2P}\delta_{13}\delta_{23}PR + \delta_{22}\Delta_{3P}\delta_{13}PR - \Delta_{2P}\delta_{12}\delta_{33}PR}{-\delta_{11}\delta_{22}\delta_{33} + \delta_{11}\delta_{23}{}^2 + \delta_{12}{}^2\delta_{33} + 2\delta_{12}\delta_{13}\delta_{23} + \delta_{22}\delta_{13}{}^2} \quad (6.17)$$

$$T_A = -\frac{\delta_{11}\Delta_{2P}\delta_{33}PR + \Delta_{1P}\delta_{12}\delta_{33}PR + \Delta_{1P}\delta_{23}\delta_{13}PR - \delta_{11}\Delta_{3P}\delta_{23}PR - \Delta_{2P}\delta_{13}{}^2PR - \delta_{12}\Delta_{3P}\delta_{13}PR}{-\delta_{11}\delta_{22}\delta_{33} + \delta_{11}\delta_{23}{}^2 + \delta_{12}{}^2\delta_{33} + 2\delta_{12}\delta_{13}\delta_{23} + \delta_{22}\delta_{13}{}^2} \quad (6.18)$$

$$F_A = -\frac{-\Delta_{1P}\delta_{12}\delta_{23}P + \delta_{11}\delta_{22}\Delta_{3P}P - \Delta_{1P}\delta_{22}\delta_{13}P - \delta_{11}\Delta_{2P}\delta_{23}P + \delta_{12}{}^2\Delta_{3P}(-P) - \Delta_{2P}\delta_{12}\delta_{13}P}{-\delta_{11}\delta_{22}\delta_{33} + \delta_{11}\delta_{23}{}^2 + \delta_{12}{}^2\delta_{33} + 2\delta_{12}\delta_{13}\delta_{23} + \delta_{22}\delta_{13}{}^2} \quad (6.19)$$

Finally, the generic expressions of bending moment (M_θ), torsional moment (T_θ) and shear force (V_θ) at any point along the beam with an angle of θ from point A in Fig. 6.13 can be obtained by substituting Eqs. (6.17) to (6.18) into Eqs. (6.4) to (6.7).

To solve for the vertical deflection at any point along the beam with an angle of θ from point A, the unit load method is adopted using applied P=1 on the beam, which yields:

$$m_\theta = m_A cos\theta + t_A sin\theta - f_A Rsin\theta \qquad \text{for } 0 < \theta \leq \alpha \quad (6.20)$$

$$t_\theta = -m_A sin\theta + t_A cos\theta + f_A R(1 - cos\theta) \qquad \text{for } 0 < \theta \leq \alpha \quad (6.21)$$

and

$$m_\theta = m_A cos\theta + t_A sin\theta - f_A Rsin\theta + Rsin(\theta - \alpha) \qquad \text{for } \alpha < \theta \leq \varphi \quad (6.22)$$

$$t_\theta = -m_A sin\theta + t_A cos\theta + f_A R(1 - cos\theta) - R(1 - cos(\theta - \alpha)) \qquad \text{for } \alpha < \theta \leq \varphi \quad (6.23)$$

Note that the lowercase letters used for the symbols denoting the actions indicate that they are developed based on the unit applied load.

The vertical deflection at any point along the beam at any position with an angle distance of $\theta = \beta$ from point A and the applied load at $\theta = \alpha$ can be expressed as:

$$\Delta_\beta = \int_0^\beta (\frac{M_\theta m_\theta}{EI} + m\frac{T_\theta t_\theta}{EI})Rd\theta + \int_\beta^\alpha (\frac{M_\theta m_\theta}{EI} + m\frac{T_\theta t_\theta}{EI})Rd\theta + \int_\alpha^\varphi (\frac{M_\theta m_\theta}{EI} + m\frac{T_\theta t_\theta}{EI})Rd\theta \ \text{ for } \ \beta \leq \alpha \tag{6.24}$$

and

$$\Delta_\beta = \int_0^\alpha (\frac{M_\theta m_\theta}{EI} + m\frac{T_\theta t_\theta}{EI})Rd\theta + \int_\alpha^\beta (\frac{M_\theta m_\theta}{EI} + m\frac{T_\theta t_\theta}{EI})Rd\theta + \int_\beta^\varphi (\frac{M_\theta m_\theta}{EI} + m\frac{T_\theta t_\theta}{EI})Rd\theta \ \text{ for } \ \alpha \leq \beta \tag{25}$$

The vertical deflection $\Delta_{\frac{\varphi}{2}}$ when the applied load acted at the mid-span of the curved beam can be subsequently obtained by substituting $\theta = \frac{\varphi}{2}$ into Eqs. (6.24) and (6.25), which is:

$$\Delta_{\frac{\varphi}{2}} = \frac{R^2}{2EI}\left[\frac{M_A}{4}(1-\cos\varphi) + (T_A - F_A R)(\frac{\varphi}{4} - \frac{\sin\varphi}{4})\right] + \frac{R}{2EI}\left[M_A\left(\cos\frac{\varphi}{2} - 1\right) + \right.$$
$$(T_A - F_A R)\sin\frac{\varphi}{2} + F_A R\frac{\varphi}{2} - \cos\frac{\varphi}{2}\left(-\frac{M_A}{4}(1-\cos\varphi) + (T_A - F_A R)\frac{(\varphi - \sin\varphi)}{4} + F_A R\frac{\varphi}{2}\right) - $$
$$\left. \sin\frac{\varphi}{2}\left(-\frac{M_A}{4}(\varphi - \sin\varphi) + \frac{(T_A - F_A R)}{4}(1-\cos\varphi) - F_A R\left(\cos\frac{\varphi}{2} - 1\right)\right)\right] \tag{6.26}$$

6.4.2 Validation of the analytical model

Tables 3 and 4 summarise the experimental and analytical mid-span deflection values and reactions that were measured with the concentrated load applied at point P1 or P2. The statistical parameters shown in Tables 3 and 4 indicate that the results of the analytical procedure developed in this study exhibited good correlation with the test data, as the slight differences seen between the analytical and experimental results could be attributed to the difference in casting direction of specimens for material property tests and actual beam specimens, in which the cylinders used for testing of compressive strength and elastic modulus of the UHPFRC were cast vertically and due to more significant edge effects in these cylinders, which may result in a change in fibre orientation.

Table. 3 Comparison between experimental and analytical results of deflection for the beam loaded at P3

Beam	Exp (mm)	Mod (mm)	Mean	SD
B0	2.03	2.04	1.00	0.01
B60	2.23	2.15	0.97	0.05
B90	2.88	2.24	0.78	0.45
B120	2.89	2.36	0.82	0.37

Table. 4 Comparison between experimental and analytical results of reaction forces for the beam loaded at P1 or P2

Beam series	Support	Reaction force for P1 (kN)				Reaction force for P2 (kN)			
		Exp	Mod	Mean	SD	Exp	Mod	Mean	SD
B60	1	16.1	18.0	1.1	1.4	17.1	16.3	1.0	0.6
	2	7.9	7.0	0.9	0.7	8.1	8.7	1.1	0.5
B90	1	17.3	18.1	1.0	0.6	16.8	16.3	1.0	0.3
	2	7.8	6.9	0.9	0.7	8.5	8.7	1.0	0.1
B120	1	17.6	18.3	1.0	0.5	17.5	16.4	0.9	0.8
	2	6.4	6.7	1.1	0.2	6.2	8.6	1.4	1.7

6.4.3 Generations of influence lines using the analytical method

Having the generic expressions developed for the internal actions of UHPFRC curved beam successfully validated, these closed-form equations then used for calculating the values for bending moment, M_θ, torsional moment, T_θ and shear force, V_θ for the fixed-ends of UHPFRC beams which were subjected to a unit load (P) moving along the beams and with different curvatures, φ and different dimensionless flexural to torsional stiffness ratios *EI/GJ*. The calculated values for M_θ, T_θ and V_θ for each point along the span of the curved beams are used to generate the influence line diagrams as shown in Fig. 6.14. It is evident from this figure that the effect of loading position on the distribution of internal shear force along the curved beam is same as that along the straight beam owing to no effects of curvature on force equilibrium at Y-direction. The influence diagram for bending moment shown in Fig. 6.15 (a) and (b) indicate that the increase in curvature or increase in bend/twist ratio of the beam results in a decrease in the moment at the mid-span of the beam and an increase in the moment at its

two supports. The effect of loading position on the bending moment distribution along the fixed-ends supported curved beam is similar to that on the fixed-ends supported straight beam as shown in Fig. 6.15 (c), where the larger moment exerts at the support which is close to the loading point. Fig. 6.16 (a) and (b) shows the influence diagram for torsional moment. As can be seen from the figure, the increase in EI/GJ leads to a reduction in the magnitude of torsional moment at a given position along the curved beam, whereas the increase in EI/GJ results in a larger magnitude of torsional moment at each of the supports of the beam. The effect of curvature on torsional moment at one of the fixed supports (T_A) is illustrated in Fig. 6.16 (b), and it indicates that for a given EI/GJ ratio, T_A increases with increasing curvature of the beam.
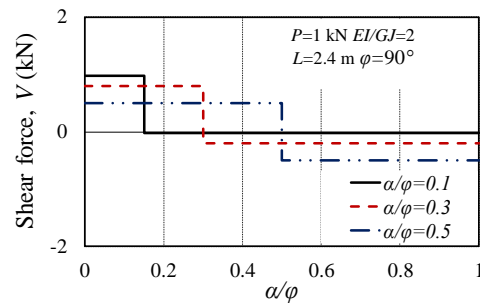
Figure 6.14. Influence diagram for shear force by varying the loading position

(a)

(b)
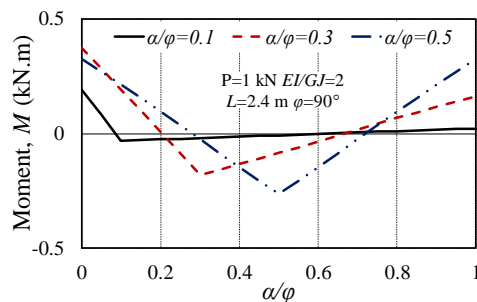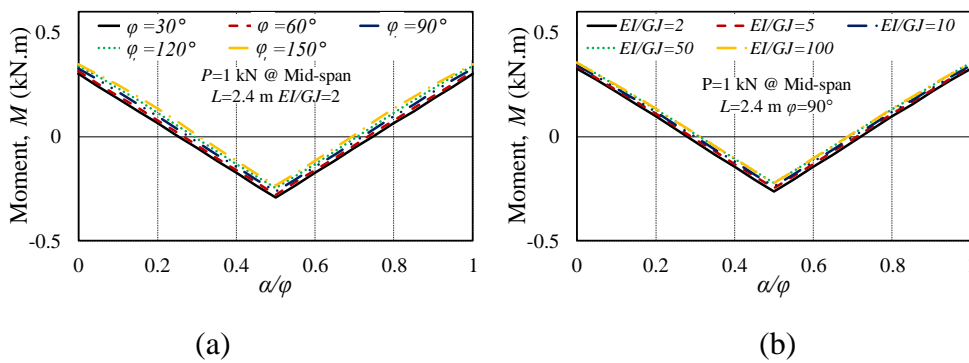
Figure 6.15. Influence diagram for bending moment by: a) curvature; b) varying the twist-to-bend ratio (EI/GJ); c) varying the loading position at the central line

(a)

(b)
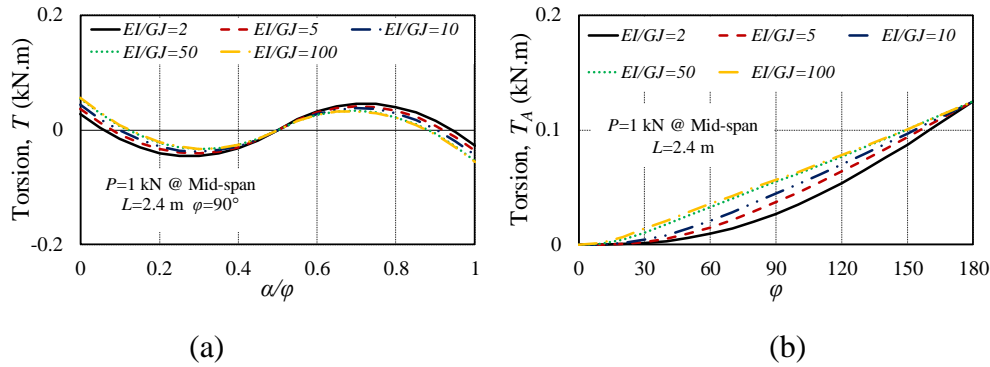
Figure 6.16. Influence diagram for torsional moment by: a) varying the twist-to-bend ratio (EI/GJ); b) by varying the curvature

6.5 CONCLUSIONS

This paper has presented the results of experimental and analytical investigations on the behaviour of horizontally curved UHPFRC beams under applied concentrated loads. From the present study, it was inferred that:

1. The change in the curvature of a UHPFRC beam leads to the change in failure mechanism of the beam, as that with increasing curvature, the effect of flexure on the failure of a UHPFRC beam becomes less significant and accordingly the effect of torsion generated near the support is more pronounced.

2. The curvature significantly affects deflection and rotation profiles of a UHPFRC beam under its linear elastic material condition, in which the increase in the curvature of the beam leads to an increasing maximum vertical deflection and a lager out of plan rotation.

3. Although the increase in the curvature of a centrally loaded UHPFRC beam results in slight reductions in flexural stiffness, ultimate load capacity and ductility of the beam, benefiting

from the strain-hardening behaviour of UHPFRC material under tension and its higher compressive strength, all UHPFRC curved beams exhibited superior load-carrying capacity and ductility over conventional high strength RC beams.

4. Closed-form analytical solutions were also derived for indeterminate, fixed-ends supported curved UHPFRC beams based on the energy methods and the predictions using the developed structural mechanics based closed-form equations correlates well with the test results of a UHPFRC curved beam.

5. Influence lines for bending moment, shear force and torsional moment are generated using the validated closed-form equations. This has been accomplished by showing that the effects of curvature, bend-to-twist ratio and loading position on the internal actions of UHPFRC curved beams.

6.6 REFERENCES

Al-Hashimy, M. A., and Eng, P. (2008). "Load distribution factors for curved concrete slab-on-steel I-girder bridges." *Ann Arbor*, 1050, 48106-41346.

Al-Hassaini, M. M. F. (1962). "Graphs and tables for the analysis and design of curved concrete beams."Doctoral dissertation, Virginia Polytechnic Institute and State University, USA.

Ashour, S. A. (2000). "Effect of compressive strength and tensile reinforcement ratio on flexural behavior of high-strength concrete beams." *Engineering structures*, 22(5), 413-423.

ASTM International (2005). "ASTM C39/C39M-05. tandard Test Method for Compressive Strength of Cylindrical Concrete Specimens." *ASTM International, West Conshohocken*.

ASTM International (2014). "ASTM C469/C469M-14. Standard Test Method for Static Modulus of Elasticity and Poisson's Ratio of Concrete in Compression." *ASTM International, West Conshohocken*.

Blais, P. Y., and Couture, M. (1999). "Precast, prestressed pedestrian bridge-world's first reactive powder concrete structure." *PCI journal*, 44, 60-71.

Chavel, B. W. (2008). "Construction and detailing methods of horizontally curved steel I-girder bridges." University of Pittsburgh.

Engineers Australia (2010). "Infrastructure Report Card." *Engineers Australia: Canberra, Australia*.

Fatemi, S., Ali, M. M., and Sheikh, A. (2016). "Load distribution for composite steel–concrete horizontally curved box girder bridge." *Journal of Constructional Steel Research*, 116, 19-28.

Fatemi, S., Sheikh, A., and Ali, M. M. (2015). "Development and application of an analytical model for horizontally curved bridge decks." *Advances in Structural Engineering*, 18(1), 107-117.

Foster, S. J. (2009). "The application of steel-fibres as concrete reinforcement in Australia: from material to structure." *Materials and Structures*, 42(9), 1209.

Gu, C., Ye, G., and Sun, W. (2015). "Ultrahigh performance concrete-properties, applications and perspectives." *Science China Technological Sciences*, 58(4), 587-599.

Hsu, T. T., Inan, M., and Fonticiella, L. "Behavior of reinforced concrete horizontally curved beams." *Proc., Journal Proceedings*, 112-123.

Infrastructure Australia (2015). "Australian Infrastructure Audit: Our Infrastructure Challenges. Infrastructure Australia, Sydney."

Ismail, N. W., and Mahyideen, J. M. (2015). "The Impact of infrastructure on trade and economic growth in selected economies in Asia."

Joe, C. D. (2016). "Cost and Ecological Feasibility of Using Ultra-High Performance Concrete in Highway Bridge Piers." University of Nevada, Reno.

Larsen, I. L., Aasbakken, I. G., O'Born, R., Vertes, K., and Thorstensen, R. T. "Determining the Environmental Benefits of Ultra High Performance Concrete as a Bridge Construction Material." *Proc., IOP Conference Series: Materials Science and Engineering*, IOP Publishing, 052096.

Lee, K., Davidson, J. S., Choi, J., and Kang, Y. (2017). "Ultimate strength of horizontally curved steel I-girders with equal end moments." *Engineering Structures*, 153, 17-31.

Lin, W., and Yoda, T. (2014). "Numerical study on horizontally curved steel-concrete composite beams subjected to hogging moment." *International Journal of Steel Structures*, 14(3), 557-569.

Mansur, M. A., and Rangan, B. V. "Study of design methods for reinforced concrete curved beams." *Proc., Journal Proceedings*, 226-254.

Mathiyazhagan, G., and Vasiraja, N. "Finite element analysis on curved beams of various sections." *Proc., Energy Efficient Technologies for Sustainability (ICEETS), 2013 International Conference on*, IEEE, 168-173.

McManus, P. F., Nasir, G. A., and Culver, C. G. (1969). "HORIZONTALLY CURVED GIRDERS-STATE OF ART." *Journal of the Structural Division*.

Noor, A. K., Greene, W. H., and Hartley, S. J. (1977). "Nonlinear finite element analysis of curved beams." *Computer Methods in Applied Mechanics and Engineering*, 12(3), 289-307.

Petrov, E., and Géradin, M. (1998). "Finite element theory for curved and twisted beams based on exact solutions for three-dimensional solids Part 2: Anisotropic and advanced beam models." *Computer methods in applied mechanics and engineering*, 165(1-4), 93-127.

Pojani, D., and Stead, D. (2017). *The urban transport crisis in emerging economies*, Springer.

Resplendino, J. "Ultra-high performance concretes—Recent realizations and research programs on UHPFRC bridges in France." *Proc., 2nd International Symposium on Ultra High Performance Concrete, Kassel*, 31-43.

Singh, M., Mohamed Ali, M., Sheikh, A., Griffith, M., and Visintin, P. (2016). "Behaviour of ultra high performance steel fibre concrete reinforced with polymer materials under compression and flexural loadings."

Singh, M., Sheikh, A., Ali, M. M., Visintin, P., and Griffith, M. (2017). "Experimental and numerical study of the flexural behaviour of ultra-high performance fibre reinforced concrete beams." *Construction and Building Materials*, 138, 12-25.

Sobuz, H., Visintin, P., Ali, M. M., Singh, M., Griffith, M., and Sheikh, A. (2016). "Manufacturing ultra-high performance concrete utilising conventional materials and production methods." *Construction and Building Materials*, 111, 251-261.

Sturm, A., Visintin, P., Oehlers, D., and Seracino, R. (2018). "Time-Dependent Tension-Stiffening Mechanics of Fiber-Reinforced and Ultra-High-Performance Fiber-Reinforced Concrete." *Journal of Structural Engineering*, 144(8), 04018122.

Sturm, A. B., Visintin, P., Ferris, K., and Oehlers, D. J. (2018). "A new testing approach for extracting the shear friction material properties of ultra-high performance fibre reinforced concrete." *ASCE Journal of Materials in Civil Engineering*.

Tanaka, Y., Maekawa, K., Kameyama, Y., Ohtake, A., Musha, H., and Watanabe, N. (2011). "The innovation and application of UHPFRC bridges in Japan." *Designing and Building with UHPFRC*, 149-188.

Visintin, P., Ali, M. M., Xie, T., and Sturm, A. B. (2018). "Experimental investigation of moment redistribution in ultra-high performance fibre reinforced concrete beams." *Construction and Building Materials*, 166, 433-444.

Worldbank (1994). "High-income, Low-income Middle-income, " Infrastructure: achievements, challenges, and opportunities"." *communications*, 9(26), 3.

Xie, T., Fang, C., Ali, M. M., and Visintin, P. (2018). "Characterizations of autogenous and drying shrinkage of ultra-high performance concrete (UHPC): An experimental study." *Cement and Concrete Composites*, 91, 156-173.

Xie, T., Mohamad Ali, M. S., Visintin, P., Oehlers, D. J., and Sheikh, A. H. (2018). "A Partial Interaction Model of Flexural Behaviour of PVA Fibre Reinforced Concrete Beams with GFRP Bars." *Journal of Composites for Construction*.

CHAPTER 7

Behaviour and Analysis of Ultra High Performance Fibre Reinforced Concrete (UHPFRC) Skew Slabs

[*1]Xie, T., [2]Mohamed Ali, M.S., [3]Visintin, P.

[1]**Mr. Tianyu Xie (Corresponding author)**

Ph. D Candidate

School of Civil, Environmental and Mining Engineering

The University of Adelaide

South Australia 5005

AUSTRALIA

[2]**Dr. M.S. Mohamed Ali**

Senior Lecturer,

 School of Civil, Environmental and Mining Engineering

The University of Adelaide

 South Australia 5005

AUSTRALIA

[3]**Dr. Phillip Visintin**

Associate Professor,

School of Civil, Environmental and Mining Engineering

The University of Adelaide

 South Australia 5005

Statement of Authorship

Title of Paper	BEHAVIOUR AND ANALYSIS OF ULTRA HIGH PERFORMANCE FIBRE REINFORCED CONCRETE (UHPFRC) SKEW SLABS
Publication Status	☐ Published ☐ Accepted for Publication ☑ Submitted for Publication ☐ Unpublished and Unsubmitted work written in manuscript style
Publication Details	Xie, T., Ali, M. M., & Visintin, P. (2018). Behaviour and Analysis of Ultra High Performance Fibre Reinforced Concrete (UHPFRC) Skew Slabs. Submitted to *Engineering Structures* (Completed first round of review with a moderate revision required)

Principal Author

Name of Principal Author (Candidate)	Tianyu Xie
Contribution to the Paper	Designing concept, conducting experiments, analysing of data, drafting manuscript
Overall percentage (%)	40
Certification:	This paper reports on original research I conducted during the period of my Higher Degree by Research candidature and is not subject to any obligations or contractual agreements with a third party that would constrain its inclusion in this thesis. I am the primary author of this paper.
Signature	Date 12/02/2019

Co-Author Contributions

By signing the Statement of Authorship, each author certifies that:

  i. the candidate's stated contribution to the publication is accurate (as detailed above);
  ii. permission is granted for the candidate in include the publication in the thesis; and
  iii. the sum of all co-author contributions is equal to 100% less the candidate's stated contribution.

iv. Name of Co-Author	Dr Mohamed Ali Sadakkathulla
Contribution to the Paper	Designing concept, supervising experiments, revising manuscript (30%)
Signature	Date 12/02/2019

Name of Co-Author	Associate Professor Phillip Visintin
Contribution to the Paper	Designing concept, analysing of data, revising manuscript (30%)
Signature	Date 12/02/2019

THIS PAGE HAS BEEN LEFT INTENTIONALLY BLANK

ABSTRACT

This study presents a systematically experimental and theoretical investigations on the performance of Ultra-high performance fibre reinforced concrete (UHPFRC) skew bridge decks. Five simply-supported UHPFRC slabs with different skew angles were tested under monotonically increasing concentrated load at their serviceability- and ultimate- limit states. It is observed that the increase in the skewness of the slab led to a more unsymmetrical vertical deflection profile and also resulted in a decrease in the magnitude of reaction forces at the acute corners and a corresponding increase in the reaction forces at the obtuse corners. The test results also show that, although a reduction in ductility is seen with increasing skewness of a slab, a slab prepared using UHPFRC still maintains desirable load carrying capacity and ductility. In addition to the experimental investigation, a fundamental mechanics based closed form model is developed based on strain energy theorem to predict the performance of a UHPFRC skew slab under linear elastic material condition. At its ultimate limit, a novel yield-line analysis using a numerically-generated mechanics based moment-rotation relationship is adopted to predict the ultimate load carrying capacity of a skew UHPFRC slab. Both the generic analytical procedures are compared and against the test results in the present study and that reported in the literature showing that these models can be used with confidence to analyse UHPFRC skew slabs.

Keywords: Ultra-high performance fibre reinforced concrete; skew slab; closed-form equations; novel yield-line analysis; generic methods.

7.1 INTRODUCTION

Transport infrastructure is critical to the productivity of cities and it provides connectivity between businesses, ideas, goods and services. Nowadays, with social developing and advance of human civilization, it has led to a great demand for performance-based design of infrastructures. Owing to the limitations of space constraints in urban areas including those from natural obstructions and manmade obstacles, it is often necessary to design structural elements with non-orthogonal reinforcements when the geometry of the structures cannot accommodate straight shape. A skew slab is an essential type of non-orthogonal structural element which has been widely utilized as bridge decks and building floor systems.

When the skew angle is small (i.e. < 20º), a skew slab performs similar to a straight slab in terms of the moment distribution, support reaction and shear force (Dhar et al. 2013; Menassa et al. 2007), in which the distribution of shear and moment in the skew slab with a smaller skew angle can be easily defined from simple mechanics. However, the analysis of a skew slab with a large inclined angle (i.e.>20º) is less-understood and scarcely researched due to the complications in the variations of stress in the slab and reactions on supports (i.e. abutments and piers for a skew bridge deck) (Gupta and Misra 2007; Nouri and Ahmadi 2011; Wei and Bruneau 2017). The findings of existing studies on skew plate elements reveal the decreases in longitudinal moment and vertical deflection of a slab with a larger skew angle offsetting by the increasing transverse-moment (Kar et al. 2012; Maleki 2002; Théoret et al. 2011). The majority of existing codes and design guidelines for skew slabs adopt the approach for straight slabs as the baseline with introducing reduction factors for each of the actions. However, due the empirical nature of the code approaches, none of them can fully characterize the underlying mechanisms of the actions in a skew slab and hence only provide conservative design for the structure with non-orthogonal reinforcements. AASHTO-2007 (AASHTO 2007) suggests to use a reduction factor for longitudinal bending moments for designing a skew slab with no

magnification factor applied for shear. Canadian Standards Association, CSA-16 (CSA 2014) imposes a limit for using an equivalent-beam method to design skewed bridge decks, but no feasible design approach is given beyond the limit. Moreover, most of the theoretical work on skews bridge decks have used finite element analysis (FEA) (Dhar et al. 2013; Harba 2011; Menassa et al. 2007) or grillage analogy method (Bakht 1988; Maleki 2002; Pandey and Maru 2015; Théoret et al. 2011) which are rather complicated and do not provide mathematical expressions to directly contribute to the codes and guidelines for designing skew slabs. Therefore, for the adequate design of structures under the conditions of various topography, it is necessary to clearly understand the effect of skew angle on the behaviour of plate elements such as bridge decks and building floor systems and also to characterize the underlying mechanisms.

Ultra-high performance fibre reinforced concrete (UHPFRC) is characterized by its superior mechanical strength material ductility, enhanced durability, and a non-negligible tensile strength (Kang et al. 2010; Kodur et al. 2018; Xie et al. 2018) which are typically achieved by using concrete mixtures with high quantities of cementitious binders (i.e. cement and silica fume), low water to binder ratios (i.e. < 0.2) and incorporation of discrete steel fibres. The presence of the internal fibres in UHPFRC not only prevent wider cracks (Xie et al. 2018; Xie and Ozbakkaloglu 2015) but also effectively act as the reinforcements to resist shear and torsion seen on the structures with skewed and curved alignments (Kodur et al. 2018; Sturm et al. 2018); and the denser matrix of UHPFRC creates a feasible solution for the problem associated with concrete deterioration caused by inner steel reinforcement corrosion. These characteristics make the material become promising to be used for constructing structural elements such as beams (Mahmud et al. 2013; Yoo and Yoon 2015), columns (Fan et al. 2018; Heinz et al. 2004; Xu et al. 2017), frames (Yeganeh 2015), and slabs (Li et al. 2015; Yoo et al.

2014), allowing for longer spans, reduced member sizes and increased design lives. The recent feasibility studies (Joe 2016; Larsen et al. 2017; Voo and Foster 2010; Woodworth 2008) have also shown that the replacement of conventional concrete and steel transport infrastructure with ultra-high performance fibre reinforced concrete (UHPFRC) has the potential to revolutionise the sector. The outcomes ((Singh et al. 2017; Sobuz et al. 2016; Visintin et al. 2018; Xie et al. 2018)) of a current project in the University of Adelaide on developing ultra-high performance fibre reinforced concrete using only conventional concrete manufacturing materials, casting and curing methods further smooth the way of utilizing the low-cost UHPFRC in any cast in-situ scenarios. Benefiting from the above-mentioned advantages of UHPFRC (in particular its higher shear/torsion resistance and strain hardening characterization under tension), using the material to construct a skew slab not only minimize the reductions in loading carrying capacity and ductility due to the skewness of the structure but also could achieve an improved performance of the UHPFRC skew slab over a conventional RC concrete straight slab for short- and long- term. To date, limit investigations have been found on the behaviour of UHPFRC skew slabs.

To address the research gaps identified thorough the above literature, in this research work, experimental and analytical investigations are undertaken to:

1). experimentally study the behaviour of simply-supported UHPFRC slabs with different skew angles at both the serviceability- and ultimate- limit states.

2). derive a closed-form solution based on the fundamental mechanics for quantifying the elastic behaviour of skew decks and to model the structural response of a skew slab at their serviceability- limit states. The advantage of this closed-form solution is that it is less

demanding on computational effort and therefore may have greater potential to be incorporated into practical design guidelines.

3). carry out a novel yield-line analysis for determining the ultimate load carrying capacity of slabs with different skewness at their ultimate limit states, where the peak moment of each yield-line section in this analysis is generated using a generic partial-interaction segmental analytical approach (Visintin et al. 2012).

To achieve these objectives, five UHPFRC slabs with a skew angle of 0, 15, 25, 35 or 45 degree are tested under monotonically increasing concentrated load applied at the selected in-plane positions. Deflection profiles and reactions at the supports of each slab are experimentally recorded. The experimental results are then used to validate the predictions using the closed-form equation and the novel yield-line method. It is expected that the outcomes of this work will:

1). present the results of original experimental work on UHPFRC skew slabs, which have been rarely reported in the literature, and initiate the research on UHPFRC skew slabs; and

2). yield information about the effect of skew angle on structural response of simply-supported UHPFRC skew slabs at both the serviceability- and ultimate- limit states; and

3). establish generic approaches with strong physical significances for analysing the behaviour of UHPFRC skew slabs and also conventional RC skew slabs at both the serviceability- and ultimate- limit states; and

4). assist in developing design guideline for UHPFRC skew slabs to avoid conducting multiple large-scale tests due to the generic nature of the analytical work including both the closed-form solutions and the yield-line analysis incorporating the displacement based segmental analytical approach.

7.2 TEST PROGRAM

7.2.1 Materials

7.2.1.1 UHPFRC

All the skew slabs and their companion specimens for evaluating mechanical properties were manufactured using a UHPFRC mix successfully developed at the University of Adelaide as a part of a project to develop UHPFRC produced using only conventional concrete mixing ingredients and equipment, and casted and cured under standard conditions (Sobuz et al. 2016). The steel fibres were added to the mix at a volume fraction of 2.25%. This ratio was the optimal fibre volume fraction as found by the authors in their previous investigations related to UHPFRC mixes (Singh et al. 2017; Visintin et al. 2018). The mix proportion of the UHPFRC is given in Table 7.1. Due to the small scale of the skew slabs, copper coated straight steel fibres with 13 mm nominal length and 0.2 mm nominal diameter was selected for the UHPFRC mix to ensure the homogenous dispersion of the fibres in the concrete. The manufacturer-reported elastic modulus and ultimate tensile strength of the steel fibre are 210 GPa and 2850 MPa, respectively.

Table. 7.1 Mix proportion of UHPFRC

	Sulfate Resistant Cement (kg/m^3)	Silica fume (kg/m^3)	Sand (kg/m^3)	Water (kg/m^3)	SP[*] (kg/m^3)	Fibre[**] (kg/m^3)
UHPFRC	834.6	222.0	1056.6	126.5	64.1	246.2

[*]. Containing 70% water

**. At 2.25% volume fraction

In preparation of the UHPFRC, two types of binder materials were utilized, namely, sulphate resisting cement and silica fume both sourced from Adelaide Brighton Cement Ltd. The physical and mechanical properties of these two binder materials can be found in references (Sobuz et al. 2016; Xie et al. 2018). The only aggregate used for the UHPFRC mixes are a type of natural river sand with a nominal particle size of 4 mm. To attain the favourable flow of the concrete, a third generation superplasticizer, namely Sika viscocrete 10, was added to each UHPFRC during mixing. For producing UHPFRCs, all the dry materials (i.e. sand and binders) were initially mixed in a rotating pan mixer with 80 L capacity for approximately 5 minutes. Subsequently, the liquid components, including water and superplasticizer, were gradually poured to the mixer and the mixing was continued until the UHPC mortar exhibited desired flow. Finally, the discrete steel fibres were added and mixed for a further ten minutes to form the UHPFRC.

7.2.1.2 Welded steel wire mesh

Welded steel wire mesh of 4 mm diameter and with both the horizontal and vertical spacing of 50 mm were used as the reinforcement in the slabs. The stress-strain relationship of the steel is shown in Fig. 7.1 and Fig. 7.2 (a) to (e) illustrates the exact steel mesh arrangement for each slab specimen.
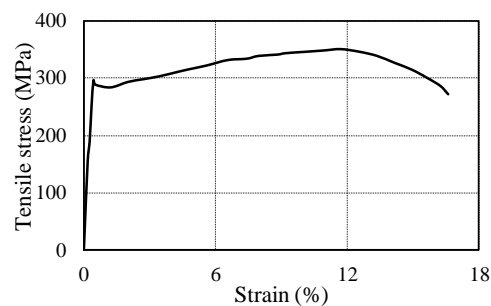
Figure 7.1. Stress-strain relationship of steel mesh

(a)

(b)

(c)

(d)

(e)
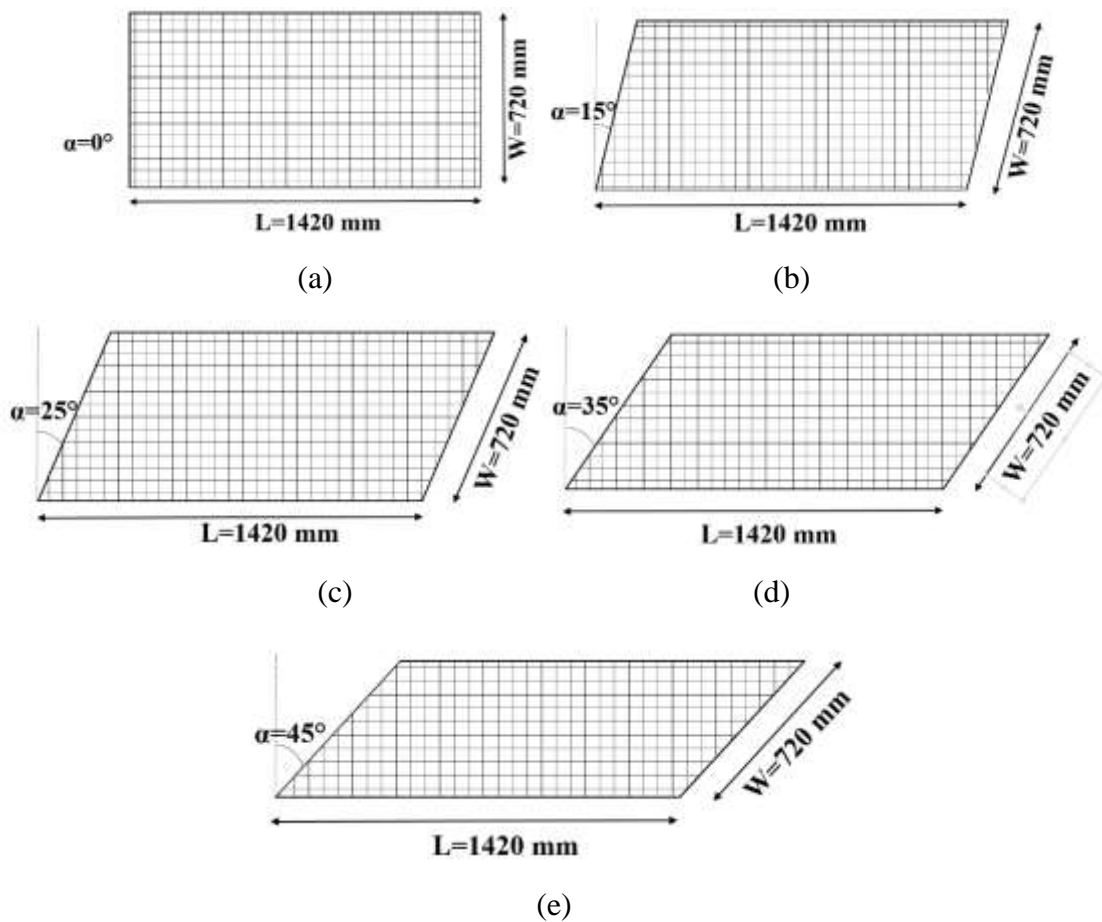
Figure 7.2. Slab geometries and steel mesh arrangement

7.2.2 Test specimens, set up, instrumentation and test procedure

7.2.2.1 Slab test

Five simply-supported slabs with a skew angle of 0, 15, 25, 35 or 45 degrees and with the thickness of 60 mm, the free edge of 1420 mm and the supported edge of 720 mm were manufactured and tested under monotonically increasing concentrated load. To establish the deflection profiles of each slab test, a total of 17 LVDTs were used, including 16 used to record the vertical deflection at different locations and another one mounted on the loading ram to measure the vertical displacement of the loading ram. A load cell was placed under all four corners of the slabs to measure the vertical reaction forces. For testing the slabs, their responses

210

within the linear elastic region (i.e. to study their performances in serviceability region) are of interest and to investigate this, each of the slabs was first loaded with the load applied up to 20 kN at a loading rate of 5 kN/min. This upper load limit of 20 kN was adopted for linear elastic tests in order to avoid the yielding of the embedded steel mesh that was found based on lower bound of prediction preliminarily using the PI-based yield line analysis for the most extreme case (i.e. concentratedly loaded S45), in which the yielding of the reinforcements in this slab initiated at the load of 28.7 kN. The tests of each of the slabs were repeated five times by shifting the loading points to five different in-plane points. Fig. 7.3 (a) to (c) illustrates the test set up, LVDT arrangements and the five selected loading points for the slab tests. Finally, the slabs were tested to failure completely by applying the concentrated load at the centre of the slabs (i.e. point E as illustrated in Fig. 7.3 (b)); in this case, the load was continuously applied at a rate of 5 kN/min until the peak load was attained and thereafter the load was applied under displacement control at a displacement rate of 0.1 mm/min until failure to obtain the complete load-deflection relationship. Note that the vertical deflection of each of the concentratedly loaded slabs can be directly measured by the LVDT attached to the loading ram. For the load applied at points A, B, C, and D, the maximum bending moment of the slab occurred at the same positions of the loading and hence the deflection occurred at the same positions. Therefore, the LVDT mounted to the loading ram was used directly to record the vertical deflection.

(a)

| (b) | (c) |
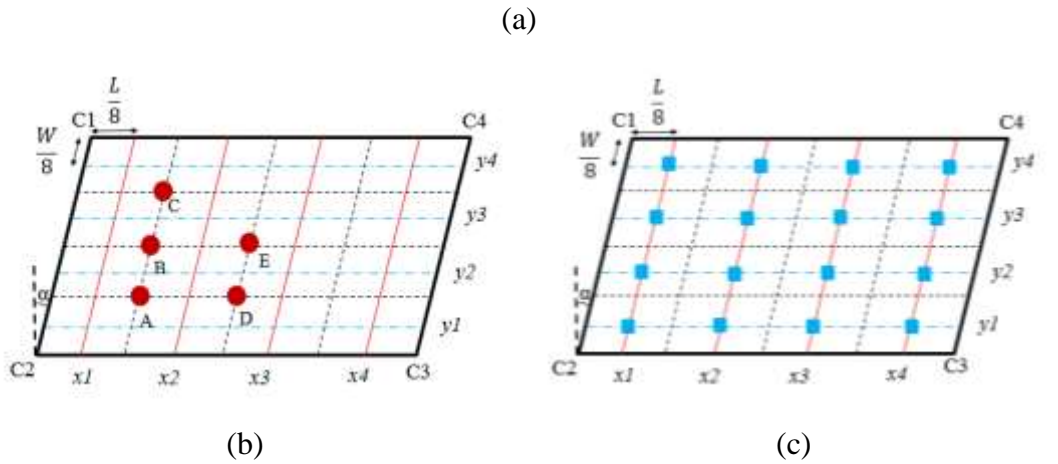
Figure 7.3. Slab test set up: a) set up; b) loading positions; c) LVDTs locations

7.2.2.2 Material tests for UHPFRC

The axial compressive strength (f'_c), elastic modulus (E_c) and Poisson's ratio (v) of the concrete were established according to the test methods prescribed by ASTM standard C39/C39M-05 (ASTM International 2005) and ASTM standard C469/C469m-14 (ASTM International 2014) using the cylindrical specimens. The cylindrical specimens used in the compression tests were 100 mm in diameter and 200mm in height. The compressive strength tests were conducted using the 3000 kN capacity universal testing machine with the loading rate of 0.3 MPa per second, as per the ASTM standard. Total deformation of the cylinder was measured with two LVDTs mounted on opposite faces of the specimen.

The characterizations of UHPFRC under direct tension, including the stress-strain relationship prior to cracking, and the post-cracking stress- crack-width behaviour were determined using dog-bone shaped specimens shown schematically in Fig. 7.4. The details of designing dog-bone specimens and test set-up and scenario can be found in Singh et al. (Singh et al. 2017). The splitting tensile strength (f_{st}) and the modulus of rupture (f_r) of the UHPFRC material reported in Table 7.2 were established as per the test methods and specimen specifications reported in ASTM C496-04 (ASTM International 2004) and ASTM C78-18 (International

2018) respectively. Fig. 7.5 shows the typical failure modes of the UHPFRC specimens for

indirect tensile and flexural tests.

Table 7.2. Material properties of UHPFRC

Compressive strength (MPa)	Elastic modulus (GPa)	Direct tensile strength (MPa)	Splitting tensile strength (MPa)	Modulus of rupture (MPa)
162.1	42.3	6.3	12.1	17.8

(a)   (b)
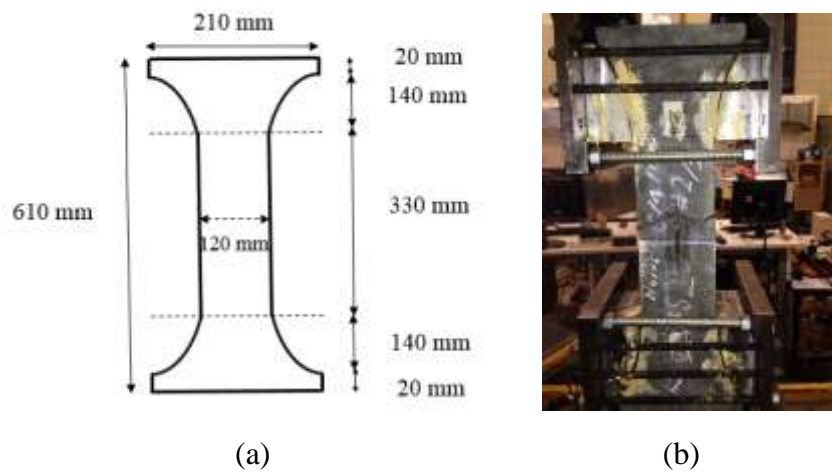
Figure 7.4. Dogbone shaped specimen for direct tension test: a) specimen details; b) test setup

(a)   (b)
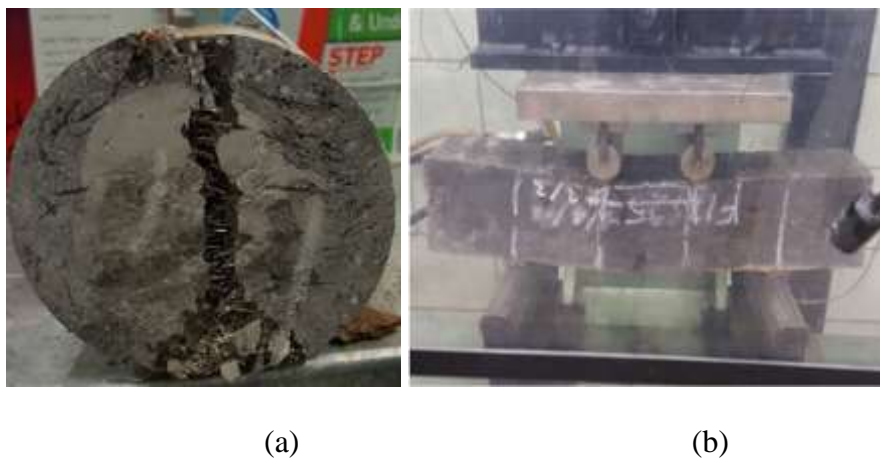
Figure 7.5. Test specimens for tensile properties of UHPFRC: a) indirect tensile test; b) flexural

test

Fig. 7.6 (a) shows the experimentally obtained axial compressive stress-strain relationship of the UHPFRC. Fig. 7.6 (b) shows the direct tensile characterizations of the UHPFRC, including its stress-strain relationship prior the cracking and the stress-crack width relationship at the post-cracking stage of the concrete.

(a)

(b)
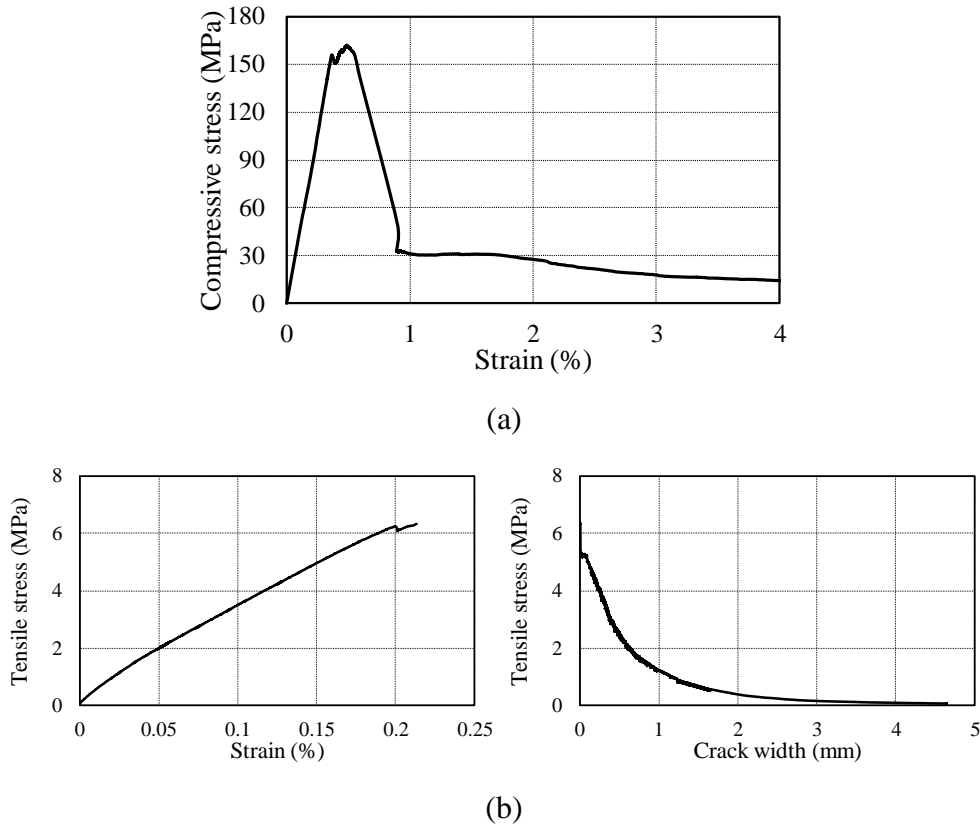
Figure 7.6. Materials properties: a) compressive stress-strain relationship of UHPFRC; (b) direct tensile characterizations of UHPFRC under direct tension.

7.3 EXPERIMENTAL RESULTS AND DISCUSSION

7.3.1 Deflection profile for slab at the linear elastic stage

The effect of skew angle on the deflection profiles for the elastic tests of the skew slabs at point A, C and E are shown in Figs. 7.7 to 7.9 and the deflection profiles of each slab loaded separately at these three points were compared as that these points of applications of load correspond to the following cases: 1) close to an acute corner (at point A); 2) close to an obtuse corner (at point C) and 3) at the centre of the slab (at point E). For the cases of the load applied

at points A and C, it is evident from Figs. 7.7 and 7.8 that even for the straight slab, the deflection profiles were unsymmetrical due to the out-plane moment induced by the load eccentricity and the vertical deflection at any of the in-plane points of the five slabs decreased with an increase in the distance between the point and the loading position. As can also be seen from Figs. 7.7 and 7.8, the difference in the deflections among all companion reference points increased with increasing skew angle of the slab. Specifically, with an increase in the skewness of the slab, for both of the loading cases (i.e. at points A and C), the vertical deflections measured adjacent to the acute corners (i.e. points $(x1, y1)$ and $(x4, y4)$) increased, on the contrary, the vertical deflections measured adjacent to the obtuse corners (i.e. points $(x1, y1)$ and $(x4, y4)$ decreased.

For the concentratedly-loaded test cases (i.e. load applied at point E), it can be seen from Fig. 7.9 that the degree of non-symmetricity of the deflection profile increased with increasing skew angle. Regardless of the change in the skewness of the slabs, as can be seen from the figure, the maximum deflection of each concentratedly-loaded slab is still located at the centre of the slab where the maximum bending moment occurred. Similar to those seen in the tests of the slabs loaded at the points A and C, an increase in skewness of the slab also led to significant increases in the deflections at locations adjacent to the obtuse corners of the slabs (i.e. points $(x1, y4)$ and $(x4, y1)$), whereas the deflections measured at the locations adjacent to the acute corners of the slabs (i.e. points $(x1, y1)$ and $(x4,y4)$) decreased with increasing skew angle. This can be attributed to the facts that the increase in the out-plane moment (anti-clockwise twist along each supporting edge) with increasing skewness of the slab, the region near each of the obtuse corners further were pushed down whereas the region close to the acute corners were lifted up (Maleki 2002; Menassa et al. 2007). This in turn causes the more severe unsymmetrical deflection profiles of the slab with a lager skewness. The above observations

also indicate that the deflection caused by bending moment predominates the vertical deflection profile of a skew slab, whereas the torsional moment caused only a slight change in the vertical deflection profile. It is also worth mentioning that for all loading cases, the slabs with the skew angle smaller than 25° exhibited comparable deflection profiles to that of their straight slab counterpart. The above observations on the deflection profiles of skew slabs agree well with those reported from previous studies on conventional RC skew slabs (Dhar et al. 2013; Kar et al. 2012; Sindhu et al. 2013)
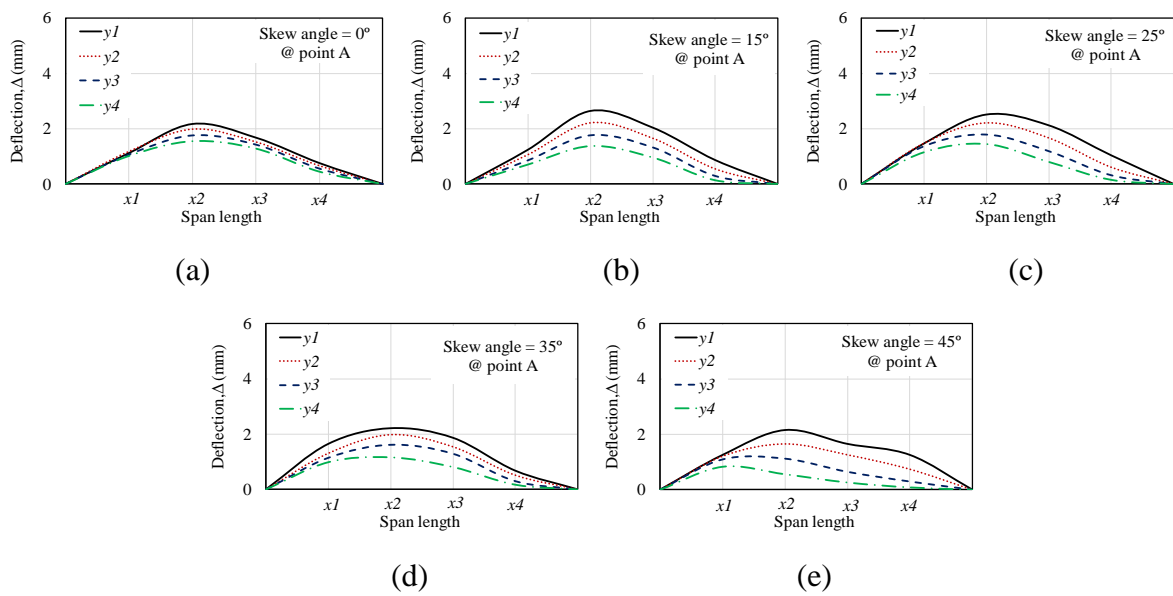
Figure 7.7. Deflection profiles of the skew slabs loaded at point A: a) S0; b) S15; c) S25; c) S35; d) S45

Figure 7.8. Deflection profiles of the skew slabs loaded at point C: a) S0; b) S15; c) S25; c) S35; d) S45

(a)

(b)

(c)

(d)

(e)
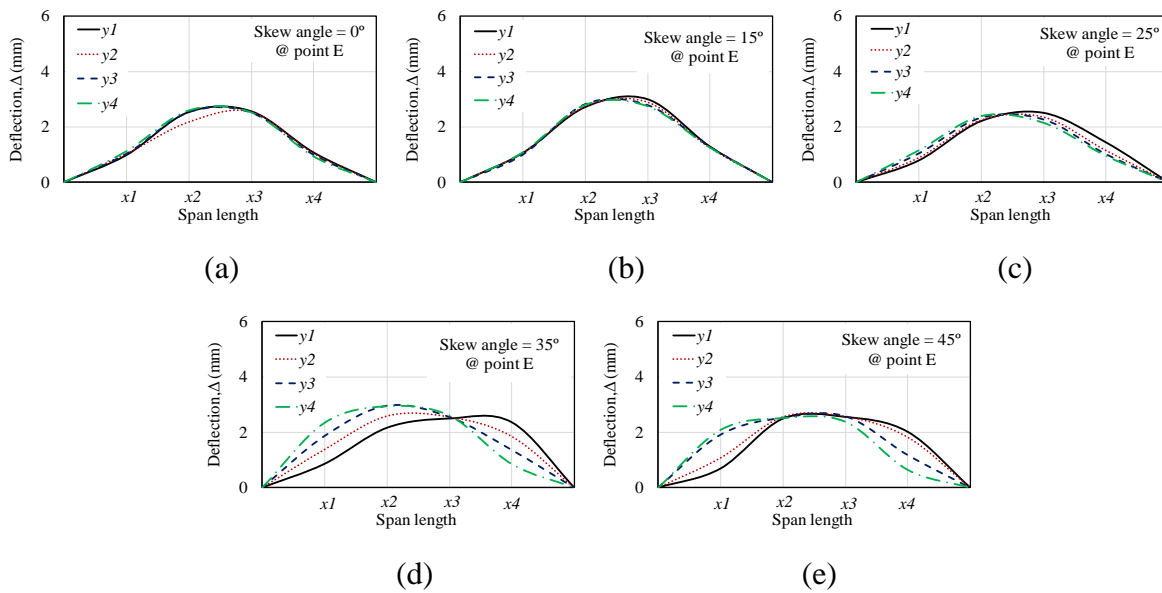
Figure 7.9. Deflection profiles of the skew slabs loaded at point E: a) S0; b) S15; c) S25; c) S35; d) S45

7.3.2 Reaction force at the linear elastic region

The reaction forces at the four corners of each slab within the elastic region were experimentally-recorded using load cells. Figures. 7.10 to 7.12 show the relationship between the load applied and the corner reaction forces measured, and it also displays the sum of the four corner reaction forces for the cases of loads applied at point A, C and E. It can be seen from the figures that the sum of the four corner reaction forces is equal to the applied load and this indicates the load cells used in the present study can provide valid and reliable measurements of the corner reaction forces. It can be seen from Figs. 7.10 and 7.11 that, for the cases of the slabs loaded at points A and C, due to the torsional moment induced by the load eccentricity, the reaction forces measured at four corners were all different for each slab and the larger reaction forces were measured at the corners close to the load. The differences among the reaction force measured at each corner changed with the change in the skewness of the slab, where an increase in the skew angle of the slab led to decreases in the reaction forces

217

measured at the acute corners (i.e. corners 2 and 4) and increases in the reaction forces measured at the obtuse corners (i.e. corners 1 and 3). As discussed in Section 3.1, this is also due to increased torsional moment generated in the plane of the slabs as the consequence of the increased skew angle which pushed the obtuse corners down (i.e. resulted in an increase in the reaction force) and lifted the acute corners up (i.e. resulted in a reduction in the reaction force). For the cases of the slabs loaded at its centre (i.e. at point E), it can be seen from Fig. 7.12 that the reaction forces measured at diagonally opposite corners were nearly identical which indicates the symmetrically distributed flexure, torsion and shear on the slab. Similar to the those observed in the eccentrically-loaded cases, the increase in skewness of the slab also resulted in decreases in the reaction forces measured at the acute corners (i.e. corners 2 and 4) and increases in the reaction forces measured at the obtuse corners. Note that for the centrically-loaded S0 slab, there were slight differences among the measured reaction forces. This unexpected observation might be attributed to the unintended load eccentricity generated on loading ram or due to slight slippage between the load cells and the supports. It is worth noting that the offset is a minor one (less than 5% of the total span length). It may also be noted that this minor error occurred only in the case E of specimen S0; there were no such discrepancies observed in all other tests.

(a)   (b)   (c)

218

(d)   (e)
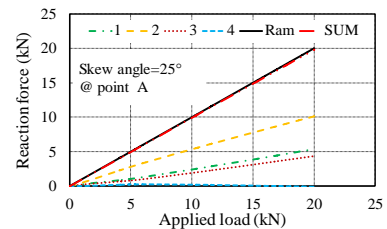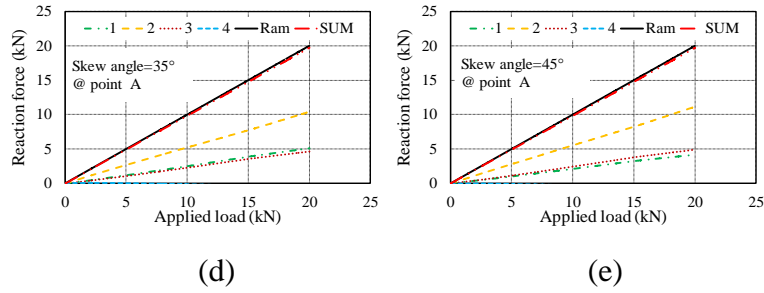
Figure 7.10. Reaction forces of the skew slabs loaded at point A: a) S0; b) S15; c) S25; c) S35; d) S45

(a)   (b)   (c)
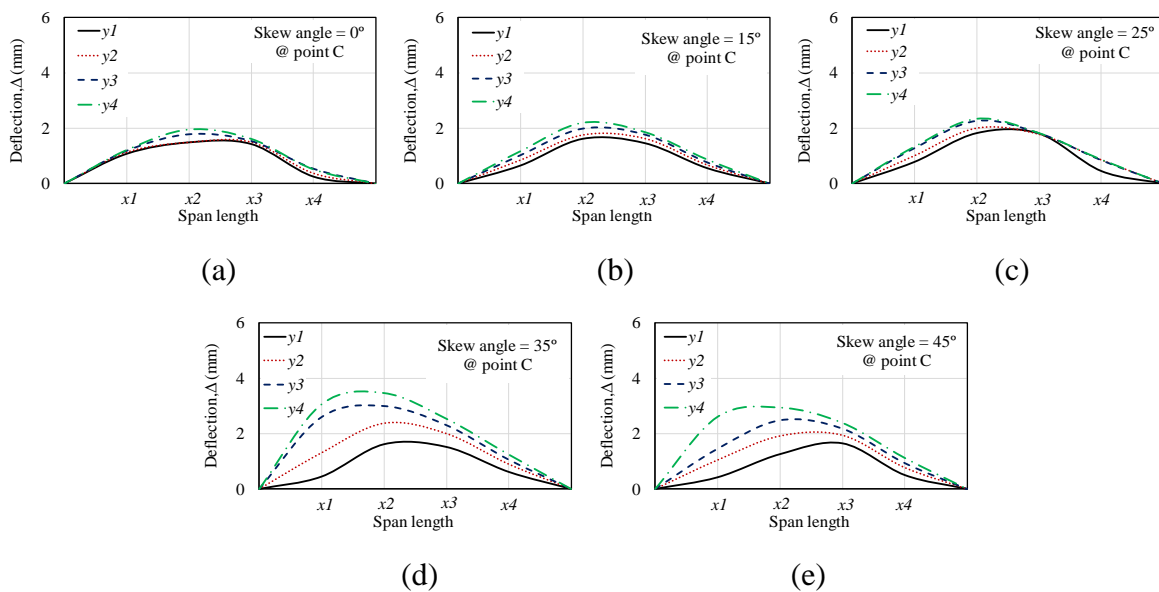

(d)   (e)
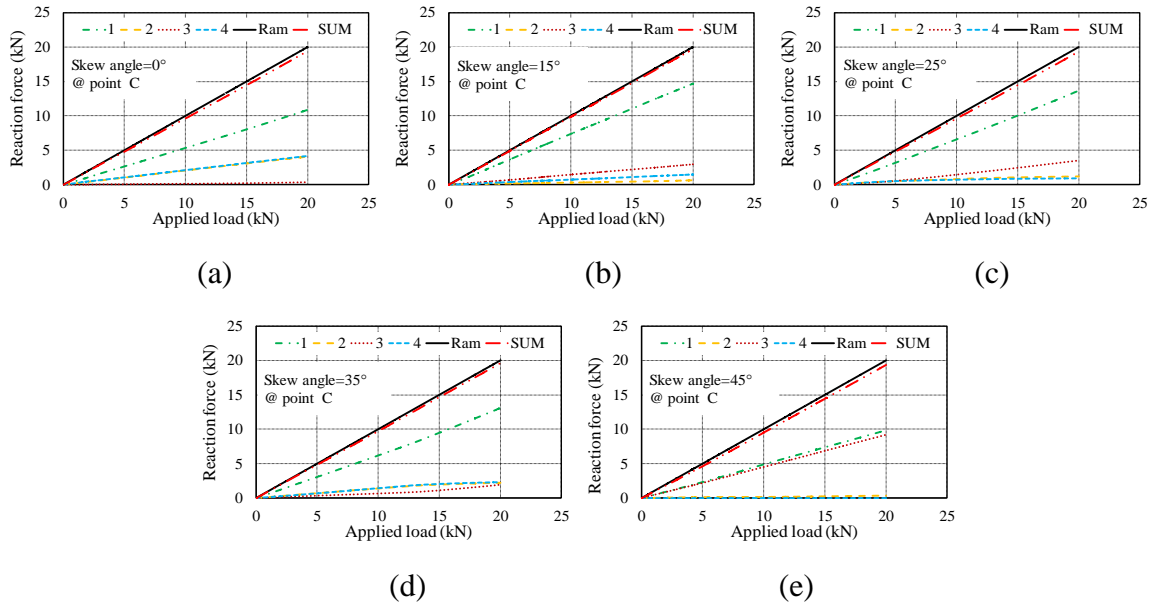
Figure 7.11. Reaction forces of the skew slab loaded at point C: a) S0; b) S15; c) S25; c) S35; d) S45
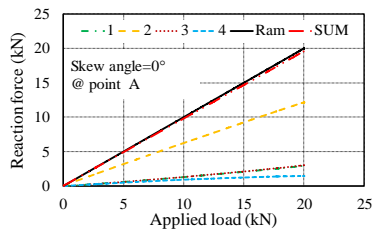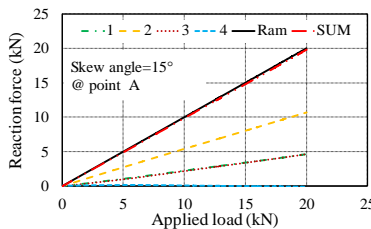

(a)   (b)   (c)

(d)   (e)
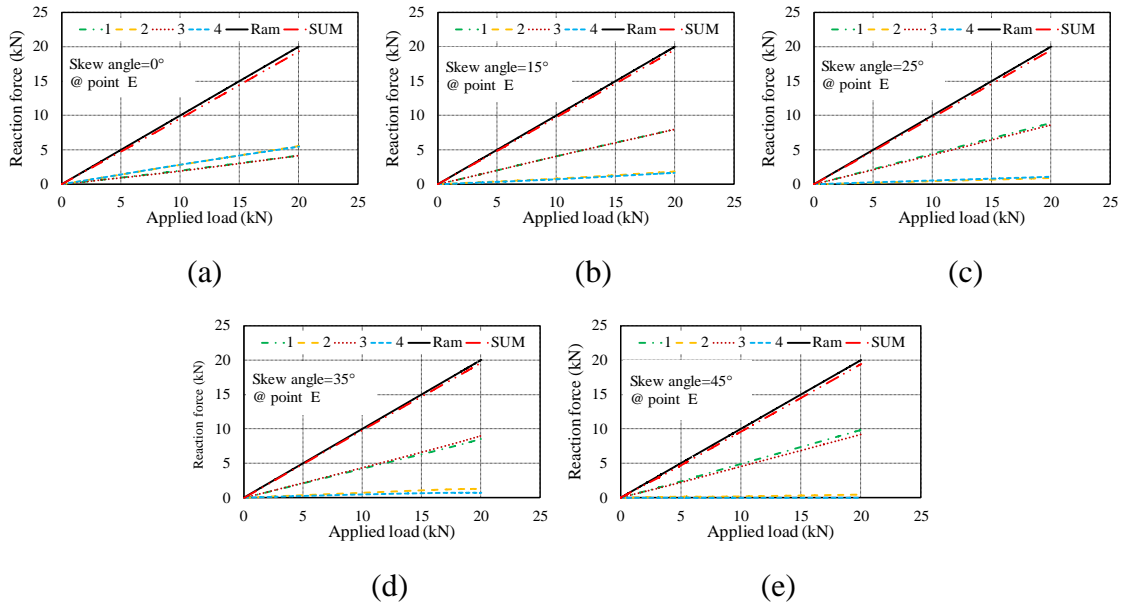
Figure 7.12. Reaction forces of the skew slab loaded at point E a) S0; b) S15; c) S25; c) S35; d) S45

7.3.3 Yield-line pattern of skew slabs

In addition to the elastic tests of the slabs, all the slabs were also loaded at their centre (i.e. point E) until failure. Fig. 7.13 illustrates the final failure patterns of the slabs. It is evident from these photographs that the yield-lines originated from the centre of the slabs and propagated along central-line that is parallel to the supported edges. This indicates that for a one-way slab, flexural failure dominates even for skew slabs. Based on the failure patterns shown in Fig. 7.13, the upper bound of the length of the yield-line will be the length of the supported edge of the slab and its lower boundary is the projection of short edge of slab on the line that is perpendicular to the central-line of the slab. The lower and upper values of the length of the yield-line are used later for the yield-line analysis.
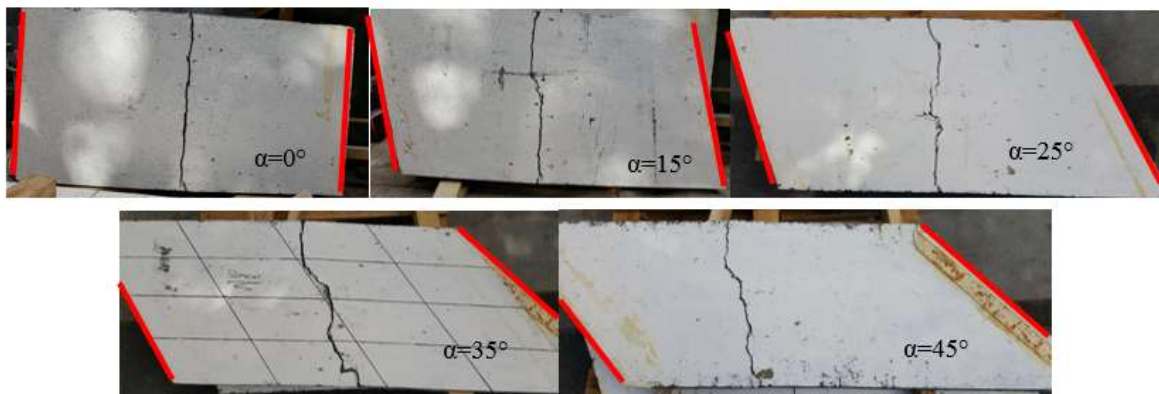
Figure 7.13. Yield-line patterns for the skew slabs

7.3.4 Complete load-deflection relationship of concentratedly loaded skew slabs

The complete load-deflection relationships of all the slabs tested to failure are illustrated in Fig. 7.14. The load-deflection relationship of all the slabs exhibited nearly identical trend up to the peak applied load. However, the skewness of the slab significantly affects the post-peak load-deflection response of the slab, in which the increase in the skewness of the slab resulted in a less gradual descending branch on its load-deflection curve. An up to around 115% decrease in the maximum mid-span deflection was observed when compared those measured from S0

and S45 series of specimens. No significant change in load carrying capacity was observed with increasing the skewness of the slabs. Note that, although the ductility of the slab reduced slightly with increasing the skewness of the slab, all the UHPFRC skew slabs exhibited desirable ductility as that their ductility factors ($\Delta_{failure}/\Delta_{yield}$) are all over 2.5. Note that some experimental variations were also observed, for instance the slightly higher load carrying capacity of the S35 series of slabs compared to those of its companion specimens. This was mostly caused by the presence of the randomly distributed fibres in the specimens whose orientations and dispersions were hard to control during the casting process of the specimens. The fibres might be more concentrated at the tensile face of S35 compared to those in the other slabs, resulting in a slightly higher ultimate load carrying capacity of S35. Moreover, the result of a similar test of conventional simply-supported reinforced concrete (RC) skew slab (series RC slab S2-502) subjected to a point load which was conducted by Kabir et al. (Kabir et al. 2002) is adopted to compare with the results in the current study to show the improvements of the performance of the skew slab by using the UHPFRC materials. Moreover, this test result is also used later in this paper in together with the current test results to validate the proposed analytical models. The material properties and geometry of this RC slab (S2-502) is reported in Table. 7.3 and the load- mid-span deflection relationship of the slab is shown in Fig. 7.14. As can be seen from Table. 7.3 and Fig. 7.14, the S2-502 slab reported in (Kabir et al. 2002) with around 67% larger cross-sectional area, approximately 5 times higher reinforcement ratio in the longitudinal direction and a only slightly shorter span length (i.e. 1200 mm vs. 1400 mm), exhibited less than 6% improvement in load bearing capacity and up to 70% higher mid-span deflection at the peak load compared to those of the two slabs S35 and S45 with similar skew angles in the presented study. These comparisons indicate that, due to its superior material properties, the application of UHPFRC materials in a skew slab can significantly reduce the

size of the specimen as well as the ratio of reinforcements required to achieve the similar performance of the structure using conventional normal strength concrete.
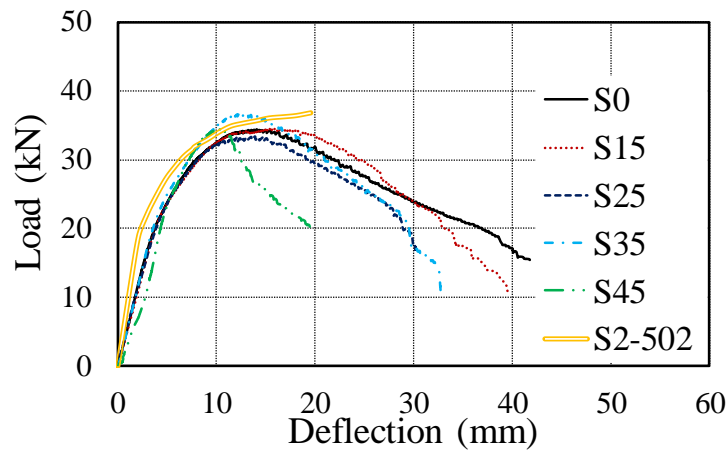
Figure 7.14. Complete load-deflection relationship of the skew slabs loaded at the centre (i.e. point E)

Table 7.3. Details of S2-502 series of specimen reported in [41]

	Material properties									
	v	L (mm)	w (mm)	t (mm)	EI/GJ	α	f'_c (MPa)	ft (MPa)	ρ_l (%)	ρ_t (%)
S2-502	0.2	1200	1000	75	0.6	40°	30.5	2.9	0.86	0.48

7.4 ANALYTICAL STUDY

7.4.1 Development of closed-form mathematic solutions for a skew UHPFRC bending element

Even under simply-support boundary conditions, a skew slab is statically indeterminate to associated torsional moments developed. In this section, a closed-form solution is developed using virtual work and force methods to solve the indeterminate skew slab problem, as per the sign convention and the coordinate system shown in Fig. 7.15. Based on the equilibrium of moments and forces: $\sum M_x = 0$, $\sum M_y = 0$, and $\sum F_z = 0$, by applying the virtual work and

force methods by considering the torsional moment on one of the supports as a redundant (i.e. T_B), the following equations are derived:

The reaction force at the centre of the supports A (R_A) and B (R_B) are:

$$R_A = (1 - \lambda) \cdot P \tag{7.1}$$

$$R_B = \lambda \cdot P \tag{7.2}$$

where λ is the factor to represent the location of the concentrated load with reference to central line of the slab, which is expressed as:

$$\lambda = \frac{x}{L} \tag{7.3}$$

The shear force, bending and torsional moments due to only the applied load P are:

For $0 \leq x \leq \lambda$

$$M_P = x \cdot (1 - \lambda) \cdot PL \tag{7.4}$$

$$T_P = 0 \tag{7.5}$$

$$V_P = (1 - \lambda) \cdot P \tag{7.6}$$

and for $\lambda \leq x \leq 1$

$$M_P = \lambda \cdot (1 - x) \cdot PL \tag{7.7}$$

$$T_P = 0 \tag{7.8}$$

$$V_P = -\lambda \cdot P \tag{7.9}$$

The shear force, bending and torsional moments caused by the redundant torsional moment (T_B) are:

$$M_{T_B} = -T_B \sin \alpha \tag{7.10}$$

$$T_{T_B} = -T_B \cos \alpha \tag{7.11}$$

$$V_{T_B} = 0 \tag{7.12}$$

Based on the virtual work method:

$$\delta_B T_B + \Delta_B = 0 \qquad (7.13)$$

where δ_b is the virtual deflection when $T_B = 1$; and Δ_B is the deflection caused by torsional moment (T_B).

$$\delta_B = \int_L^0 \frac{\bar{M}^2}{EI} dx + \int_L^0 \frac{\bar{T}^2}{GJ} dx \qquad (7.14)$$

$$\Delta_B = \int_L^0 \frac{\bar{M} M}{EI} dx + \int_L^0 \frac{\bar{T} T}{GJ} dx \qquad (7.15)$$

where $\bar{M}$ and $\bar{T}$ are the bending and torsional moment when $T_B = 1$. By substituting Eqs. (7.10) to (7.12) into Eqs. (7.14) and (7.15) respectively, δ_B and Δ_B are:

$$\delta_B = \sin^2 \alpha \cdot \left(1 + \frac{EI}{GJ} \cot^2 \alpha\right) \cdot \frac{L}{EI} \qquad (7.16)$$

$$\Delta_B = \int_L^0 \frac{\bar{M} M}{EI} dx + \int_L^0 \frac{\bar{T} T}{GJ} dx = -\sin \alpha \cdot \frac{PL^2 \cdot (1-\lambda) \cdot \lambda}{2EI} \qquad (7.17)$$

The torsional moment at support A (T_A) and B (T_B) hence are:

$$T_B = -T_A = -\frac{\Delta_B}{\delta_B} = \frac{\lambda(1-\lambda) \cdot PL}{2 \cdot \sin \alpha \cdot \left(1 + \frac{EI}{GJ} \cot^2 \alpha\right)} \qquad (7.18)$$

The reaction force at the corners 1 (R_1), 2 (R_2), 3 (R_3), and 4 (R_4) can be calculated using T_B and the reaction force (i.e. R_A and R_B) at the centre of each support:

$$R_1 = \frac{R_A}{2} - \frac{T_B \cos \alpha}{B_0} = \frac{L-x}{2L} \cdot P \cdot \left[1 - \frac{x \cot \alpha}{B_0 (1 + \frac{EI}{GJ} \cot^2 \alpha)}\right] \qquad (7.19)$$

$$R_2 = \frac{R_A}{2} + \frac{T_B \cos \alpha}{B_0} = \frac{L-x}{2L} \cdot P \cdot \left[1 + \frac{x \cot \alpha}{B_0 (1 + \frac{EI}{GJ} \cot^2 \alpha)}\right] \qquad (7.20)$$

$$R_3 = \frac{R_B}{2} + \frac{T_B \cos \alpha}{B_0} = \frac{x}{2L} \cdot P \cdot \left[1 - \frac{(L-x) \cot \alpha}{B_0 (1 + \frac{EI}{GJ} \cot^2 \alpha)}\right] \qquad (7.21)$$

$$R_4 = \frac{R_B}{2} - \frac{T_B \cos \alpha}{B_0} = \frac{x}{2L} \cdot P \cdot \left[1 + \frac{(L-x) \cot \alpha}{B_0 (1 + \frac{EI}{GJ} \cot^2 \alpha)}\right] \qquad (7.22)$$

where B_0 is the projection of supported edge of slab on the line that is perpendicular to the central-line of slab, as shown in Fig. 7.15.

The generic expressions of bending moment (M), torsional moment (T) and shear force (V) along the central line of the slab are:

For $0 \leq x \leq \lambda$

$$M = (1 - \lambda)(x - \frac{\lambda}{2\left(1+\frac{EI}{GJ}\cot^2\alpha\right)}) \cdot P \cdot L \tag{7.23}$$

$$T = -\frac{\lambda(1-\lambda)\cdot P\cdot L\cdot\cot\alpha}{2\left(1+\frac{EI}{GJ}\cot^2\alpha\right)} \tag{7.24}$$

$$V = (1 - \lambda) \cdot P \tag{7.25}$$

and for $\lambda \leq x \leq 1$

$$M = \left[\left(1 - \frac{1}{2\left(1+\frac{EI}{GJ}\cot^2\alpha\right)}\right) - \left(x - \frac{\lambda}{2\left(1+\frac{EI}{GJ}\cot^2\alpha\right)}\right)\right] \cdot \lambda \cdot P \cdot L \tag{7.26}$$

$$T = -\frac{\lambda(1-\lambda)\cdot P\cdot L\cdot\cot\alpha}{2\left(1+\frac{EI}{GJ}\cot^2\alpha\right)} \tag{7.27}$$

$$V = -\lambda \cdot P \tag{7.28}$$

The generic expressions of the rotation (θ) along the central line of the slab are:

For $0 \leq x \leq \lambda$

$$\theta = \frac{Pl^3}{6EI}(1 - \lambda) \cdot \left[(2\lambda - \lambda^2 - 3 \cdot \lambda^2) - \frac{3\cdot\lambda(1-2\cdot x)}{2\left(1+\frac{EI}{GJ}\cot^2\alpha\right)}\right] \tag{7.29}$$

and for $\lambda \leq x \leq 1$

$$\theta = \frac{Pl^3}{6EI}\lambda \cdot \left[(2 - 6 \cdot x + 3 \cdot x^2 + \lambda^2) - \frac{3\cdot(1-\lambda)(1-2\cdot x)}{2\left(1+\frac{EI}{GJ}\cot^2\alpha\right)}\right] \tag{7.30}$$

The generic expression of the deflection (Δ) along the central line of the slab are:

For $0 \leq x \leq \lambda$

$$\Delta = \frac{PL^3}{6EI}(1-\lambda)\cdot x \cdot \left[(2\lambda - \lambda^2 - x^2) - \frac{3\cdot\lambda(1-x)}{2\left(1+\frac{EI}{GJ}\cot^2\alpha\right)}\right] \quad (7.31)$$

and for $\lambda \leq x \leq 1$

$$\Delta = \frac{PL^3}{6EI}(1-x)\cdot \lambda \cdot \left[(2x - x^2 - \lambda^2) - \frac{3\cdot x(1-\lambda)}{2\left(1+\frac{EI}{GJ}\cot^2\alpha\right)}\right] \quad (7.32)$$
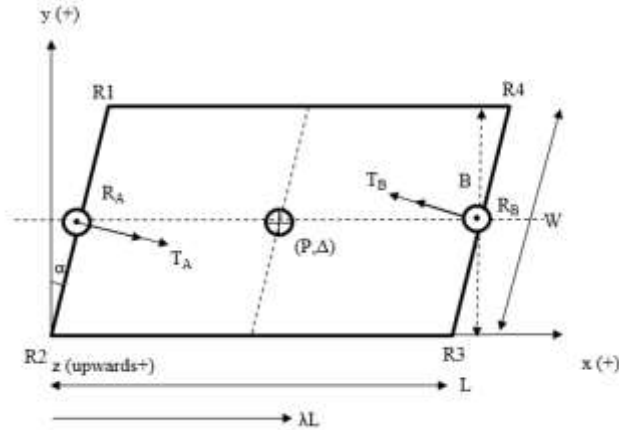
Figure 7.15. Sign convention and coordinate system of simply-supported skew slab loaded at its central line

Table 7.4 summarizes the key material properties and specimen geometries of the slab used for model validation, including Poisson's ratio (v), span length (L) and width (w). Tables 7.4 and 7.5 report the experimentally- and analytically-obtained maximum deflection and reactions that were measured at four corners of each slab loaded at point E and D respectively. The statistics shown in Tables 7.5 and 7.6 indicate that the analytical procedure developed in this study has excellent correlation with the test results. Although the model simulates well the structural response of the skew slabs for the most of the cases (see Tables 7.5 and 7.6), some predictions exhibited over 50% errors, such as for R4 of S25 loaded at point D, R4 of S45 loaded at point D, R4 of S35 loaded at point E and R2 of S45 loaded at point E. As discussed in Sections 3.1 and 3.2, unlike the experimental variation seen in the statically determinate case of the straight slab S0 whose reaction forces at the supports are only related to the geometry of the specimen, the reaction forces at the supports of the statically indeterminate skew slabs system are related

not only to the geometry but also the material properties. Therefore, the unexpected errors seen between the experimental and theoretical results of the skew slabs could be mostly attributed to the fact that the fibres distributions and orientations in the specimens were rather random, leading to the inhomogeneous material properties, in which the theoretical models assumed the homogenous material properties

Table 7.4. Materials properties for the validation of the analytical model

	v	L (mm)	w (mm)	t (mm)	EI/GJ
UHPFRC	0.233	1420	720	60	0.611

Table 7.5. Comparison between experimental and analytical results for the slabs loaded at point D

	Corner	Reaction force				Deflection			
		Exp (kN)	Mod (kN)	Mean	SD	Exp (mm)	Mod (mm)	Mean	SD
S0	1	6.82	7.46	1.09	0.46	2.21	2.08	0.94	0.09
	2	8.23	7.46	0.91	0.54				
	3	1.94	2.54	1.31	0.43				
	4	2.71	2.54	0.94	0.12				
S15	1	8.87	8.96	1.01	0.06	2.12	1.94	0.92	0.12
	2	6.11	5.96	0.98	0.11				
	3	4.19	4.04	0.96	0.11				
	4	1.25	1.04	0.83	0.15				
S25	1	9.63	9.75	1.01	0.09	1.62	1.80	1.11	0.13
	2	5.55	5.18	0.93	0.26				
	3	3.88	4.82	1.24	0.67				
	4	0.51	0.25	0.50	0.18				

	Corner	Exp (kN)	Mod (kN)	Mean	SD	Exp (mm)	Mod (mm)	Mean	SD
S35	1	9.25	10.31	1.11	0.75				
	2	6.20	5.39	0.87	0.58	1.47	1.29	0.87	0.13
	3	4.29	4.61	1.08	0.23				
	4	0.04	0.03	0.75	0.01				
S45	1	9.63	10.67	1.11	0.74				
	2	5.75	5.75	1.00	0.00	1.15	0.99	0.86	0.11
	3	4.55	4.25	0.93	0.21				
	4	-0.20	-0.67	3.32	0.33				

Table 7.6. Comparison between experimental and analytical results for the slabs loaded at point E

		Reaction force				Deflection			
	Corner	Exp (kN)	Mod (kN)	Mean	SD	Exp (mm)	Mod (mm)	Mean	SD
S0	1	4.39	5.00	1.14	0.43				
	2	5.53	5.00	0.90	0.38	2.71	2.73	1.00	0.01
	3	4.30	5.00	1.16	0.49				
	4	5.43	5.00	0.92	0.31				
S15	1	7.03	6.81	0.97	0.16				
	2	2.81	2.95	1.05	0.10	2.76	2.56	0.93	0.14
	3	7.00	6.81	0.97	0.14				
	4	2.67	2.95	1.10	0.20				
S25	1	8.38	8.02	0.96	0.26				
	2	1.65	1.98	1.21	0.24	2.53	2.33	0.92	0.14
	3	7.90	8.02	1.01	0.08				
	4	1.51	1.98	1.31	0.33				

S35	1	8.59	8.76	1.02	0.12				
	2	1.27	1.24	0.98	0.02	2.35	2.24	0.95	0.08
	3	8.83	8.76	0.99	0.05				
	4	0.74	1.24	1.67	0.35				
S45	1	9.82	9.24	0.94	0.42				
	2	0.48	0.76	1.58	0.20	2.22	2.03	0.91	0.14
	3	9.18	9.24	1.01	0.04				
	4	0.65	0.76	1.18	0.08				

The analytical models were also used to simulate the response of askew slab tested by others (Kabir et al. 2002), so as to establish its generic nature and reliability. The details of this experiment was shown in Section 3.4 and its load-mid-span deflection curve and the marital properties used for the model validations are shown in Fig. 7.14 and reported in Table 7.3, respectively. Table 7.7 presents the comparison between the experimentally-obtained and the predicted mid-span deflections within the linear elastic region and the statistics shown in this table indicates that the predictions correlates well with the test results.

Table 7.7. Validation of the proposed model using the result from [41]

	Mid-span deflection at 16.04 kN			
	Exp (mm)	Mod (mm)	Mean	SD
S2-502	1.74	1.72	0.99	0.014

7.4.2 Generation of influence line using the analytical method

Using the generic expressions developed in Eqs. (7.11) and (7.15) to (7.18) for calculating bending moment, torsional moment and shear force, the values for the M, T and V are calculated for simply-supported skew slabs with different skew angles α (i.e. 0 to 180°) and different

dimensionless bend-to-twist ratios $\frac{EI}{GJ}$ (i.e. 0 to 10) which were subjected to a unit load (P) moving along the central-line of the skew slabs. The calculated values are plotted where the unit load is applied and subsequently, the obtained value of M, T, V and Δ for each point along the central-line of the skew slabs is used to generate the influence line diagrams as shown in Figs. 7.16 (a) to (c). As can be seen from Fig. 7.16 (a), the slab with skew angles of 90° performs exactly like a fixed-end straight slab with infinite rigidity on its supports, in which the maximum moment and deflection of the concentratedly-loaded slab with skew angles of 90° is $\frac{pL}{8EI}$ and $\frac{pL^3}{192EI}$, respectively. Fig. 7.16 (b) shows that for a given skew angle of the slab, the increase in bend-to-twist ratio $\frac{EI}{GJ}$ leads to increase in bending moment and Fig. 7.16 (c) shows the influence of loading position on bending moment of the skew slab, where the largest bending moment occurs when the load is applied at the centre of the slab. It can be seen from Fig. 7.17 (a) that for a slab with a given skew angle, the absolute value of the in-plane torsional moment (T) increases with a decrease in $\frac{EI}{GJ}$, and for a given $\frac{EI}{GJ}$, the increase in T with increasing skew angle only up to a certain value (i.e. α=45°) and further increase in skew angle leads to a decrease in T. Fig. 7.17 (b) shows that a slab with a skew angle of 45° exhibits the largest torsional moment for the slab loaded at a given point, and it is also observed that the less torsional moment is generated for the slab loaded at a position closer to one of the supports. For the influence lines generated for shear force, it can be seen from Fig. 7.18 that the shear force profile for a skew slab strongly depends on the loading position and this is exactly same as that of a simply-supported straight slab. It can be seen from Fig. 7.19 that the deflection of a skew slab decreases with increasing skew angle and the deflection is also seen to increase with an increase in $\frac{EI}{GJ}$.

(a)

(b)

(c)
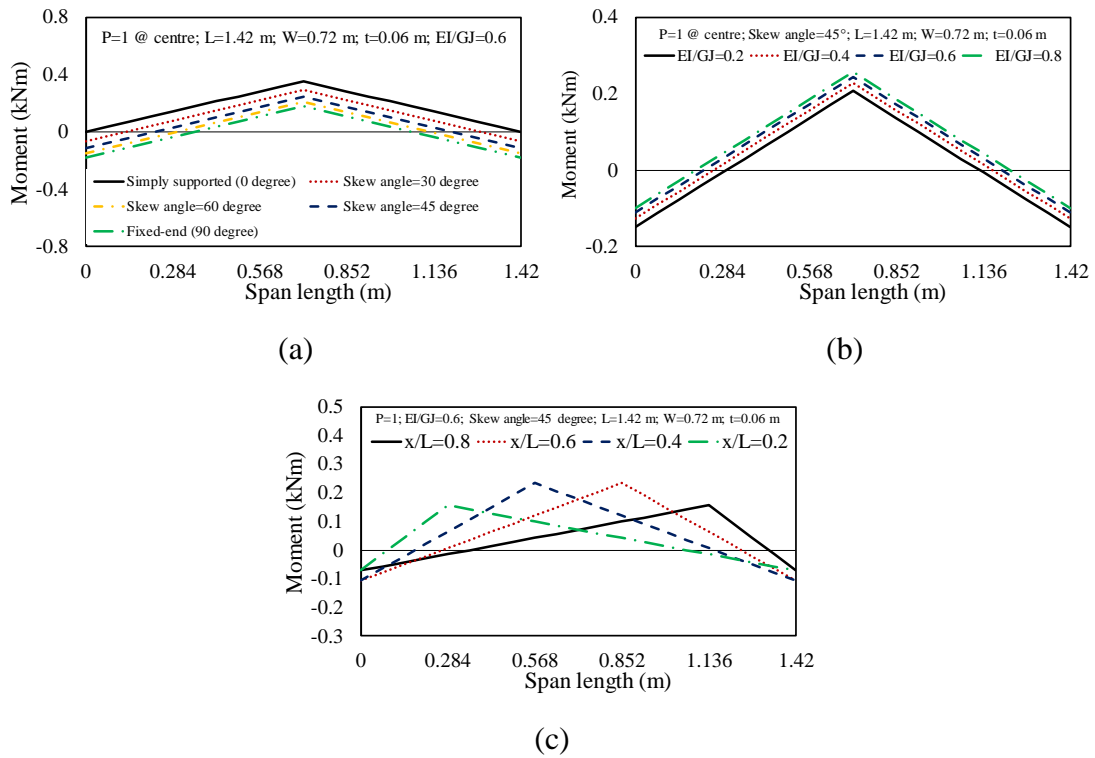
Figure 7.16. Influence diagram for bending moment by: a) varying the skew angle; b) varying the bend-to-twist ratio (*EI/GJ*); c) varying the loading position at the central line

(a)

(b)
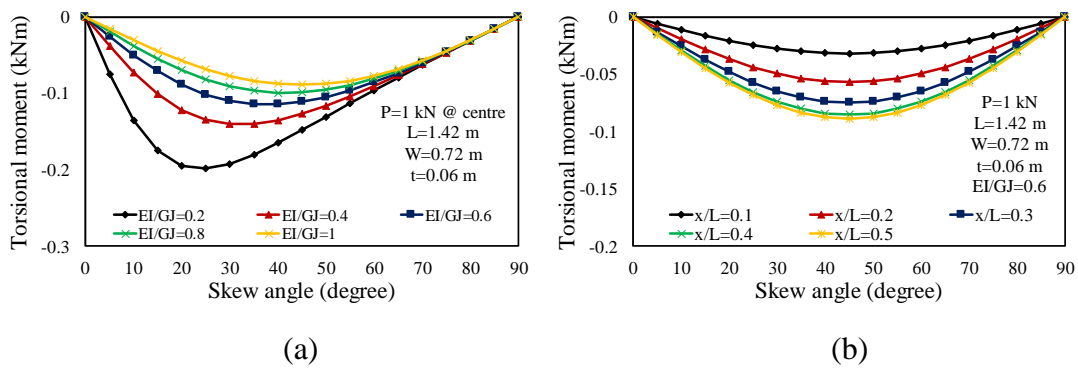
Figure 7.17. Influence diagram for torsional moment by: a) varying the bend-to-twist ratio (*EI/GJ*); b) varying the loading position at the central line
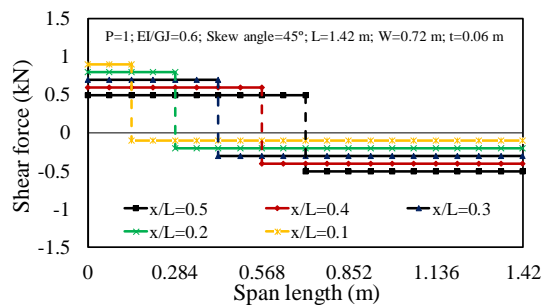
Figure 7.18. Influence diagram for shear force by varying the loading position at the central line
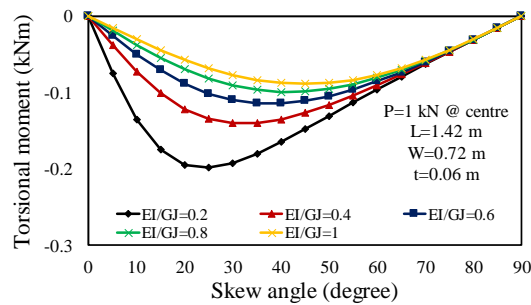
Figure 7.19. Influence diagram for deflection by: a) varying the skew angle; b) varying the span length

7.4.3 Yield-line analysis

In this section, the ultimate bending capacity of the skew slabs is determined using yield-line analysis. The upper ($l_{y\text{-}max}$) and lower ($l_{y\text{-}min}$) bounds of the yield-line length as explained in Section 3.4 and can be defined using Eqs. (7.33) and (7.34):

$$l_{y-max} = w \qquad (7.33)$$

$$l_{y-min} = w \cdot \cos \alpha \qquad (7.34)$$

The calculated upper and lower bounds of the yield-line length of each slab are summarized in Table 7.8. To conduct yield-line analysis, it requires that at failure the potential energy expended by loads displacing the slab must equal the energy dissipated (or work done) rotating yield lines, which is depicted in Fig. 7.20 and can be defined as follows:

$$\sum P \times \Delta = \sum m \times l_y \times \theta \qquad (7.35)$$

where P is the peak load in (kN), Δ is the vertical displacement of the load in (m), m is the moment of resistance of slab per length crossing the yield-line in (mm/mm), l_y is the total length of yield-line in (mm), and θ is the rotation of slab. For the current case as shown in Fig. 7.20, Eq. (7.35) can be simplified as:

$$P \times \Delta = 2 \times m \times l_y \times \theta \qquad (7.36)$$

The moment capacity ($M = m \times l_y$) of each section where the yield-line appeared can be obtained using a partial-interaction segmental analytical approach developed in (Visintin et al. 2012) as shown in Fig. 7.21 and the details of this modelling approach can be found in references (Ali 2017; Muhamad et al. 2012; Oehlers et al. 2014; Oehlers et al. 2014; Visintin and Oehlers 2016; Visintin and Oehlers 2017). The approach is a direct utilization of the Euler-Bernoulli theorem of plane section remain plane without the corollary of a linear strain profile. Hence a similar solution technique to that which is followed when undertaking a moment-curvature analysis is applied, with the major difference being the starting point is the imposition of a deformation rather than strain profile. This change is significant as it allows for the direct application of partial interaction theory to simulate localized behaviours such as crack formation, widening and tension stiffening (Muhamad et al. 2012) in the tension region and concrete softening using shear friction theory in the compression region (Chen et al. 2013).

In Eq. (7.36) the rotation of slab can be determined using the vertical displacement of the load (Δ) and half of the span length of the slab ($L/2$), as the expression given in Eq. (7.37)

$$\theta = \frac{\Delta}{L/2} \qquad (7.37)$$

By substituting Eq. (7.37) in to Eq. (7.36), we get:

$$P = \frac{4M}{L} \qquad (7.38)$$

Table 7.8 also summaries the peak moment of the yield-line sections of each slab established using the partial-interaction segmental analytical approach and the calculated the upper and lower bounds of the ultimate load carrying capacity of each slab. The comparisons shown in Table 7.8 suggest that the yield-line analysis using the partial-interaction segmental analytical approach is capable of estimating the ultimate bending capacity of skew slabs.
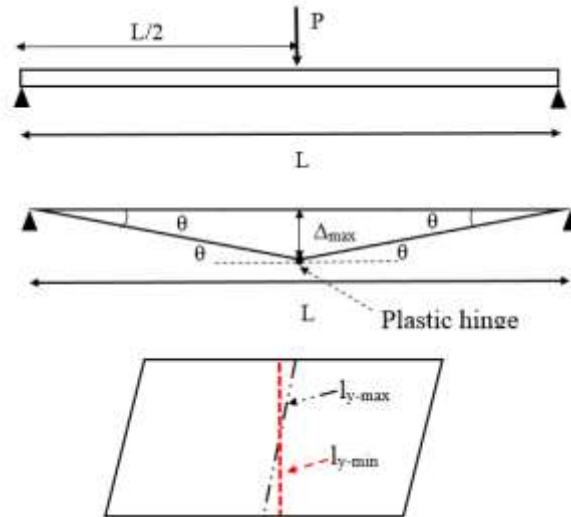
Figure 7.20. Yield-line analysis

| (a) | (b) |
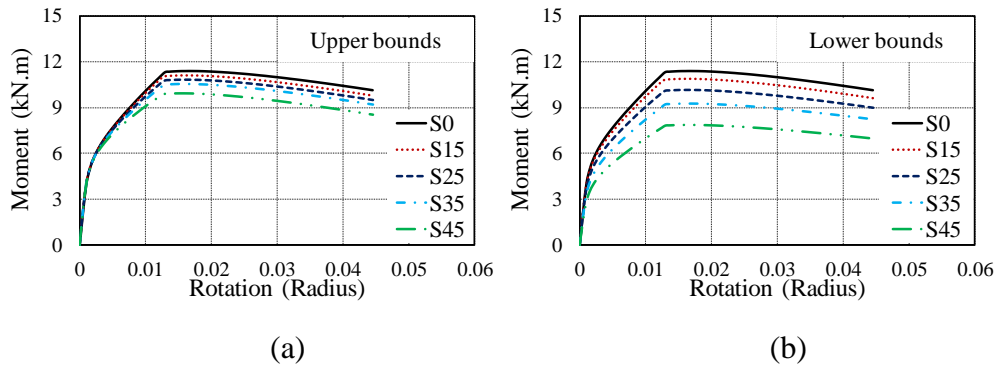
Figure 7.21. Moment-rotation relationship of the skew slab sections: a) Upper bounds; b) Lower bonds

Table 7.8. Summary of the results from yield–line analysis

	P_{exp} (kN)	Upper bonds					Lower bonds				
		$l_{y\text{-}max}$ (mm)	$M_{y\text{-}max}$ (kN.m)	P_{mod} (kN)	Mean	SD	$l_{y\text{-}min}$ (mm)	$M_{y\text{-}min}$ (kN.M)	P_{mod} (kN)	Mean	SD
S0	34.0	720	11.4	33.0	1.0	0.7	720	11.4	33.0	0.97	0.69
S15	34.2	720	11.1	32.2	0.9	1.4	695	10.9	31.5	0.92	1.91
S25	32.9	720	10.8	31.4	1.0	1.1	653	10.2	29.4	0.89	2.45
S35	36.2	720	10.5	30.5	0.8	4.0	590	9.3	26.8	0.74	6.64
S45	34.2	720	10.5	30.5	0.9	2.6	509	7.9	22.8	0.67	8.03

7.5 CONCLUSIONS

In this research, an experimental program and analytical studies were carried to investigate the performance of UHPFRC skew slabs/ bridge decks under applied concentrated loads. Based on the results obtained from both the experimental and analytical studies, the following inferences can be made:

1. The skewness of a slab significantly affects its deflection profiles and reactions at its supports, in which the increase in the skewness of the slab leads to a more unsymmetrical vertical deflection distribution and also results in a decrease in the magnitude of reaction at the acute corners of and a corresponding increase in the reaction at the obtuse corner. The effect of slab skewness on the performance of the slab is particularly significant when the skew angle exceeds 25°.

2. It is observed that compared to those minor effect caused by torsional moment, the maximum vertical deflection of a concentratedly -loaded UHPC skew slab predominates by the flexure bending. However, reactions forces measured at the supports of the slabs significantly affected by the torsion, in which under a significantly higher out-plane moment, reaction forces measured at the acute corner even change from compression to tension.

3. Increasing the skew angle of a concentratedly loaded slab has a minor effect on the load-deflection relationship prior to attaining the ultimate load, whereas a significant reduction in ductility with an increase (i.e. up to 115% reduction in the maximum mid-span deflection) in the skew angle is observed at the post-peak stage of the load-deflection curve of the slab.

4. The application of UHPFRC material in a skew slab can achieve a comparable performance to that of a conventional normal strength concrete with a similar skew angle, larger cross-sectional area and 5 times higher longitudinal reinforcement ratio.

5. Within the linear elastic range, the predictions using the developed mechanic-based closed-form equations correlates well with experimentally established reactions and maximum deflection of a slab loaded at its central-line. The experimental variations and some errors seen in the model predictions are mostly caused by the inhomogeneous material properties of the slabs as the consequences of the randomly distributed fibres in the specimens.

6. Closed-form analytical solutions were derived for indeterminate, simply supported skew slab/bridge decks based on the virtual work method to generate influence lines for bending moment, shear force, reaction force and torsional moment.

7. Yield-line analysis using moment-curvature relationship from the partial-interaction segmental analytical approach can properly determine the upper and lower bounds of the ultimate load carrying capacity of a skew slab.

7.6 LIST OF NOTATIONS

B_0 – Projection of supported edge of slab on the line that is perpendicular to the central-line of slab

E_c – Elastic modulus of the UHPFRC

EI – Bending stiffness

EI/GJ – Bend-to-twist ratio

F_z – Force at z direction

f_c' – Axial compressive strength of the UHPFRC

f_r – Modulus of rupture of the UHPFRC

f_{st} – Splitting tensile strength of the UHPFRC

GJ – Torsional stiffness

L – Span length of a slab or the length of the longer edge of a slab

l_{y-max} – Length of yield-line

l_{y-max} – Upper bound of yield-line length

l_{y-min} – Lower bound of yield-line length

M – Bending moment

M_P – Bending moment due to the applied load P only

M_{T_B} – Bending moment due to the redundant action T_B

M_x – Moment in x direction

M_y – Moment in y direction

$\bar{M}$ – Bending moment when $T_B = 1$

m – Moment of resistance of slab per length crossing the yield-line in (mm/mm)

P – Applied load

R_A – Reaction force at the centre of the supports A

R_B – Reaction force at the centre of the supports B

R_1, R_2, R_3, R_4 – The reaction forces at the corners 1, 2, 3 and 4

T – Torsional moment

T_P – Torsional moment due to the applied load P only

T_{T_B} – Torsional moment due to the redundant action T_B

$\bar{T}$ – Torsional moment when $T_B = 1$

t – Thickness of each slab

V – Shear force

V_P – Shear force due to the applied load P only

V_{T_B} – Shear force due to the redundant action T_B

v – Poisson's ratio of the UHPFRC

w – Length the shorter edge of a slab

α – Skew angle of a slab

Δ – Vertical displacement of the load in the yield line analysis

Δ_B – Deflection caused by torsional moment (T_B)

δ_b – Virtual deflection when $T_B = 1$

θ – Rotation of slab due to the applied load

λ – Factor to represent the location of the concentrated load with reference to central line of the slab

ρ_l – Reinforcement ratio in the longitudinal direction

ρ_t – Reinforcement ratio in the transverse direction

7.9 REFERENCES

AASHTO, L. (2007). "AASHTO LRFD bridge design specifications." *Transportation (Amst). American Association of State Highway and Transportation Officials, Inc.: Washington, DC*.

Ali, M. M. (2017). "Analytical models to predict structural behaviour of reinforced concrete beams bonded with prestressed fibre-reinforced polymer laminates." *Advances in Structural Engineering*, 1369433217732666.

ASTM International (2004). "ASTM C496/C496M-04. Standard Test Method for Splitting Tensile Strength of Cylindrical Concrete Specimens." *ASTM International, West Conshohocken*.

ASTM International (2005). "ASTM C39/C39M-05. tandard Test Method for Compressive Strength of Cylindrical Concrete Specimens." *ASTM International, West Conshohocken*.

ASTM International (2014). "ASTM C469/C469M-14. Standard Test Method for Static Modulus of Elasticity and Poisson's Ratio of Concrete in Compression." *ASTM International, West Conshohocken*.

Bakht, B. (1988). "Analysis of some skew bridges as right bridges." *Journal of Structural Engineering*, 114(10), 2307-2322.

Chen, Y., Visintin, P., Oehlers, D., and Alengaram, U. (2013). "Size-dependent stress-strain model for unconfined concrete." *Journal of Structural Engineering*, 140(4), 04013088.

CSA (2014). "Canadian highway bridge design code." Rexdale Toronto.

Dhar, A., Mazumder, M., and Karmakar, M. C. S. (2013). "Effect of skew angle on longitudinal girder (support shear, moment, torsion) and deck slab of an IRC skew bridge." *IndIan ConCreTe Journal*, 46.

Fan, W., Xu, X., Zhang, Z., and Shao, X. (2018). "Performance and sensitivity analysis of UHPFRC-strengthened bridge columns subjected to vehicle collisions." *Engineering Structures*, 173, 251-268.

Gupta, T., and Misra, A. (2007). "Effect on support reactions of T-beam skew bridge decks." *ARPN Journal of engineering and applied sciences*, 2(1), 01-08.

Harba, I. S. (2011). "Effect of Skew Angle on Behaviour of Simply Supported RC T-Beam Bridge Decks." *ARPN Journal of Engineering and Applied Sciences*, 6(8), 1-14.

Heinz, D., Dehn, F., and Urbonas, L. "Fire resistance of ultra high performance concrete (UHPC)–Testing of laboratory samples and columns under load." *Proc., International Symposium on Ultra High Performance Concrete*, 703-716.

International, A. (2018). "ASTM C78 / C78M-18, Standard Test Method for Flexural Strength of Concrete (Using Simple Beam with Third-Point Loading)." *ASTM International, West Conshohocken*.

Joe, C. D. (2016). "Cost and Ecological Feasibility of Using Ultra-High Performance Concrete in Highway Bridge Piers." University of Nevada, Reno.

Kabir, A., Nizamud-Doulah, S., and Kamruzzaman, M. "Effective reinforcement layout for skew slabs." *Proc., 27th Conference on our World in Concrete & Structures*, 29-30.

Kang, S.-T., Lee, Y., Park, Y.-D., and Kim, J.-K. (2010). "Tensile fracture properties of an Ultra High Performance Fiber Reinforced Concrete (UHPFRC) with steel fiber." *Composite Structures*, 92(1), 61-71.

Kar, A., Khatri, V., Maiti, P., and Singh, P. (2012). "Study on effect of skew angle in skew bridges."

Kodur, V., Solhmirzaei, R., Agrawal, A., Aziz, E. M., and Soroushian, P. (2018). "Analysis of flexural and shear resistance of ultra high performance fiber reinforced concrete beams without stirrups." *Engineering Structures*, 174, 873-884.

Larsen, I. L., Aasbakken, I. G., O'Born, R., Vertes, K., and Thorstensen, R. T. "Determining the Environmental Benefits of Ultra High Performance Concrete as a Bridge Construction Material." *Proc., IOP Conference Series: Materials Science and Engineering*, IOP Publishing, 052096.

Li, J., Wu, C., and Hao, H. (2015). "Investigation of ultra-high performance concrete slab and normal strength concrete slab under contact explosion." *Engineering Structures*, 102, 395-408.

Mahmud, G. H., Yang, Z., and Hassan, A. M. (2013). "Experimental and numerical studies of size effects of Ultra High Performance Steel Fibre Reinforced Concrete (UHPFRC) beams." *Construction and Building Materials*, 48, 1027-1034.

Maleki, S. (2002). "Deck modeling for seismic analysis of skewed slab-girder bridges." *Engineering Structures*, 24(10), 1315-1326.

Menassa, C., Mabsout, M., Tarhini, K., and Frederick, G. (2007). "Influence of skew angle on reinforced concrete slab bridges." *Journal of Bridge Engineering*, 12(2), 205-214.

Muhamad, R., Ali, M. M., Oehlers, D. J., and Griffith, M. (2012). "The tension stiffening mechanism in reinforced concrete prisms." *Advances in Structural Engineering*, 15(12), 2053-2069.

Nouri, G., and Ahmadi, Z. (2011). "Influence of skew angle on continuous composite girder bridge." *Journal of Bridge Engineering*, 17(4), 617-623.

Oehlers, D. J., Visintin, P., Chen, J. F., and Ibell, T. J. (2014). "Simulating reinforced concrete members. Part 1: partial interaction properties." *Proceedings of the Institution of Civil Engineers: Structures and Buildings*, 167(11), 646-653.

Oehlers, D. J., Visintin, P., Chen, J. F., and Ibell, T. J. (2014). "Simulating reinforced concrete members. Part 2: Displacement-based analyses." *Proceedings of the Institution of Civil Engineers-Structures and Buildings*, 167(12), 718-727.

Pandey, K. K., and Maru, S. (2015). "Modelling of Skew Bridge Deck Slab by Grillage." *International Journal of Engineering Research and General Science*, 3(4), 617-623.

Sindhu, B., Ashwin, K., Dattatreya, J., and SV, D. (2013). "Effect Of Skew Angle On Static Behaviour Of Reinforced Concrete Slab Bridge Decks." *International Journal of Research in Engineering and Technology*, 2(1), 50-58.

Singh, M., Sheikh, A., Ali, M. M., Visintin, P., and Griffith, M. (2017). "Experimental and numerical study of the flexural behaviour of ultra-high performance fibre reinforced concrete beams." *Construction and Building Materials*, 138, 12-25.

Sobuz, H., Visintin, P., Ali, M. M., Singh, M., Griffith, M., and Sheikh, A. (2016). "Manufacturing ultra-high performance concrete utilising conventional materials and production methods." *Construction and Building Materials*, 111, 251-261.

Sturm, A. B., Visintin, P., Ferris, K., and Oehlers, D. J. (2018). "A new testing approach for extracting the shear friction material properties of ultra-high performance fibre reinforced concrete." *ASCE Journal of Materials in Civil Engineering*.

Théoret, P., Massicotte, B., and Conciatori, D. (2011). "Analysis and design of straight and skewed slab bridges." *Journal of Bridge Engineering*, 17(2), 289-301.

Visintin, P., Ali, M. M., Xie, T., and Sturm, A. B. (2018). "Experimental investigation of moment redistribution in ultra-high performance fibre reinforced concrete beams." *Construction and Building Materials*, 166, 433-444.

Visintin, P., Oehlers, D., Wu, C., and Haskett, M. (2012). "A mechanics solution for hinges in RC beams with multiple cracks." *Engineering Structures*, 36, 61-69.

Visintin, P., and Oehlers, D. J. (2016). "Mechanics closed form solutions for moment redistribution of RC beams." *Structural Concrete*.

Visintin, P., and Oehlers, D. J. (2017). "Fundamental mechanics that govern the flexural behaviour of reinforced concrete beams with fibre-reinforced concrete." *Advances in Structural Engineering*, 1369433217739705.

Voo, Y. L., and Foster, S. J. (2010). "Characteristics of ultra-high performance 'ductile' concrete and its impact on sustainable construction." *The IES Journal Part A: Civil & Structural Engineering*, 3(3), 168-187.

Wei, X., and Bruneau, M. (2017). "Analytical investigation of Buckling Restrained Braces' applications in bidirectional ductile end diaphragms for seismic performance of slab-on-girder bridge." *Engineering Structures*, 141, 634-650.

Woodworth, M. A. (2008). "Optimization of Highway Bridge Girders for Use with Ultra-High Performance Concrete (UHPC)." Virginia Tech.

Xie, T., Fang, C., Ali, M. M., and Visintin, P. (2018). "Characterizations of autogenous and drying shrinkage of ultra-high performance concrete (UHPC): An experimental study." *Cement and Concrete Composites*, 91, 156-173.

Xie, T., Mohamad Ali, M. S., Visintin, P., Oehlers, D. J., and Sheikh, A. H. (2018). "A Partial Interaction Model of Flexural Behaviour of PVA Fibre Reinforced Concrete Beams with GFRP Bars." *Journal of Composites for Construction*.

Xie, T., and Ozbakkaloglu, T. (2015). "Behavior of steel fiber-reinforced high-strength concrete-filled FRP tube columns under axial compression." *Engineering Structures*, 90, 158-171.

Xu, S., Wu, C., Liu, Z., Han, K., Su, Y., Zhao, J., and Li, J. (2017). "Experimental investigation of seismic behavior of ultra-high performance steel fiber reinforced concrete columns." *Engineering Structures*, 152, 129-148.

Yeganeh, A. E. (2015). "STRUCTURAL BEHAVIOUR OF REINFORCED HIGH PERFORMANCE CONCRETE FRAMES SUBJECTED TO MONOTONIC LATERAL LOADING."

Yoo, D.-Y., Min, K.-H., Lee, J.-H., and Yoon, Y.-S. (2014). "Shrinkage and cracking of restrained ultra-high-performance fiber-reinforced concrete slabs at early age." *Construction and Building Materials*, 73, 357-365.

Yoo, D.-Y., and Yoon, Y.-S. (2015). "Structural performance of ultra-high-performance concrete beams with different steel fibers." *Engineering Structures*, 102, 409-423.

CHAPTER 8

An Innovative Insulated Sandwich Panel with FRP Reinforced Ultra-high Performance

Concrete Face Sheets：Concept and Behaviour

[1*]Xie, T., [2]Mohamed Ali, M.S., [3]Elchalakani, M., [4]Fang, C.

[1]Mr. Tianyu Xie (Corresponding author)

Ph. D Candidate

School of Civil, Environmental and Mining Engineering

The University of Adelaide

South Australia 5005

AUSTRALIA

[2]Dr M.S. Mohamed Ali

Senior Lecturer,

School of Civil, Environmental and Mining Engineering

The University of Adelaide

South Australia 5005

AUSTRALIA

[3]Dr Mohamed Elchalakani

Senior Lecturer

School of Civil, Environmental and Mining Engineering

The University of Western Australia

Western Australia 6009

AUSTRALIA

[4]Mr Chengfeng Fang

Ph. D Candidate

School of Civil, Environmental and Mining Engineering

The University of Adelaide

South Australia 5005

AUSTRALIA

Statement of Authorship

Title of Paper	AN INNOVATIVE INSULATED SANDWICH PANEL WITH FRP REINFORCED ULTRA-HIGH PERFORMANCE CONCRETE FACE SHEETS : CONCEPT AND BEHAVIOUR
Publication Status	☐ Published ☐ Accepted for Publication ☑ Submitted for Publication ☐ Unpublished and Unsubmitted work written in manuscript style
Publication Details	Xie, T., Ali, M. M., Elchalakani, M & Moya, D. (2018). An Innovative Insulated Sandwich Panel with FRP Reinforced Ultra-high performance Concrete Face Sheets : Concept and Behaviour. Submitted *to Composite Part B: Engineering*.

Principal Author

Name of Principal Author (Candidate)	Tianyu Xie		
Contribution to the Paper	Designing concept, conducting experiments, analysing of data, drafting manuscript		
Overall percentage (%)	40		
Certification:	This paper reports on original research I conducted during the period of my Higher Degree by Research candidature and is not subject to any obligations or contractual agreements with a third party that would constrain its inclusion in this thesis. I am the primary author of this paper.		
Signature		Date	12/02/2019

Co-Author Contributions

By signing the Statement of Authorship, each author certifies that:

i. the candidate's stated contribution to the publication is accurate (as detailed above);

ii. permission is granted for the candidate in include the publication in the thesis; and

iii. the sum of all co-author contributions is equal to 100% less the candidate's stated contribution.

iv. Name of Co-Author	Dr Mohamed Ali Sadakkathulla		
Contribution to the Paper	Designing concept, supervising experiments, analysing of data, proofreading (30%)		
Signature		Date	12/02/2019

Name of Co-Author	Dr Mohamed Elchalakani		
Contribution to the Paper	Designing concept, analysing of data, proofreading (20%)		
Signature		Date	7-2-2019

Please cut and paste additional co-author panels here as required.

Name of Co-Author	Mr Chengfeng Fang		
Contribution to the Paper	Drafting manuscript, analysing of data (20%)		
Signature		Date	12/02/2019

Name of Co-Author	Mr Chengfeng Fang
Contribution to the Paper	Drafting manuscript, analysing of data (20%)

THIS PAGE HAS BEEN LEFT INTENTIONALLY BLANK

ABSTRACT

Inspired by the concept of bubble deck system and aiming to optimize performances of conventional structural panel systems, in the present study, novel forms of light weighted composite sandwich structures are developed and their behaviours are investigated. Three sandwich panels comprised of two basalt fibre reinforced polymer (BFRP) mesh reinforced ultra-high performance concrete (UHPC) faces sheets with their core layers are fabricated by combining light-weighted normal strength mortar and expanded Polystyrene (EPS) foam of different configurations are prepared and tested. The structural responses of these novel sandwich panel are experimentally studied as that they are tested as one-way slabs under three-point flexure bending. In addition to the experimental investigations, elementary sandwich panel theory (EST) and advanced sandwich theory (AST) are applied to provide feasible approaches to predict the behaviours of the sandwich panels at their serviceability limit states. The findings of this study indicate that partially replacing the NSM layer using horizontally placed EPS cylinders in a sandwich panel can effectively reduce the self-weight of the slab without significantly compromising its mechanical properties under flexure, whereas the smooth and flat surface of a EPS foam board causes delamination between the foam and normal strength mortar (NSM) in the core of the sandwich panel system. Moreover, the modified EST and AST can successfully reproduce the behaviour of the composite sandwich panels within their linear elastic material conditions.

Keywords: ultra-high performance concrete (UHPC); basalt fibre reinforced polymer (BFRP) mesh; bubble deck system; sandwich panel; elementary and advanced sandwich theory

8.1 INTRODUCTION

Rising demand for constructing multifunctional buildings requires energy-efficient designs, which are significantly beneficial for a sustainable and low-carbon built-environment (Elchalakani et al. 2018; Elchalakani et al. 2018; Elchalakani et al. 2018). Based on the current statistics, the creation, running, and maintenance of buildings are responsible for around 50% of energy consumption and climate-change emissions worldwide (Omer 2008; Xie et al. 2018; Xie and Visintin 2018). Insulated concrete sandwich panel is a promising technique, which offers a feasible solution to address the current shortcomings seen in conventional building designs. A sandwich panel, as a stiff, light, and robust structural element, typically comprises of two thin face sheets (also known as wythes) and one inner layer of insulation in between the two external layers; and is commonly used for envelopes of wide range of multiunit residential, commercial, and warehouse buildings (Kulpa and Siwowski 2018; Lameiras et al. 2013; Norris and Chen 2016; Tomlinson and Fam 2016). Traditionally, the conventional reinforced concrete layers are utilized as the face sheets in a sandwich panel system to maintain the load bearing capacity of the composite system; and the light weighted material, for instance the expanded Polystyrene (EPS) foam (Mohamed et al. 2015; Norris and Chen 2016), is adopted as the core material to achieve effective and durable thermal insulation in together with absolute water and vapour barrier. As widely recognized, the light weighted precast sandwich panels are sustainable, convenient for construction and can also reduce the cost for fabricating and transporting them (Carlsson and Kardomateas 2011; Choi et al. 2019; Mastali et al. 2015; Wang et al. 2019) and hence they have received considerable practices and research attentions in the last few decades.

The applications of ultra-high performance cementitious composite/concrete (UHPC) in civil engineering area have been undergoing steady growth due to the superior characteristics of the material such as its superior mechanical properties, ductility and better durability-related

properties (Sobuz et al. 2017; Visintin et al. 2018; Xie et al. 2018). Moreover, the use of UHPC materials in buildings and other types of infrastructures can also effectively address the shortcomings of conventional construction work which is rather labour-intensive and time-consuming (Larsen et al. 2017; Sobuz et al. 2016). Due to these advantages, UHPC assists in constructing structural elements with longer spans, reduced member sizes and increased design lives. Recent research and development activities at the University of Adelaide focusing on developing UHPC mix recipe using conventional materials and manufacturing methods will expedite the adoption of UHPC in actual construction due to improved economy (Sobuz et al. 2016; Sturm et al. 2018; Sturm et al. 2018; Sturm 2018; Visintin et al. 2018; Xie et al. 2018). In continuation of these research efforts, the current study aims to adopt such a high performance material as an alternative to conventional concrete as the wythes in sandwich panel systems to keep maintaining the geometry of the composite structures and also to further improve its performance.

In conventional RC structures, the corrosion of steel reinforcements causes significant damage of the structures and economic loss. In the past three decades, fibre reinforced polymer composites of different forms have been well recognized as corrosion-resistant alternatives to conventional steel reinforcements in RC structures (CoDyre and Fam 2016; Xie et al. 2018; Xie and Ozbakkaloglu 2015; Xie and Ozbakkaloglu 2016). Therefore, the replacement of steel reinforcements by the light weighted and highly durable FRP reinforcements in a sandwich panel can further reduce its self-weight, resist the corrosion of the components under extreme environments, and meanwhile maintain the satisfactory mechanical properties of the composite system.

Of late years, many research efforts have been put on developing new forms of sandwich panel systems incorporating UHPC and FRP materials and their behaviours have also been carefully investigated (refs). It has been noticed that the existing research work on UHPC-FRP based sandwich panels systems either used light-weighted concrete or expanded Polystyrene (EPS) foam as the single core material, in which either of them have their own disadvantages structurally. With only using light-weighted concrete, it cannot efficiently reduce the structural dead load (i.e. self-weight) and with only adopting EPS form, it cannot provide sufficient shear resistance to maintain the composite actions of the system. Inspired by the principles of developing bubble deck systems (as depicted in Fig. 8.1), whose core layer is fabricated by virtually eliminating the core concrete which provides insignificant contributions regarding flexural behaviour of the composite panel, by hollow balls (Harding 2004; Lai 2010; Surendar et al. 2016), in the present study, the EPS foam of different configurations are designed to replace core concrete that contributes less to the mechanical properties of a UHPC-FRP sandwich panel. In the proposed novel sandwich panel systems, basalt fibre reinforced polymer (BFRP) mesh reinforced UHPC panels are adopted as the external face sheets/wythes; EPS foam of different configurations (i.e. either as cylinders or a board with drilled holes) wrapped by light-weighted normal strength mortar that acts as stuffing bulking agent and also provides mechanical bond and shear connections to achieve the partial composite action of the system.

Hollow polyethylene balls
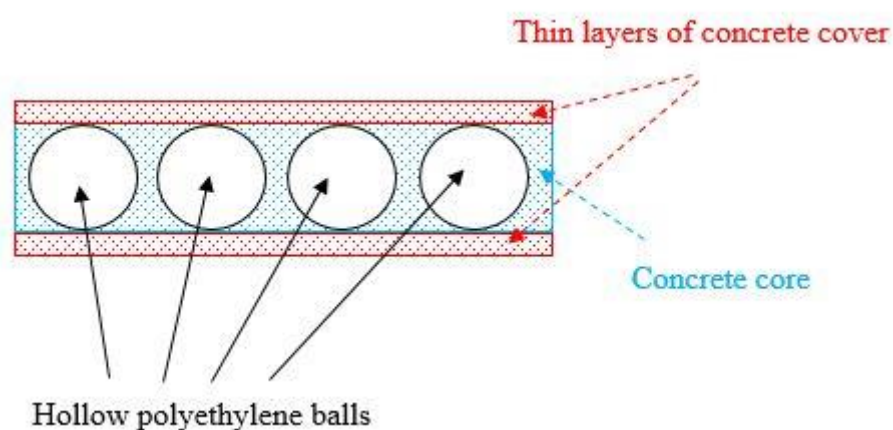
Figure. 8.1 Bubble deck system.

In the present study, three novel UHPC-FRP based sandwich panels, including a reference specimen with only using light-weighted normal strength mortar (NSM) as the core layer and two others with their cores fabricated using the NSM and EPS foam of different configurations, were prepared and tested under flexure. In addition to the experimental investigations, analytical studies were undertaken, where two classical methods for simulating the behaviour of sandwich panels at the serviceability limit state, namely elementary sandwich panel theory (EST) and advanced sandwich theory (AST) were applied with further modifications to accommodate the effects of composite core materials. This research was undertaken with the objectives of:

1). evaluating the feasibility and efficiency of transferring the design philosophy of bubble deck system to design conventional sandwich panel system and;

2). experimentally establishing the performance of the novel UHPC-FRP based sandwich panel systems and;

3). providing reliable approaches for predicting the elastic behaviour of the novel UHPC-FRP based sandwich panels, which could also help to initiate the analysis and design of the novel sandwich panel systems.

Significantly, this study is believed to contribute to civil engineering field by the following aspects:

1). The newly developed sandwich panel systems is promising to be used in civil engineering as that it is produced by revolutionarily combining the advantages of the bubble deck systems

(light-weighted and material efficient) and the sandwich panel systems (energy efficient and cost effective) and;

2). The findings of this study will also redound to facilitate to advancements of the high performance and low cost UHPC and FRP materials into the applications to infrastructures; and;

3). The selected approaches with further modifications can serve as reliable bases for the analysis and design of the novel sandwich panel system; and hence to promote the future research and applications of such an advanced structural element.

8.2. TEST PROGRAM

8.2.1 Principle of designing the novel sandwich panel systems

The novel composite systems reported in the present study were developed following the design philosophies of bubble deck and conventional sandwich panel systems and aiming: 1) to maintain the load bearing capacity and ductility; 2) meanwhile to reduce the self-weight and tendency of corrosion of the components under extreme environments; 3) to rapidly and economically constructed; and 4) to achieve effective and durable thermal insulation in together with absolute water and vapour barrier. Table 8.1 presents the materials selected to construct each component of the composite sandwich panels in conjunctions with their inherent advantages. The experimental program has been devised to evaluate the performance of three different types of sandwich panel systems.

Table. 8.1 Descriptions of materials selected to construct the novel sandwich panels

Materials	Components	Advantages	Density (kg/m^3)
UHPC	Face sheets (Top and bottom)	Superior mechanical and durability-related properties	2342
C30 NSM	Stuffing bulking agent/shear connectors	Commercially-available with desirable mechanical and durability-related properties, acting as stuffing bulking agent with good fluidity	2280
EPS plates or cylinders	Core	Light weighted, chemically stable, lower permeability, not biodegradable	26[*]
BFRP mesh	Reinforcements of face sheets	Light weighted, higher tensile strength, good corrosion resistance	2650[*]

[*] Manufacturer reported properties

8.2.2 One-way slab test specimens

8.2.2.1 Slab configurations

Figure 8.2 (a) to (c) graphically shows the configurations and the components of the three sandwich panel systems investigated in the present study. All the sandwich panels were designed as one-way slabs with dimension of 1500mm × 720mm × 70mm (1440mm clear span). Their top and bottom face sheets were all BFRP mesh reinforced UHPC composite panels of 10mm thickness and different types and configurations of the core materials were utilized. Note that, in each face sheet, the BFRP mesh was embedded in the UHPC matrix to achieve more composite actions. For the reference specimen (Type I sandwich panel), the core material used was only the C30 grade of normal strength mortar (NSM). Type II and III sandwich panels were constructed using the core materials by combining EPS foam and NSM of different configurations. As reported in Shams et al. (Shams et al. 2015), owing to excessive tensile stress exerted in the adhesive zone, the delamination between the face sheets and the core materials (particularly due to the smooth surface of EPS foam) tends to occur. To address this shortcoming, when designing the Type II and III sandwich panels, the NSM was used as stuffing bulking agent as well as shear connector to integrate with the EPS materials and to bond with the face sheets to prevent premature delamination between the face sheets and the core. An EPS foam board (Fig. 8.3 (a)) was used in Type II sandwich panel with drilled holes of 40 mm diameter and at 120 mm spacing to let the stuffing bulking agent (i.e. NSM) to penetrate through them. Instead of using an EPS form board, EPS cylinders (Fig. 8.3 (b)) were adopted in Type III sandwich panel. These cylinders are 30mm in diameter and 1440 mm in length, which were placed horizontally along the long span of the panel to partially replace the NSM. As shown in Fig. 8.2 (b) and (c), the top and bottom of the EPS materials were covered

by a 5 mm-layer of NSM and the bond between NSM and BFRP mesh reinforced UHPC face sheets was achieved using a two-component mortar based solvent free epoxy resin adhesive, namely, Sikadur 30, which is highly flowable and offers an adhesive bond strength over 4 MPa without reacting with cementitious components (i.e. UHPC or NSM). The brief descriptions of the three sandwich panels are summarized in Table 8.2 and as can be seen from the table, for a given size of the sandwich panel, the specimen produced using EPS board had the lowest self-weight (i.e. nearly 50% reduction in the self-weight compared to the reference specimen) and the utilization of EPS cylinders to partially replace the NSM in the system also led to around 25% reduction in its self-weight.

(a)

(b)

(c)

Figure. 8.2 Slab configurations: a) type I; b) type II; c) type III.

(a)   (b)

Figure. 8.3 Different configurations of EPS foam in the core layer: a) EPS foam board with drilled holes; b) horizonally placed EPS foam cylinders.

Table 8.2. Descriptions of each test sandwich panel

Series	Face sheet	Core material	Adhesive material	Self-weight (kg)
Type I (ref)	UHPC-BFRP mesh composite thin panel	NSM	Sikadur 30	170.65
Type II		NSM wrapped EPS foam board		90.88

Type III	NSM wrapped horizontally placed EPS cylinders	130.09	

8.2.2.2 Manufacture process of the novel sandwich panel systems

In order to facilitate the construction process of the sandwich panels, each of their components, including the face sheets, EPS foam in different forms, and NSM were prepared individually and then assembled together. In preparation of each of the face sheets, a layer of UHPC with 5 mm thickness was initially poured into the formwork and its top surface was carefully levelled and smoothed to ensure that the BFRP mesh can be well placed. Following the placement of the BFRP mesh another 5 mm layer of UHPC was poured over the BFRP mesh to complete the construction process of one face sheet. The core layer prepared for type I sandwich panel was simply casted using a 1500mm × 720mm × 50mm NSM based slab. When preparing the core layers for type II and III sandwich panels, an intermediate layer of NSM with 5 mm thickness was initially poured into the formwork. Following this, either EPS foam board with drilled holes or EPS foam cylinders were carefully placed on the top of the NSM layer and the rest of NSM was subsequently poured over it. Due to the good flowability of the NSM prepared using *w/c* ratio of 0.5, only gentle vibrations were applied to ensure the NSM integrated with EPS foam well. After 28-day casting, the prefabricated components including the face sheets and cores were glued together using the epoxy resin adhesive, Sikadur 30. The specimens were continued cured for another 7days under ambient condition to allow the sufficient bond strength developed.

8.2.2.3 Test setup and instrumentations

The three sandwich panels were all tested as one-way slabs and each of them was simply supported at each short edge and the load was applied at the middle span of each slab through a spread steel I-beam. Schematic and view of the test set-up and instrumentations used are shown in Fig. 8.4. To measure the vertical deflections of each slab, a total of four LVDTs were used, including three placed underneath each of the slabs and another one mounted on the loading ram to measure its vertical displacement. A universal testing machine with 1000 kN load capacity was used to apply monotonically increasing load at the mid-span of each of the slabs. For each slab test, the load was continuously applied at a rate of 5 kN/min until the peak load was attained and thereafter the load was applied under displacement control at a displacement rate of 0.1 mm/min until failure to obtain the complete load-defection relationship.
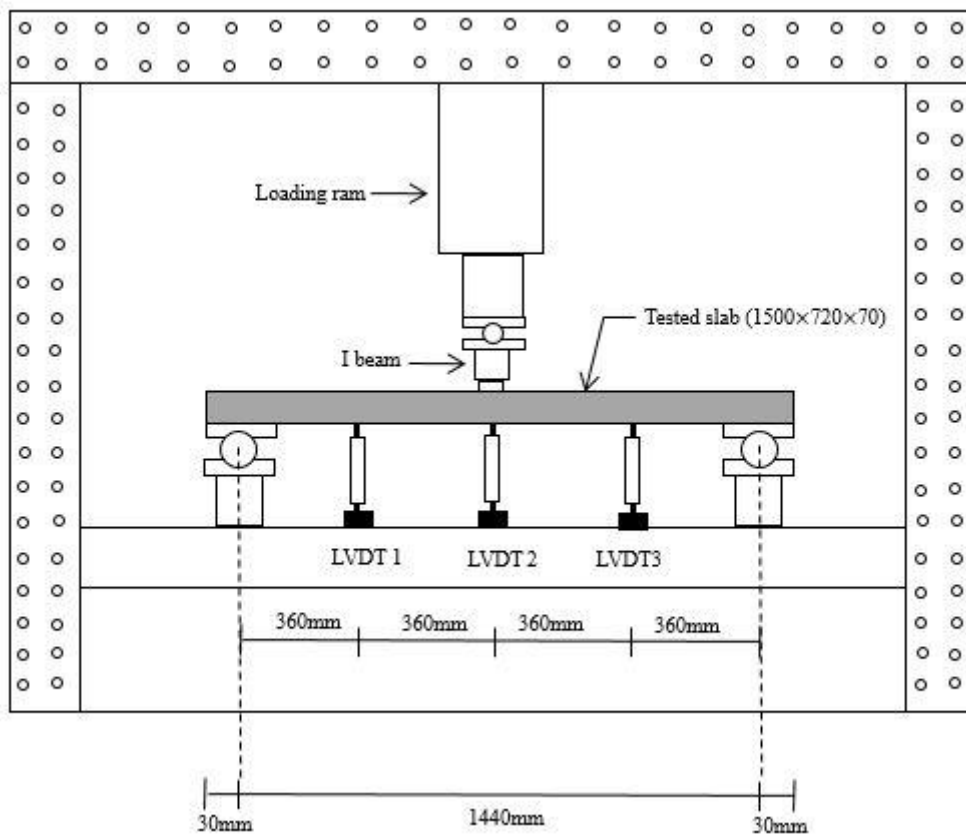
(a)

Figure. 8.4 Slab test details: a) setup and instrumentiaons: b) elevation of a slab test.

8.2.3 Tests of materials properties

8.2.3.1 Compression tests

The mix proportions of the UHPC and NSM are summarized in Table 8.3. To obtain the compressive stress-strain relationships of the UHPC and NSM, uniaxial compression tests were conducted on cylindrical specimens with 100 mm diameter and 200 height as per ASTM C469/C469M-14 (ASTM International 2014). The compressive behaviour of EPS foam was established using cubic specimens with dimension of 75 mm. Fig. 8.5 illustrates the representative EPS foam specimen after flatwise compression test, where the representative compressive stress-strain curves of the UHPC, NSM and EPS foam are shown in Fig. 8.6 (a) to (c).

Figure. 8.5 The representative EPS foam specimen after flatwise compression test.

(a)

(b)

(c)
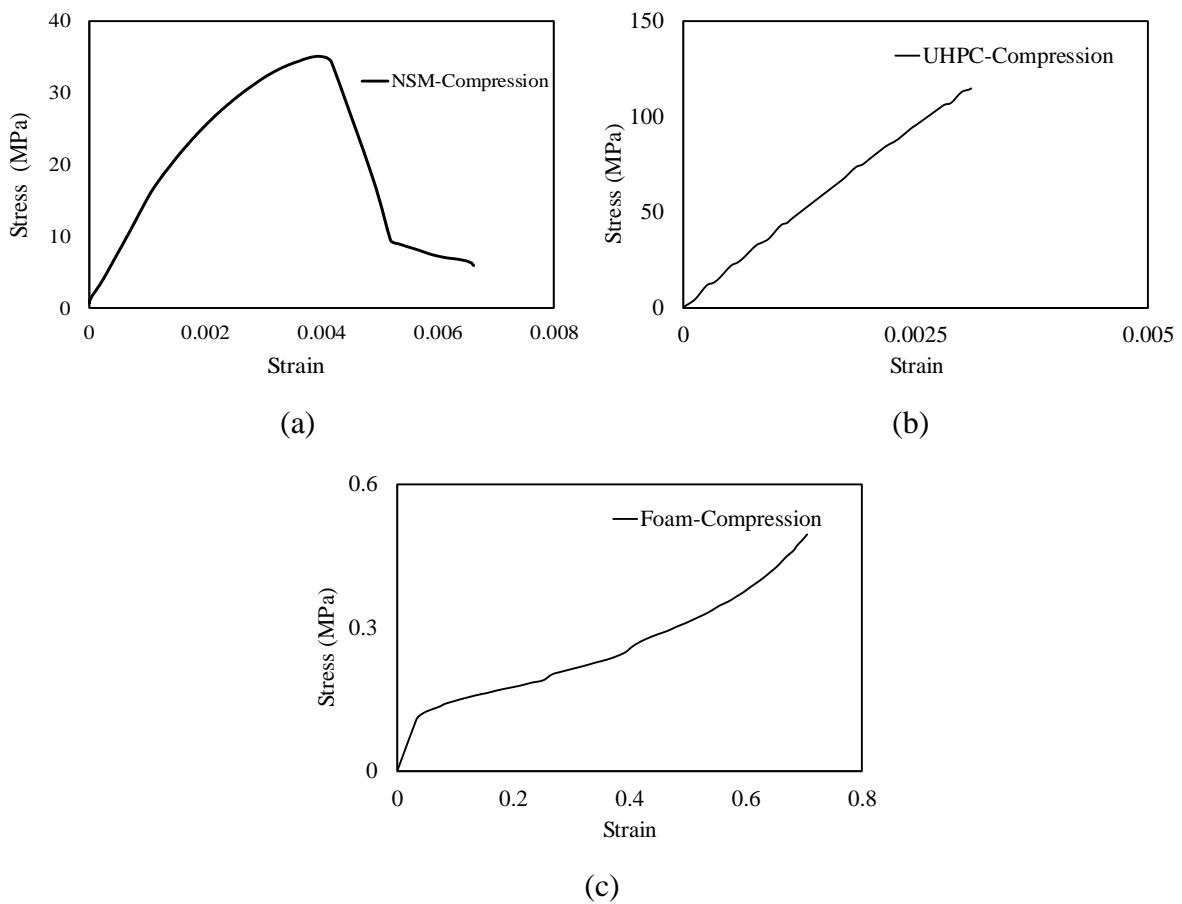
Figure. 8.6 Compressive stress-strain relasitonship of: a) C30 NSM; b) UHPC; c) EPS foam

Table 8.3. Mix proportions of the UHPC and NSM

Material	Sulfate Resistant Cement (kg)	Silica Fume (kg)	Sand (kg)	Water (kg)	SP (kg)	*w/b* ratio
UHPC	0.79	0.21	1.00	0.12	0.06	0.13
NSM	0.8	-	1.28	0.4		0.5

8.2.3.2 Direct tension tests

The direct tensile stress-strain behaviours of the components, including UHPC, BFRP mesh, EPS and BFRP mesh reinforced UHPC composite were also experimentally established. Two types of dog-bone shaped specimens were used for the direct tension tests of UHPC and BFRP mesh reinforced UHPC composite and the specimens were tested under displacement control at a constant rate of 0.025 mm/s. Their typical failure modes under direct tension are illustrated in Fig. 8.7 (a) and (b). EPS foam's flatwise tensile behaviour was determined using cubic specimens with dimension of 75 mm and the typical failure mode of the EPS foam under direct tension is shown in Fig. 8.7 (c). The BFRP mesh with 10 mm × 10 mm mesh size was fabricated using unidirectional fibre strip of 10 mm nominated width and 0.18 mm nominated thickness and the tensile properties of the BFRP material were obtained flat coupon tests as per ASTM D3039M-08 (ASTM International 2008). The representative tensile stress-stain curves of including UHPC, EPS and BFRP mesh reinforced UHPC composite are illustrated in Fig. 8.8 (a) to (c).

(a)

263

Figure. 8.7 Typeical tensile failure mode of: a) UHPC; b) UHPC-BFRP mesh composite; c)
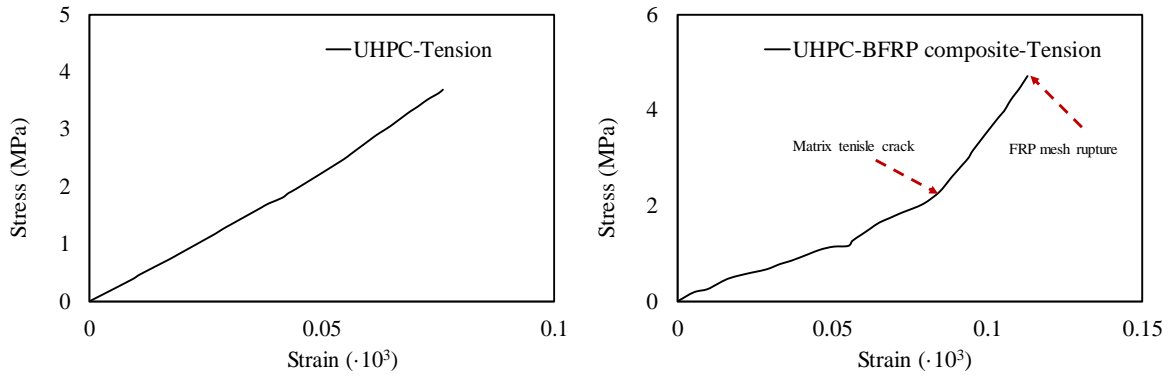
EPS foam.

(a)   (b)
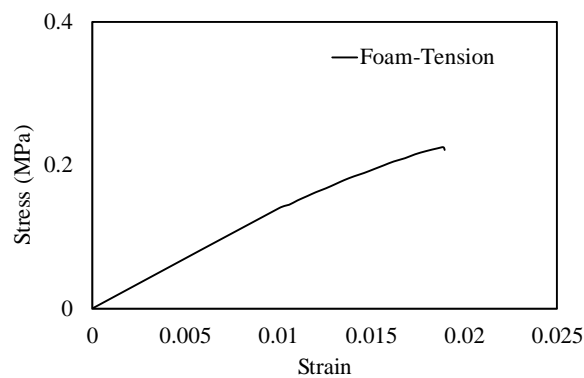
(c)

Figure. 8.8 Tensile stress-strain relasitonship of: a) UHPC; b) UHPC-BFRP mesh composite;

c) EPS foam.

The key properties of each component established using the compression and tension tests,

including their elastic modulus (E), Poisson's ratio (v), compressive and tensile strength (f'_c

and f_t, respectively) in together with the calculated shear modulus (G) using Eq. (8.1) are also

summarized in Table 8.4.

$$G = \frac{E}{2(1 \times v)} \qquad (8.1)$$

Table 8.4. Summary of material properties

Material	Compressive strength, f'_c (MPa)	Tensile strength, f_t (MPa)	Poisson's ratio, v	Elastic modulus, E (MPa)	Shear mdoulus, G (MPa)	Yield stress (MPa)
UHPC	114.7	3.7	0.213	44800	18467	
NSM	35.2		0.202	15600	6489	
UHPC-BFRP composite		4.72				
BFRP		2200		97000		
EPS foam		0.225	0.105[*]	6.09	2.8	0.12

[*] Manufacturer reported properties

8.3 EXPERIMENTAL RESULTS AND DISCUSSIONS

8.3.1 General observations of slab tests

The failure modes of all sandwich panels are shown in Fig. 8.9 (a) to (c). The observed failure modes of type I and III panels are typical flexural failure modes with a major tensile crack initially appeared on the bottom face sheet at their mid-span and then gradually propagated towards the neutral axis position. Consequently, types I and III panels both failed due to the tensile fracture of the bottom face sheet and crushing of the top sheet. Note that the change of the configuration of the core layer resulted no distinct difference in the failure mode of the sandwich panels. However, type II panel experienced an unexpected premature failure due to the delamination occurred at the interface between the NSM and the EPS foam plate in the core right after the formation of the primary tensile crack. This premature failure was further inspected and the details are shown in Fig. 8.10. It is worth mentioning that the NSM still bonded tightly with the bottom UHPC face sheet after the debonding occurred between the NSM and the EPS layers. As is evident from Fig. 8.10, the debonding occurred between the

NSM layer and the EPS board is mainly due to the relatively flat and smooth surface of the

EPS board, which offered weaker mechanical bond between the two components.

(a)
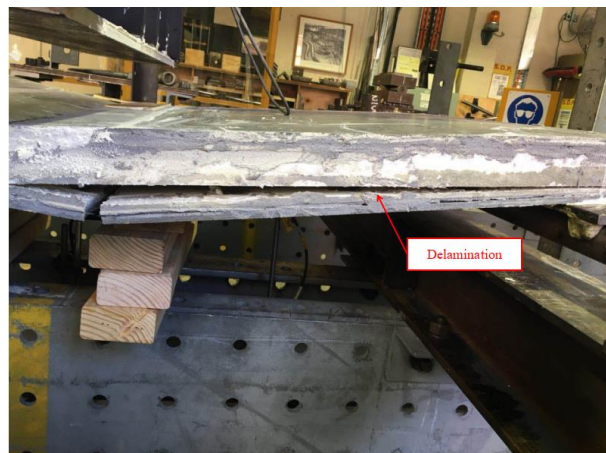
(b)

(c)

Figure. 8.9 Failure modes of: a) type I sandwich panel; b) type II sandwich panel; c) type III sandwich panel.
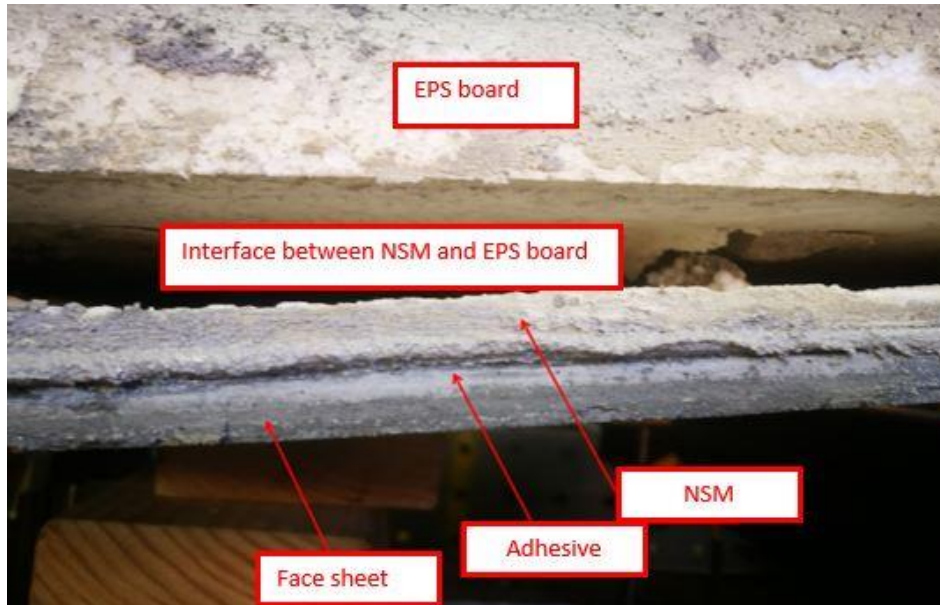
Figure. 8.10 Inspections of failure mode of type II sandwich panel.

8.3.2 Load-deflection relationship

The experimentally-recorded load-deflection curves of the three sandwich panel systems are illustrated in Fig. 8.11. As can be seen from the figure, the relationship between the applied load and the deflection measured at the mid-span of type I and III sandwich panels nearly followed a nearly identical linear ascending trend till reaching the peak load. It is also observed that the panel produced using EPS foam cylinders exhibited a slightly lower flexural rigidity on the initial ascending branch of its load-deflection curve compared to those of type I and III specimens owing to the relative lower stiffness of EPS foam. Type I and III sandwich panels showed sudden drops in their load bearing capacity immediately after the peak point in their load-deflection curves and no significant yielding plateau was observed due to that no conventional steel reinforcements were used in both the sandwich panel systems. With the incorporation of the EPS foam in its core layer, type III panel exhibited slightly improved ductile behaviour compared to that of the reference panel, in terms of its longer descending branch with a decreased slope of the load-deflection curve. For type II panel which experienced

premature failure caused by the delamination along the interface between the NSM and the EPS forma board, prior to the debonding occurred, the comparisons of the load-deflection curves between type II panel and the other two panels, as shown in Fig. 8.11, indicate that type II panel produced using EPS at a highest volume among the three comparing specimens exhibited significantly lower flexural stiffness.
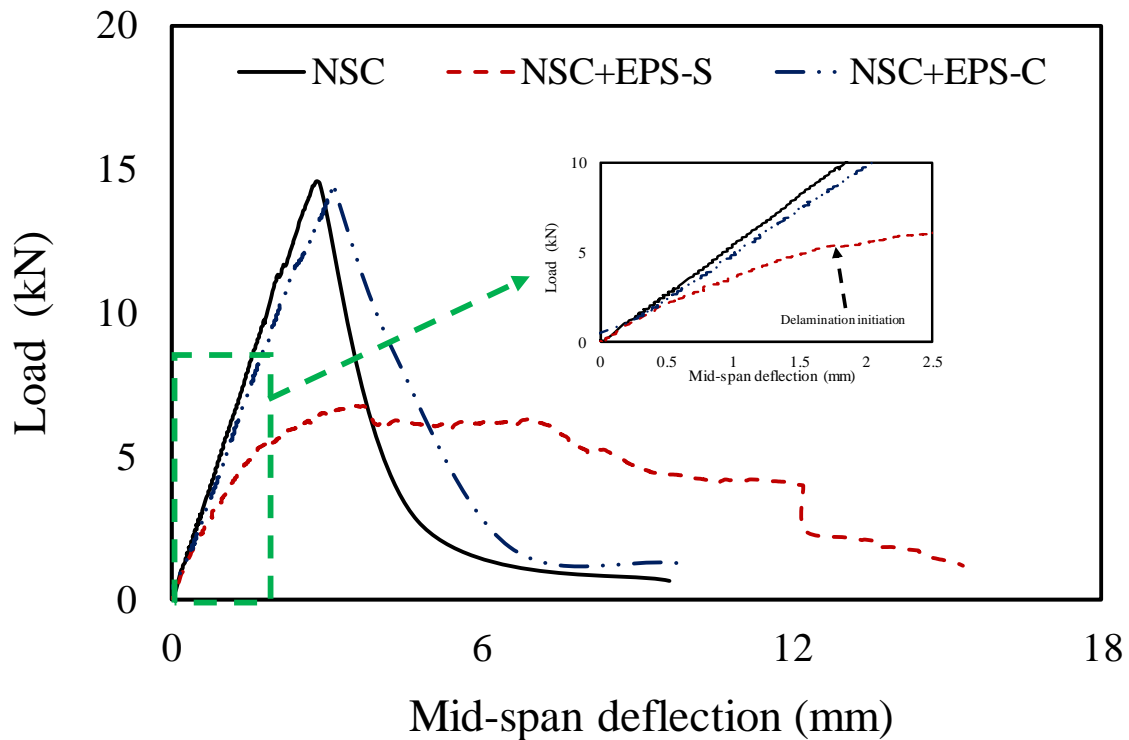
Figure. 8.11 Load-deflection relationship of the sandwich panels.

8.4 ANALYTICAL MODELS FOR PREDICTING THE ELASTIC LOAD-DEFLECTION OF THE SANDWICH PANELS

The two widely accepted analytical methods for sandwich panel system in the literature, namely Elementary Sandwich Panel Theory (EST) proposed by Allen (Allen 1969) and Advanced Sandwich Panel Theory (AST) reported in (Allen 2013) are used in this study to provide analytical solutions for the behaviour of the newly-developed sandwich panel system. In this section, these two methods are applied by maintaining their original forms or with

further modifications to evaluate the feasibilities of using them to simulate the structural responses of the three novel UHPC-based sandwich panel systems at their serviceability limit states, that is, the behaviour of the panels under linear elastic material conditions.

8.4.1 Elementary sandwich panel theory (EST)

The modified EST method adopted in the present study to simulate the elastic load-deflection behaviour of the sandwich panels with thin face sheets proposed in the present study. The modifications of the EST method were made to accommodate the properties of composite core materials through the superposition of the properties of the components, whereas the method was originally only considered a single of type of core material in a sandwich panel system. The details of the modified are given in the remainder of this section.

Taking $h/2$ location as centroid axis, the flexural rigidity (D) of a sandwich panel can be expressed as:

$$D = E_f \cdot (bt^3/6) + E_f \cdot (btd^2/2) + E_c \cdot (bc^3/12) \tag{8.2}$$

where E_f and E_c are elastic moduli of face and core materials, respectively, and t is the thickness of a face sheet, b is the width of the panel cross-section, d is the distance between centre lines of top and bottom faces. For core formed by combining different types of materials, based on the superposition principle of strength of materials, its elastic modulus can be determined by evaluating the volumetric average moduli as follows:

$$E_c = \frac{E_{c-foam} \cdot vr_{foam}\% + E_{c-NSM} \cdot vr_{NSM}\%}{100\%} \tag{8.3}$$

where $E_{c\text{-}foam}$ and E_{c-NSM} are the elastic modulus of the foam and the NSM in the core layer, respectively and $vr_{foam}\%$ and $vr_{NSM}\%$ are the volumetric fraction of the foam and the NSM

in the core layer, respectively. Note that in Eq. (8.2), the first and third components represent the second moments of the area of the face sheets about their own centroids and the bending stiffness of the core; the second component is the second moments of the area of the face sheets about the centroid of the sandwich panel. Considering that the face sheets are relatively thin and the properties of the core materials are inferior, their contributions towards the overall performance of a sandwich panel may not be significant and hence their effects might be neglected when the following conditions applied:

$$\frac{E_f \cdot (bt^3/6)}{E_f \cdot (btd^2/2)} = \frac{1}{3(d/t)^2} < 1\% \tag{8.4}$$

$$\frac{E_c \cdot (bc^3/12)}{E_f \cdot (btd^2/2)} = \frac{1}{6(E_f/E_c)(t/c)(d/t)^2} < 1\% \tag{8.5}$$

Having the flexural rigidity (E_cI) established, at its serviceability limit state, the deflection of a sandwich caused by flexure can be easily determined using:

$$\Delta_1 = \frac{PL^3}{48D} \tag{8.6}$$

The generic equations of calculating the deflection caused by shear are given as:

$$\Delta_2 = \frac{PL}{4U} \tag{8.7}$$

where the shear rigidity U is:

$$U = G_c \cdot A \tag{8.8}$$

and:

$$A = \frac{b \cdot d^2}{c} \tag{8.9}$$

Note that in the original expressions reported in (Allen 1969), G_c represents the shear modulus of a single type of material, which may not be applicable for the current cases using composite

core layer (i.e. type II and III panels which have composite materials in there cores). Therefore, the shear modulus G used in Eq. (8.8) is modified to accommodate the properties of composite core materials and their volumetric fraction, which can be expressed as:

$$G_c = \frac{G_{foam} \cdot vr_{foam}\% + G_{NSM} \cdot vr_{NSM}\%}{100\%} \tag{8.10}$$

And the total deflection of a sandwich panel (Δ_{total}) can be obtained by summing the deflections caused by flexure and shear, which is:

$$\Delta_{total} = \Delta_1 + \Delta_2 \tag{8.11}$$

8.4.2 Advanced sandwich theory (AST)

Considering the deflection due to bending is more localized on thicker face sheets comparing to that is on thinner faces sheets on a sandwich panel (Allen 2013), the assumption in the EST that the shear deflection occurs only at the vertical direction may not be appropriate for calculating the deflection of a sandwich panel with thicker face sheets. In this AST, the deflection components caused by shear in the EST is refined as:

$$\Delta_2 = \frac{PL}{4U} \cdot (1 - \frac{I_f}{I}) \cdot \varphi_1 \tag{8.12}$$

where I is the second moments of area of the face sheets about the centroid of a sandwich panel; I_f is the sum of the second moments of area of the face sheets about their own centroid; the parameter φ_1 can be calculated using Eqs. (8.13) and (8.14).

$$\varphi_1 = 1 - \frac{\sinh\theta + \tanh\theta \cdot (1 - \cosh\theta)}{\theta} \tag{8.13}$$

where the parameter θ is:

$$\theta = \frac{L}{c}\left[\frac{G_c}{2E_f}\frac{c}{t}\left(1 + \frac{3d^2}{t^2}\right)\right]^{0.5} \tag{8.14}$$

8.4.3 Validations of model predictions.

Figure. 8.12 (a) and (c) show the comparisons between the experimental results (i.e. the results of type I and II panels which failed under flexure) and the predictions using both analytical methods. It can be seen from the figures that both the methods can well-predict the load-deflection relationship of the sandwich panels at their serviceability limit states. Note that due to the overestimation of the shear deflection of a sandwich panel by the modified EST, the EST method slightly overestimated the overall deflection of the slab at a given load compared to the AST. Note that the theoretical elastic load-deflection relationship of type II slab, which experienced premature failure, was also simulated using the AST and compared with the theoretical curves generated using the AST of other two slabs. The comparisons show in Fig. 8.12 (b) indicates that due to the higher volumetric ratio of the EPS foam used in the core of the sandwich panel, type II panel exhibited a lower flexural rigidity compared to the other two panels at their serviceability limit states. This finding using the analytical mode is in support of the observation from the experiment as introduced in Section 3.2.

(a)   (b)

272
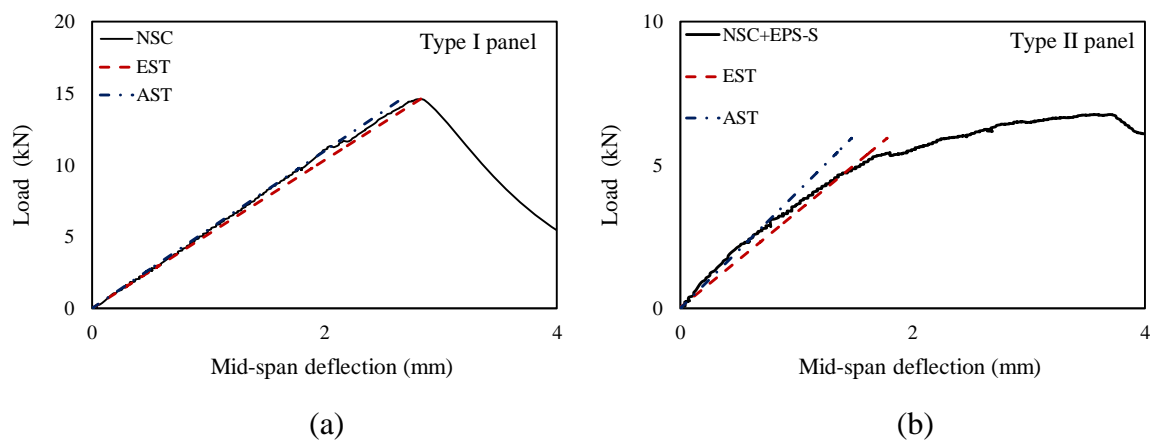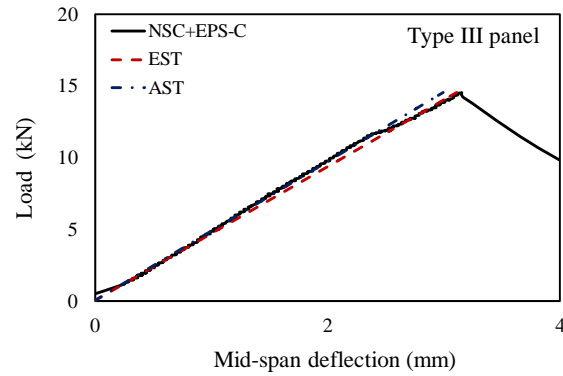
(c)

Figure. 8.12 Comparisons among theoretical and experimental results: a) Type I panel; b) type II panel; c) type III panel.

8.5 CONCLUSIONS

The purpose of the current study was to develop sandwich panel systems as per the design philosophy of bubble deck system. The newly-developed sandwich panel systems were produced by combining high strength and ductility of BFRP mesh reinforced UHPC face sheets, highly flowable normal strength mortar and light weighted EPS foam of different configurations. The sandwich panels were tested as one-way slabs under pure bending and their physical and mechanical properties were experimentally established. In addition to the experimental investigations, the behaviours of the sandwich panels at their serviceability limit states were modelled using the modified elementary sandwich panel theory and the advanced sandwich panel theory. Based on the experimental and theoretical investigations, the following conclusion can be drawn:

1. The design philosophy of bubble deck systems can be feasibly transferred to design sandwich systems.

273

2. Partially replaced the NSM layer using horizontally placed EPS cylinders in a sandwich panel can effectively reduce the self-weight of the slab without significantly compromising its mechanical properties.

3. The proper inclusion of EPS foam into a sandwich panel (i.e. of horizontally placed cylinders) maintain the load-carrying capacity and slightly improve the ductility of the system under bending compared to those of its conventional form without using EPS foam.

4. Using C30 grade of NSM as stuffing bulking agent to warp the EPS foam cylinders in the core layer can provide adequate shear connections for the components to prevent the premature shear failure of the sandwich panel.

5. For the core layer of a sandwich panel with combining NSM and EPS foam board, the smooth and flat surface of an EPS foam board is not beneficial for creating a strong mechanical bond between it and the adjacent NSM layer, where the delamination tends to occur. It is hence recommended to apply adhesive layer between the EPS and the NSM for future construction of Type II sandwich panel

6. The modified EST with considering the composite action between foam and NSM in the core of a sandwich panel can accurately predict its load-deflection behaviour at the serviceability limit state with only a slight overestimation.

7. The AST with correcting the refined the shear deflection components from the EST can more accurately predict the elastic behaviour load-deflection behaviour at the serviceability limit state of the system.

8.6 REFERENCES

Allen, H. (1969). "Analysis and Design of Structural Sandwich Panels London Pergamon Press."

Allen, H. G. (2013). *Analysis and design of structural sandwich panels: the commonwealth and international library: structures and solid body mechanics division*, Elsevier.

ASTM International (2008). "ASTM D3039/D3039M–08, Standard Test Method for Tensile Properties of Polymer Matrix Composite Materials." *ASTM International, West Conshohocken*.

ASTM International (2014). "ASTM C469/C469M-14. Standard Test Method for Static Modulus of Elasticity and Poisson's Ratio of Concrete in Compression." *ASTM International, West Conshohocken*.

Carlsson, L. A., and Kardomateas, G. A. (2011). *Structural and failure mechanics of sandwich composites*, Springer Science & Business Media.

Choi, W., Jang, S.-J., and Yun, H.-D. (2019). "Design properties of insulated precast concrete sandwich panels with composite shear connectors." *Composites Part B: Engineering*, 157, 36-42.

CoDyre, L., and Fam, A. (2016). "The effect of foam core density at various slenderness ratios on axial strength of sandwich panels with glass-FRP skins." *Composites Part B: Engineering*, 106, 129-138.

Elchalakani, M., Dong, M., Karrech, A., Li, G., Mohamed Ali, M., Xie, T., and Yang, B. (2018). "Development of Fly Ash-and Slag-Based Geopolymer Concrete with Calcium Carbonate or Microsilica." *Journal of Materials in Civil Engineering*, 30(12), 04018325.

Elchalakani, M., Hassanein, M., Karrech, A., Fawzia, S., Yang, B., and Patel, V. "Experimental tests and design of rubberised concrete-filled double skin circular tubular short columns." *Proc., Structures*, Elsevier, 196-210.

Elchalakani, M., Karrech, A., Dong, M., Ali, M. M., and Yang, B. "Experiments and Finite Element Analysis of GFRP Reinforced Geopolymer Concrete Rectangular Columns Subjected to Concentric and Eccentric Axial Loading." *Proc., Structures*, Elsevier, 273-289.

Harding, P. (2004). "BubbleDeck–Advanced structure engineering." *BubbleDeck article*, 4-7.

Kulpa, M., and Siwowski, T. (2018). "Stiffness and strength evaluation of a novel FRP sandwich panel for bridge redecking." *Composites Part B: Engineering*.

Lai, T. (2010). "Structural behavior of BubbleDeck® slabs and their application to lightweight bridge decks." Massachusetts Institute of Technology.

Lameiras, R., Barros, J., Valente, I. B., and Azenha, M. (2013). "Development of sandwich panels combining fibre reinforced concrete layers and fibre reinforced polymer connectors. Part I: Conception and pull-out tests." *Composite Structures*, 105, 446-459.

Larsen, I. L., Aasbakken, I. G., O'Born, R., Vertes, K., and Thorstensen, R. T. "Determining the Environmental Benefits of Ultra High Performance Concrete as a Bridge Construction Material." *Proc., IOP Conference Series: Materials Science and Engineering*, IOP Publishing, 052096.

Mastali, M., Valente, I. B., Barros, J. A., and Gonçalves, D. M. (2015). "Development of innovative hybrid sandwich panel slabs: Experimental results." *Composite Structures*, 133, 476-498.

Mohamed, M., Anandan, S., Huo, Z., Birman, V., Volz, J., and Chandrashekhara, K. (2015). "Manufacturing and characterization of polyurethane based sandwich composite structures." *Composite Structures*, 123, 169-179.

Norris, T. G., and Chen, A. (2016). "Development of insulated FRP-confined Precast Concrete Sandwich panel with side and top confining plates and dry bond." *Composite Structures*, 152, 444-454.

Omer, A. M. (2008). "Energy, environment and sustainable development." *Renewable and sustainable energy reviews*, 12(9), 2265-2300.

Shams, A., Stark, A., Hoogen, F., Hegger, J., and Schneider, H. (2015). "Innovative sandwich structures made of high performance concrete and foamed polyurethane." *Composite Structures*, 121, 271-279.

Sobuz, H., Visintin, P., Ali, M. M., Singh, M., Griffith, M., and Sheikh, A. (2016). "Manufacturing ultra-high performance concrete utilising conventional materials and production methods." *Construction and Building Materials*, 111, 251-261.

Sobuz, H. R., Oehlers, D. J., Visintin, P., Hasan, N. M. S., Hoque, M. I., and Akid, A. S. M. (2017). "Flow and Strength Characteristics of Ultra-high Performance Fiber Reinforced Concrete: Influence of Fiber Type and Volume-fraction." *Journal of Civil Engineering and Construction*, 6(1), 15.

Sturm, A., Visintin, P., Oehlers, D., and Seracino, R. (2018). "Time-Dependent Tension-Stiffening Mechanics of Fiber-Reinforced and Ultra-High-Performance Fiber-Reinforced Concrete." *Journal of Structural Engineering*, 144(8), 04018122.

Sturm, A. B., Visintin, P., Ferris, K., and Oehlers, D. J. (2018). "A new testing approach for extracting the shear friction material properties of ultra-high performance fibre reinforced concrete." *ASCE Journal of Materials in Civil Engineering*.

Sturm, A. B., Visintin, P., Oehlers, D.J., Seracino, R (2018). "Time dependent tension stiffening mechanics of fibre reinforced and ultra-high performance fibre reinforced concrete." *ASCE Journal of Structural Engineering*.

Surendar, M., Ranjitham, M., and Scholar, P. (2016). "Numerical and Experimental Study on Bubble Deck Slab." *Department of Civil Engineering, Dr. Mahalingam College of Engineering and technology, Coimbatore, India*.

Tomlinson, D., and Fam, A. (2016). "Analysis and parametric study of partially composite precast concrete sandwich panels under axial loads." *Journal of Structural Engineering*, 142(10), 04016086.

Visintin, P., Ali, M. M., Xie, T., and Sturm, A. B. (2018). "Experimental investigation of moment redistribution in ultra-high performance fibre reinforced concrete beams." *Construction and Building Materials*, 166, 433-444.

Wang, Z., Li, Z., and Xiong, W. (2019). "Experimental investigation on bending behavior of honeycomb sandwich panel with ceramic tile face-sheet." *Composites Part B: Engineering*, 164, 280-286.

Xie, T., Elchalakani, M., Mohamed Ali, M. S., Dong, M., Karrech, A., and Li, G. (2018). "Mechanical and durability properties of self-compacting concrete with blended binders." *Computers and Concrete, An International Journal*, 22(4).

Xie, T., Fang, C., Ali, M. M., and Visintin, P. (2018). "Characterizations of autogenous and drying shrinkage of ultra-high performance concrete (UHPC): An experimental study." *Cement and Concrete Composites*, 91, 156-173.

Xie, T., Mohamad Ali, M. S., Visintin, P., Oehlers, D. J., and Sheikh, A. H. (2018). "A Partial Interaction Model of Flexural Behaviour of PVA Fibre Reinforced Concrete Beams with GFRP Bars." *Journal of Composites for Construction*.

Xie, T., and Ozbakkaloglu, T. (2015). "Behavior of steel fiber-reinforced high-strength concrete-filled FRP tube columns under axial compression." *Engineering Structures*, 90, 158-171.

Xie, T., and Ozbakkaloglu, T. (2016). "Behavior of recycled aggregate concrete-filled basalt and carbon FRP tubes." *Construction and Building Materials*, 105, 132-143.

Xie, T., and Visintin, P. (2018). "A unified approach for mix design of concrete containing supplementary cementitious materials based on reactivity moduli." *Journal of Cleaner Production*, 203, 68-82.

CHAPTER 9

THESIS OUTCOMES

Despite the steady growth in the popularity of fact that the popularity of high- and ultra-high performance concrete, many uncertainties still exist regarding the materials time-dependent behaviour and the performance of structural elements at all limit states. The research work presented in this thesis aims to contribute to the current state-of-the-art at both a material and structural as follows:

At material level

Autogenous shrinkage predominates the overall shrinkage of UHPC, this is in contrast to conventional concrete in which it is often an order of magnitude lower than drying shrinkage. With the aim of reducing the shrinkage of UHPC, three techniques including reducing the binder content, incorporating high levels of shrinkage reducing admixture, and using crushed ice to partially replace mixing water were investigated and shown to reduce shrinkage without significantly compromising its mechanical strength. In addition to the modifications of the UHPC matrix, it was found that incorporations of randomly distributed discrete steel fibres into a UHPC mortar mix can also effectively reduce the total- and autogenous- shrinkage of the concrete. Further it was shown how the configurations of the included fibres, in terms of their volume fraction, shape and geometry, also affect the efficacy of reducing the shrinkage impacts.

At structural level

To aid in the development of a design guideline for fibre-reinforced flexural members, a generic analytical approach, which is equally applicable to both conventional concrete and FRC beams reinforced with steel or FRP reinforcing bars is applied. Predicted load-deflection and load crack width responses are in very good correlation for the results of the pilot experimental study on flexural behaviour of simply-supported fibre reinforced concrete members, showing the reliability of this developed approach.

Further investigations on FRC, UHPC and UHPFRC members with more complicated forms, the results of an experimental study of the moment redistribution capacity of four two-span continuous beams constructed from ultra-high performance fibre reinforced concrete (UHPFRC) show that for beams where the hinge formed at the support, the observed moment redistribution was greater than the code predictions. However for the beam where the hinge formed under the load points, observed moment redistribution was significantly less than codes predictions. Hence, the results of this study show current design guidelines do not always provide a conservative prediction of moment redistribution in UHPFRC beams. Moreover, the behaviour of two types of non-orthogonal structural members made of UHPFRC namely

simply-supported skew slab and fixed end curved beam, are experimentally studied. The experimental results indicate that due to the strain-hardening behaviour of FRC and UHPFRC materials under tension, a non-orthogonal UHPFRC flexural member even exhibits improved load carrying capacity and ductility over the conventional straight reinforced concrete flexural elements. The responses of these non-orthogonal UHPFRC flexural members under combined flexure and torsion at the serviceability- and ultimate- limit states are numerically and analytically modelled using the developed PI based approach and energy theorems.

Finally, beside the conventional forms of structural elements, inspired by the concept of bubble deck system and also aiming to optimize performances of conventional structural panel systems, novel forms of light weighted composite sandwich structures comprised of two basalt fibre reinforced polymer (BFRP) mesh reinforced UHPC faces sheets and their core layers were fabricated by combining light-weighted normal strength mortar and expanded Polystyrene (EPS) foam of different configurations are developed and their behaviours are investigated. The findings of this research work indicates that partially replacing the normal strength mortar (NSM) layer with horizontally placed EPS cylinders in a sandwich panel can effectively reduce the self-weight of the slab without significantly compromising its mechanical properties under flexure, whereas the smooth and flat surface of a EPS foam board led to delamination between the foam and NSM. Modified elementary sandwich panel theory (EST) and advanced sandwich theory (AST) are applied to successfully predict the behaviour of the composite sandwich panels within their linear elastic material conditions.

RECOMMENDATIONS FOR FUTURE RESEARCH

Following on from the research work presented in this thesis, further extensions of the investigation on high- and ultra-high performance concrete should be undertaken:

At material level:

To conduct studies on the behaviour of FRC, UHPC and UHPFRC materials subjected to sustainable static loads (creep) and dynamic loads (fatigue) and;

To develop reliable material models to quantify time-dependent behaviour of the high- and ultra-high performance concrete and;

To develop new mixing methods or techniques to manufacture FRC and UHPFRC structural elements with tightly controlled fibre orientation and distribution.

At structure level

To develop structural models that accommodate these time-dependent properties of FRC, UHPC and UHPFRC and;

To establish the constitutive law for the interfacial properties between the high-/ultra-high-performance concrete and conventional concrete and;

Hence to explore the feasibility of using high- and ultra-high- performance concrete only as the critical components on structures (i.e. beam-column joint, plastic hinge) which predominates the performance of the whole members.

APPENDIX I

Copy of Paper 1 (As published)

Copy of Paper 3 (As published)

Copy of Paper 4 (As published)

Characterizations of autogenous and drying shrinkage of ultra-high performance concrete (UHPC): An experimental study

T. Xie, C. Fang, M.S. Mohamad Ali, P. Visintin*

School of Civil, Environmental and Mining Engineering, The University of Adelaide, South Australia 5005, Australia

A B S T R A C T

Due to the high content of binder and low water to cement ratio, ultra-high performance concrete (UHPC), exhibits higher levels of autogenous shrinkage compared to ordinary concrete. This shrinkage has been shown to lead to a reduction in strength over time as a result of the formation of thermal and shrinkage cracks. Aiming to mitigate the negative impacts associated with shrinkage, the efficacy of three different techniques to reduce the impact of shrinkage are investigated, namely: reducing the binder content; incorporating high levels of shrinkage reducing admixture; and using crushed ice to partially replace mixing water. The effects of these techniques are experimentally investigated and the underlying mechanisms of the actions are characterized. It is found that autogenous shrinkage predominates the overall shrinkage of UHPC and that the three techniques can effectively reduce shrinkage without significantly compromising its mechanical strength. The results also suggest, that from the perspective of reducing shrinkage: the optimal binder-to-sand ratio is in the range of 1–1.1; the optimal dosage rate of shrinkage reducing admixture is 1%; and replacing of mixing water by crushed ice up to 50% by weight has also induced a significant reduction in shrinkage.

1. Introduction

Ultra-high performance concrete (UHPC) is characterized by very high compressive strength and superior durability [1–5]. These characteristics are typically achieved using mix designs with high quantities of binder (cement and silica fume) and low water to cement ratios (in the order of 0.2 or less). As a result, partially hydrated binder is often present within the mortar resulting in an increase in autogenous shrinkage [6,7] up to an order of magnitude greater than that of conventional concrete [8–13]. Hence total shrinkage strains in UHPC (including both the autogenous- and drying-shrinkage) are expected to be higher than conventional concrete. This is significant as high early age shrinkage strains may result in early age cracking [4,9,14–16]; and if containing fibers, a reduction in strength over time due to the restraint provided by fibers [9,11,17,18].

The importance of quantifying shrinkage strains has led to a number of recent studies aimed at understanding the underlying mechanisms governing autogenous shrinkage of UHPC and its impact on performance. For example, experimental programs conducted by Yoo et al. [15,19,20] and Şahmaran et al. [16,21,22] systematically examined the effects of mixing proportion, curing condition, geometry and specimen restraint on autogenous shrinkage of UHPC specimens. Research has also identified several means for reducing both the magnitude of

shrinkage strains, as well as the time over which they develop. For example, Rößler et al. [23] have shown that by curing at a temperature of 20 °C, a reduction of 85% in autogenous shrinkage strains is possible compared to those obtained under at 90 °C heat curing. Alternatively [24,25] have shown that it is possible to reduce drying shrinkage via the inclusion of moisture retaining superabsorbent polymers into the mix. These release water over time, replacing that lost due to hydration and drying, resulting in a reduction of shrinkage strains of up to 75%. The effects of shrinkage reducing admixtures on the autogenous shrinkage of UHPC have been investigated by Refs. [11,26,27].

In this paper a standard UHPC mix which has been widely investigated at both the material [14,28,29] and member levels [1,30,31] is taken as a baseline, and simple means for improving its dimensional stability is investigated. Approaches considered in this study include:

- The use of iced water in the mix design to lower concrete temperature and hence reduce the potential for autogenous shrinkage and temperature induced deformations [32].
- Varying mix design proportions to identify the beneficial restraining influence of (fine) aggregate, and the presence of unhydrated binders that may act as a filler providing additional dimensional stability.
- Varying mix design proportions to identify the reduction in

Table 1
Mix proportion of the UHPCs.

Mix	Cement (wr)	Silica fume (wr)	Sand (wr)	water (wr)	Crushed ice (wr)	SRA[1] (wr)	SP[2] (wr)	w/b	b/s	Paste weight fraction	Mixing water weight fraction
U-0.8	0.632	0.168	1.000	0.104			0.024	0.152	0.800	0.480	0.063
U-0.9	0.711	0.189	1.000	0.117			0.027	0.152	0.900	0.509	0.067
U-1.0/SRA-0/ Ice-0	0.790	0.210	1.000	0.130			0.030	0.152	1.000	0.535	0.070
U-1.1	0.869	0.231	1.000	0.143			0.033	0.152	1.100	0.559	0.073
U-1.266	1.000	0.266	1.000	0.165			0.038	0.152	1.266	0.593	0.078
SRA-1	0.790	0.210	1.000	0.129		0.008	0.030	0.152	1.000	0.535	0.070
SRA-2	0.790	0.210	1.000	0.127		0.016	0.030	0.152	1.000	0.535	0.070
SRA-3	0.790	0.210	1.000	0.126		0.024	0.030	0.152	1.000	0.535	0.070
Ice-25/75	0.790	0.210	1.000	0.098	0.033		0.030	0.152	1.000	0.535	0.070
Ice-50/50	0.790	0.210	1.000	0.065	0.065		0.030	0.152	1.000	0.535	0.070

[1]. Containing 20% water.
[2]. Containing 70% water.

(a)   (b)

Fig. 1. Shrinkage test specimens: a) sealed prism for autogenous shrinkage measurement; b) unsealed prism for free total shrinkage measurements.

Table 2
Influence of binder-to-sand ratio on rheological properties of fresh UHPCs.

Specimen	b/s ratio	Slump (mm)	Flow table (mm)	J-ring (mm)
U-0.8	0.8	165	375	412
U-0.9	0.9	240	440	451
U-1.0	1	235	425	443
U-1.1	1.1	250	430	455
U-1.266	1.266	250	470	506
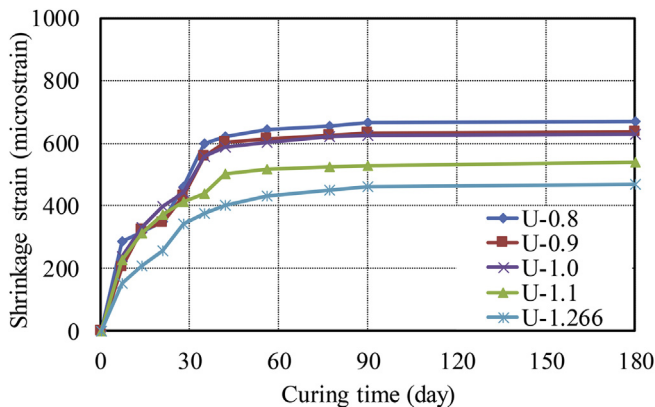
Fig. 2. Effect of binder-to-sand ratio on autogenous shrinkage.
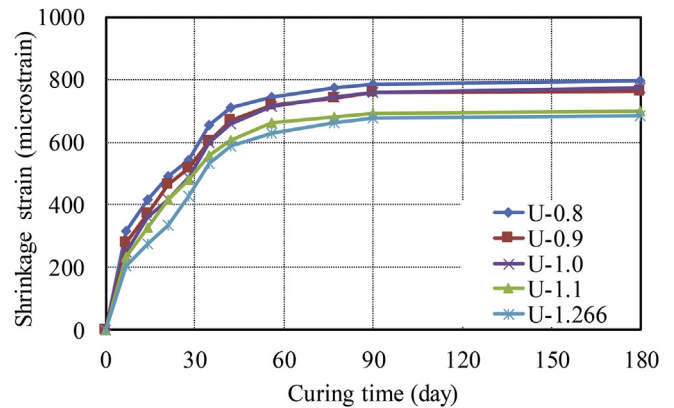
Fig. 3. Effect of binder-to-sand ratio on free total shrinkage.

characterization tests are conducted to determine the relative effectiveness of each approach, as well as the underlying mechanism of action. It is envisaged that this work will assist in allowing concrete technologists to decide on the most appropriate means for achieving the desired reduction in shrinkage.

In the remainder of the paper the characteristics and constituents of the UHPC materials investigated are first described. This is followed by a description of the experimental method and tests conducted; finally, the change in autogenous and drying shrinkage achieved by each approach is presented as well as a discussion of the mechanism of action.

2. Experimental program

2.1. Ingredients used for UHPC mix

Two types of cementitious binder were used, namely sulphate resisting cement and silica fume. The sulphate resisting cement, which

autogenous shrinkage due to a reduction in cementitious binder content.
• The use of high dosages of conventional shrinkage reducing admixtures to physically reduce shrinkage by reducing the surface tension in the concrete pore water.

For each approach investigated a range of material and
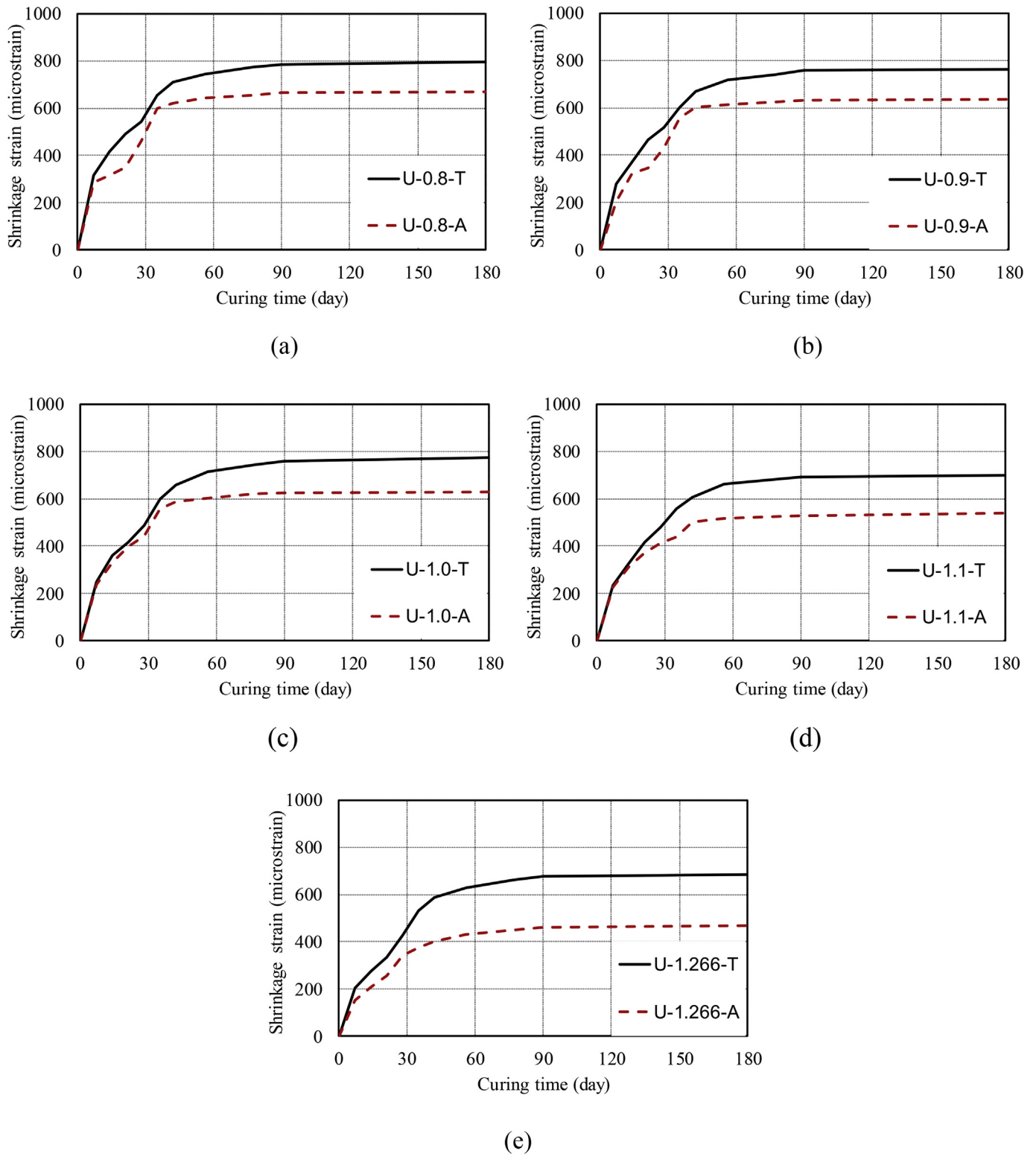
Fig. 4. Effect of binder-to-sand ratio on free drying component: a) U-0.8; b) U-0.9; c) U-1.0; d) U-1.1; (e) U-1.266.

contains 3–8% gypsum by weight, has a 28-day compressive strength of 60 MPa and a 28-day mortar shrinkage strain of 650 (microstrain) as determined through the tests performed as per AS 2350. 11 [33] and AS 2350. 13 [34], respectively. The undensified silica has a bulk density of 635 kg/m³ and has a silicon dioxide (SiO_2) content over 89.6%. A natural washed river sand with a maximum nominal grain size of 0.4 mm was used as the fine aggregate for all UHPC mixes. A third

generation high range water reducer with an added retarder was added to each UHPC during the mixing. For the purpose of further minimizing shrinkage, a shrinkage reducing admixture (SRA), which meets and exceeds all requirements of Australian Standard 1478.1–2000 [35] as special purpose admixture type (SN), was added to the UHPC mix with different dosages. As an alternative to the use of an SRA, aiming to prevent the generation of a large amount of heat and therefore
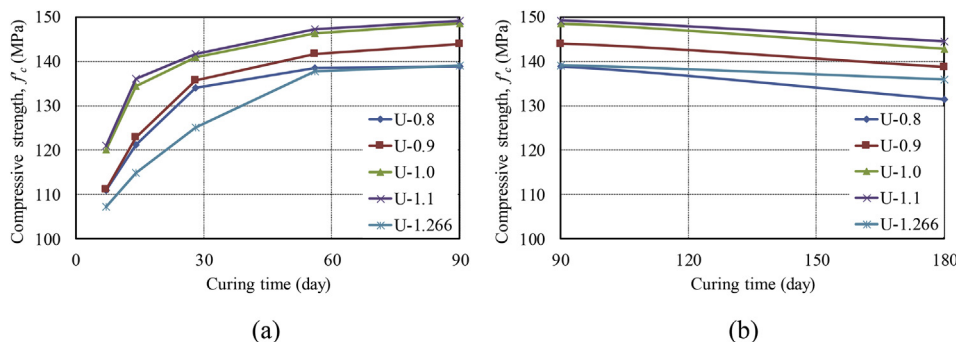
Fig. 5. Effect of binder-to-sand ratio on compressive strength: (a) curing time from 0 to 90 day; (b) curing time from 90 to 180 day.
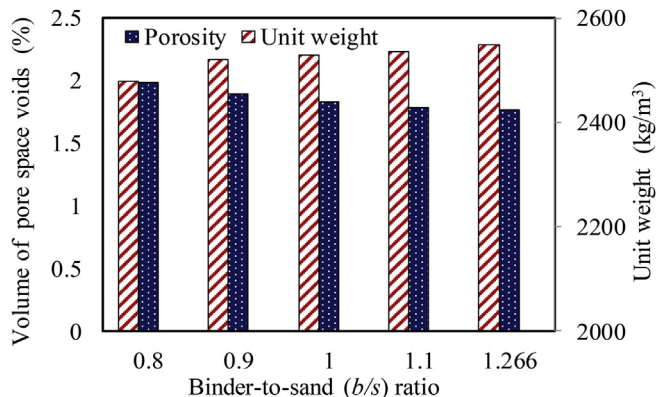
Fig. 6. Effects of binder-to-sand ratio on unit weight and porosity of hardened UHPCs.
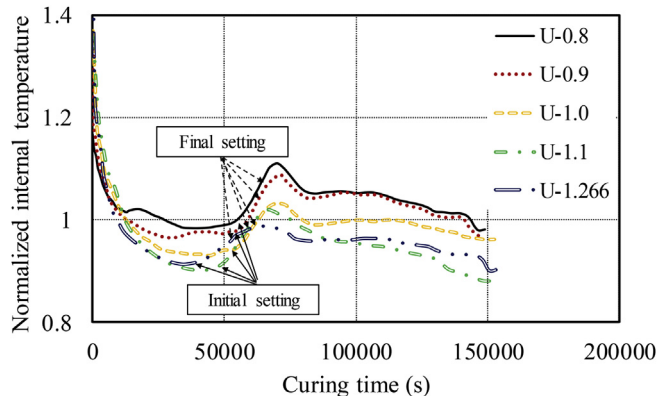
Fig. 7. Effect of binder-to-sand ratio on variations of the internal temperature with curing time.

thermally and chemically induced plastic shrinkage cracks, the use of crushed ice to partially replace mixing water is also examined.

A total of ten batches of UHPC mortar were manufactured. The first five batches of UHPCs designated as U- series were prepared using the same water-to-binder (w/b) ratio but with different binder-to-sand (b/s) ratios. A UHPC mix with a b/s ratio of 1.266 and w/b ratio of 0.152, which was identified as optimal using the same raw materials in the previous study [14], was used as the reference mix design. Note that the water content from the chemical admixtures (i.e. 20% in SRA and 70% in SP) has been included in the calculation of the water-to-binder ratio for each mix. In the first stage of testing, the compressive strengths and total shrinkage strains of five batches of UHPC with varying b/s ratio were measured. The mix with the overall best performance was then taken for the second stage of testing. This stage included: the addition of SRA to three mixes in dosages of SRA-to-cement weight ratio of 1, 2

or 3% (designated as SRA series) or the addition of crushed ice (designated as Ice series) was incorporated into the remaining two UHPC mixes as a partial replacement of water by a weight ratio of 25 or 50%. The proportions of all mixes are given in Table 1. For manufacturing UHPCs, all the dry materials, including sand and binders were initially mixed in an 80 L capacity rotating pan mixer with fixed blades for approximately 5 min. Following the dry mixing, water, crushed ice, superplasticizer and SRA, were subsequently added to the mixer and the mixing was continued until the concrete started to flow.

2.2. Test concepts and methods

To assess the effectiveness of each approach in reducing shrinkage, standard shrinkage tests were performed according to Australian Standard 2350.13 [34] over a period of 180 days when subjected to constant environmental conditions (25 °C and humidity < 50%).

To monitor the total shrinkage properties of UHPCs, square prism specimens which were 75 mm wide, and 285 mm long (shown in Fig. 1 (a)) were regularly monitored to measure the change in length. To provide an indication of the drying shrinkage relative to the total observed shrinkage, autogenous shrinkage was determined from the length change of the prisms in Fig. 1(b) which were carefully sealed with water-proof aluminum tape to prevent the moisture loss to the environment.

It is known that the evolution of autogenous shrinkage of cementitious composite is strongly related to the time when the paste develops a 'stable' solid skeleton to transfer tensile stress, which is defined as 'time-zero' for autogenous shrinkage measurement. In the present study, the final setting time obtained from calorimetry curve was adopted as the 'time-zero' where autogenous shrinkage initiated in according to ASTM C1698-09 [36] and the studies reported previously [37,38].

To further characterize the materials tested, and in order to identify the mechanisms controlling the change in shrinkage, a series of further material and characterization tests were undertaken as follows:

2.2.1. Compressive strength
The compressive strengths (f'_c) of the UHPCs at different concrete ages were obtained through axial compression tests, performed on cylinders (100 mm diameter × 200 mm height) in accordance with Australian Standard [39].

2.2.2. Flowability and passing ability
The rheological properties of each mix was assessed through a slump flow test performed in accordance with ASTM standard C143/C143M [40] and a flow-table test according to ASTM C1621 [41] including the use of a J-ring to assess passing ability around reinforcement.

2.2.3. Exothermic reaction at early curing ages
Heat generated as a result of the exothermic reaction associated

(a)

(b)

(c)

(d)

(e)

Fig. 8. SEM images of the fracture surface of the UHPCs (1000× magnification): a) U-0.8; b) U-0.9; c) U-1.0; d) U-1.1; e) U-1.266.

with cement hydration accelerates the autogenous shrinkage of the concrete [42,43] and may result in the formation of micro-cracks [44–46]. To examine the exothermic reaction of the UHPCs, a thermal sensor was embedded at the center of a 100 mm cubic specimen. The ambient room temperature and internal concrete temperature was also continuously recorded monitored for a period of three days, after which no significant change in temperature occurred.

2.2.4. Unit weight and porosity

The unit weight of the hardened UHPCs was obtained by weighing concrete cylinders (100 mm diameter ×200 mm height) 90 days after casting, such that the hydration reaction can be considered to be complete. The porosity of each series of the UHPC was quantified by measuring the volume of pore space voids in disc specimens of 150 mm diameter and 50 mm thickness through tests performed in accordance with ASTM C642-13 [47] using a hot water bath. Measurements of porosity were taken because porosity of concrete is an essential

indicator associated with not only the mechanical strength but also the durability characteristics of the concrete.

2.2.5. Scanning electron microscopy (SEM) analysis and energy-dispersive X-ray spectroscopy (EDS)

Scanning electron microscopy (SEM) characterization was performed to evaluate the microstructure of the UHPC matrix and hence assist in identifying the: unreacted binder component, homogeneity of the matrix, and pores and cracks seen in the microstructure of the matrix. Energy-dispersive X-ray spectroscopy (EDS) analysis was also conducted to identify any change in the hydration products resulting from the shrinkage reduction methods applied.

2.2.6. Thermal gravity (TG) analysis

Thermal gravity (TG) analysis was undertaken to estimate the degree of hydration of the UHPC 90-days after casting. The analysis was undertaken to assess both the non-evaporable water content and the
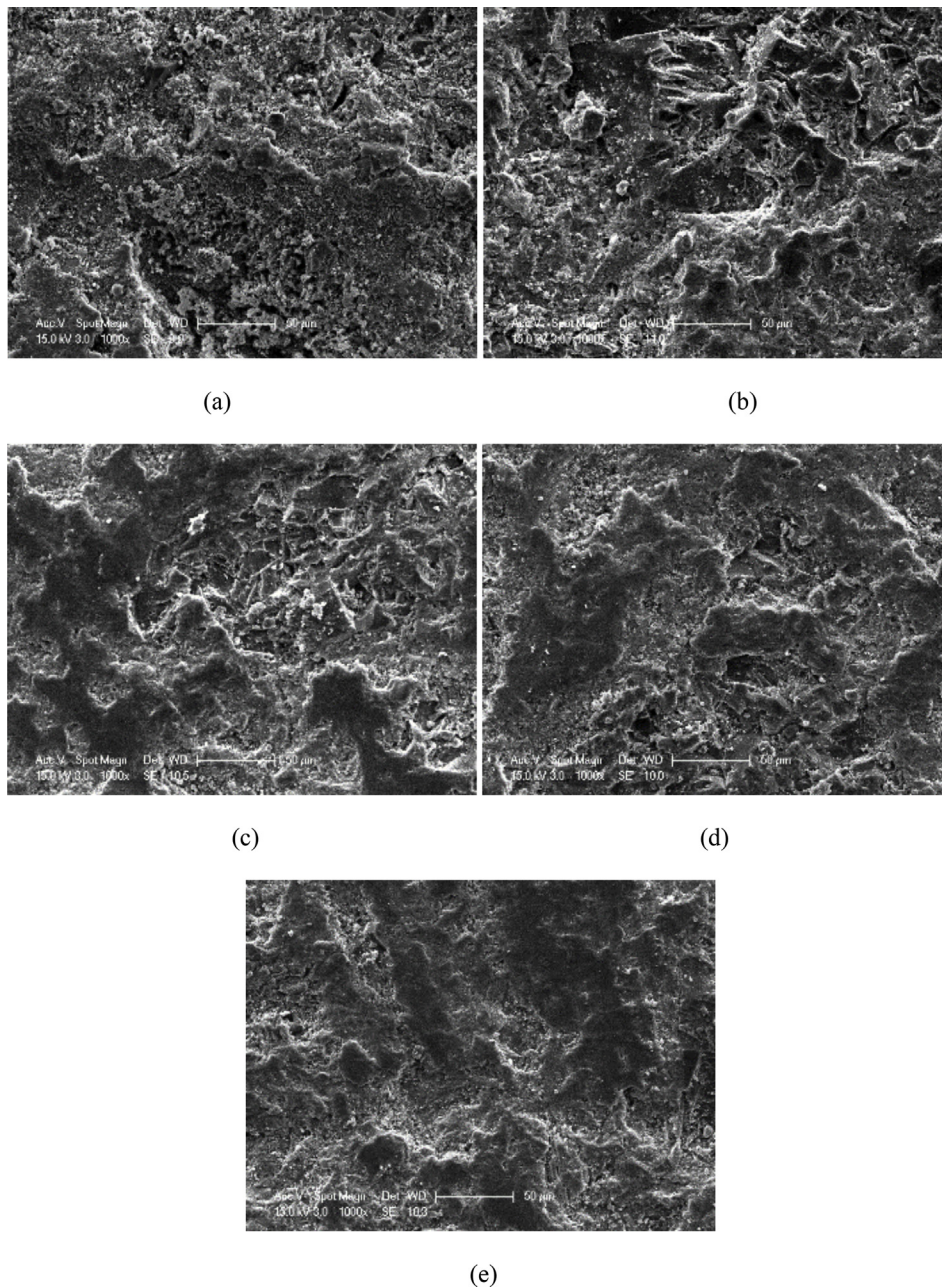
160
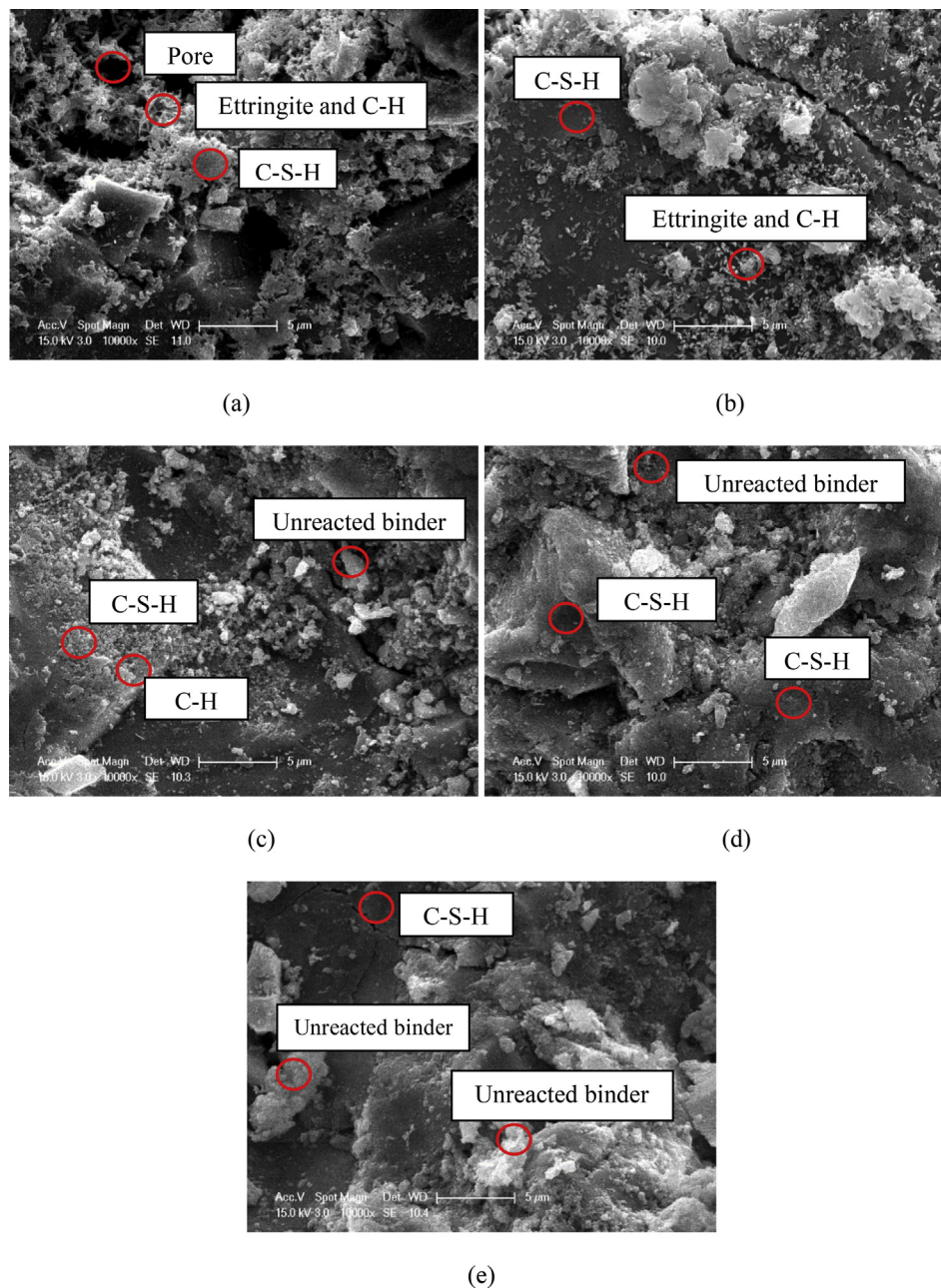
Fig. 9. SEM images of the fracture surface of the UHPCs (10000× magnification): a) U-0.8; b) U-0.9; c) U-1.0; d) U-1.1; e) U-1.266.

calcium hydroxide $(Ca(OH)_2)$ content. These approaches have been commonly applied cementitious mortar, for example see Refs. [48–50].

TG analysis was conducted using METTLER TOLEDO TGA testing machine, for each mix a sample weighing 2.5 kg was oven-dried at 105 °C for 24 h to remove the evaporable water, and the sample was then pulverized to a size of < 45 μm. About 20 μg of this sample was placed in a ceramic crucible and heated in the furnace from ambient temperature to 900 °C in a nitrogen atmosphere at a rate of 10 °C/min to determine the weight loss of matrix due to decomposition of the hydration products.

2.2.6.1. Non-evaporable water content. The amount of hydration products and the degree of hydration (D_h) of UHPC is obtained by determining the non-evaporable water content (W_{ne}) using loss-on-ignition (LOI) method. Cementitious paste is commonly used for this test as the non-evaporable water content is present due to the reactive cementitious binders only, and the degree of hydration is strongly

correlated with the *w/b* ratio of the cementitious paste [51–53]. The effects of coarse and fine aggregates on hydration are usually ignored due to their inertness. It is worth noting that in this study cement mortar was used instead of cement paste as the: pore diameter, paste-to-aggregate interfacial transition zone (ITZ), distribution of aggregate and the mixing efficiency are all affected by the aggregate content, and hence their effects on hydration cannot be neglected. The LOIs of the UHPC mortar were estimated using the LOIs of cementitious powder without moisture damage and considering the LOIs of the sand [48–50].

Previous studies by Lam et al. and Wong et al. [53,54] have shown that absolute hydration of 1g anhydrous cement can produce approximately 0.23g of non-evaporable water and this non-evaporable water content-to-cement ratio (W_{ne0}/C_0) of 0.23g/g was applied as the reference value to determine the degree of hydration of the UHPCs in the following calculations for D_h.

To calculate D_h, the LOI_{raw} of the raw cementitious powder, silica fume and sand are firstly calculated using:

Fig. 10. Observed shrinkage induced micro-cracks in the micro-structure of the UHPC.

Fig. 11. TG analysis for U-0.8, -0.9, -1.0, -1.1, and -1.266 UHPC series.

Fig. 12. Effect of binder-to-sand ratio on degree of hydration and C-H content.

Table 3
Effect of SRA content on rheological properties of fresh UHPCs.

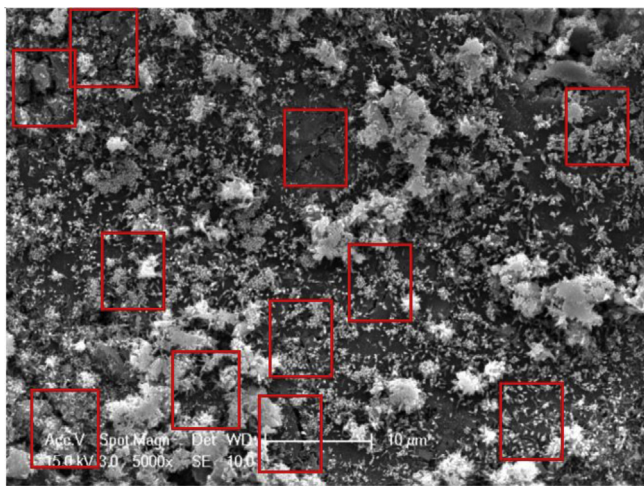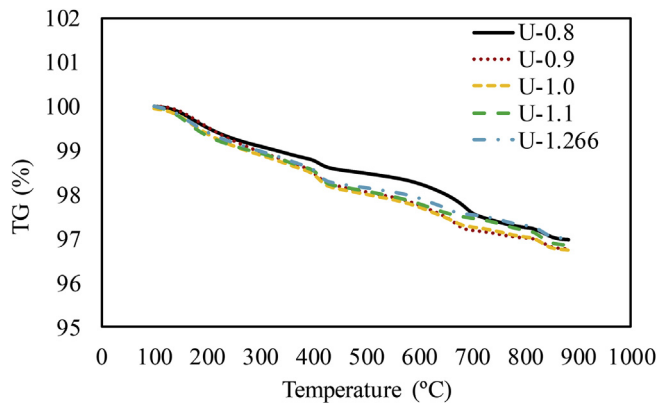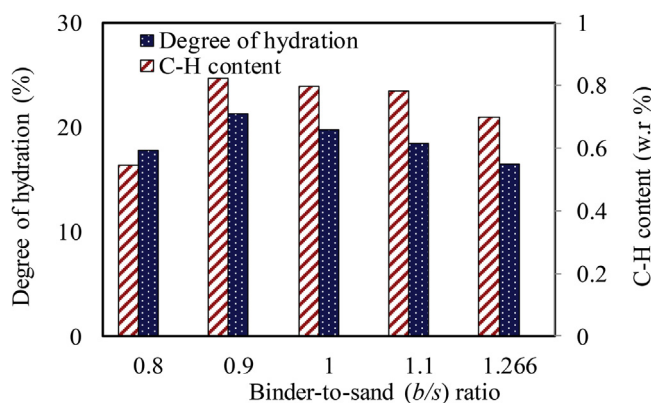| Specimen	*b/s* ratio	SRA content (%)	Slump (mm)	Flow table (mm)	J-ring (mm)
SRA-0	1	0	235	425	443
SRA-1	1	1	280	512	529
SRA-2	1	2	Full	579	568
SRA-3	1	3	Full	560	585

$$LOI_{raw} = \frac{(W_{d-raw} - W_{i-raw})}{W_{i-raw}} \qquad (1)$$

where W_{d-raw} is the dry weight of the as-received raw material, and W_{i-raw} is the ignited weight of the as-received raw material after TG test. These LOI_{raw} values are required to correct the calculations of non-evaporable water content (W_{ne}) as follows:

$$W_{ne} = [W_{d-U} - W_{i-U}*(1 + \sum LOI_{raw})] \qquad (2)$$

where W_{d-u} is the dry weight of the UHPC mortar sample, W_{i-u} is the ignited weight of the UHPC mortar sample after TG test and $\sum LOI_{raw}$ is the total ignited weight of the as-received raw materials, including sand cement and silica fume. The effective residual cementitious binder content (C_{eff}) is calculated by

$$C_{eff} = \left[W_{i-U}*\left(1 - \frac{\sum LOI_{raw}}{W_{ne0}/C_0}\right) \right] \qquad (3)$$

Finally, the degree of hydration of UHPC (D_h) is defined as the function of W_{ne}, effective residual cementitious binder content (C_{eff}) and the reference value of the non-evaporable water content-to-cement ratio (W_{ne0}/C_0), as given in Eq. (4):

$$D_h(\%) = \frac{W_{ne}/C_{eff}}{W_{ne0}/C_0} \times 100 \qquad (4)$$

The loss of the non-evaporable water that is chemically bonded in hydration products can be determined by calculating the difference in weights between at 100 °C and 700 °C from TG. This temperature interval is selected to avoid the interference due to the water evaporation at 100 °C and de-carbonation of calcium carbonate ($CaCO_3$) of the composite when the temperature overs 700 °C [55].

2.2.6.2. Calcium hydroxide (Ca(OH)$_2$) content. A fully hydrated cementitious-silica fume material usually consists of dicalcium silicate (C_2S) and tricalcium silicates (C_3S) [56–58]. The formations of these calcium silicates (C_nS) consume around 20–25% by weight of the water in the mix and produce 20–25% by weight of the calcium hydroxide (Ca(OH)$_2$). Therefore, the degree of hydration of the UHPC can also be assessed by the Ca(OH)$_2$ content in the concrete. The amount of Ca(OH)$_2$ products can be determined by calculating the drop in weight of the sample within 400–450 °C during TG tests [55,59], which indicates the decomposition of Ca(OH)$_2$ in the hydration products.

In the remainder of the paper the effectiveness of each shrinkage reduction approach including 1) reducing binder usage; 2) using SRA; 3) partially reducing mixing water with crushed ice will be presented and the mechanism of their action explored using the characterization tests above.

3. Effect of binder-to-sand ratio on the properties of the UHPCS

3.1. Flowability of concrete

Table 2 presents the results of slump flow and flow-table tests of the UHPC specimens, from which it can be inferred that the flow- and passing ability of the UHPC generally increased with an increase in the *b/s* ratio. This can be attributed to the fact that the increased *b/s* ratio in the UHPC mix resulted in an increased volume of paste that covered the surface of the fine aggregates leading to the reduction in friction between the sand particles in the fresh UHPC [60].

3.2. Autogenous shrinkage

The autogenous shrinkage strains (ε_a) plotted in Fig. 2 for each mix with a different *b/s* ratio, were measured using the sealed prisms shown in Fig. 1(b). These values can be seen to decrease with an increase in *b/s* ratio. Further it is also observed that for all mixes, regardless of the

Table 4
Effect of crushed ice dosage on rheological properties of fresh UHPCs.

Specimen	b/s ratio	Crushed ice dosage (%)	Slump (mm)	flow table (mm)	J-ring (mm)
Ice-0	1	0	235	425	443
Ice-25/75	1	25	240	418	456
Ice-50/50	1	50	235	431	462

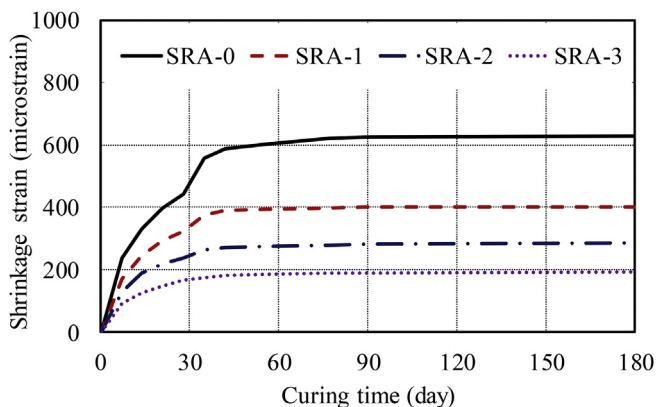**Fig. 13.** Effect of SRA content on autogenous shrinkage properties.
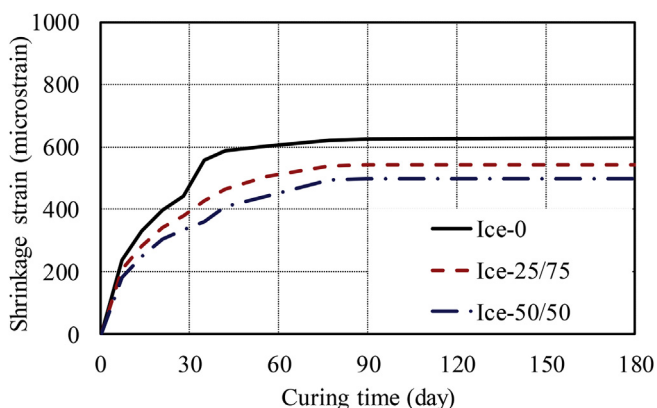

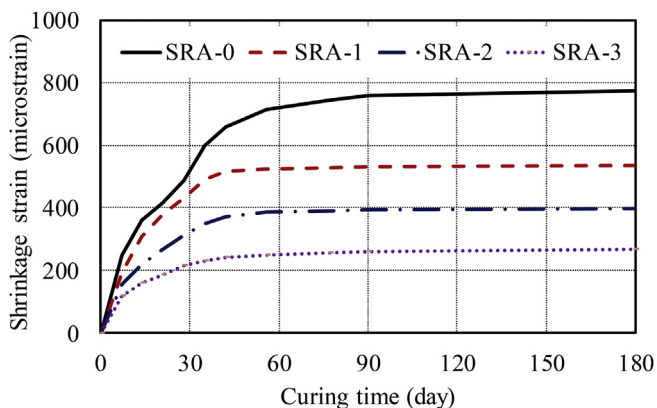**Fig. 14.** Effect of crushed ice dosage on autogenous shrinkage properties.

Fig. 15. Effect of SRA content on total shrinkage.

variation in b/s, the autogenous shrinkage began to plateau 42 days after casting, indicating the completion of hydration. At the concrete age of 42 days, the ε_a of U-1.266 was up to 35% lower than those of the companion specimens. Furthermore, the UHPC prepared using a higher b/s ratio (i.e. U-1.1 and -1.266 series) exhibited a lower rate of

autogenous shrinkage gain which can be inferred by the reduced slope of the curves.

Moreover, when comparing the autogenous shrinkage strains in Fig. 2 with those expected from conventional concrete (e.g. Refs. [61,62]) for a given age (i.e. concrete age of 28 days), the autogenous shrinkage of UHPCs (> 400 macrostrain) are significantly higher than those of the conventional normal- and high-strength concrete (< 150 macrostrain). This difference is because the increased binder and reduced mixing water in UHPC means it tends to undergo a more rapid self-desiccation than conventional concrete and potentially to form more micro-cracks as further shown and discussed in section 3.8.

3.3. Free total shrinkage

Fig. 3 illustrates the effect of b/s ratio on free total shrinkage measured using the unsealed prisms shown in Fig. 2(a). Similar to the results of the autogenous shrinkage tests, the free total shrinkage strains (ε_t) of the UHPC specimens generally decreased with an increase in b/s ratio for a given concrete age. Unlike the autogenous shrinkage tests, where the shrinkage deformations stabilized at 42 days, it is observed that the free total shrinkage increased in all five mixes continued up to the concrete age of 90 days. This is due to the continuous drying of the UHPCs, which is associated with loss of moisture from the concrete to the environment and is in contrast to the significant slowing of autogenous shrinkage after 42 days as a result of the decreased rate of hydration.

3.4. Assessment of free drying component

The free drying shrinkage component of the UHPCs can be estimated and assessed by the difference between the free total (solid line) and autogenous (dashed line) shrinkage properties shown in Fig. 4 (a) to (e). It is evident from the Fig. 4 that at the early curing ages (i.e. before the concrete age of 7 days), the difference between the free total and autogenous shrinkage of each UHPC series was negligible. The difference between the ε_a and ε_t of each series increased up to 110% with an increase in the b/s ratio from 0.8 to 1.266 at the concrete age of 180 days. Note that although the w/b ratio for a UHPC mix is low, with adequate mixing energy the moisture (including water and superplasticizer) can be evenly distributed to form a high paste volume [63,64]. This suggests that more moisture was able to diffuse from the UHPC for mixes with a higher paste volume owing to the higher b/s ratio, as reported in Table 1, and the observation is in consistent with previous research [65–67]. In addition, as illustrated in Fig. 4 (a) and (b), the drying shrinkage component of each specimen was significantly lower than the corresponding autogenous shrinkage at each given concrete age, indicating that the autogenous shrinkage predominates the overall free total shrinkage of UHPCs.

3.5. Compressive strength

The effect of b/s ratio on f'_c is shown in Fig. 5. It is observed that the U-1.266 series developed a lower compressive strength than the other four companion mixes for a given age. The reduction in strength associated with the reduction in fine aggregate could be a result of the mechanism of stress transfer within the concrete as per the well-known theory for conventional mortars [68]. That is the transfer of normal force in a mortar is largely due to the interaction of sand to sand interfaces. For the UHPC with a lower w/b ratio, its compressive strength is not predominated by failures of cementitious paste but by adhesive failures between aggregates and cementitious materials [69,70]. The presence of excessive unhydrated cementitious materials in the UHPC series with higher binder content weakened the interfacial transition zones (ITZs) between the fine aggregate and binder, which led to the observed reduction in compressive strength. It is also worth noting in Fig. 5 that, all these five UHPC series experienced reduction (up to
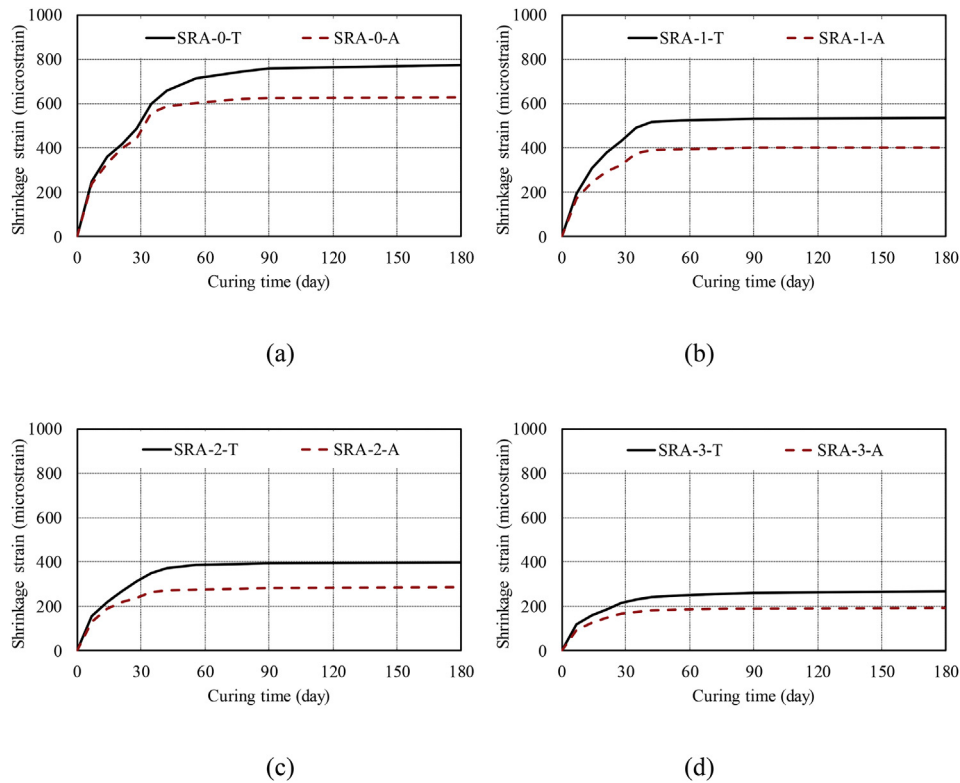
163

Fig. 16. Effect of SRA content on free drying component: (a) SRA = 0%; (b) SRA = 1%; (c) SRA = 2%; (d) SRA = 3%.
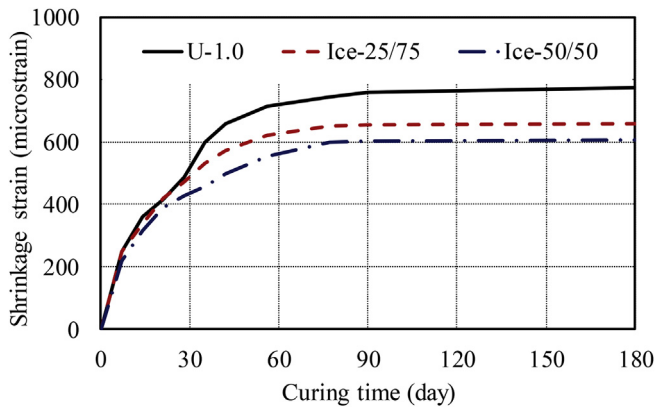

Fig. 17. Effect of crushed ice dosage on total shrinkage.

5.3%) in their compressive strengths within the curing age from 90 to 180 days, as shown in Fig. 5. This reduction in the f'_c was caused by the formation of internal micro cracks (discussed further in section 3.8) as a consequence of the increased shrinkage of the concrete [14]. The above observations indicate that the most appropriate b/s ratio for UHPC should be within 1–1.1 to achieve adequate aggregate interaction without compromising the f'_c.

3.6. Unit weight and porosity of the UHPCs

Fig. 6 shows the effect of b/s ratio on the unit weight and porosity of the hardened UHPCs measured at the concrete age of 28 days. It is observed that the unit weight of the UHPC increased with an increase in b/s ratio due to the higher unit weight of the cementitious materials (approximate 3500 kg/m³) compared to that of the sand (approximate 2000 kg/m³). The porosity of the UHPC also decreased approximately 10% with an increase in b/s ratio from 0.8 to 1.266. This reduction in porosity may be attributed to the increased amount of residual

unhydrated binder which fills the pore spaces. The reduction in binder also reduces the total amount of porous ITZs around the sand particles [71,72].

3.7. Exothermic reaction at early curing period

Fig. 7 illustrates the variations of internal temperature of the five different specimens with the curing time. It is worth noting that the temperature measured at the center of each UHPC series was normalized by the corresponding ambient temperature in order to remove its influence. From the calorimetry curves in Fig. 7, it can be observed that a decrease in b/s ratio led to an increase in the magnitude of the peak temperature measured at the center of the sample, with the maximum magnitude of change being approximately 10%. The increase in temperature with a reduction in b/s indicates that the UHPC with a lower b/s ratio had a higher degree of exothermic reaction and generated more heat as the consequence of a higher degree of reaction. This is due to the residual unhydrated binders in the UHPC with a higher b/s which act to fill the pores and voids and absorbed water to their surface, which hindered the level and rate of hydration in the concrete [73]. These facts can be further verified using the TG analysis and SEM characterizations presented in the following sections. The above observation indicates that the UHPC prepared using a lower b/s ratio underwent a more significant chemical reaction process, which consumed more raw materials and achieved a higher degree of hydration. Therefore, UHPC prepared using a lower b/s ratio tended to have a more significant autogenous shrinkage at the early curing stage, which can be inferred from the curves in Fig. 2.

The initial and final setting times of each mix can be identified as the first trough and the end point of the linear ascending branch on the calorimetry curves in Fig. 7. These points were also affected by the b/s ratio, in which the initial and final setting time of the UHPC were delayed by approximately 4 h when the highest quantity of aggregate was considered. This could be explained by the fact that the increased amount of aggregates hindered the contact between water and binder
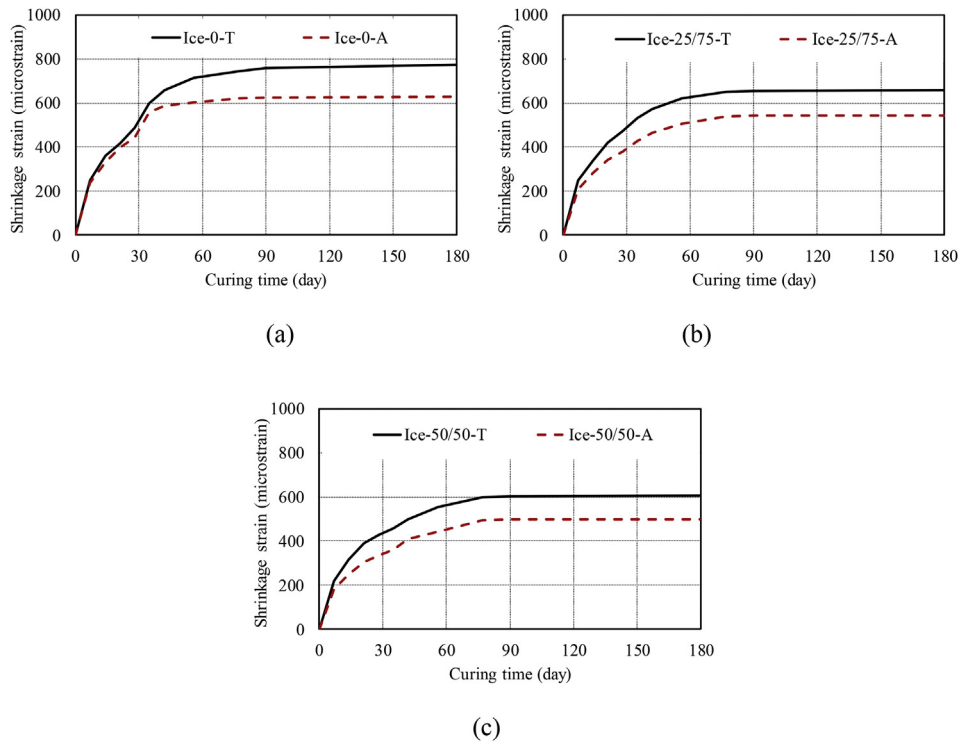
Fig. 18. Effect of ice replaced water ratio on free drying shrinkage: (a) Ice = 0%; (b) Ice = 25%; (c) Ice = 50%.
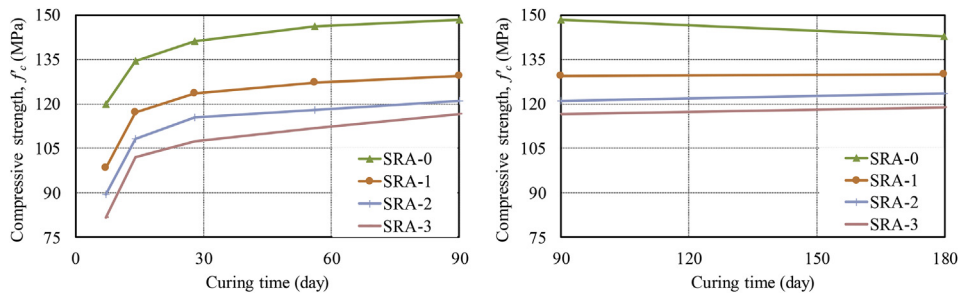
Fig. 19. Effect of SRA content on compressive strength: (a) curing time from 0 to 90 day; (b) curing time from 90 to 180 day.
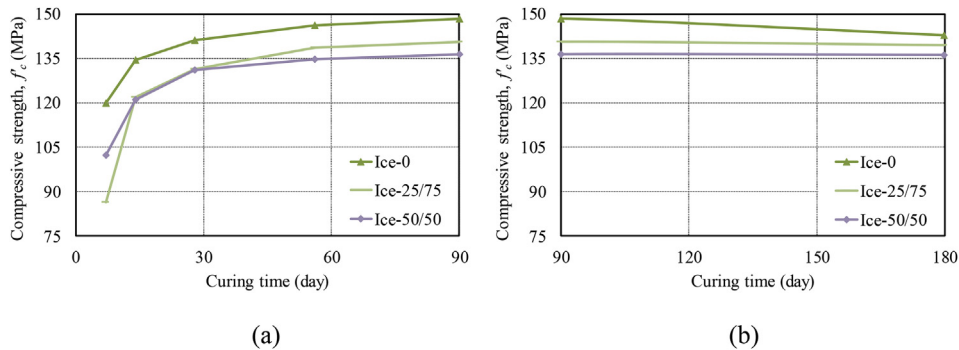
Fig. 20. Effect of ice replaced water ratio on compressive strength: (a) curing time from 0 to 90 day; (b) curing time from 90 to 180 day.

which led to a longer induction period (referred to the initial gentle trough stage) and resulted in this later setting of the concrete [74,75].

3.8. Morphological characterization by scanning electron microscopy (SEM) and energy-dispersive X-ray spectroscopy (EDX)

The scanning electron microscopy (SEM) micrographs were evaluated to investigate the effect of b/s ratio on the microstructure of the

UHPCs, as depicted in Figs. 8 and 9 at different magnifications. It is evident from the SEM micrographs at $1000\times$ magnification that the increased volume of cementitious paste (at higher b/s ratio) led to a much denser microstructure as a result of the reduction in volume fraction of the porous aggregate-paste ITZs. This fact also caused by the micro-filler effect offered by unreacted cementitious binders. Moreover, as shown on the SEM micrographs at $10000\times$ magnification, a large amount of ettringite ($3CaO \cdot Al_2O_3 \cdot 3CaSO_4 \cdot 32H_2O$) and calcium
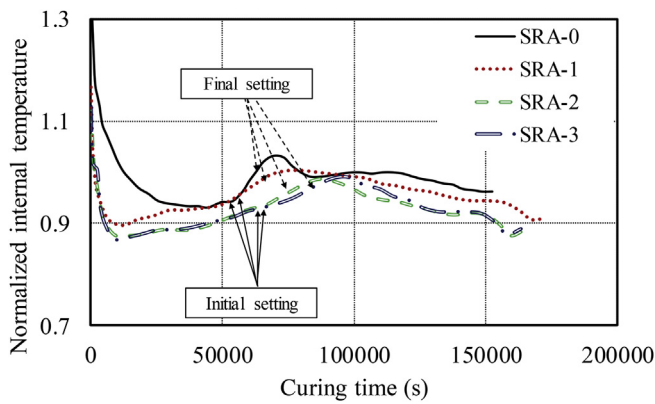
Fig. 21. Effect of SRA content on variations of the internal temperature with curing time.
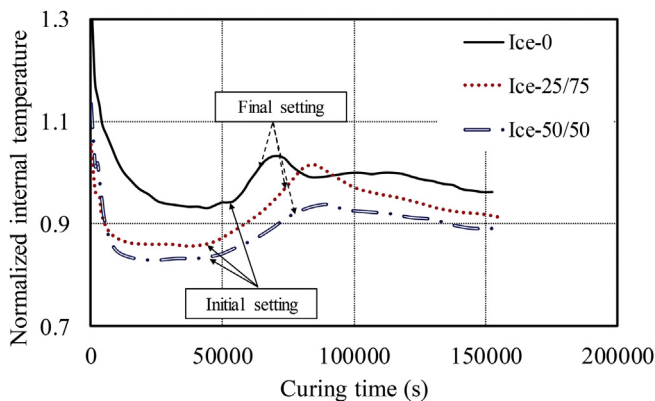
Fig. 22. Effect of ice replaced mixing water ratio on variations of the internal temperature with curing time.
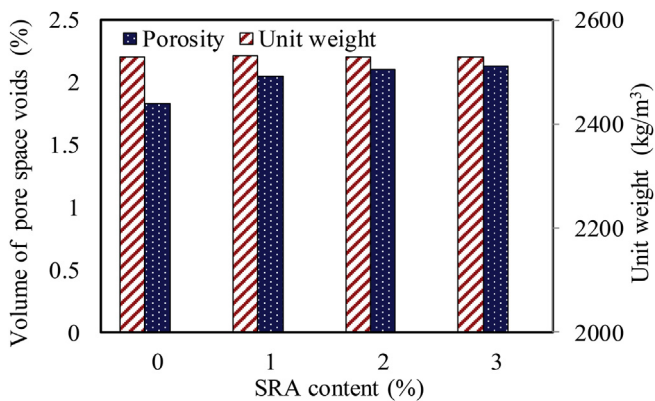
Fig. 23. Effects of ice replaced water ratio on unit weight and porosity of hardened UHPCs.

hydroxide (C-H) were observed and characterized using EDX spectroscopy in the microstructure of the UHPC prepared using the lower b/s ratio (i.e. U-0.8, and -0.9). This is because the increased porosity in the concrete provided the space for the growth of ettringite and C-H crystals owing to their expansive nature [76]. For the UHPC prepared using a relatively higher b/s ratio (i.e. U-1.0, -1.1 and -1.266), a larger amount of unreacted cementitious materials were detected, as indicated in Fig. 9. Ettringite and C-H crystals were rarely observed in the matrix of U-1.0, -1.1 and -1.266 series owing to the increased denseness and reduced pore space in their matrix shown in Fig. 8. The presence of these unreacted binders may restrain the shrinkage of the matrix contributing to the reduction in autogenous- and drying-shrinkage shown

in Figs. 2 and 3. The presence of the unreacted binder is also a clear indication of the decreased degree of hydration in the UHPC prepared using a higher b/s ratio. It is worth mentioning that the observed increased pore space in UHPC adversely affected the drying shrinkage of the concrete, which seemingly contradicts to the observations reported in the literature [77]. The possible explanation is that the expansion resulting from the abundance of crystalline ettringite and C-H in the pores and cracks was more significant than the drying shrinkage of the concrete [76,78]. To verify the deduction on the decrease in mechanical strength of UHPC after a long-term curing, Fig. 10 illustrates a representative SEM micrograph of U-1.1 series with the indications of the micro-cracks that were induced by thermal and autogenous shrinkage.

3.9. Results of thermal gravity (TG) analysis

The TGA curves of the comparing UHPCs are shown in Fig. 11 and the effect of binder to sand ratio on the degree of hydration and C-H content are shown in Fig. 12. It should be noted that the paste weight fraction factor for each specimen series, as given in Table 1, was considered in the calculations of the chemically bonded water and C-H content of the paste that is the actual materials for hydration. In general, except for U-0.8 series, the calculated degree of hydration and the C-H content decreased with an increase in the b/s ratio (i.e. up to approximately 18% lower). While the w/b ratio remained the same for the mixes being compared, the UHPC prepared using a higher b/s underwent a lower degree of hydration and hence contained less hydration products. This further confirmed the previously observed less significant autogenous shrinkage for the UHPC prepared using a lower b/s ratio.

3.9.1. Selection of the mix for further investigations to migrate autogenous shrinkage

A comprehensive study of the experimental results of among U-0.8,-0.9, -1.0 -1.1 and -1.266 UHPC series led to the selection of the mix design of U-1.0 as the mix for further investigation. These investigations include: the incorporation of shrinkage reducing admixture (SRA) and the used crushed ice to partially replace mixing water. Mix designs for the second stage of this work are shown in Table 3.

4. Effects of applied techniques on the properties of the UHPCS

4.1. Flowability

4.1.1. Effect of shrinkage reducing admixture (SRA) content

For the flow test results reported in Table 3, it can be seen that the UHPC series prepared with a higher SRA content exhibited better flowability and passing ability. This is due to the higher liquid content (i.e. 80% of the organic liquid component in SRA) in the UHPC mix with a higher SRA content that provides better lubrication, resulting in a better rheology of the UHPC.

4.1.2. Effect of crushed ice dosage

The flow test results presented in Table 4 indicate that the replacement of water with crushed ice had negligible impact on the flowability and passing ability of the UHPC as the added crush ice completely melted after sufficient mixing. The temperature of the mixing water was recorded immediately prior to adding to the mixer. For mixes without using crushed ice the water temperature was found to be the same as the ambient temperature (i.e. 25 °C) while for water with crushed ice the temperature was found to be 2.6 °C and 1.2 °C at 25% and 50% replacement ratio (by weight) respectively. The incorporations of crushed ice in a UHPC mix are expected to reduce the internal temperature of the specimens and hence lessen the potential formations of thermal cracks.

Fig. 24. Effects of SRA content on unit weight and porosity of hardened UHPCs.

(a)

(b)

(c)

(d)
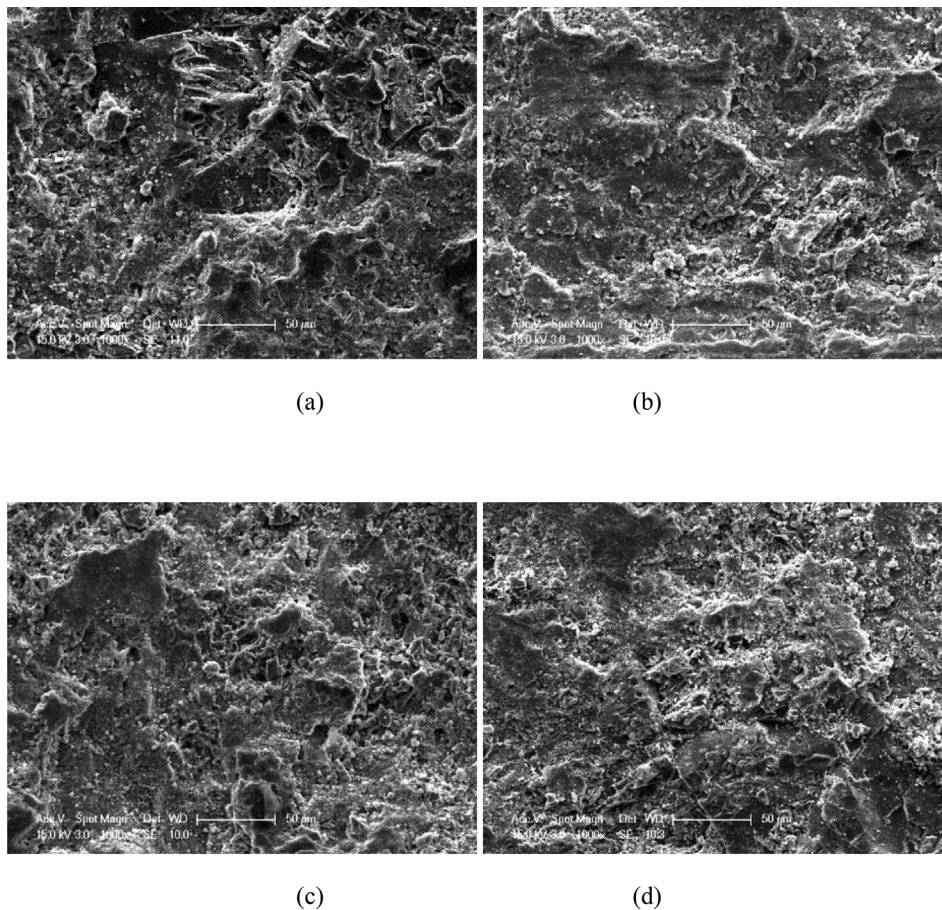
Fig. 25. SEM images of the fracture surface of the UHPCs (1000× magnification): a) SRA-0; b) SRA-1; c) SRA-2; d) SRA-3.

4.2. Autogenous shrinkage

4.2.1. Effect of shrinkage reducing admixture (SRA) content

Fig. 13 shows the effects of SRA contents on the autogenous shrinkage of the UHPC. It can be seen that the ε_a of the UHPC decreased significantly with an increasing SRA content (up to approximately 69% for UHPC at age of 90 days). It is also observed that the SRA started

reducing the autogenous shrinkage right after the initial casting of the UHPC. As stated by Collepardi et al., Folliard et al. [79,80] and Lura et al. [44], SRA incorporation eases the surface tension in the capillary pores of the concrete and subsequently reduces the drying- and auto-genous-shrinkage of the concrete. The reduction in autogenous shrinkage with incorporation of SRA seen in the present study is also in reasonable agreement with those reported by studies on UHPC mortar.
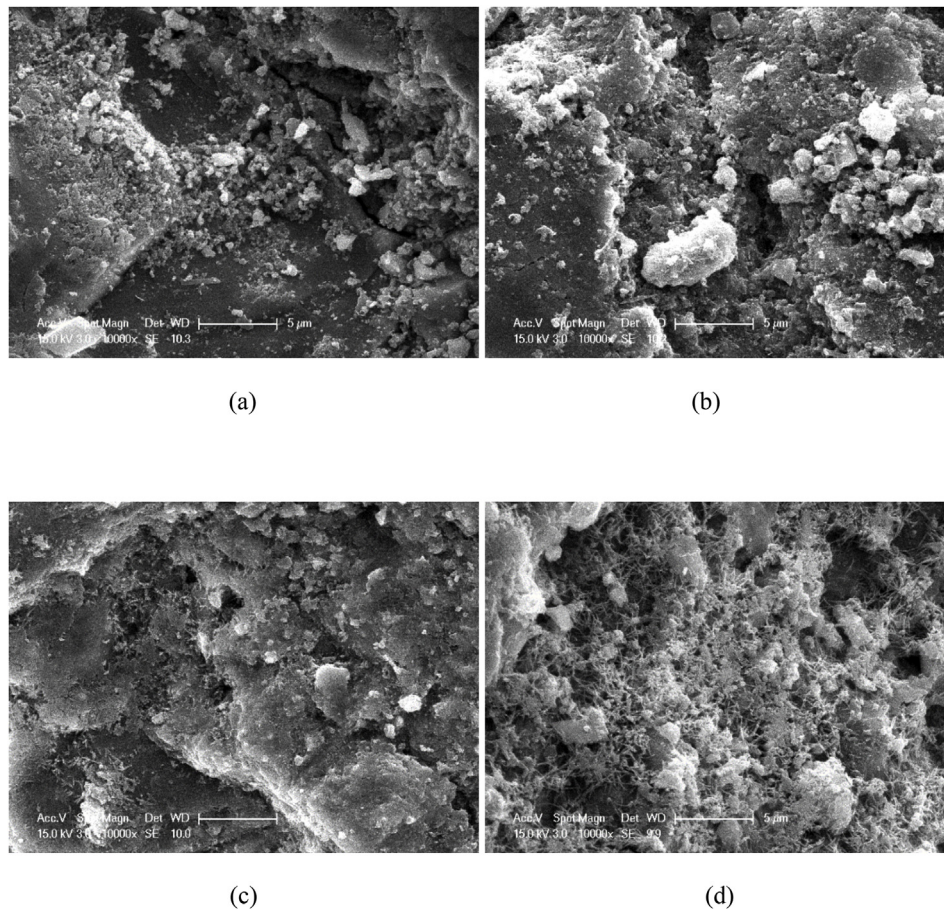
Fig. 26. SEM images of the fracture surface of the UHPCs (10000× magnification): a) SRA-0; b) SRA-1; c) SRA-2; d) SRA-3.

For example, Su et al. [81] reported an up to 95% reduction in autogenous shrinkage with 2% SRA dosage at 7 days (compared to 65.6% as reported in the present study) and an approximated 61% reduction in autogenous shrinkage with 2% SRA dosage at 160 days was observed by Soliman and Nehdi [11] (compared to 57.8% as reported in the present study). In addition, the comparison of the efficacy of using SRA on autogenous shrinkage between UHPC and conventional cementitious mortar (i.e. as reported in Ref. [82]) suggests the nearly the same performance of SRA to reduce autogenous shrinkage at a given dosage of SRA.

4.2.2. Effect of crushed ice dosage

The effect of crushed ice on the autogenous shrinkage of the UHPCs is depicted in Fig. 14. At each given curing age, the UHPC manufactured using a higher crushed ice exhibited a lower ε_a (up to approximately 19% at concrete age of 180 days). This observation is expected as the internal temperature of UHPC decreased with the incorporation of crushed ice, which led to the deceleration of the rate of hydration of the concrete and hence reduced autogenous shrinkage.

4.3. Free total shrinkage and assessment of free drying component

4.3.1. Effect of shrinkage reducing admixture (SRA) content

The effect of SRA content on the free total shrinkage of the UHPC is illustrated in Fig. 15, where it can be seen that the UHPC prepared using a higher content of SRA exhibited a lower ε_t. Fig. 16 (a) to (c) illustrate the comparisons between the free total shrinkage and the autogenous shrinkage at all curing ages of each of the four comparing UHPC series, in which the difference between the free total shrinkage and the autogenous shrinkage of each UHPC series yields

approximately the free drying shrinkage component of the concrete. It is observed that the UHPC prepared using a higher SRA content developed a lower drying shrinkage than their counterparts with lower SRA contents. This observation is consistent with the findings of previous studies by Yoo et al. [9,12] and suggests that the SRA is particularly effective to mitigate the free drying shrinkage of the UHPC through reducing the surface tension in the capillary pores of the concrete during the drying process.

4.3.2. Effect of crushed ice

The ε_t of the UHPC series with different crushed ice dosages were also periodically measured up to the concrete age of 180 days and illustrated in Fig. 17 as the corresponding values of the ε_r and ε_a are also shown in Fig. 18. It is observed that the ε_t of the UHPC decreased with an increase in crushed ice dosage whereas the replacement of mixing water with crushed ice led to no impact on the free drying shrinkage property of the concrete. This is observed because the drying shrinkage only depends on the moisture movement out of the concrete.

4.4. Compressive strength

4.4.1. Effect of shrinkage reducing admixture (SRA) content

The effect of SRA content on f'_c at all curing time are illustrated in Fig. 19. For each given concrete age, f'_c decreased significantly with an increase in the SRA dosage (up to 21.5% decrease in f'_c at 90 days with SRA content of 3%), which is in agreement with those reported in the previous studies on UHPCs [12,13]. It is also worth noting that the mixes incorporating SRA exhibited no compressive strength losses ($\Delta f'_c$) for the concrete age ranging between 90 and 180 days. This finding further validates the hypothesis of Sobuz et al. [14] that the reduction

168

(a)   (b)

(c)

Fig. 27. SEM images of the fracture surface of the UHPCs (1000× magnification): (a) Ice = 0%; (b) Ice = 25%; (c) Ice = 50%.

in strength of UHPC over time is due to the formation of micro-shrinkage cracks.

4.4.2. Effect of crushed ice dosage

Fig. 20 illustrates the variations of f'_c with curing time of the UHPCs manufactured using different crushed ice replacement ratios. For a given concrete age, the U-25/75 and -50/50 series, which were prepared with crushed ice, developed a lower f'_c than the corresponding UHPC without crushed ice (up to 8% reduction when replacing 50% of water by crushed ice), whereas there was only a slight difference in f'_c between U-25/75 and -50/50 series. This is likely due to the small difference in temperature between mix U-25/75 and -50/50 compared to the control without ice. Moreover, as shown in Fig. 20, U-25/75 and -50/50 UHPC series all exhibited insignificant strength losses (< 1%) between concrete age between 90 and 180 days compared to that seen in U-1.0. This can be explained by the fact that less thermal and plastic shrinkage cracks formed during the exothermic reaction stage, due to the reduction in the heat generation by the incorporation of crushed ice at the early curing stage (i.e. within 72 h after casting). This will be shown in the calorimetry curves of these UHPC series are presented and their effects are discussed in the following sections. This finding indicates that the simple replacement of a proportion of the mixing water with ice may be all that is required to mitigate the excessive shrinkage strains which causes a reduction in strength of UHPC over time.

4.5. Exothermic reaction at early curing ages: effects of SRA and crushed ice dosage

The effects of SRA content and crushed ice dosage on the internal temperature of the UHPC are depicted in Figs. 21 and 22, respectively. As can be seen from both figures, the incorporation of SRA or replaced mixing water by crushed ice in the UHPC mix can significantly delay

the initial and final setting time and reduce the magnitude of peak temperature, which indicates a lower degree of hydration. It is also observed that the strength development period (referred to the width of the hump of the temperature history curve) was increased by using SRA or replacing mixing water with crushed ice. This indicates that the UHPC mixed with SRA or crushed ice could experience a slightly slower strength gain within the very early age (i.e. 72 h) due to the decelerated reaction rate.

4.6. Unit weight and porosity of the hardened UHPCs

As illustrated in Fig. 23, it is observed that the SRA content has marginal effect on the unit weight of the hardened UHPC, however it did lead to an increase in the volume of pore space. This was as expected as SRA, which is a type of organic substance (mainly chemically stable ethanol derivatives) [83], is inert to during hydration and thus causes formation of additional pores in the UHPCs.

The test results of the unit weight and porosity of the hardened UHPCs shown in Fig. 24 suggest that partially replacing the mixing water by crushed ice resulted had no significant effect on the unit weight of the concrete. However, a slight increase in the porosity of the UHPC with an increase in the crushed ice dosage was observed due to the decreased reaction rate. This is because the lower temperature caused amount of unreacted raw materials (i.e. water and binder) to remain in the structure of the matrix. The gradual evaporation of the residual water subsequently led to the increased porosity of the concrete.

4.7. Morphological characterization of the UHPCs

4.7.1. Effect of SRA content
Figs. 25 and 26 illustrated the SEM micrographs of the fracture

(a)

(b)

(c)

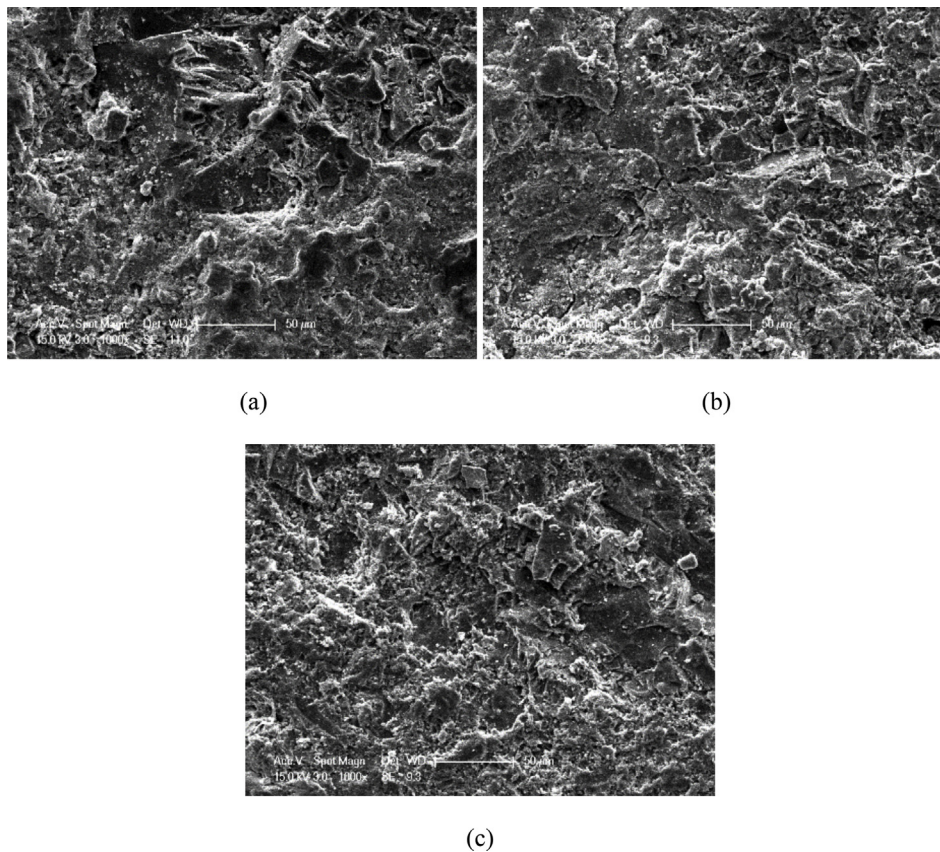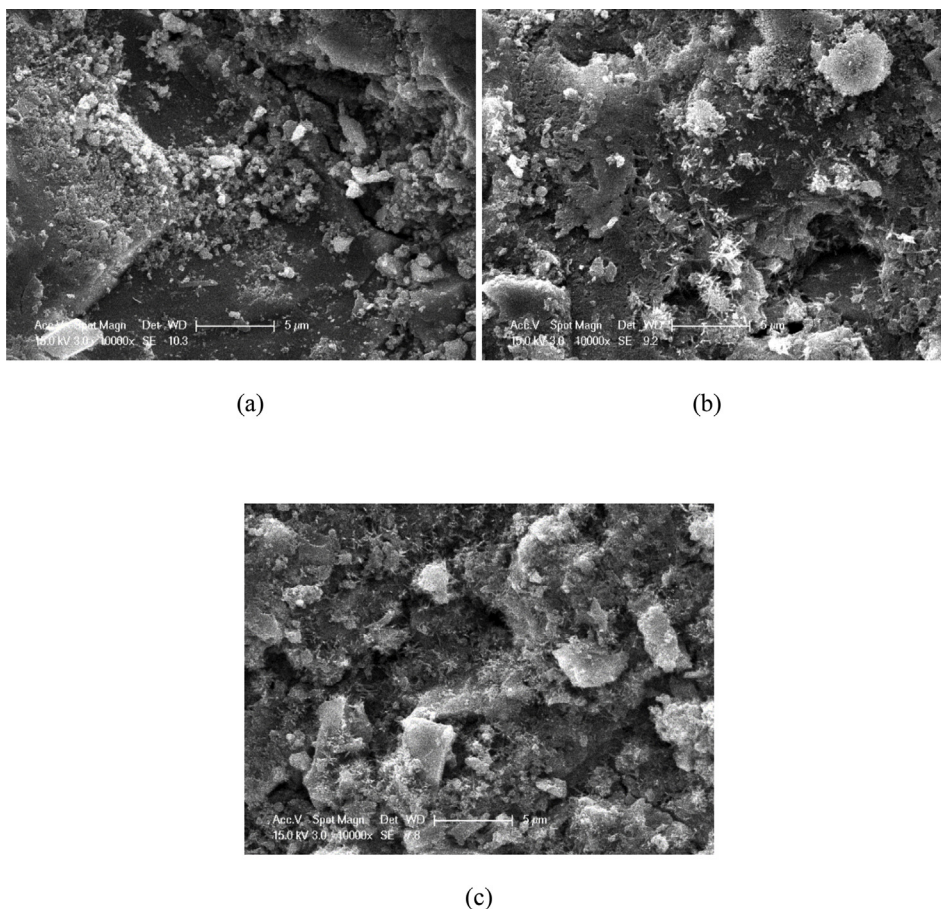**Fig. 28.** SEM images of the fracture surface of the UHPCs (10000× magnification): (a) Ice = 0%; (b) Ice = 25%; (c) Ice = 50%.
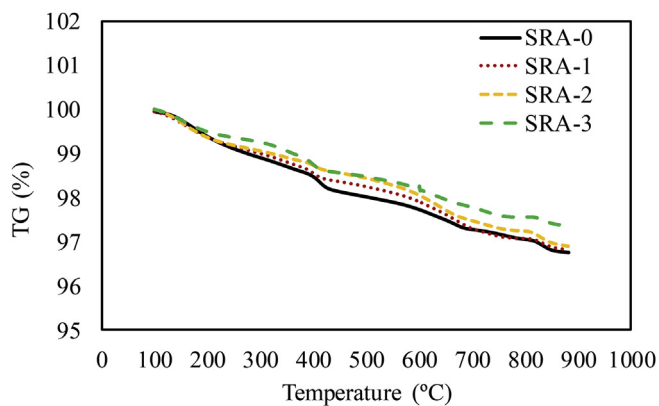
Fig. 29. TG analysis for SRA -0,-1, -2 and -3 UHPC series.

surface of SRA -0, -1, -2 and -3 UHPCs with different magnifications. The comparisons among these micrographs at the lower magnification (i.e. 1000×) suggest that the increased SRA content in the UHPC mix led to increased porosity of the concrete, which is in agreement with the findings from the porosity test mentioned earlier. For the SEM micrographs at the higher magnification (i.e. 10000×), an increased amount of unhydrated binder and ettringite were observed, which indicated lower degree of hydration and increased pore space in the concrete. As discussed previously, this arises because the SRA does not participate in the hydration process but rather acts to slow the hydration process by reducing the contact between the water and binder. In addition, based on the porosity tests results and SEM micrograph, the increased porosity of the UHPC with SRA incorporation might be another potential

explanation for the reduction in the autogenous shrinkage of the concrete, where the presence of pores limited the space for the autogenous shrinkage of the matrix for a given content of aggregate in the mix.

4.7.2. Effect of crushed ice dosage

Figs. 27 and 28 show SEM micrographs of the fracture surface of Ice -0, -25/75, and -50/50 UHPCs at the different magnifications. From SEM micrographs of these UHPC series at the lower magnification (i.e. 1000×), the denseness of the UHPC is observed to decrease with an increase in the crushed ice dosage, indicating an increase in porosity. The comparisons of the SEM micrographs at the higher magnification (i.e. 10000×) show the increased amount of unhydrated binder and ettringite, which suggest the lower degree of hydration and increased pore space for the UHPC prepared using a higher crushed ice replaced water ratio. The increased porosity, formation of ettringite in the concrete and the reduced heat of hydration together explain the mechanism by which the replacement of mixing water with crushed ice reduces self-desiccation.

4.8. Thermal gravity (TG) analysis

The TGA curves of SRA -0,-1, -2 and -3 UHPC series and Ice -0, -25/75, and -50/50 UHPC series are shown in Figs. 29 and 30 respectively and the degree of hydration of these UHPCs at their hardened stage are shown in Figs. 31 and 32 in conjunction with the calculated C-H contents. It is evident from Fig. 31 that the increased SRA content generally lowered the degree of hydration of the UHPCs (i.e. up to around 20%). An even more pronounced reduction in the degree of hydration (i.e. up to approximately 95%) was observed for the UHPC using a higher crushed ice replaced dosage. These characterizations further confirm
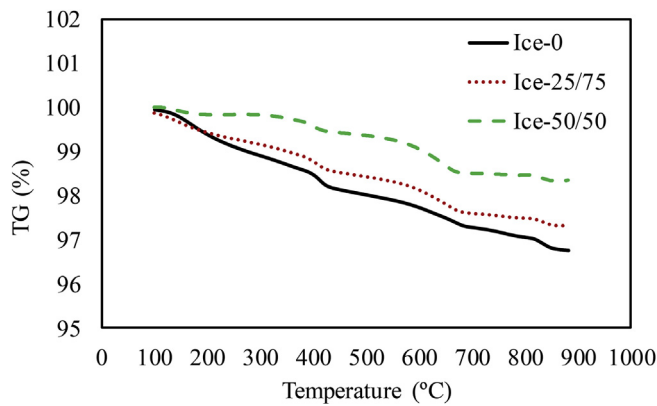
Fig. 30. TG analysis Ice = 0%, Ice = 25% and Ice = 50% UHPC series.
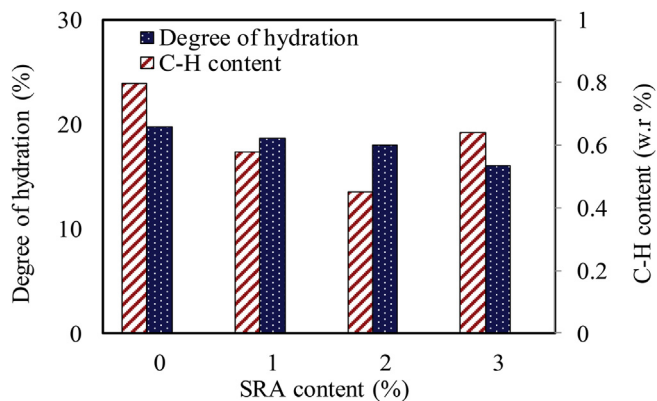
Fig. 31. Effect of SRA content on degree of hydration and C-H content.
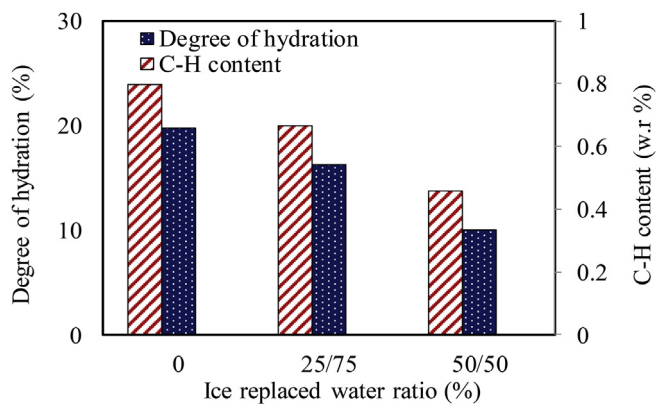
Fig. 32. Effect of ice replaced water ratio on degree of hydration and C-H content.

that using SRA or replacing mixing water by crushed ice can efficiently reduce the shrinkage of UHPC due to chemical reaction.

5. Comparisons among the three techniques and further suggestions for UHPC mix

To compare the effectiveness of the three techniques used in the present study to mitigate shrinkage of the UHPCs, the key findings of each test are summarized in Table 5. To make a valid comparison, the test results of each UHPC series are compared with the reference mix, U-1.0 series. It can be seen from Table 5 that compared to U-1 series, both U-1.1 and 1.266 had significantly lower 90-day autogenous- and total-shrinkage strains and a marked $\Delta f'_c$ at 90 days. All five U-series of UHPCs experienced strength drop after 90 days. Incorporation of SRA

Table 5
Effects of nominated techniques on shrinkage and other properties of the UHPCs.

Specimen	Change in autogenous shrinkage strain at 90 days	Change in total shrinkage strain at 90 days	Change in f'_c at 90 days	$\Delta f'_c$ between 90 and 180 days
U-0.8	6.4%	3.3%	−6.5%	−5.3%
U-0.9	0.8%	−0.2%	−3.0%	−3.6%
U-1.0/SRA-0/Ice-0	0.0%	0.0%	0.0%	−3.8%
U-1.1	−15.7%	−8.6%	0.5%	−3.9%
U-1.266	−26.3%	−10.9%	−6.3%	−2.3%
SRA-1	−36.1%	−30.0%	−12.9%	0.6%
SRA-2	−69.6%	−47.9%	−18.5%	2.0%
SRA-3	−55.0%	−65.7%	−21.5%	1.8%
Ice-25/75	−13.5%	−13.7%	−5.3%	−0.8%
Ice-50/50	−20.7%	−20.4%	−8.1%	−0.2%

and partially replaced of mixing water in UHPC mix by crushed ice can both led to the reduction in autogenous- and total-shrinkage of the concrete, hence minimizing the compressive strength loss ($\Delta f'_c$) after long term. While the use of SRA is more efficient in reducing shrinkage and the associated reduction in strength over time than replaced mixing water by ice, the low cost and simplicity of using ice has significant benefits. However, it is also noted that the application of either of the technique causes a reduction the maximum compressive strength achieved. Therefore, from this study, it can be concluded that the best mix for reducing the impact of shrinkage without significant $\Delta f'_c$ in the long-term will be 1) SRA-1 using 1% SRA dosage and 2) Ice-50/50 prepared using crushed ice dosage of 50%.

6. Conclusions

The following major inferences can be made from the results of the present study to investigate the effects of *b/s* ratio, SRA content and crushed ice dosage on the shrinkage properties of the UHPC:

1. Autogenous shrinkage of the UHPC decreases with an increase in the *b/s* ratio due to the more significant shrinkage restraint provided by the residual binders in the UHPC prepared with a higher *b/s* ratio.
2. An increase in the *b/s* ratio in the UHPC mix leads to a decrease in the porosity of the concrete. For UHPC prepared using a lower *b/s* ratio, the abundance of crystalline ettringite and C-H seen in the pores and cracks in the concrete minimized the drying shrinkage of the concrete
3. An optimal *b/s* ratio will be 1–1.1 for a typical UHPC mix to minimize the shrinkage effect without significantly comprising f'_c.
4. The autogenous shrinkage has more significant effect than the drying shrinkage on total shrinkage of the UHPCs.
5. The porosity and the amount of unreacted binder, which are related to the degree of hydration of the concrete, are the two influential factors on the shrinkage properties of UHPCs.
6. SRA is not only able to reduce the drying shrinkage but also the autogenous shrinkage (i.e. up to 55% at 90 days with 3% of SRA dosage) of UHPCs
7. The replacement of half of the mixing water by crushed ice in a UHPC mix can reduce the autogenous shrinkage of the UHPC up to 22% and has nearly no effect on the drying shrinkage properties of the UHPCs. This technique is cost-effective and relatively practical to apply in any cast in-situ or pre-casting scenarios.

References

[1] M. Singh, A. Sheikh, M.M. Ali, P. Visintin, M. Griffith, Experimental and numerical study of the flexural behaviour of ultra-high performance fibre reinforced concrete beams, Construct. Build. Mater. 138 (2017) 12–25.

[2] M.A. Mosaberpanah, O. Eren, Relationship between 28-days compressive strength and compression toughness factor of ultra high performance concrete using design of experiments, Procedia Eng. 145 (2016) 1565–1571.

[3] D.-Y. Yoo, N. Banthia, Mechanical properties of ultra-high-performance fiber-reinforced concrete: a review, Cement Concr. Compos. 73 (2016) 267–280.

[4] D. Wang, C. Shi, Z. Wu, J. Xiao, Z. Huang, Z. Fang, A review on ultra high performance concrete: Part II. Hydration, microstructure and properties, Construct. Build. Mater. 96 (2015) 368–377.

[5] C. Shi, Z. Wu, J. Xiao, D. Wang, Z. Huang, Z. Fang, A review on ultra high performance concrete: Part I. Raw materials and mixture design, Construct. Build. Mater. 101 (2015) 741–751.

[6] D. Youssef, The Use of Lightweight Sand for Internal Curing and its Effect on Performance of HPC Used for Concrete Infrastructures, Université de Sherbrooke, 2013.

[7] L. Wu, N. Farzadnia, C. Shi, Z. Zhang, H. Wang, Autogenous shrinkage of high performance concrete: a review, Construct. Build. Mater. 149 (2017) 62–75.

[8] Ç. Yalçınkaya, H. Yazıcı, Effects of ambient temperature and relative humidity on early-age shrinkage of UHPC with high-volume mineral admixtures, Construct. Build. Mater. 144 (2017) 252–259.

[9] D.-Y. Yoo, K.-H. Min, J.-H. Lee, Y.-S. Yoon, Shrinkage and cracking of restrained ultra-high-performance fiber-reinforced concrete slabs at early age, Construct. Build. Mater. 73 (2014) 357–365.

[10] J.-J. Park, D.-Y. Yoo, S.-W. Kim, Y.-S. Yoon, Benefits of using expansive and shrinkage-reducing agents in UHPC for volume stability, Mag. Concr. Res. 66 (14) (2014) 745–750.

[11] A. Soliman, M. Nehdi, Effects of shrinkage reducing admixture and wollastonite microfiber on early-age behavior of ultra-high performance concrete, Cement Concr. Compos. 46 (2014) 81–89.

[12] D.-Y. Yoo, S.-T. Kang, J.-H. Lee, Y.-S. Yoon, Effect of shrinkage reducing admixture on tensile and flexural behaviors of UHPFRC considering fiber distribution characteristics, Cement Concr. Res. 54 (2013) 180–190.

[13] A. Soliman, M. Nehdi, Effect of drying conditions on autogenous shrinkage in ultra-high performance concrete at early-age, Mater. Struct. 44 (5) (2011) 879–899.

[14] H. Sobuz, P. Visintin, M.M. Ali, M. Singh, M. Griffith, A. Sheikh, Manufacturing ultra-high performance concrete utilising conventional materials and production methods, Construct. Build. Mater. 111 (2016) 251–261.

[15] D.-Y. Yoo, J.-J. Park, S.-W. Kim, Y.-S. Yoon, Influence of ring size on the restrained shrinkage behavior of ultra high performance fiber reinforced concrete, Mater. Struct. 47 (7) (2014) 1161–1174.

[16] M. Şahmaran, M. Lachemi, K.M. Hossain, V.C. Li, Internal curing of engineered cementitious composites for prevention of early age autogenous shrinkage cracking, Cement Concr. Res. 39 (10) (2009) 893–901.

[17] D.-Y. Yoo, N. Banthia, Y.-S. Yoon, Ultra-high-performance fiber-reinforced concrete: shrinkage strain development at early ages and potential for cracking, J. Test. Eval. 45 (6) (2017) 2061–2070.

[18] D.-Y. Yoo, J.-J. Park, S.-W. Kim, Y.-S. Yoon, Influence of reinforcing bar type on autogenous shrinkage stress and bond behavior of ultra high performance fiber reinforced concrete, Cement Concr. Compos. 48 (2014) 150–161.

[19] D.-Y. Yoo, M.-J. Kim, S. Kim, G.-S. Ryu, K.-T. Koh, Effects of mix proportion and curing condition on shrinkage behavior of HPFRCCs with silica fume and blast furnace slag, Construct. Build. Mater. 166 (1) (2018) 241–256.

[20] D.-Y. Yoo, N. Banthia, Y.-S. Yoon, Geometrical and boundary condition effects on restrained shrinkage behavior of UHPFRC slabs, KSCE J. Civil Eng. 22 (1) (2018) 185–195.

[21] M. Sahmaran, M. Lachemi, K.M. Hossain, R. Ranade, V.C. Li, Influence of aggregate type and size on ductility and mechanical properties of engineered cementitious composites, Mater. J. 106 (3) (2009) 308–316.

[22] M. Şahmaran, M. Al-Emam, G. Yıldırım, Y.E. Şimşek, T.K. Erdem, M. Lachemi, High-early-strength ductile cementitious composites with characteristics of low early-age shrinkage for repair of infrastructures, Mater. Struct. 48 (5) (2015) 1389–1403.

[23] C. Rößler, D.-D. Bui, H.-M. Ludwig, Rice husk ash as both pozzolanic admixture and internal curing agent in ultra-high performance concrete, Cement Concr. Compos. 53 (2014) 270–278.

[24] O.M. Jensen, Use of superabsorbent polymers in concrete, Concr. Int. 35 (1) (2013) 48–52.

[25] L. Dudziak, V. Mechtcherine, Mitigation of volume changes of ultra-high performance concrete (UHPC) by using super absorbent polymers, Proceedings of the 2nd International Symposium on Ultra High Performance Concrete, Kassel University Press, Kassel, 2008, pp. 425–432.

[26] D.-Y. Yoo, N. Banthia, Y.-S. Yoon, Effectiveness of shrinkage-reducing admixture in reducing autogenous shrinkage stress of ultra-high-performance fiber-reinforced concrete, Cement Concr. Compos. 64 (2015) 27–36.

[27] K. Koh, G. Ryu, S. Kang, J. Park, S. Kim, Shrinkage properties of ultra-high performance concrete (UHPC), Adv. Sci. Lett. 4 (3) (2011) 948–952.

[28] H.R. Sobuz, D.J. Oehlers, P. Visintin, N.M.S. Hasan, M.I. Hoque, A.S.M. Akid, Flow and strength characteristics of ultra-high performance fiber reinforced concrete: influence of fiber type and volume-fraction, J. Civil Eng. Construct. 6 (1) (2017) 15.

[29] P. Visintin, A.B. Sturm, M.M. Ali, D.J. Oehlers, Blending macro and micro fibres to enhance the serviceability behaviour of UHPFRC, Aust. J. Civ. Eng. (2018), http://

dx.doi.org/10.1080/14488353.2018.1463608.

[30] P. Visintin, M.M. Ali, T. Xie, A.B. Sturm, Experimental investigation of moment redistribution in ultra-high performance fibre reinforced concrete beams, Construct. Build. Mater. 166 (2018) 433–444.

[31] A.B. Sturm, P. Visintin, K. Ferris, D.J. Oehlers, A new testing approach for extracting the shear friction material properties of ultra-high performance fibre reinforced concrete, ASCE J. Mater. Civil Eng. (2018).

[32] B.G. Smith, Durability of silica fume concrete exposed to chloride in hot climates, J. Mater. Civ. Eng. 13 (1) (2001) 41–48.

[33] Australian Standard, AS/NZS 2350.11. Methods for Testing Portland, Blended and Masonry Cements, Standards Australia, Sydeny, 2006.

[34] Australian Standard, AS/NZS 2350.13. Methods for Testing Portland, Blended and Masonry Cements – Determination of Drying Shrinkage of Cement Mortars, Standards Australia, Sydney, 2006.

[35] Australian Standard, AS 1478.1–2000. Chemical Admixtures for Concrete, Mortar and Grout Admixtures for Concrete, Standards Australia, Sydney, 2000.

[36] ASTM A, C1698–09 Standard Test Method for Autogenous Strain of Cement Paste and Mortar, ASTM International, West Conshohocken, PA, 2009.

[37] A. Darquennes, S. Staquet, B. Espion, Determination of time-zero and its effect on autogenous deformation evolution, Eur. J. Environ. Civil Eng. 15 (7) (2011) 1017–1029.

[38] V. Mechtcherine, M. Gorges, C. Schroefl, A. Assmann, W. Brameshuber, AnB. Ribeiro, et al., Effect of internal curing by using superabsorbent polymers (SAP) on autogenous shrinkage and other properties of a high-performance fine-grained concrete: results of a RILEM round-robin test, Mater. Struct. 47 (3) (2014) 541–562.

[39] Standard Australia, AS 1012.9:2014. Methods of Testing Concrete Compressive Strength Tests - Concrete, Mortar and Grout Specimens, Standards Australia, Sydeny, 2014.

[40] ASTM International, ASTM C143/C143M - 00, Standard Test Method for Slump of Hydraulic Cement Concrete, ASTM International, West Conshohocken, 2000.

[41] ASTM International, ASTM C1621/C1621M–09 Standard Test Method for Passing Ability of Self-consolidating Concrete by J-ring, ASTM International, West Conshohocken, 2009.

[42] B. Langan, K. Weng, M. Ward, Effect of silica fume and fly ash on heat of hydration of Portland cement, Cement Concr. Res. 32 (7) (2002) 1045–1051.

[43] E.-H. Kadri, R. Duval, Hydration heat kinetics of concrete with silica fume, Construct. Build. Mater. 23 (11) (2009) 3388–3392.

[44] P. Lura, O.M. Jensen, K. van Breugel, Autogenous shrinkage in high-performance cement paste: an evaluation of basic mechanisms, Cement Concr. Res. 33 (2) (2003) 223–232.

[45] P. Aïtcin, 17 autogenous shrinkage measurement, Autogenous Shrinkage of Concrete: Proceedings of the International Workshop, Organised by JCI (Japan Concrete Institute), vol. 1999, Taylor & Francis, Hiroshima, June 13-14, 1998, p. 257.

[46] G.-Y. Kim, E.-B. Lee, J.-S. Nam, K.-M. Koo, Analysis of hydration heat and autogenous shrinkage of high-strength mass concrete, Mag. Concr. Res. 63 (5) (2011) 377–389.

[47] ASTM International, ASTM C642–13. Standard Test Method for Density, Absorption, and Voids in Hardened Concrete, ASTM International, West Conshohocken, 2013.

[48] Y. Maltais, J. Marchand, Influence of curing temperature on cement hydration and mechanical strength development of fly ash mortars, Cement Concr. Res. 27 (7) (1997) 1009–1020.

[49] X. Chen, S. Wu, Influence of water-to-cement ratio and curing period on pore structure of cement mortar, Construct. Build. Mater. 38 (2013) 804–812.

[50] D.P. Bentz, Capitalizing on Self-desiccation for Autogenous Distribution of Chemical Admixtures, Lund University, Citeseer, 2005.

[51] M. Yio, J. Phelan, H. Wong, N. Buenfeld, Determining the slag fraction, water/binder ratio and degree of hydration in hardened cement pastes, Cement Concr. Res. 56 (2014) 171–181.

[52] W. Huang, H. Kazemi-Kamyab, W. Sun, K. Scrivener, Effect of cement substitution by limestone on the hydration and microstructural development of ultra-high performance concrete (UHPC), Cement Concr. Compos. 77 (2017) 86–101.

[53] L. Lam, Y. Wong, C. Poon, Degree of hydration and gel/space ratio of high-volume fly ash/cement systems, Cement Concr. Res. 30 (5) (2000) 747–756.

[54] H. Wong, N. Buenfeld, Determining the water–cement ratio, cement content, water content and degree of hydration of hardened cement paste: method development and validation on paste samples, Cement Concr. Res. 39 (10) (2009) 957–965.

[55] R. Vedalakshmi, A.S. Raj, S. Srinivasan, K.G. Babu, Quantification of hydrated cement products of blended cements in low and medium strength concrete using TG and DTA technique, Thermochim. Acta 407 (1) (2003) 49–60.

[56] S. Brunauer, D. Kantro, The hydration of tricalcium silicate and β dicalcium silicate from 5 C to 50 C, Chem. Cement 1 (1964) 287.

[57] S.P. Newman, S.J. Clifford, P.V. Coveney, V. Gupta, J.D. Blanchard, F. Serafin, et al., Anomalous fluorescence in near-infrared Raman spectroscopy of cementitious materials, Cement Concr. Res. 35 (8) (2005) 1620–1628.

[58] B. Hasanzadeh, F. Liu, Z. Sun, Monitoring hydration of UHPC and conventional paste by quantitative analysis on Raman patterns, Construct. Build. Mater. 114 (2016) 208–214.

[59] J. Dweck, P.M. Buchler, A.C.V. Coelho, F.K. Cartledge, Hydration of a Portland cement blended with calcium carbonate, Thermochim. Acta 346 (1) (2000) 105–113.

[60] G. Hermida, M. Moranville, R. Flatt, The role of paste volume on performance of concrete, Spec. Publ. 261 (2009) 201–214.

[61] A. Bentur, Kovler K. Igarashi S-i, Prevention of autogenous shrinkage in high-

strength concrete by internal curing using wet lightweight aggregates, Cement Concr. Res. 31 (11) (2001) 1587–1591.

[62] M. Zhang, C. Tam, M. Leow, Effect of water-to-cementitious materials ratio and silica fume on the autogenous shrinkage of concrete, Cement Concr. Res. 33 (10) (2003) 1687–1694.

[63] H.G. Russell, B.A. Graybeal, Ultra-high Performance Concrete: a State-of-the-art Report for the Bridge Community, (2013).

[64] P. Schießl, O. Mazanec, D. Lowke, SCC and UHPC—effect of Mixing Technology on Fresh Concrete Properties. Advances in Construction Materials 2007, Springer, 2007, pp. 513–522.

[65] J. Ma, M. Orgass, F. Dehn, D. Schmidt, N. Tue, Comparative investigations on ultra-high performance concrete with and without coarse aggregates, Proceedings of International Symposium on Ultra High Performance Concrete, Germany, 2004, pp. 205–212.

[66] A. Soliman, M. Nehdi, Effect of partially hydrated cementitious materials and su-perabsorbent polymer on early-age shrinkage of UHPC, Construct. Build. Mater. 41 (2013) 270–275.

[67] W. Shen, X. Li, G. Gan, L. Cao, C. Li, J. Bai, Experimental investigation on shrinkage and water desorption of the paste in high performance concrete, Construct. Build. Mater. 114 (2016) 618–624.

[68] B.V. Reddy, A. Gupta, Influence of sand grading on the characteristics of mortars and soil–cement block masonry, Construct. Build. Mater. 22 (8) (2008) 1614–1623.

[69] P.J. Jun, K.S. Tae, R.G. Sung, K.S. Wook, L.J. Hwa, The effect of material factors on the compressive strength of ultra-high strength Steel Fiber Reinforced Cementitious Composites, Proceedings of the Korea Concrete Institute Conference, Korea Concrete Institute, 2004.

[70] J.J. Park, S.T. Kang, K.T. Koh, S.W. Kim, Influence of the ingredients on the com-pressive strength of UHPC as a fundamental study to optimize the mixing propor-tion, Proceedings of the International Symposium on Ultra-high Performance Concrete, Structural Materials and Engineering Series, 2008, pp. 105–112.

[71] K.L. Scrivener, A.K. Crumbie, P. Laugesen, The interfacial transition zone (ITZ) between cement paste and aggregate in concrete, Interface Sci. 12 (4) (2004) 411–421.

[72] A. Brough, A. Atkinson, Automated identification of the aggregate–paste interfacial

[73] transition zone in mortars of silica sand with Portland or alkali-activated slag ce-ment paste, Cement Concr. Res. 30 (6) (2000) 849–854.

[73] R. Yu, P. Spiesz, H. Brouwers, Effect of nano-silica on the hydration and micro-structure development of Ultra-High Performance Concrete (UHPC) with a low binder amount, Construct. Build. Mater. 65 (2014) 140–150.

[74] I. Odler, Hydration, setting and hardening of Portland cement, Lea's Chemistry of Cement and Concrete 4 (1998) 241–297.

[75] H. Jennings, P. Pratt, An experimental argument for the existence of a protective membrane surrounding Portland cement during the induction period, Cement Concr. Res. 9 (4) (1979) 501–506.

[76] P.K. Mehta, Mechanism of expansion associated with ettringite formation, Cement Concr. Res. 3 (1) (1973) 1–6.

[77] M.Y. Han, R.L. Lytton, Theoretical prediction of drying shrinkage of concrete, J. Mater. Civ. Eng. 7 (4) (1995) 204–207.

[78] P. Yan, F. Zheng, J. Peng, X. Qin, Relationship between delayed ettringite formation and delayed expansion in massive shrinkage-compensating concrete, Cement Concr. Compos. 26 (6) (2004) 687–693.

[79] M. Collepardi, A. Borsoi, S. Collepardi, J.J.O. Olagot, R. Troli, Effects of shrinkage reducing admixture in shrinkage compensating concrete under non-wet curing conditions, Cement Concr. Compos. 27 (6) (2005) 704–708.

[80] K.J. Folliard, N.S. Berke, Properties of high-performance concrete containing shrinkage-reducing admixture, Cement Concr. Res. 27 (9) (1997) 1357–1364.

[81] S. Anshuang, Q. Ling, Z. Shoujie, Z. Jiayang, L. Zhaoyu, Effects of shrinkage re-ducing agent and expansive admixture on the volume deformation of ultrahigh performance concrete, Adv. Mater. Sci. Eng. 2017 (2017).

[82] D. Bentz, M.R. Geiker, K.K. Hansen, Shrinkage-reducing admixtures and early-age desiccation in cement pastes and mortars, Cement Concr. Res. 31 (7) (2001) 1075–1085.

[83] N. Shlonimskaya, J.J. Biernacki, H.M. Kayello, D.P. Visco, An application of com-puter-aided molecular design (CAMD) using the signature molecular Descriptor–Part 2. Evaluating Newly identified surface tension-reducing substances for potential use as shrinkage-reducing admixtures, J. Am. Ceram. Soc. 97 (2) (2014) 378–385.

Partial Interaction Model of Flexural Behavior of PVA Fiber–Reinforced Concrete Beams with GFRP Bars

T. Xie[1]; M. S. Mohamed Ali[2]; P. Visintin[3]; D. J. Oehlers[4]; and A. H. Sheikh[5]

Abstract: This paper describes experimental and analytical investigations on a highly durable composite structural system comprising polyvinyl alcohol (PVA) fiber-reinforced concrete (PVA-FRC) reinforced with glass fiber-reinforced polymer (GFRP) bars. To aid in the development of a design guideline for this novel composite beam system, a generic analytical approach that is equally applicable to both conventional concrete and FRC beams reinforced with steel or FRP rebar is applied. Predicted load-deflection and load-crack width responses are compared to the experimental results, showing very good correlation for the flexural behavior of PVA fiber–reinforced concrete members. **DOI:** [10.1061/(ASCE)CC.1943-5614.0000878](#). © 2018 American Society of Civil Engineers.

Author keywords: Polyvinyl alcohol (PVA) fibers; Glass fiber-reinforced polymer (GFRP) bars; Partial interaction (PI) analysis; Flexural behavior; Fiber-reinforced concrete (FRC).

Introduction

Degradation of steel reinforced concrete (RC) infrastructure due to reinforcement corrosion results in significant damage and economic loss ([Almusallam 2001](#); [Feng et al. 2016](#)). In the last three decades, glass fiber-reinforced polymer (GFRP) reinforcement has been used as a corrosion-resistant alternative to conventional steel reinforcement ([Alsayed 1998](#); [Barris et al. 2009](#); [Goldston et al. 2017](#); [Jakubovskis et al. 2014](#); [Mazaheripour et al. 2016](#)). Due to the elastic brittle nature of GFRP, the design of glass fiber-reinforced polymer reinforced concrete (GFRPRC) at the ultimate limit is generally restricted to overreinforced sections in which member ductility arises from concrete crushing ([Kachlakev and McCurry 2000](#); [Qu et al. 2009](#)). Moreover, due to the low elastic modulus of GFRP and the weaker bond between GFRP and the surrounding concrete, deflections and crack widths in GFRPRC beams at the serviceability limit may be greater than that of conventional steel RC beams ([Toutanji and Deng 2003](#)).

A recent focus of concrete technology has been the incorporation of randomly distributed fibers to form fiber-reinforced concrete (FRC). These materials have been shown to improve the flexural ductility of members by restraining postpeak sliding of concrete wedges ([Matthys 2017](#); [Visintin and Oehlers 2017](#)) and to reduce deflections and crack widths due to the ability to transfer stresses across tensile cracks ([Altun et al. 2007](#); [Schumacher 2006](#); [Visintin and Oehlers 2017](#); [Yoo et al. 2015](#)). Hence, the incorporation of

fibers into GFRPRC may provide a means for compensating for the lower ductility and larger deflections and crack widths seen in this form of construction.

In this paper, a highly durable structural system is proposed by combining the durability of GFRP reinforcement with polyvinyl alcohol (PVA) FRC. The paper first describes an experimental program to establish the fundamental material properties that control the behavior of GFRP-reinforced PVA-FRC; namely, the compressive and tensile stress-strain relationships of the PVA-FRC and the local bond stress-slip relationship between the PVA and FRC are determined. Having quantified the fundamental material properties, the results of four tests on PVA-FRC beams with GFRP bars are reported. It is then shown how an existing mechanics-based analysis technique for predicting the load-deflection and load-crack width behaviors of conventional concrete beams can be extended for the analysis of FRC beams.

The application of a generic approach is considered important because an increasingly large number of design options are becoming available to practitioners, and hence, for widespread application of new materials to occur, standardized analysis procedures, which can be applied to a range of material types, are required. The segmental approach proposed here has already been widely applied to a wide range of materials and loading scenarios, including the short- and long-term performance of steel- and FRP-reinforced concrete ([Feng et al. 2016](#); [Knight et al. 2014a](#); [Visintin et al. 2013](#)) and prestressed concrete ([Knight et al. 2014b](#), [c](#)) beams, and it will be shown here that it can be further applied to GFRP-reinforced FRC. Significantly, in applying the analytical approach to this novel system, it is shown how very few experimental inputs are required in order to adequately predict the load-deflection and load-crack width behaviors of the member. Hence, the proposed analysis approach should allow for a more rapid development of novel materials as well as a faster transition from lab technologies to real-world applications.

Experimental Program

Aiming to apply the segmental analytical approach ([Visintin et al. 2012](#); [Visintin and Oehlers 2017](#); [Visintin et al. 2016](#)) to the prediction of the load-deflection and load-crack width behaviors of the

[1]Ph.D. Candidate, School of Civil, Environmental and Mining Engineering, Univ. of Adelaide, Adelaide, SA 5005, Australia (corresponding author). Email: tianyu.xie@adelaide.edu.au

[2]Senior Lecturer, School of Civil, Environmental and Mining Engineering, Univ. of Adelaide, Adelaide, SA 5005, Australia.

[3]Senior Lecturer, School of Civil, Environmental and Mining Engineering, Univ. of Adelaide, Adelaide, SA 5005, Australia.

[4]Emeritus Professor, School of Civil, Environmental and Mining Engineering, Univ. of Adelaide, Adelaide, SA 5005, Australia.

[5]Associate Professor, School of Civil, Environmental and Mining Engineering, Univ. of Adelaide, Adelaide, SA 5005, Australia.

FRC-FRP system, an experimental program was formulated to establish the fundamental material properties required for the analysis. The required material properties include the compressive and direct tensile behavior of the PVA-FRC and the bond between the GFRP reinforcement and PVA-FRC. To then show the predictive capability of the segmental approach, four beam tests were conducted to obtain the load-deflection and load-crack width behaviors.

Materials

PVA-FRC

Test specimens used in the experimental program were manufactured using two different PVA fiber–reinforced normal-strength concretes. These two mixes were both prepared using a water-to-cement ratio (w/c) of 0.5, and to investigate the influence of fiber content, the fiber weight fraction was either 6 kg/m^3 (designated as FRC-6), or 12 kg/m^3 (designated as FRC-12). The PVA fiber had a length of 30 mm and a nominal diameter of 0.75 mm (with the aspect ratio of 40). The manufacturer-reported tensile strength and density of the fiber are 1,620 MPa and 1.3 g/cm^3, respectively. The full mix proportions of the FRCs are given in Table 1.

GFRP Bar

The GFRP bars were sand-coated with a nominal diameter of 12 mm. For analysis, the GFRP bars were assumed to behave in a linear elastic-brittle manner in which the ultimate tensile strength and elastic modulus of GFRP bar are 1,186 MPa and 66.3 GPa, respectively. These properties were obtained from the manufacturer of the GFRP and were determined by averaging the results of 12 direct tension tests.

Test Methods

Material Tests

Compressive Stress-Strain Relationship
To quantify the axial compressive stress-strain relationship of the PVA-FRC, compression tests according to Australian standard 1012.9 (AS 2014) were conducted on standard cylindrical specimens with 100-mm diameter and 200-mm height. Axial deformations were recorded using two 10-mm LVDTs installed along the full height of the specimens.

Tensile Stress-Strain Relationship
The precracking stress-strain and postcracking stress-crack width behaviors of the FRC were determined in accordance with the RILEM TC 162-TDF standard (Rilem 2002). In these tests, cylindrical specimens with 150-mm diameter and 150-mm height

were tested under uniaxial tension by applying a force to steel plates adhesively bonded to the ends of the specimens (Fig. 1). During testing, a tensile force was applied to maintain a displacement rate of 0.1 mm per minute, and to obtain the stress-crack width behavior, the deformation across a circumferential notch with a depth of 15 mm and width of 2.5 mm was recorded using two LVDTs.

Pullout Tests

To obtain the local bond stress-slip behavior of the FRC-FRP bar interface, pullout tests were conducted using the specimens shown in Fig. 2. These specimens consisted of a 200-mm × 200-mm square prism with a height of 350 mm into which a 12-mm GFRP bar with a bonded length of 60 or 300 mm was embedded. The short embedment length tests (60 mm) were used to assess the local bond-slip response for the subsequent modeling of tension stiffening and crack opening in the beams. In these tests, a 60-mm bonded length was chosen to ensure the bond stresses along the bar were approximately evenly distributed, which ensures that the average bond stress at failure is close to the actual local bond stress (Feng et al. 2016; Haskett et al. 2008).

Additionally, in order to ensure the reinforcement was fully anchored in the beam tests, specimens with a longer embedment length (300 mm) and different fiber contents (i.e., 0 or 6 kg/m^3) were also prepared and tested with the plain concrete designated as FRC-0.

For all bond tests, in order to avoid concrete conical pullout failure, the bond was broken over the first 25 mm of the embedded length using a PVC tube as a bond breaker. During testing, the bar was pulled from the concrete block at a rate of 6 kN/min, and the slip of the bar relative to the top of the concrete block was measured using an LVDT as shown in Fig. 2. For the purpose of examining the effects of the fiber content on the bond-slip behavior, a series of reference specimens without fibers were also tested. Although the concrete surrounding the reinforcement in pull tests is in a state of compression, the bond properties derived from this form of test are commonly used to simulate behavior in which the concrete surrounding the reinforcement is in tension. For example, bond properties have been used to simulate crack formation and crack widening in Achillides and Pilakoutas (2004), Mo et al. (2016), Visintin et al. (2018), Visintin et al. (2016), and Zhang et al. (2016). Although this is a generally accepted approach, the use of bond properties extracted from half-beam tests more closely matches the state of stress experience in the tensile region of a beam (Ashtiani et al. 2013; Jakubovskis et al. 2014).

Table 1. Mix proportions of concrete

Components	FRC-6	FRC-12
Fiber content (kg/m^3)	6	12
Water (kg/m^3)	166	166
Cement (kg/m^3)	332	332
Water-to-cement ratio	0.5	0.5
Sand (kg/m^3)	875	830
Aggregate-10 mm (kg/m^3)	330	330
Aggregate-20 mm (kg/m^3)	700	700
Density (kg/m^3)	2,409	2,370

Fig. 1. Details of direct tension test specimen and setup.

© ASCE 04018043-2 J. Compos. Constr.

301
J. Compos. Constr., 2018, 22(5): 04018043
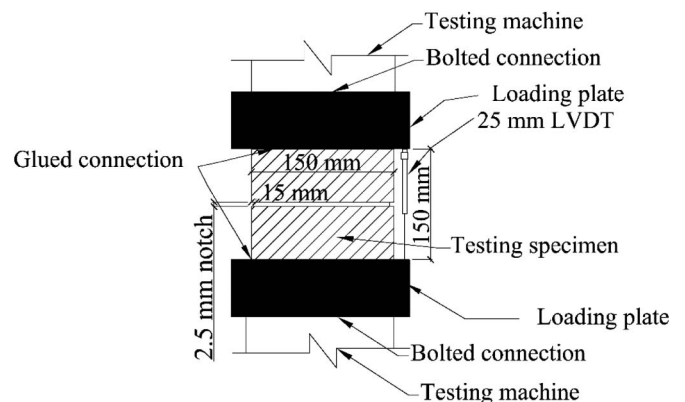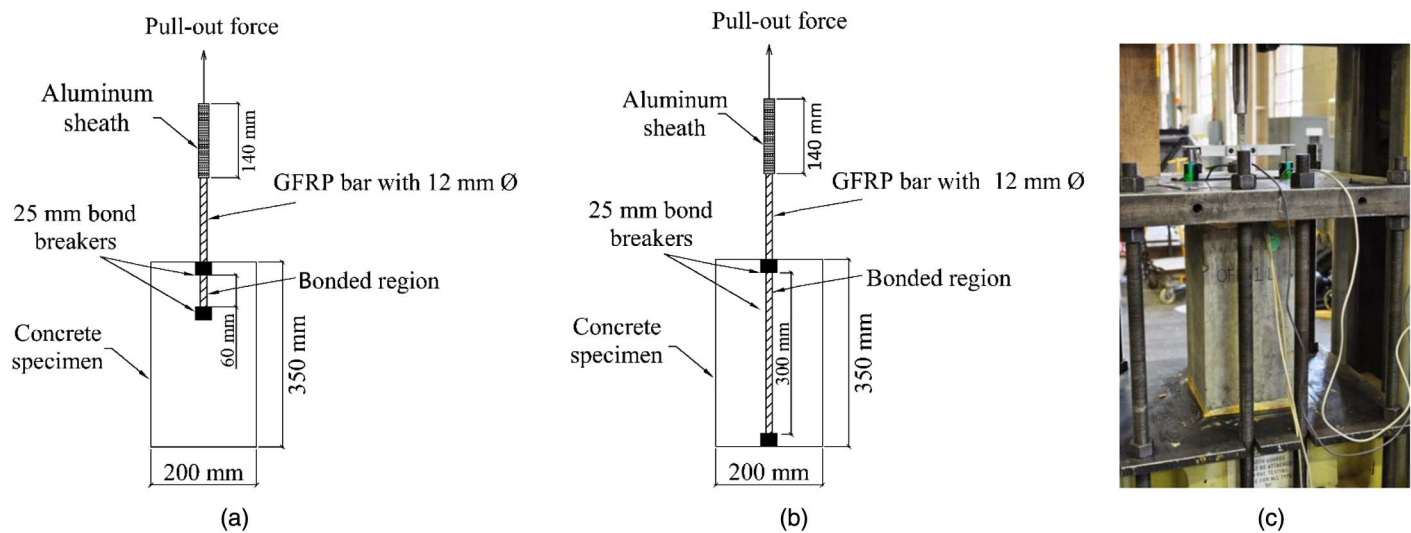
Fig. 2. Details of pullout test: (a) test specimen with a shorter embedment length (60 mm); (b) test specimen with a longer embedment length (300 mm); and (c) pullout test setup.
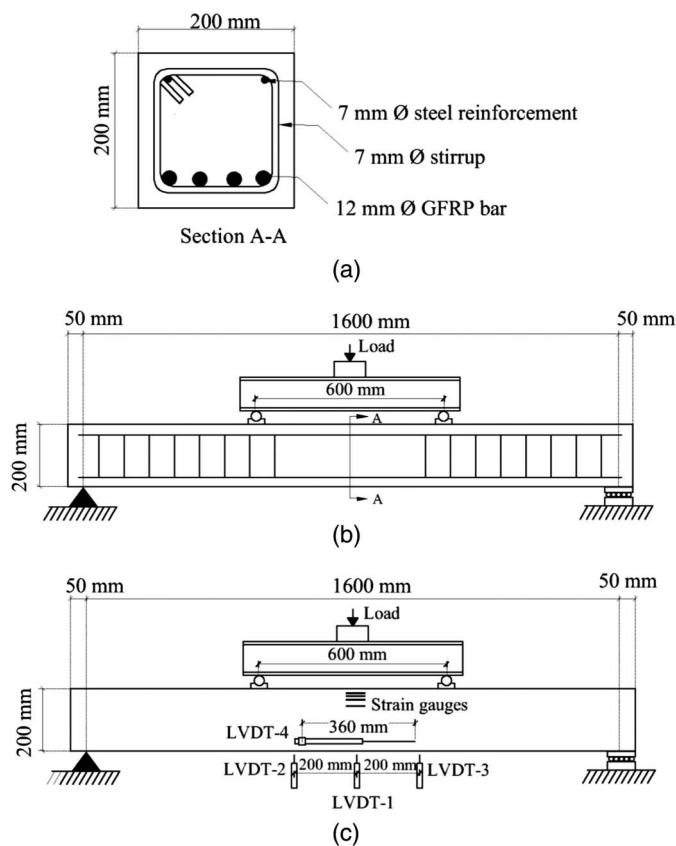
Fig. 3. Details of beam specimen and test setup: (a) details of beam cross section; (b) details of the beam specimen; and (c) test setup.

Beam Tests

In order to experimentally establish the flexural behavior of PVA fiber–reinforced members with GFRP bars, and for validation of the proposed model, two series of beams prepared using FRC with different fiber weight fractions were manufactured and tested. Two nominally identical specimens were tested for each beam series in order to establish any variation in behavior due to differences in the distribution of fiber density or orientation that may occur during casting.

Designed to be overreinforced, each beam had a cross section of 200 mm × 200 mm and was reinforced with four 12-mm GFRP bars at an effective depth of 170 mm. To prevent shear failure, adequate shear reinforcements were also provided and consisted of 7-mm diameter stirrups spaced at 120-mm centers. No shear reinforcement was provided in the constant moment region (the central 600 mm) in order to avoid any confining effect that may occur. The details of the cross section of test beams are shown in Fig. 3(a). To hang the stirrups, two steel bars with a 7-mm diameter, located at an effective depth of 30 mm, were included in the compression region.

Figs. 3(b and c) schematically illustrate the details of the beam test setup. All members were tested as simply supported under four-point bending. The first beam was tested with a span of 1,600 mm between the two supports and with the concentrated loads positioned at a spacing of 600 mm; however, this arrangement resulted in unexpected shear failure. To avoid such a shear failure in subsequent tests, the length of the constant moment region was reduced to 500 mm. Throughout testing, the deflection of the beam was measured by 50-mm LVDTs positioned at the location of each loading point and at the midspan of the beam. To record crack width, a lateral LVDT was placed in the center of the beam at the level of the tensile reinforcement.

Results and Discussions

Material Properties

Compressive Strength and Stress-Strain Behavior

Fig. 4 illustrates the axial compressive stress-strain relationship for each FRC, from which it can be seen that, regardless of fiber content, the axial stress-strain relationships of the concrete are nearly identical until the peak stress is reached. After the peak stress is reached, an increase in ductility with an increase in fiber content is observed. These observations are in close agreement with those reported in previous studies on the compressive stress-strain behavior of FRCs (Bhargava et al. 2006; Ezeldin and Balaguru 1992; Olivito and Zuccarello 2010; Wang et al. 2012) in which the increase in ductility can be attributed to the additional confining

© ASCE   04018043-3   J. Compos. Constr.

302
J. Compos. Constr., 2018, 22(5): 04018043

Fig. 4. Compressive stress-strain relationship of FRCs.

effect provided by the internal fibers. To model the compressive stress-strain behavior of the PVA-FRC, Hognestad's (Hognestad et al. 1955) model for conventional concrete was modified to induce a linear descending branch. A general expression that can describe the compressive stress-strain behavior of FRC with different PVA fibers is given in Eq. (1) as follows:

$$\sigma_c = \begin{cases} f'_c\left(\dfrac{2\varepsilon_c}{\varepsilon_o} - \left(\dfrac{\varepsilon_c}{\varepsilon_o}\right)^2\right) & if \ \varepsilon_c \leq \varepsilon_o \\ f'_c(1 - \alpha(\varepsilon_c - \varepsilon_o)) & if \ \varepsilon_c > \varepsilon_o \end{cases} \quad (1)$$

where ε_o = concrete strain corresponding to the peak stress; and α = shape factor for the descending b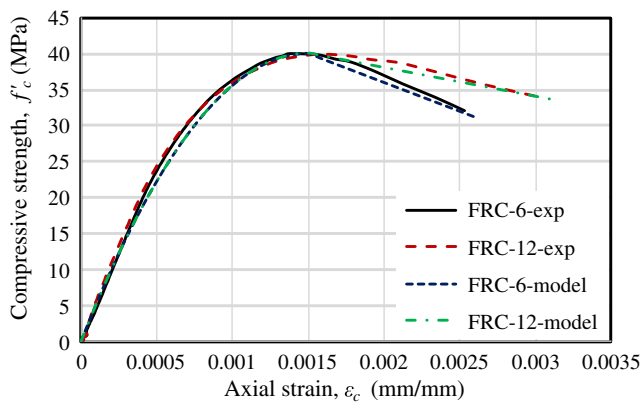ranch of the compressive stress-strain curves of FRC with different content fibers. In the present study, α was taken as 200 for mixes with 6 kg/m³ of fibers, and 100 for mixes with 12 kg/m³ of fibers. Fig. 4 shows that the proposed expressions for the $\sigma - \varepsilon$ relationship well reproduce the test results.

Tensile Strength and Stress-Strain Behavior

The tensile behavior of the FRC-6 and FRC-12 is shown in Fig. 5. Prior to cracking of the FRC, its tensile stress-strain relationship is shown in Fig. 5(a), and in the post-cracking stage, its tensile stress-crack width relationship is shown in Fig. 5(b). Comparing the behavior with different fiber contents, it can be seen that the mix with a higher fiber content (FRC-12) exhibited a higher tensile strength prior to cracking and required a higher tensile strength to attain the same crack width as that of FRC-6 at the postcracking stage. This improvement in the tensile behavior of FRC can be attributed to the increase in the number of fibers crossing the crack as the fiber content increases (Olivito and Zuccarello 2010; Xu et al. 1998). From this experimental data, the general expression in Eq. (2) is proposed to represent the tensile characterization of the FRCs with different PVA fiber content as follows:

$$\sigma_t = \begin{cases} E_{ct}\varepsilon_t & \text{prior mircocracking} \\ f_{t1} + E_{t1}(\varepsilon_t - \varepsilon_{t1}) & \text{crack straining stage} \\ f_t - \beta W_{cr} & \text{crack opening stage} \\ 0.035f_t & \text{residual tensile stress} \end{cases} \quad (2)$$

where E_{ct} = modulus of the FRC prior to cracking; f_{t1} and ε_{t1} = tensile stress and strain, respectively, corresponding to the initiation of the crack; E_{t1} = modulus for the crack straining stage; f_t = peak tensile stress of the FRC; W_{cr} = crack width of the FRC in mm; and β = slope of the descending branch of the stress crack width curve of the FRC. Figs. 5(a and b) show that the proposed model provided a close match to the experimental results.
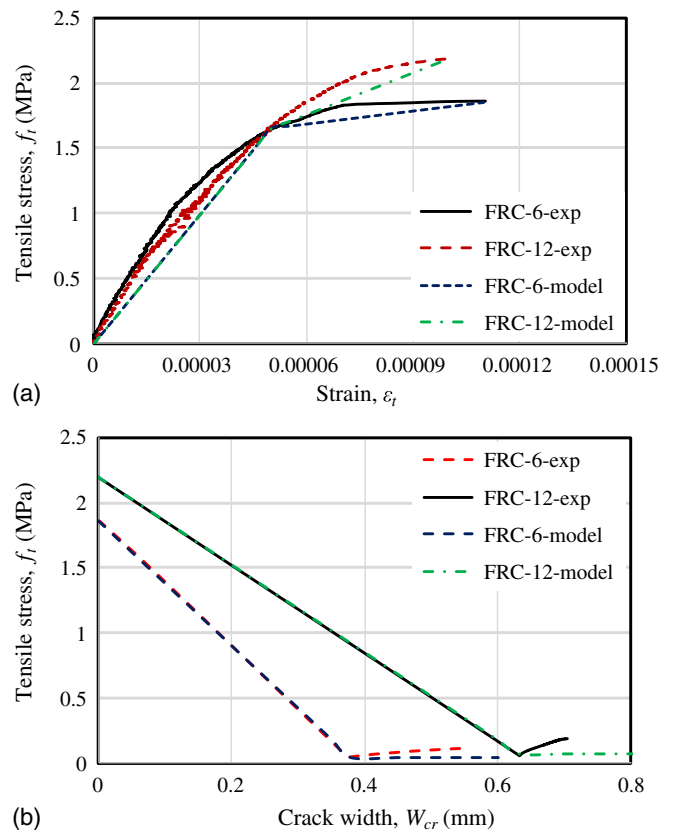
Fig. 5. Tensile response of FRCs.

Pullout Test Results

Global Load-Slip (P/Δ) Relationship

Key values used for defining the global load-slip (P/Δ) relationship are presented in Table 2. In all but two cases, the specimens failed by pullout of the reinforcing bar. A typical bar following pullout is shown in Fig. 6. Pullout failure occurred once the shear strength of the bond between the rebar and concrete was exceeded. At this point, the bar began to pull out at a gradually decreasing load, and all that remained was the residual strength due to friction between the bar and adjacent concrete, which simulated the process of the intermediate crack (IC) debonding of the FRP bar. The typical local load-slip relationship of each concrete series is illustrated in Fig. 7. Regardless of the fiber content used in the tests, a similar ascending branch was observed; however, when compared with the plain concrete mix, the FRC mix showed a slight increase in the peak load and a steeper ascending branch as a stronger bond was present for smaller slips. These observations are in agreement with those studies reported previously on bond-slip response of FRP bars in FRCs (Mazaheripour et al. 2013) and could be explained by two factors: the fibers providing more friction as the bars pull out, or more likely, the passive confinement exerted by increasing fiber content as the concrete starts failing in tension locally. The fracture failure of the FRP in each test series, which is different than IC debonding cases, indicates that 300 mm is nearly sufficient to fully anchor the FRP bar in either plain concrete of 40-MPa strength or PVA-FRC with 6-kg/m³ fiber content.

Local Bond Stress-Slip (τ/δ) Relationship

In order to model the tension-stiffening behavior of the fiber-reinforced concrete beams reinforced with GFRP bars used in this research, the local bond-slip (τ/δ) relationship needs to be extracted

© ASCE 04018043-4 J. Compos. Constr.

303
J. Compos. Constr., 2018, 22(5): 04018043

Table 2. Pull test results

Specimen	Embedment length (mm)	Bar diameter (mm)	Fiber content (kg/m³)	P_{max} (kN)	Average (kN)	τ_{av} (MPa)	Average (MPa)	Failure mode
FRC-0-L-1	300	12	0	136	—	12.0	—	Pullout
FRC-0-L-2	300	12	0	164[a]	141	14.5	12.5	FRP bar rupture
FRC-0-L-3	300	12	0	146	—	12.9	—	Pullout
FRC-6-L-1	300	12	6	154	—	13.6	—	Pullout
FRC-6-L-2	300	12	6	145	150	12.9	13.3	Pullout
FRC-6-L-3	300	12	6	164[a]	—	14.5	—	FRP bar rupture
FRC-0-S-1	60	12	0	26.6	—	11.7	—	Pullout
FRC-0-S-2	60	12	0	27.9	28.3	12.4	12.5	Pullout
FRC-0-S-3	60	12	0	30.4	—	13.4	—	Pullout
FRC-6-S-1	60	12	6	30.3	—	13.4	—	Pullout
FRC-6-S-2	60	12	6	31.4	29.8	13.9	13.2	Pullout
FRC-6-S-3	60	12	6	27.5	—	12.2	—	Pullout
FRC-12-S-1	60	12	12	33.7	—	14.9	—	Pullout
FRC-12-S-2	60	12	12	34.3	34.7	15.2	15.3	Pullout
FRC-12-S-3	60	12	12	36.0	—	15.9	—	Pullout

[a]Excluded for calculating the average value.

Fig. 6. FRP bar pullout failure.

Fig. 7. Global load-slip relationship response for each fiber content.

from the experimental global load-slip (P/Δ) relationship obtained from the pullout tests. Based on typical pullout test results obtained for specimens with 60-mm bond length as shown in Fig. 8, it was decided that a trilinear local τ/δ relationship a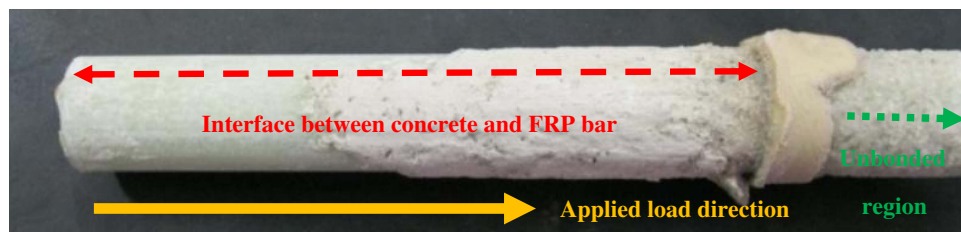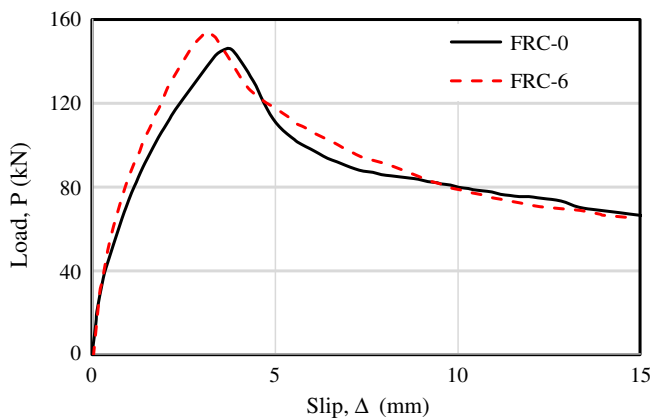s shown in the same figure would be suitable to simulate the results obtained. Based on the experimental data, the general expressions in Eqs. (3)–(5) are developed to represent the local bond stress-slip relationship of the FRCs as follows:

$$\tau_{max} = \gamma_1 \sqrt{f_c'} \tag{3}$$

$$\tau = \tau_{max}(\delta/\delta_1)^{\gamma_2} \tag{4}$$

$$\tau_{resd} = \gamma_3 \tau_{max} \tag{5}$$

where τ_{max} = maximum bond stress in MPa; δ_1 (in mm) = slip corresponding to the maximum bond stress; and γ_1, γ_2, γ_3 = empirical coefficients dependent on different fiber contents in FRC, in which $\gamma_1 = 2.0$, $\gamma_2 = 0.30$, and $\gamma_3 = 0.45$ for the FRC-6 series, and $\gamma_1 = 2.4$, $\gamma_2 = 0.15$, and $\gamma_3 = 0.33$ for the FRC-12 series. Figs. 8(a and b) present the comparison between the experimental and modeled local bond stress-slip relationships of each concrete series.

Structural Behaviors

General Observations of the Beam Tests

The failure modes of all beam specimens are presented in Figs. 9(a–d). The observed failure modes of all the beams are typical flexural failure modes, except the first of the two FRC beams with 6-kg/m³ fibers (FRC-6-1), which experienced a premature failure due to web shear cracking [shown in Fig. 9(a)]. The test result of the FRC-6-1 beam is reported but is not used in any further comparisons or model validations. To ensure the subsequent beams failed in typical flexural failure modes, the locations of loading points and supports of the rest of the beams were adjusted to increase the length of the constant bending moment region. In the beams that experienced flexural failure, it was observed that the flexural cracks initially formed within the constant moment area and propagated upward to the neutral axis position. This in turn led to a series of flexural cracks in the constant bending moment region. Compression wedges then gradually formed, accompanied with the buckling of compression bars. Consequently, the specimen failed with the concrete crushing. As can be seen from Figs. 9(b)–(d), the change of fiber content in the beams lead to no distinct change in the
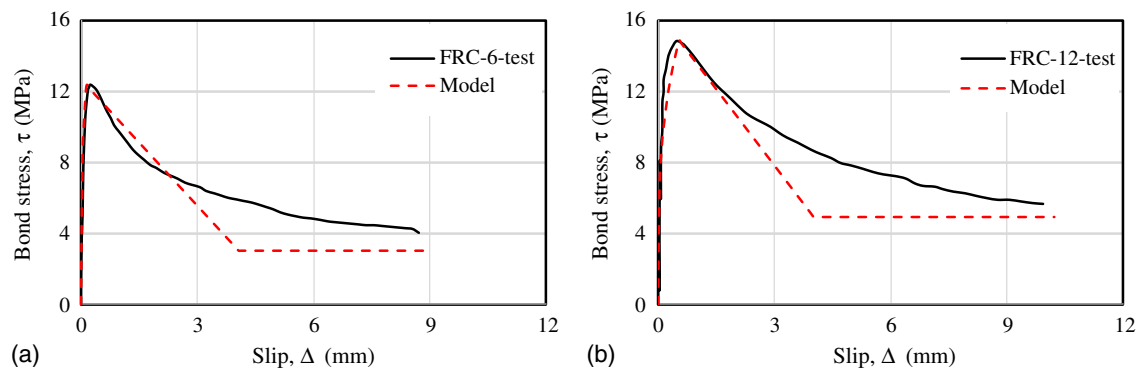
Fig. 8. Local bond stress-slip relationship of FRCs.
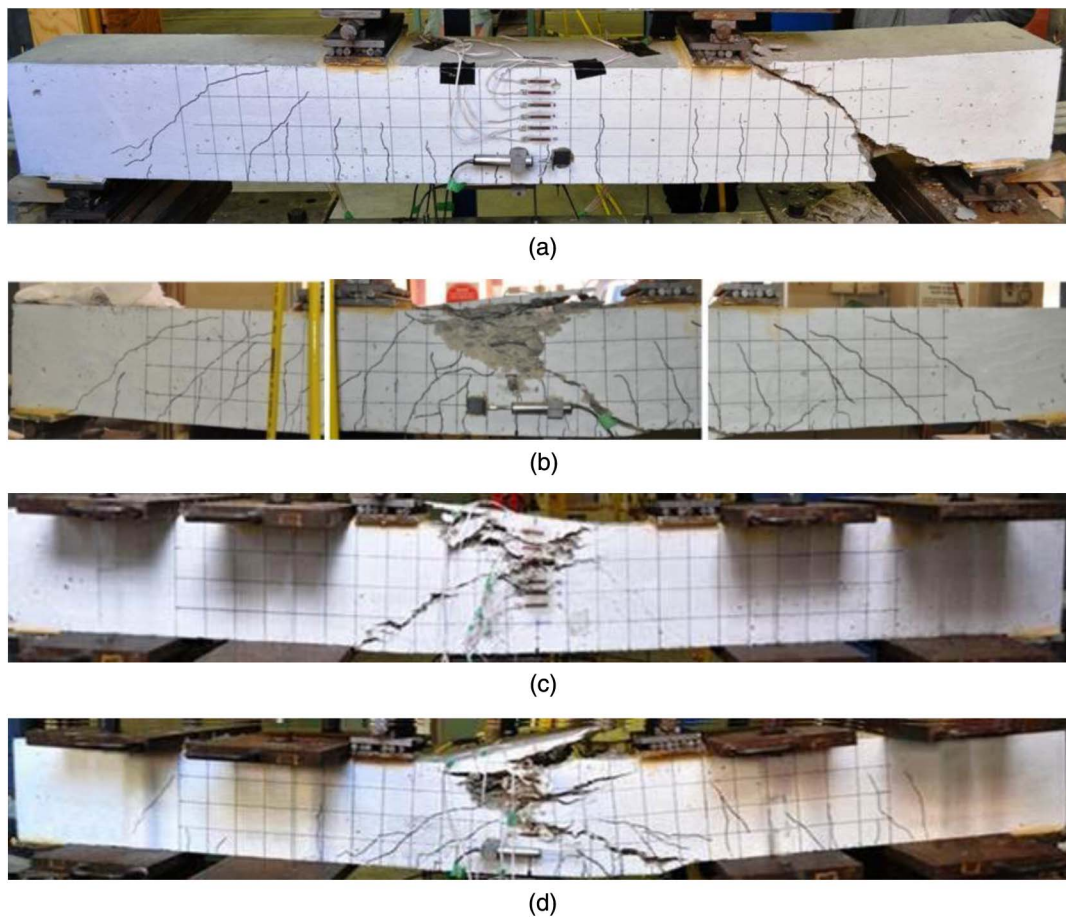
Fig. 9. Failure modes of beam specimens: (a) FRC-6-1; (b) FRC-6-2; (c) FRC-12-1; and (d) FRC-12-2.

failure mode of the specimen under flexure. The failure mode of all the beam tests and the critical data, including the peak load and the corresponding midspan deflection, are summarized in Table 3.

Load-Deflection Relationship: Experimental Results

The experimentally recorded load-deflection relationship of each beam series is illustrated in Fig. 10, in which it can be seen that the load-deflection relationship of all the beams followed a similar trend. Beam FRC-6-1 was loaded with a longer constant moment region and hence has a higher stiffness in Fig. 10. For each set of the identical beams, their load-deflection curves initially exhibit

similar stiffness and load prior to the first flexural cracks formed. Following this, a nearly linear ascending load-deflection relationship is observed up to the peak point of the load-deflection curves of all the beams. At the peak load point, all the beams exhibited sudden drops in their load-carrying capacities in their load-deflection curves, which is referred to as the concrete wedge failure. Once the steel reinforcement at the top yielded, the steel compressive force did not compensate for the reduction in the strength of the softening concrete, and the beam consequently failed due to concrete crushing. Fig. 10 shows the comparison of the load-deflection curve between the FRC-6 and FRC-12 series of specimens. As the comparisons illustrate in this figure, the FRC-12 series

© ASCE 04018043-6 J. Compos. Constr.

305
J. Compos. Constr., 2018, 22(5): 04018043

Table 3. Summary of beam test results

	Peak load (kN)		Deflection at peak load (mm)		Failure mode
Specimen	Experimental	Modeling	Experimental	Modeling	
FRC-6-1	159	162	21.1	29.5	Shear[a]
FRC-6-2	164		24.4		FRP bar rupture
FRC-12-1	168	170	26.0	31.1	FRP bar rupture
FRC-12-2	180		26.9		FRP bar rupture

[a]Premature failure; will be excluded for further analysis and model validation.
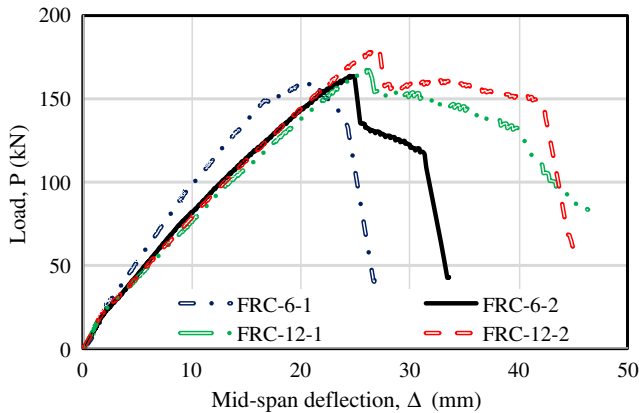
Fig. 10. Load-deflection relationship of test beams: experimental results.

of beams exhibited a slightly improved flexural behavior, including increases in peak load and ultimate deflection, compared to that of its companion FRC-6 series of beams. This observation suggests that the load-deflection properties of PVA-FRC beams are improved by using an increased fiber content in the concrete owing to the additional internal confining effect by the fibers.

Simulations of Flexural Behavior of PVA Fiber–Reinforced Concrete Beams with GFRP Bars

Segmental Approach

This section presents the application of a displacement-based analysis technique previously developed by the authors. The approach, which has been widely validated for the flexural and shear analysis of both conventional and prestressed concrete with either steel or FRP reinforcement (Knight et al. 2014a, b, 2015; Oehlers et al. 2016) and which has recently been extended to allow for the analysis of steel fiber–reinforced concrete (Visintin and Oehlers 2017), is based on the direct simulation of localized partial interaction behavior. The basic mechanics of the approach will now be summarized, and the reader referred to an extensive list of publications in which the development of the approach is covered in greater depth. The approach is a direct application of the Euler-Bernoulli theorem of plane section remaining plane without the corollary of a linear strain profile. Hence, a similar solution technique to that which is followed when undertaking a moment-curvature analysis is applied, with the major difference being

Fig. 11. Segment of fiber-reinforced concrete beam.

the starting point is the imposition of a deformation rather than strain profile. This change is significant because it allows for the direct application of partial interaction theory to simulate localized behaviors such as crack formation, widening and tension stiffening in t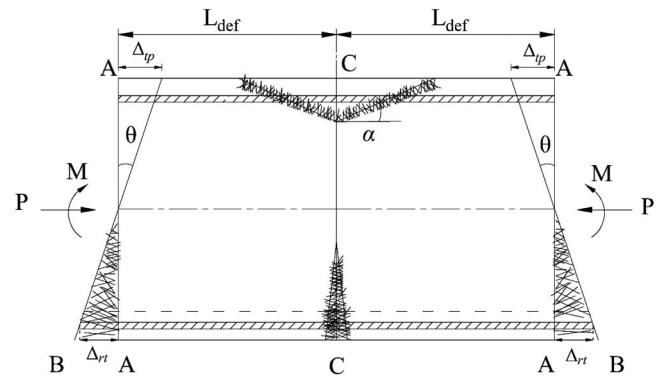he tension region, and concrete softening in the compression region. Consider the extracted segment of a fiber-reinforced concrete beam in Fig. 11. The segment is of length equal to a crack spacing S_{cr} and is subjected to a Euler-Bernoulli deformation causing an end rotation θ.

For analysis, it is considered that a constant moment is applied to the segment, and hence, due to symmetry about the center point, only a single side of the segment A-A and C-C in Fig. 11 needs to be considered. The application of a rotation θ causes a deformation of the segment end δ in Fig. 12(a). The deformation can be divided into two categories: (1) the full interaction deformations that occur in regions in which the concrete is not softening in compression or cracked in tension, and (2) partial interaction deformations that result in localized relative displacements or slips. These local behaviors include concrete-to-concrete sliding, which results in concrete softening, or the slip between the reinforcement and the surrounding concrete, which results in tension stiffening and crack widening. In the case of fiber-reinforced concrete, the behavior of cracked concrete in tension is considered to be adequately modeled using the results of a direct-tension test to obtain a stress crack-width relationship as in Fig. 5(b). An alternative to this approach is to use micromechanics to simulate the load-slip behavior of each fiber, such as in Naaman et al. (1991a, b), and Sumitro and Tsubaki (1998).

In the full interaction regions, dividing the deformation from A-A to B-B by the deformation length L_{def}, which is equal to half the crack spacing, gives the strain profile C-C in Fig. 12(b). Based on the distribution of strain and knowledge of the stress-strain relationships, the distribution of stress in Fig. 12(c) and force in Fig. 12(d) can be determined. For cracked concrete in which the fibers have not pulled out, the material stress crack-width relationship in Fig. 5(b) may be directly applied to determine the force in the cracked concrete.

Partial Interaction Tension Stiffening Region

Slip between the reinforcement and the surrounding concrete results in the formation and widening of cracks as well as the phenomena of tension stiffening (Muhamad et al. 2016; Zhang et al. 2016). In order to describe the relationship between the slip of the reinforcement from the crack face and the force developed in the reinforcement, partial interaction (PI) tension stiffening mechanics are considered. That is, for a given slip form, the crack face Δ, which is equal to half the total crack width, the transfer of stresses

© ASCE

04018043-7

J. Compos. Constr.
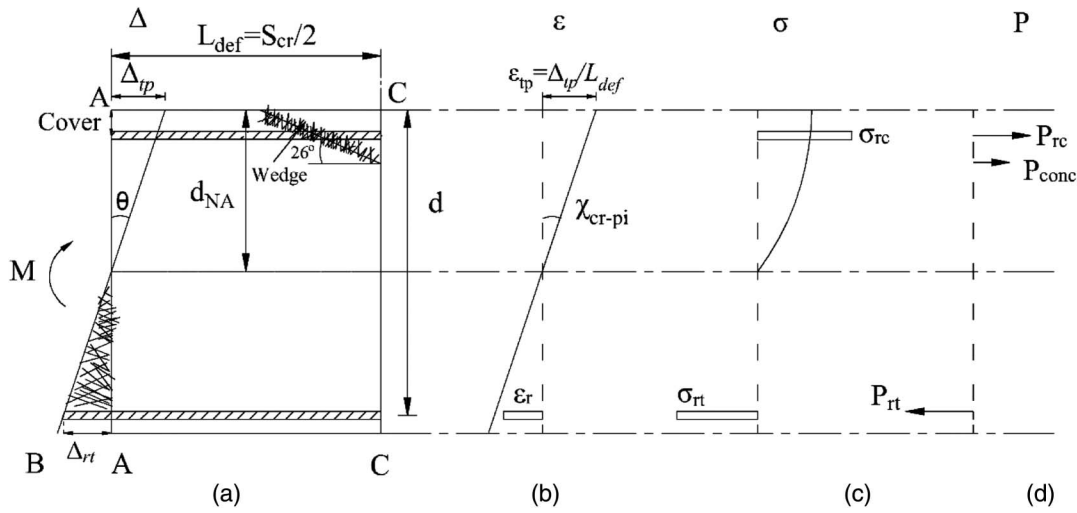
Fig. 12. Segment for analysis.
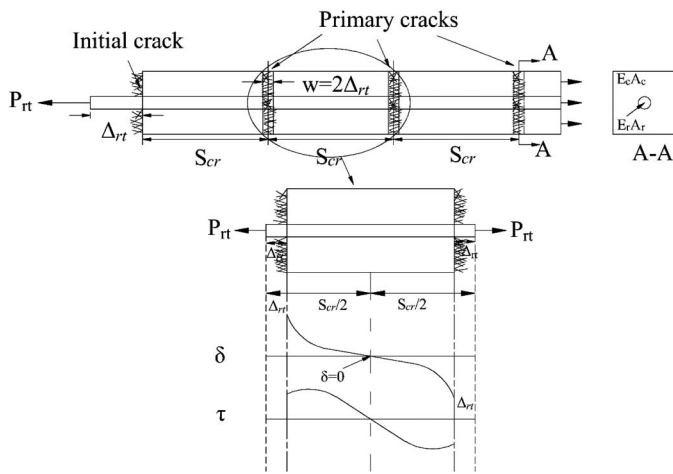
Fig. 13. Partial interaction tension-stiffening prism.

Fig. 14. Compression test.

from the reinforcement to the concrete through bond is determined to directly give the force in the reinforcing P_{rt} in Fig. 12(d).

After the formation of an initial crack, the force resisted in the prism in Fig. 13 is resisted by a combination of the fibers at the crack face P_{fib} and the reinforcing bar force P_{rt}. The reinforcing bar force P_{rt} induces a slip of the reinforcement in Fig. 11, which has a maximum at the crack face and results in a transfer of stress from the reinforcement to the concrete, which is controlled by the local bond stress-slip relationship in Fig. 8. For analysis, a shooting method can be applied to determine the variation in reinforcement slip and the distribution of strain in the reinforcement and the concrete (Haskett et al. 2008; Zhang et al. 2016). By considering the full interaction boundary conditions to this partial interaction problem, it is possible to determine not only the crack spacing but also the load slip tension stiffening behavior of the reinforcement, both of which are required for the preceding analysis (Haskett et al. 2008; Zhang et al. 2016). A full description of the partial interaction tension stiffening model is widely available (e.g., Muhamad et al. 2011, 2016; Oehlers et al. 2014a, b; Sturm et al. 2018).

PI Concrete Softening

Similarly, in the PI compression region, concrete softening of the concrete is associated with partial interaction sliding along the
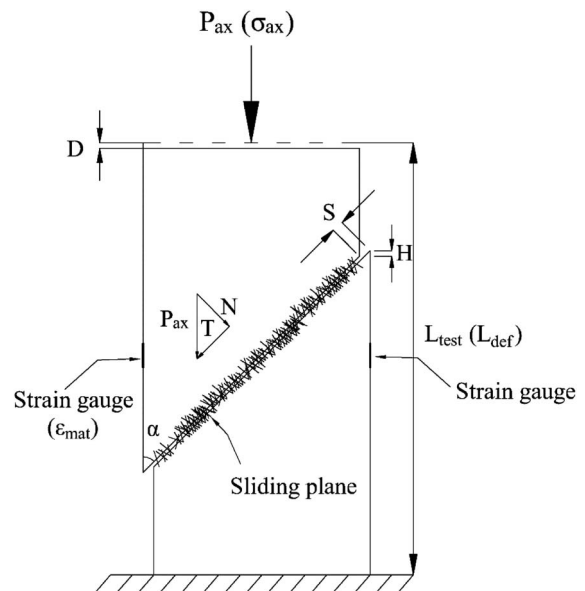
concrete-to-concrete interface of the softening wedge (Chen et al. 2014; Haskett et al. 2011). As reported in Chen et al. (2014), a size-dependent stress-strain relationship can be developed from the results of standard cylinder tests by breaking the total deformation of a cylinder into its material component that is dependent on the length of the test specimen and a PI sliding component, which is controlled by the mechanics of shear friction theory that occurs along the sliding wedge. This approach, which has been successfully applied to conventional concrete in Chen et al. (2014) and has been further extended to steel fiber FRCs by Visintin and Oehlers (2017), is therefore applied here. That is, for analysis, the stress-strain relationship obtained from a standard cylinder test in Fig. 14 is made size dependent. The height of the cylinder would be $2L_{def}$ in Fig. 12(a), in which the stress-strain relationship of the cylinder with the length of $2L_{def}$ can be obtained by applying the expression given in Eq. (6) as follows to convert the stress-strain behavior extracted empirically from a standard compressive test specimen with the length of 200 mm:

© ASCE 04018043-8 J. Compos. Constr.

307
J. Compos. Constr., 2018, 22(5): 04018043

$$\varepsilon_{Ldef} = \varepsilon_{mat} + (\varepsilon_{test} - \varepsilon_{mat})\frac{200}{L_{def}} \qquad (6)$$

where ε_{mat} = material strain; ε_{test} = total strain from the standard compression test; and L_{def} = deformation length in M/θ analysis in mm. Having now determined all forces in Fig. 12(d), it is simply a matter of shifting the neutral axis in Fig. 12(a) until equilibrium of forces is obtained, after which the moment corresponding to the rotation θ can be determined.

Member Modeling

Having obtained the moment-rotation for each of the concrete sections in Fig. 15, the load-deflection and load-crack width behavior of the beam can be determined using a standard analytical procedure. That is, by dividing the rotation in Fig. 15(a) by the deformation length L_{def}, the moment-curvature behavior of a cross section shown in Fig. 15(b) is obtained. This is not the same as that which would be obtained from a standard moment-curvature analysis because the partial interaction behaviors associated with concrete cracking and softening have been directly simulated using partial interaction approaches. Having obtained the moment-curvature relationship of the cross section, it is simply a matter of integrating the distribution of curvature along the beam twice in order to determine deflection as in standard analysis. In addition, the change in the curvature following the commencement of concrete softening is associated with the formation of the hinge in which the hinge length is defined in terms of the length of the softening wedge. In the modeling process, the rotation due to the multiple discrete cracks with the variations in the moment within the hinge region was incorporated when calculating the load and deflection of the beam.
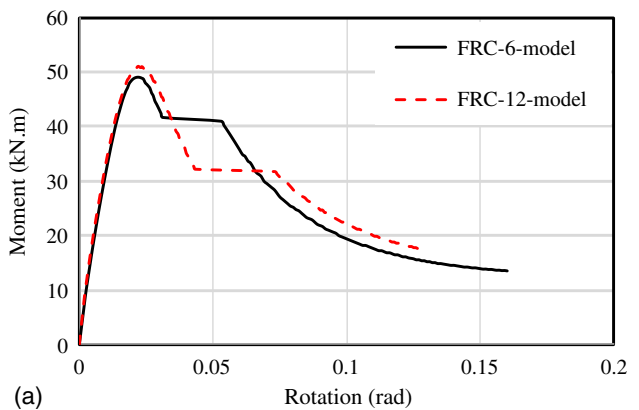
Similarly, to determine the load-crack width behavior, the moment-crack width relationship in Fig. 16 is a direct consequence of the segmental analysis technique: for any given moment distribution applied to the beam, the distribution of crack width is known, where the crack width (W_{cr}) is the sum of the slip of the reinforcement relative to each crack face, that is, $2\Delta_{rt}$.

Cracking Behavior

In the present study, the crack widths (W_{cr}) at all load levels of each beam were measured using LVDTs mounted at the GFRP position of the FRC beams along the longitudinal direction. Fig. 15 provides the experimentally recorded and simulated load-crack width relationships of FRC-6 and FRC-12 beam series, respectively. The numerically generated crack width was established using the relative slip between the tensile reinforcem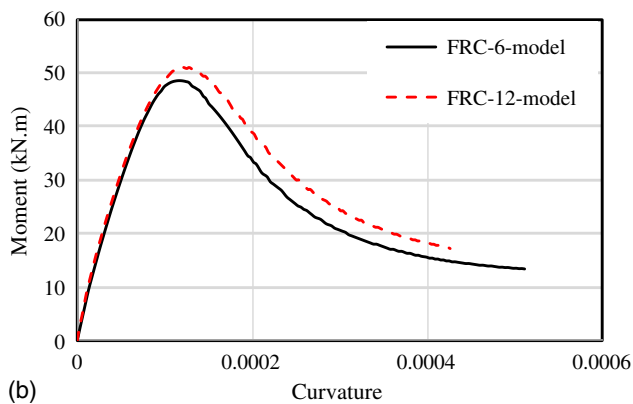ent (i.e., the GFRP bar) and surrounding FRC, in which the magnitude of the crack width for a given load is twice the relative slip between the FRC and GFRP bar. As illustrated in Fig. 15, the experimental and theoretical load-crack width relationships are matched closely. Fig. 15 provides the comparison between the load-crack width relationships of the FRC-6 and the companion FRC-12 series. It is evident from the figure that, in general, for a given load, the beam prepared using FRC with higher fiber content had a smaller crack width. This observation is similar to the aforementioned observation on the crack spacing of FRC beams and can be explained by the delayed formation of cracks as the result of the increased fiber content.

Simulated Load-Deflection Behaviors

The comparisons in Figs. 17(a and b) indicate that the simulated load-deflection relationships of the FRCs are in good agreement with the experimental results. Although the model well simulates the flexural behavior of the PVA-FRC beam with GFRP bars, it slightly overestimates the midspan deflection, as shown in Figs. 17(a and b). This might be attributed to the fact that fiber distributions in material test specimens are different than those in the beam specimens, which may be due to the difference in casting direction of the cylinders and beams or due to more significant edge effects in cylinders, which may result in a change in fiber orientation. Another potential explanation of the variations between the numerical and experimental results is the early failure of the individual GFRP fibers due to the anisotropy and inhomogeneity of the bar (Rizkalla et al. 2003). This leads to a type of premature

Fig. 15. Simulated moment-rotation and moment-curvature relationship of each beam cross section: (a) moment-rotation relationship; and (b) moment-curvature relationship.

Fig. 16. Load-crack width relationship for each beam series.

© ASCE   04018043-9   J. Compos. Constr.

308
J. Compos. Constr., 2018, 22(5): 04018043
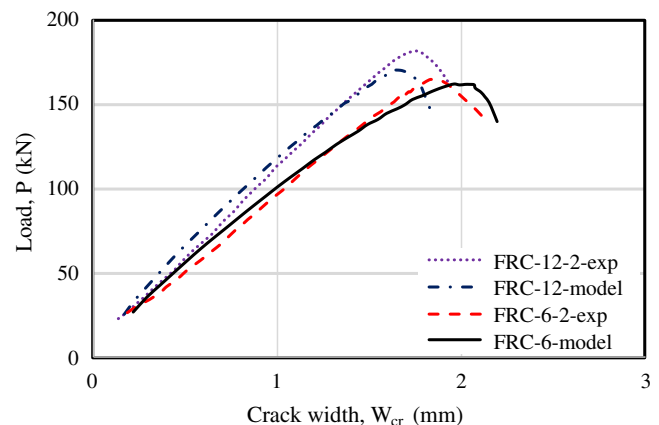
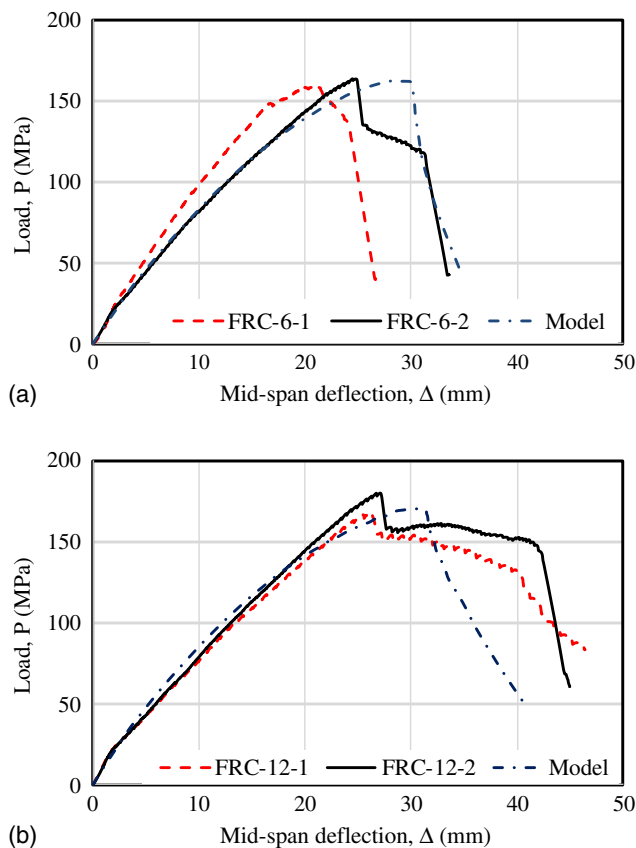**Fig. 17.** Load-deflection relationship of test beams: comparison between simulated and experimental results: (a) FRC-6 series; and (b) FRC-12 series.

failure of the FRP bars and hence results in a less ductile behavior of the beams seen in the experiments.

Conclusions

Based on the experimental investigations and the numerical analysis to simulate the flexural behavior of PVA-FRC beams with GFRP bars, the following conclusions can be drawn:

PVA fiber content is an influential parameter to affect the material properties of the FRC. The peak and postpeak behaviors of the FRC under axial compression and tension are improved with increased PVA fiber content. The results from a series of pullout tests performed to establish the bond properties between GFRP bars and fiber concrete showed that the ascending slope of the bond stress-slip relationship was steeper for specimens containing fibers when compared to specimens with no fibers, indicating that FRP bars embedded in fiber concrete will experience smaller slips for a given load.

Based on the beam test results, FRC content had nearly no effect on the stiffness of the GFRP PVA-FRC beam at the service region, whereas the beam with a higher FRC content exhibited a slightly more improved flexural behavior, including the increases in the peak load and ultimate deflection. The crack response of GFRP PVA-FRC beams has a strong correlation with the fiber content in FRC, in which an increase in FRC content results in a smaller crack width for a given load. The displacement-based moment-rotation numerical model is able to predict the behavior well, and this approach for beam analysis is applicable to simulate the flexural behavior of any

type of FRC beams or beams with any type of FRP bars as tension reinforcements.

Acknowledgments

The authors would like to extend their gratitude to Messrs. Guest, Pritchard, Sedev, and Stapleton, who performed the experimental program presented in this paper. The authors also thank Dr. Matthew Haskett for his valuable suggestions for this project.

References

Achillides, Z., and K. Pilakoutas. 2004. "Bond behavior of fiber reinforced polymer bars under direct pullout conditions." *J. Compos. Constr.* 8 (2): 173–181. https://doi.org/10.1061/(ASCE)1090-0268(2004)8:2(173).

Almusallam, A. A. 2001. "Effect of degree of corrosion on the properties of reinforcing steel bars." *Constr. Build. Mater.* 15 (8): 361–368. https://doi.org/10.1016/S0950-0618(01)00009-5.

Alsayed, S. H. 1998. "Flexural behaviour of concrete beams reinforced with GFRP bars." *Cem. Concr. Compos.* 20 (1): 1–11. https://doi.org/10.1016/S0958-9465(97)00061-9.

Altun, F., T. Haktanir, and K. Ari. 2007. "Effects of steel fiber addition on mechanical properties of concrete and RC beams." *Constr. Build. Mater.* 21 (3): 654–661. https://doi.org/10.1016/j.conbuildmat.2005.12.006.

Ashtiani, M. S., R. Dhakal, A. Scott, and D. Bull. 2013. "Cyclic beam bending test for assessment of bond-slip behaviour." *Eng. Struct.* 56: 1684–1697. https://doi.org/10.1016/j.engstruct.2013.08.005.

AS (Standard Australia). 2014. *Methods of testing concrete compressive strength tests-Concrete, mortar and grout specimens*. AS 1012.9:2014. Sydney, Australia: AS.

Barris, C., L. Torres, A. Turon, M. Baena, and A. Catalan. 2009. "An experimental study of the flexural behaviour of GFRP RC beams and comparison with prediction models." *Compos. Struct.* 91 (3): 286–295. https://doi.org/10.1016/j.compstruct.2009.05.005.

Bhargava, P., U. K. Sharma, and S. K. Kaushik. 2006. "Compressive stress-strain behavior of small scale steel fibre reinforced high strength concrete cylinders." *J. Adv. Concr. Technol.* 4 (1): 109–121. https://doi.org/10.3151/jact.4.109.

Chen, Y., P. Visintin, D. Oehlers, and U. Alengaram. 2014. "Size-dependent stress-strain model for unconfined concrete." *J. Struct. Eng.* 140 (4): 04013088. https://doi.org/10.1061/(ASCE)ST.1943-541X.0000869.

Ezeldin, A. S., and P. N. Balaguru. 1992. "Normal-and high-strength fiber-reinforced concrete under compression." *J. Mater. Civ. Eng.* 4 (4): 415–429. https://doi.org/10.1061/(ASCE)0899-1561(1992)4:4(415).

Feng, Q., P. Visintin, and D. J. Oehlers. 2016. "Deterioration of bond-slip due to corrosion of steel reinforcement in reinforced concrete." *Mag. Concr. Res.* 68 (15): 768–781. https://doi.org/10.1680/jmacr.15.00217.

Goldston, M., A. Remennikov, and M. N. Sheikh. 2017. "Flexural behaviour of GFRP reinforced high strength and ultra high strength concrete beams." *Constr. Build. Mater.* 131: 606–617. https://doi.org/10.1016/j.conbuildmat.2016.11.094.

Haskett, M., D. J. Oehlers, and M. M. Ali. 2008. "Local and global bond characteristics of steel reinforcing bars." *Eng. Struct.* 30 (2): 376–383. https://doi.org/10.1016/j.engstruct.2007.04.007.

Haskett, M., D. J. Oehlers, M. M. Ali, and S. K. Sharma. 2011. "Evaluating the shear-friction resistance across sliding planes in concrete." *Eng. Struct.* 33 (4): 1357–1364. https://doi.org/10.1016/j.engstruct.2011.01.013.

Hognestad, E., N. W. Hanson, and D. McHenry. 1955. "Concrete stress distribution in ultimate strength design." *J. Proc.* 52 (12): 455–480.

Jakubovskis, R., G. Kaklauskas, V. Gribniak, A. Weber, and M. Juknys. 2014. "Serviceability analysis of concrete beams with different arrangements of GFRP bars in the tensile zone." *J. Compos. Constr.* 18 (5): 04014005. https://doi.org/10.1061/(ASCE)CC.1943-5614.0000465.

Kachlakev, D., and D. McCurry. 2000. "Behavior of full-scale reinforced concrete beams retrofitted for shear and flexural with FRP laminates."

Downloaded from ascelibrary.org by The University of Adelaide on 04/16/19. Copyright ASCE. For personal use only; all rights reserved.

© ASCE 04018043-10 J. Compos. Constr.

309
J. Compos. Constr., 2018, 22(5): 04018043

Composites Part B 31 (6): 445–452. https://doi.org/10.1016/S1359 -8368(00)00023-8.

Knight, D., P. Visintin, and D. J. Oehlers. 2015. "Displacement-based simulation of time-dependent behaviour of RC beams with prestressed FRP or steel tendons." *Struct. Concr.* 16 (3): 406–417. https://doi.org /10.1002/suco.201400039.

Knight, D., P. Visintin, D. J. Oehlers, and M. M. Ali. 2014a. "Simulation of RC beams with mechanically fastened FRP strips." *Compos. Struct.* 114: 99–106. https://doi.org/10.1016/j.compstruct.2014.04.012.

Knight, D., P. Visintin, D. J. Oehlers, and M. M. Ali. 2014b. "Simulating RC beams with unbonded FRP and steel prestressing tendons." *Composites Part B* 60: 392–399. https://doi.org/10.1016/j.compositesb.2013 .12.039.

Knight, D., P. Visintin, D. J. Oehlers, and M. Mohamed Ali. 2014c. "Short-term partial-interaction behavior of RC beams with prestressed FRP and steel." *J. Compos. Constr.* 18 (1): 04013029. https://doi.org/10.1061 /(ASCE)CC.1943-5614.0000408.

Matthys, T. S. S. 2017. "Shear-stress transfer across a crack in steel fibre-reinforced concrete." *Cem. Concr. Compos.* 82: 1–13. https://doi.org/10 .1016/j.cemconcomp.2017.05.010.

Mazaheripour, H., J. A. Barros, J. Sena-Cruz, and F. Soltanzadeh. 2013. "Analytical bond model for GFRP bars to steel fiber reinforced self-compacting concrete." *J. Compos. Constr.* 17 (6): 04013009. https://doi .org/10.1061/(ASCE)CC.1943-5614.0000399.

Mazaheripour, H., J. A. Barros, F. Soltanzadeh, and J. Sena-Cruz. 2016. "Deflection and cracking behavior of SFRSCC beams reinforced with hybrid prestressed GFRP and steel reinforcements." *Eng. Struct.* 125: 546–565. https://doi.org/10.1016/j.engstruct.2016.07.026.

Mo, K. H., P. Visintin, U. J. Alengaram, and M. Z. Jumaat. 2016. "Bond stress-slip relationship of oil palm shell lightweight concrete." *Eng. Struct.* 127: 319–330. https://doi.org/10.1016/j.engstruct.2016.08.064.

Muhamad, R., M. M. Ali, D. Oehlers, and A. H. Sheikh. 2011. "Load-slip relationship of tension reinforcement in reinforced concrete members." *Eng. Struct.* 33 (4): 1098–1106. https://doi.org/10.1016/j.engstruct.2010 .12.022.

Muhamad, R., M. M. Ali, D. J. Oehlers, and M. Griffith. 2016. "The tension stiffening mechanism in reinforced concrete prisms." *Adv. Struct. Eng.* 15 (12): 2053–2069. https://doi.org/10.1260/1369-4332.15.12.2053.

Naaman, A. E., G. G. Namur, J. M. Alwan, and H. S. Najm. 1991a. "Fiber pullout and bond slip. I: Analytical study." *J. Struct. Eng.* 117 (9): 2769–2790. https://doi.org/10.1061/(ASCE)0733-9445(1991)117:9(2769).

Naaman, A. E., G. G. Namur, J. M. Alwan, and H. S. Najm. 1991b. "Fiber pullout and bond slip. II: Experimental validation." *J. Struct. Eng.* 117 (9): 2791–2800. https://doi.org/10.1061/(ASCE)0733-9445(1991) 117:9(2791).

Oehlers, D. J., P. Visintin, J. F. Chen, and T. J. Ibell. 2014a. "Simulating reinforced concrete members. Part I: partial interaction properties." *Proc. Inst. Civ. Eng. Struct. Build.* 167 (11): 646–653. https://doi.org /10.1680/stbu.13.00071.

Oehlers, D. J., P. Visintin, J. F. Chen, and T. J. Ibell. 2014b. "Simulating reinforced concrete members. Part II: Displacement-based analyses." *Proc. Inst. Civ. Eng. Struct. Build.* 167 (12): 718–727. https://doi .org/10.1680/stbu.13.00072.

Oehlers, D. J., P. Visintin, and W. Lucas. 2016. "Fundamental mechanics governing FRP-retrofitted RC beams with anchored and prestressed FRP plates." *J. Compos. Constr.* 20 (6): 04016047. https://doi.org/10 .1061/(ASCE)CC.1943-5614.0000710.

Olivito, R., and F. Zuccarello. 2010. "An experimental study on the tensile strength of steel fiber reinforced concrete." *Composites Part B* 41 (3): 246–255. https://doi.org/10.1016/j.compositesb.2009.12.003.

Qu, W., X. Zhang, and H. Huang. 2009. "Flexural behavior of concrete beams reinforced with hybrid (GFRP and steel) bars." *J. Compos. Constr.* 13 (5): 350–359. https://doi.org/10.1061/(ASCE)CC.1943-5614 .0000035.

Rilem, T. 2002. "162-TDF. Test and design methods for steel fibre reinforced concrete." *Mater. Struct.* 35: 579–582.

Rizkalla, S., T. Hassan, and N. Hassan. 2003. "Design recommendations for the use of FRP for reinforcement and strengthening of concrete structures." *Prog. Struct. Eng. Mater.* 5 (1): 16–28. https://doi.org/10 .1002/pse.139.

Schumacher, P. 2006. *Rotation capacity of self-compacting steel fiber reinforced concrete.* Delft, Netherlands: Delft Univ. of Technology.

Sturm, A. B., P. Visintin, D. J. Oehlers, and R. Seracino. 2018. "Time-dependent tension-stiffening mechanics of fiber-reinforced and ultra-high-performance fiber-reinforced concrete." *J. Struct. Eng.* 144 (8): 04018122. https://doi.org/10.1061/(ASCE)ST.1943-541X.0002107.

Sumitro, S., and T. Tsubaki. 1998. "Micromechanical fiber pullout model for steel fiber reinforced concrete." *Doboku Gakkai Ronbunshu* 1998 (599): 155–163. https://doi.org/10.2208/jscej.1998.599_155.

Toutanji, H., and Y. Deng. 2003. "Deflection and crack-width prediction of concrete beams reinforced with glass FRP rods." *Constr. Build. Mater.* 17 (1): 69–74. https://doi.org/10.1016/S0950-0618(02)00094-6.

Visintin, P., M. M. Ali, T. Xie, and A. B. Sturm. 2018. "Experimental investigation of moment redistribution in ultra-high performance fibre reinforced concrete beams." *Constr. Build. Mater.* 166: 433–444. https://doi.org/10.1016/j.conbuildmat.2018.01.156.

Visintin, P., D. Oehlers, R. Muhamad, and C. Wu. 2013. "Partial-interaction short term serviceability deflection of RC beams." *Eng. Struct.* 56: 993–1006. https://doi.org/10.1016/j.engstruct.2013.06.021.

Visintin, P., D. Oehlers, C. Wu, and M. Haskett. 2012. "A mechanics solution for hinges in RC beams with multiple cracks." *Eng. Struct.* 36: 61–69. https://doi.org/10.1016/j.engstruct.2011.11.028.

Visintin, P., and D. J. Oehlers. 2017. "Fundamental mechanics that govern the flexural behaviour of reinforced concrete beams with fibre-reinforced concrete." *Adv. Struct. Eng.* 21 (7): 1088–1102. https://doi .org/10.1177/1369433217739705.

Visintin, P., D. J. Oehlers, and A. B. Sturm. 2016. "Mechanics solutions for deflection and cracking in concrete." *Proc. Inst. Civ. Eng. Struct. Build.* 169 (12): 1–13.

Wang, S., M.-H. Zhang, and S. T. Quek. 2012. "Mechanical behavior of fiber-reinforced high-strength concrete subjected to high strain-rate compressive loading." *Constr. Build. Mater.* 31: 1–11. https://doi.org /10.1016/j.conbuildmat.2011.12.083.

Xu, G., S. Magnani, and D. J. Hannant. 1998. "Tensile behavior of fiber-cement hybrid composites containing polyvinyl alcohol fiber yarns." *Mater. J.* 95 (6): 667–674.

Yoo, D.-Y., Y.-S. Yoon, and N. Banthia. 2015. "Flexural response of steel-fiber-reinforced concrete beams: Effects of strength, fiber content, and strain-rate." *Cem. Concr. Compos.* 64: 84–92. https://doi.org/10.1016/j .cemconcomp.2015.10.001.

Zhang, T., P. Visintin, and D. J. Oehlers. 2016. "Partial-interaction tension-stiffening properties for numerical simulations." *Adv. Struct. Eng.* 20 (5): 812–821. https://doi.org/10.1177/1369433216660654.
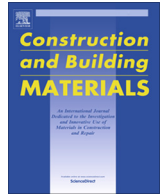
Experimental investigation of moment redistribution in ultra-high performance fibre reinforced concrete beams

P. Visintin *, M.S. Mohamad Ali, T. Xie, A.B. Sturm

School of Civil, Environmental and Mining Engineering, The University of Adelaide, South Australia 5005, Australia

HIGHLIGHTS

- An experimental study of moment redistribution in UHPC 2 span continuous beams.
- Shows members fail through rupture of reinforcement.
- Approaches in national codes of practice are not always conservative.

ARTICLE INFO

ABSTRACT

In the design of statically indeterminate structures the concept of moment redistribution is used to reduce the absolute magnitudes of moments in critical regions, to fully utilise the capacity of non-critical cross sections, and to simplify detailing by enabling a reduction in reinforcement ratios. Due to the complex mechanisms which control the formation and rotation of plastic hinges, moment redistribution capacities are commonly empirically based, and hence not necessarily applicable outside of the bounds of the testing regime from which they were derived. This paper presents the results of an experimental study of the moment redistribution capacity of four two-span continuous beams constructed from ultra-high performance fibre reinforced concrete (UHPFRC) and with various reinforcement ratios, such that the suitability of extending of exiting empirical design approaches to UHPFRC can be investigated. The results of the experimental investigation show that for beams where the hinge formed at the support, the observed moment redistribution was greater than the code predictions. However for the beam where the hinge formed under the load points, observed moment redistribution was significantly less than codes predictions. Hence, the results of this study show current design guidelines do not always provide a conservative prediction of moment redistribution in UHPFRC beams.

© 2018 Elsevier Ltd. All rights reserved.

1. Introduction

The recent expansion in research directed towards high performance materials has seen the development of a number of reliable mix designs for ultra-high performance fibre reinforced concretes (UHPFRC), including a number of commercially available products [4,3,23]. These materials which are characterised by a very high compressive strength, a non-negligible tensile strength, high material ductility and enhanced durability have the potential to revolutionise the design of structures allowing for longer spans, reduced member sizes and increased design lives. To date numerous studies have focused on developing mix designs and characterising material performance, and in a more limited way structural tests have been performed on simple beam elements [8,27,28,19]. This

research has culminated in the development of initial design guidelines for the use of UHPFRC [10,1]. While these guidelines present methodologies for the design of simple structural members the behaviour of indeterminate UHPC members has not yet been considered.

In statically indeterminate beams, a redistribution of internal forces arises due to the inelastic nature of reinforced concrete. The phenomenon of moment redistribution occurs at all limit states due to a difference in the relative stiffness of individual cross sections [17], but is typically utilised by designers at the ultimate limit. Moment redistribution allows the designer to reduce both the maximum hogging and sagging elastic moments, thereby reducing the overall moment demanded across a span, enabling a reduction in reinforcement requirements. Additionally, the ability to shift moments away from less efficient cross sections towards other more efficient cross sections may allow for savings in reinforcement costs and the easing reinforcement congestion [16].

---

* Corresponding author.
 E-mail address: phillip.visintin@adelaide.edu.au (P. Visintin).

These factors may be particularly important for UHPFRC which has higher material costs than conventional concrete and has the potential to perform poorly in regions of congested reinforcement if fibres cannot be uniformly distributed around reinforcement.

At the ultimate limit, moment redistribution occurs due to the formation and gradual rotation of plastic hinge regions, and has also been shown to be highly dependent on the stiffness or flexural rigidity of the non-hinge regions [14,17,25]. Hence the mechanics of moment redistribution is incredibly complex as it is defined by the localised mechanism which control crack widening and tension stiffening as well as the formation and sliding of concrete softening wedges [25]. Due to the complexity of the problem an empirical approach is often adopted to quantify hinge rotation and moment redistribution, and a review of approaches by Panagiotakos and Fardis [15] has shown that these typically perform poorly outside of the bounds of the test results from which they were derived.

To date the majority of experimental investigations into moment redistribution have been performed on members constructed from normal strength concrete, with few studies considering the influence of high-strength concrete (HSC). In these studies [6,17,7] it has been suggested that the brittle nature of HSC may influence hinge rotation and that the increased bond between the reinforcement and concrete may lead to a higher tension stiffening effect in cracked regions and therefore a significant deviation away from the behaviour expected from conventional concrete members. To allow for the change in behaviour which occurs with increased concrete strengths, national codes of practice often set different limits for moment redistribution in HPC [9], it is however unknown if these expressions can be further extended to UHPFRC beams.

Previous studies into the material performance of UHPFRC have shown that the addition of fibres to concrete improves the bond between reinforcement and concrete and restrains sliding along concrete to concrete interfaces, thereby improving shear-friction material properties and compressive ductility [23,26]. It can therefore be expected that the addition of fibres to concrete will change the magnitude of hinge rotation and therefore moment redistribution in statically indeterminate beams. Although the addition of fibres can be expected to influence moment redistribution, little experimental work has been undertaken to date, with that available limited to members without reinforcement [12,13].

In this paper the moment redistribution behaviour of two span continuous beams manufactured from UHPFRC is investigated on beams with a range of reinforcing ratios. Existing methods for predicting moment redistribution prescribed by various national codes of practice are then applied to determine if they can be extended for application to UHPFRC.

2. Experimental program

The experimental program has been devised to provide both an experimental investigation of the moment redistribution behaviour of UHPFRC beams and also to provide a range of material properties such that the results may be of use in the future validation of novel analytical procedures. As such in addition to four continuous beam tests, material tests were undertaken to quantify the compressive and tensile stress-strain and stress-crack width behaviour of the UHPFRC and the stress-strain characteristics of the reinforcement.

3. Mix design

All beams were cast using a mix design developed at the University of Adelaide as part of a project to develop ultra-high

performance fibre reinforced concretes which require only conventional concrete manufacturing materials and equipment, and which do not require special curing regimes [23]. It may also be worth noting that these mixes have also been used for extensive material and member level testing reported elsewhere [23,19].

The full mix design is given in Table 1, in which the sulphate resisting cement had a fineness modulus of 365 m^2/kg, a 28 day compressive strength as determined in accordance with AS 2350.11 [21] of 60 MPa and a 28 day mortar shrinkage strain determined in accordance with AS 2350.13 [22] of 650 microstrain. The silica fume was undensified with a bulk density of 625 kg/m^3. The steel fibres were cold drawn hooked end wire fibres with a total length of 35 mm, an aspect ratio of 64 and a minimum yield strength of 1100 MPa. The superplasticiser was a third generation high range water reducer with an added retarder.

The concrete was manufactured by first mixing the cement, silica fume and sand for 1 min in a 750 L pan mixer until well blended. The water and superplasticiser were then added and the concrete mixed until visibly flowable; this took approximately 35 min. After the concrete started to flow, the fibres were added and mixed for a further 5 min. All specimens were cast in 4 batches on different days with each batch consisting of one beam as well as cylinders to determine the compressive and tensile strengths of the concrete. All dog-bone specimens were cast along with beam 3. Note that to achieve a uniform distribution of fibres, sufficient mixing time was applied to ensure that the fibres were evenly mixed with the matrix. When placing the concrete, to avoid settlement of fibres, all beams were cast horizontally by pouring the concrete into the form in layers which were individually compacted.

3.1. Beam test specimens

To investigate the moment redistribution capacity of UHPFRC, four two-span continuous beams were tested. Note that a rectangular section was chosen in order to simplify analysis and because it is the most common beam cross section tested. It may however be useful to investigate T-sections in the future. As shown in Fig. 1 these beams had a total length of 5500 mm and were tested with point loads located at the mid-point of each span of length 2500 mm. To investigate the influence cross sectional ductility on the moment redistribution capacity each beam had a different tensile reinforcement ratio ranging from 1.48% to 1.94% in the sagging region and 1.28% to 1.94% in the hogging region. The reinforcement arrangement was chosen for the first three beams to investigate the relationship between reinforcement ratio and moment redistribution, and in the final beam to investigate the behaviour when moment redistribution occurs from the sagging to the hogging region. To prevent shear failure, 6 mm diameter stirrups were placed at 100 mm centres. Full details of the reinforcement are given in Table 1.

3.2. Instrumentation and testing

To capture the deformation of the hinge region a series of five linear variable displacement transducers (LVDTs) were placed at

Table 1
UHPFRC mix design.

Material	kg/m^3
Sulphate resisting cement	937.50
Washed river sand	937.50
Silica fume	250.00
Steel fibres	165.00
Water	160.00
High range water reducing agent	52.50
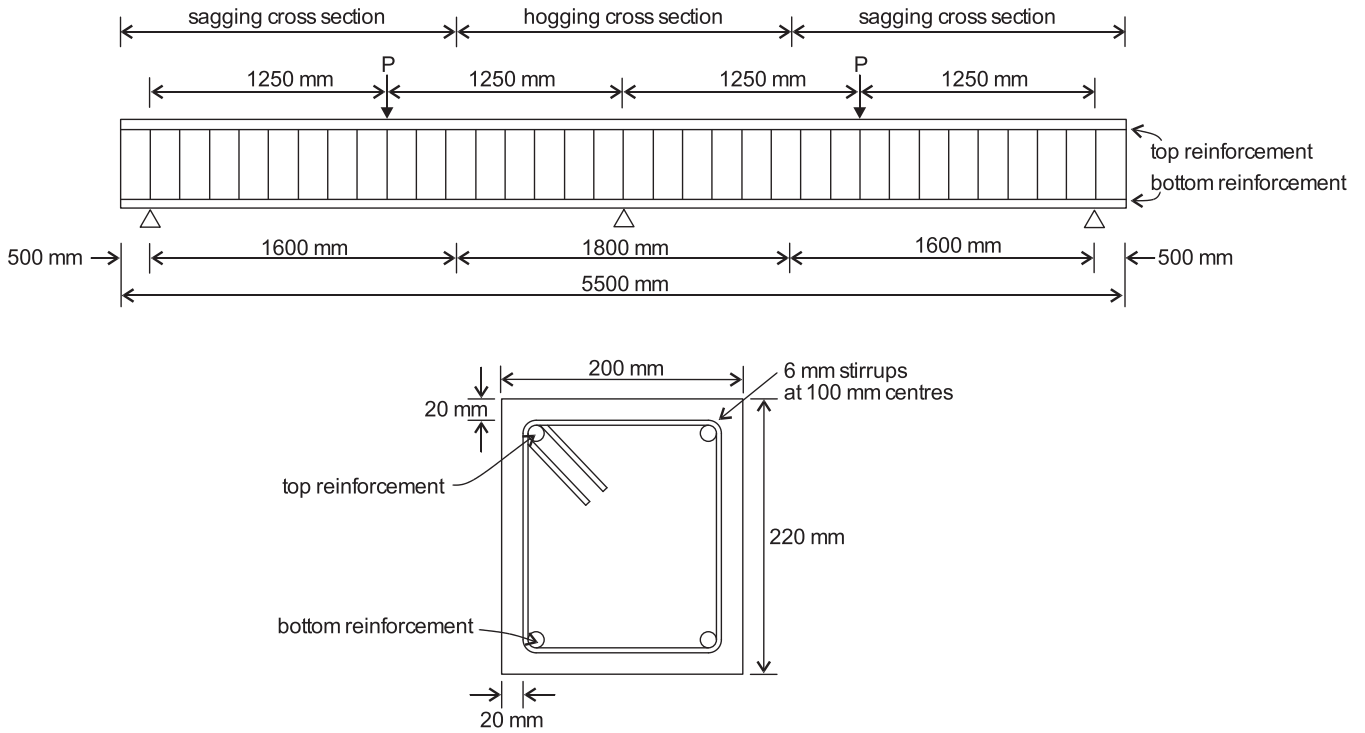
Fig. 1. Beam specimens.

the expected location of the plastic hinge in the sagging region. The location of each of the LVDTs is shown in Fig. 2.

During testing a hydraulic ram applied a load to displace the mid-span of the beam at a rate of 0.8 mm/min. To experimentally record the reactions 225 kN load cells were located at each loading point and a 1000 kN load cell at the centre support as shown in Fig. 2. Note that in this study LVDTs were used in preference to strain gauges as they can capture the deformations associated with localised deformations such as crack opening and concrete to concrete sliding along the softening wedge. It can also be noted that LVDTs were also used by Schumacher [18] to directly measure hinge rotation.

4. Material tests

4.1. Concrete in compression

To determine the compressive stress-strain behaviour of the UHPFRC, three cylinders of 100 mm diameter and 200 mm height were cast with each batch of concrete. During testing, specimens were loaded at a rate of 50 kN/min until an estimated 90% of their peak load and then at a displacement rate of 0.1 mm/min until failure. To determine the full stress-strain relationship of the concrete,

each specimen was instrumented with a pair of 30 mm axial strain gauges, additionally, 4 LVDTs recorded to total deformation of the specimen between loading platens throughout testing.

The average stress-strain relationship obtained from each set of three cylinder tests manufactured from concrete cast with each beam are shown in Fig. 3. It should be noted that the cylinder tests were conducted on the day of beam testing and hence the time since casting of the specimens ranged from 24 to 67 days.

4.2. Concrete in tension

To determine the stress strain behaviour of UHPFRC prior to cracking, as well as the stress- crack-width behaviour following cracking, direct tensile tests were conducted two dog-bone shaped specimens shown in Fig. 4. The design of these dog-bone specimens and test set-up has been described in detail elsewhere [19] and hence will only be summarised here.

The specimens in Fig. 4(a) have an overall height 610 mm and a thickness of 120 mm. The width of the specimen tapers from 210 mm at the top to a shank of 120 mm breadth and 330 mm height. During testing the dog-bone shaped specimens were gripped with a steel loading plate having the same radius as the tapered concrete region. These loading plates were bolted to the loading frame
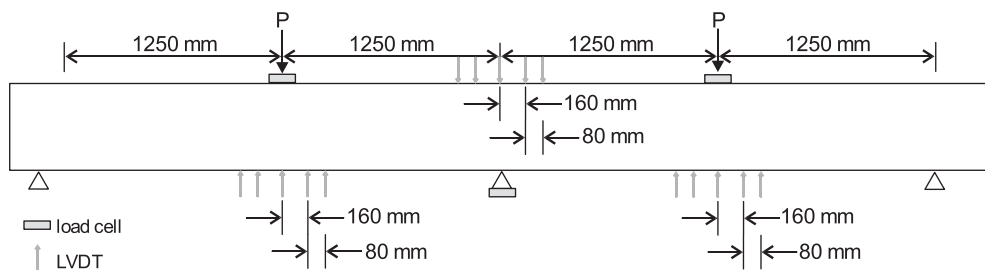
Fig. 2. Instrumentation for beam tests.
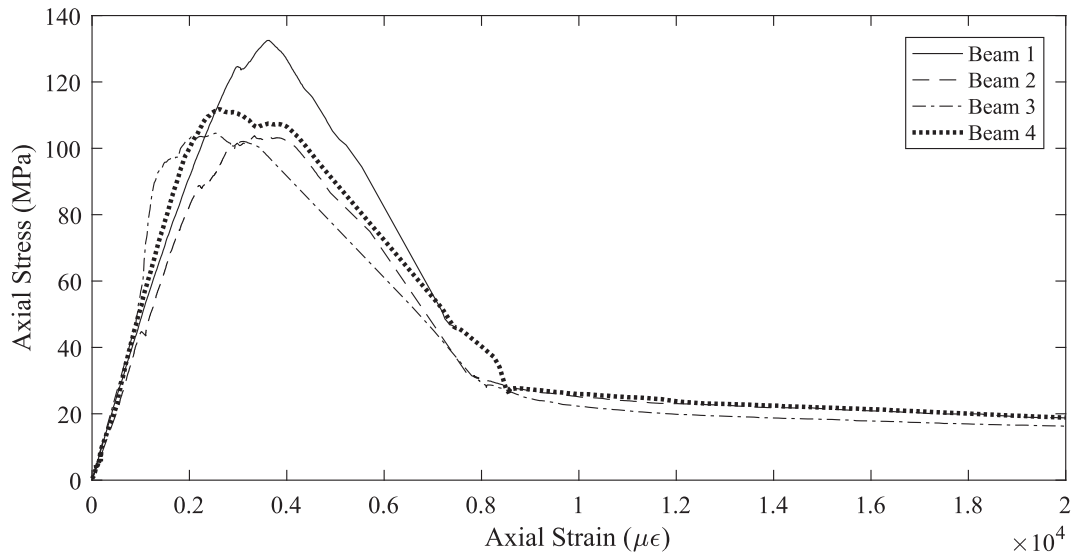
Fig. 3. Compressive stress strrain relationship.
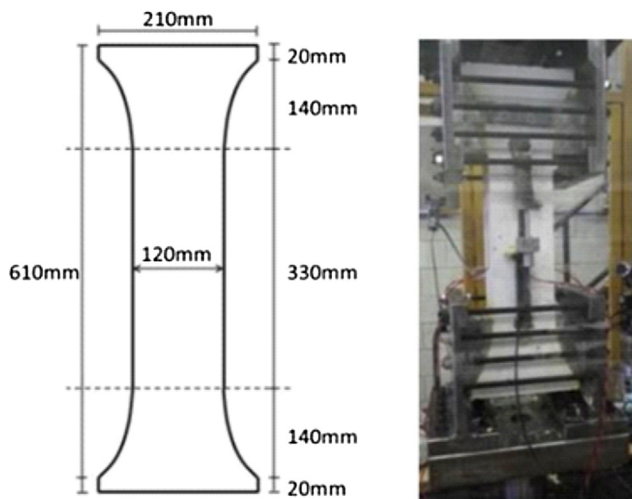
Fig. 4. Dog-bone specimens.

which was mounted into the universal testing machine which applied a load such that a displacement rate of 0.05 mm/min was observed throughout the test. Axial strain in the concrete was measured using a pair of 30 mm strain gauges glued to the concrete surface, additionally the total deformation of the shank having a reduced area is measured with 2 LVDTs located on opposite faces.

The tensile stress-train behaviour of the UHPFRC prior to cracking in Fig. 4(a) was determined based on the strain gauge readings and found to be in good agreement with that determined from the deformation recorded by the LVDTs. As only a single major crack was observed post cracking, the stress-crack width behaviour in Fig. 5(b) was extracted from the total deformation readings by subtracting the elastic deformation from the total recorded deformation. It should be noted that at the time of testing of the dog bones the corresponding compressive strength of the concrete was 156 MPa.

4.3. Reinforcement

The experimental stress-strain relationships for the longitudinal reinforcement is illustrated in Fig. 6. This was obtained from

4 a direct tension test on the 12 mm and 16 mm longitudinal reinforcing bars in which the measured strain obtained from extensometer readings.

5. Beam test results

The load-deflection response of both spans of each of the beams tested are shown in Fig. 7 and a photograph of a typical failed beams in Fig. 8. In Fig. 7 key points have been identified as follows: the yield point is indicated by a cross, the peak load by a circle and the first rupture of the tensile reinforcement by a triangle. In the load deflection responses it can be observed that each beam exhibited typical approximately bi-linear behaviour, in which a significant increase in deformation occurred after the yielding of the tensile reinforcement. In each case ultimate failure of the member occurred due to rupture of the 12 mm tensile reinforcing bars, and upon inspection it could be observed that significant necking of the 16 mm bars had also occurred. As failure of the beam was due to reinforcement rupture, beams with the greatest reinforcement ratio exhibited the largest deformation and ductility. This suggests that in order to make use of the full potential of UHPFRC the use of high strength reinforcement may be required.

The experimentally derived moment-rotation relationship of each hinge region is shown in Fig. 9. The rotation of the hinge was determined by considering the relative difference in beam deformation recorded by the LVDT readings concentrated about the location of the applied load and central support in Fig. 2. The end of the hinge region was identified from the step change in the rotation derived from adjacent LVDTs. The deformation readings outside of the hinge region were ignored. It should be noted that this measurement follows the work of [24] who suggest that the hinge region must capture the deformations associated with the sliding of the softening wedge as well as the opening of all cracks beneath and immediately adjacent to the softening wedge as shown in Fig. 10.

From the photograph of a typical hinge region in Fig. 10 it is observed that the depth of the softening region is shallow despite the high reinforcing ratio of the beams. In normal strength reinforced concrete beams, Visintin and Oehlers [25] postulated that compressive failure and moment redistribution is controlled by shear-friction sliding of the softening wedge identified in Fig. 10. Hence as a comparison to conventional concrete the angle at which

a)

b)
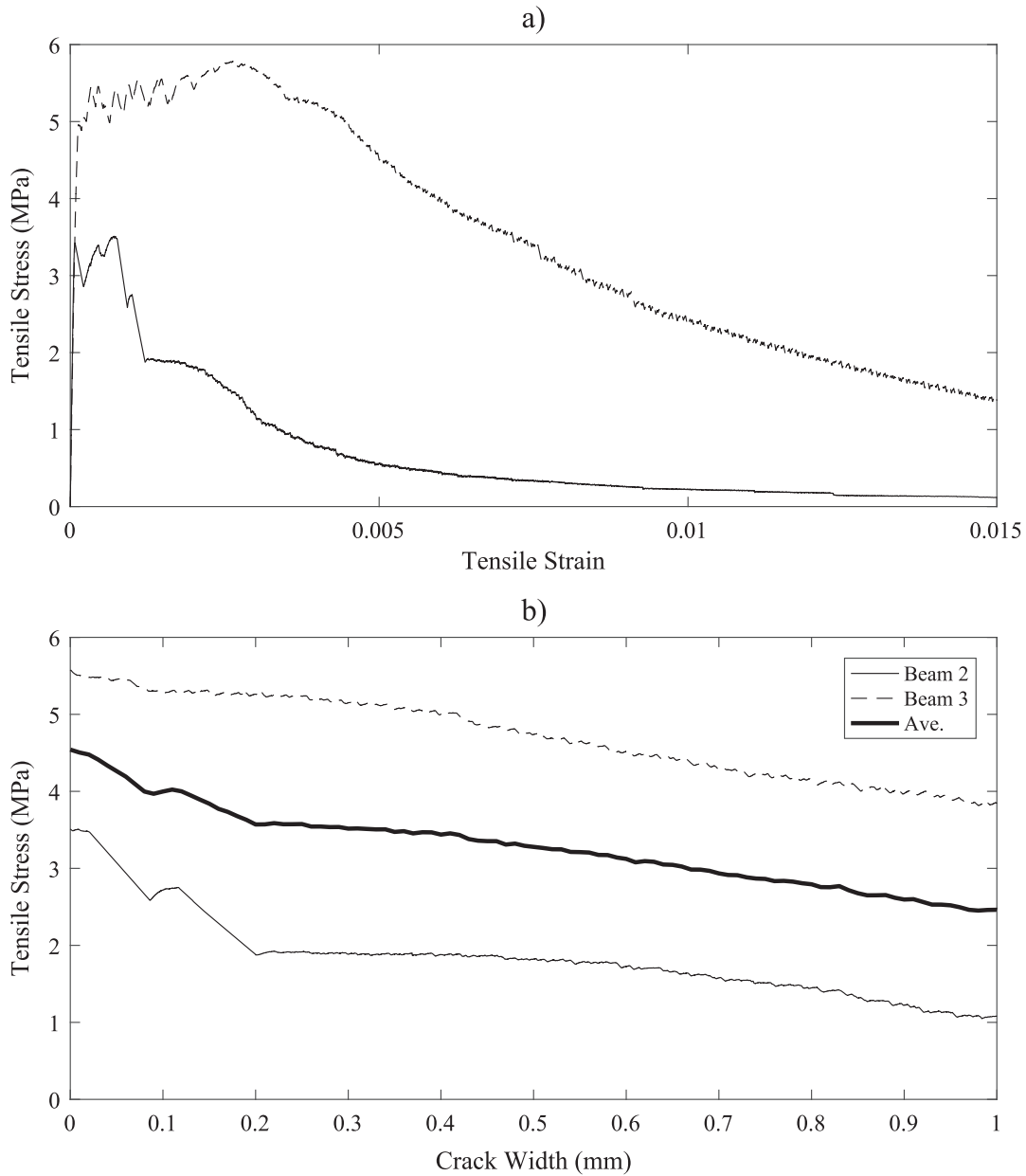
Fig. 5. Axial stress-strain and stress-crack width relationship.

shear friction sliding occurs along the softening wedge in the UHPFRC beams was measured and found to vary between 23 and 53 degrees with an average of 37 degrees. This is, in contrast to that of conventional concrete where the softening wedge typically forms at 26 degrees and increases with increased confinement [5]. This implies that significant confinement of the concrete is provided by the fibre reinforcement, and the scatter within results is likely due to local variation in fibre quantity and orientation.

5.1. Moment redistribution

Fig. 11 shows the degree of moment redistribution at each hinge location (mid span of each beam and central support) as a function of the total applied load P_{total}. In Fig. 11 percentage of moment redistribution calculated as

$$K_{MR} = \frac{M_{el} - M_{exp}}{M_{el}} \qquad (1)$$

where M_{el} is the theoretical elastic moment and M_{exp} is the experimental moment which includes the effect of the plastic behaviour.

It can be observed in Fig. 11 that moment redistribution begins at first loading. This behaviour can be attributed to variation in stiffness along the span due to the difference in reinforcement ratio in the hogging and sagging region, and due to the presence of flexural cracks which may arise either due to shrinkage or loading of the beam [17].

After the initial spike in redistribution with occurs around the point of first cracking, moment redistribution becomes more strongly dependent on the reinforcement ratio where for beams 1–3 redistribution occurs from the hogging to the sagging region and for beam 4 from the sagging to the hogging region.

In Fig. 12 the bending moment diagrams at corresponding the load at maximum moment redistribution in Fig. 11 are compared to the elastic bending moment diagrams. These demonstrates the effect of moment redistribution in equalising the moment between
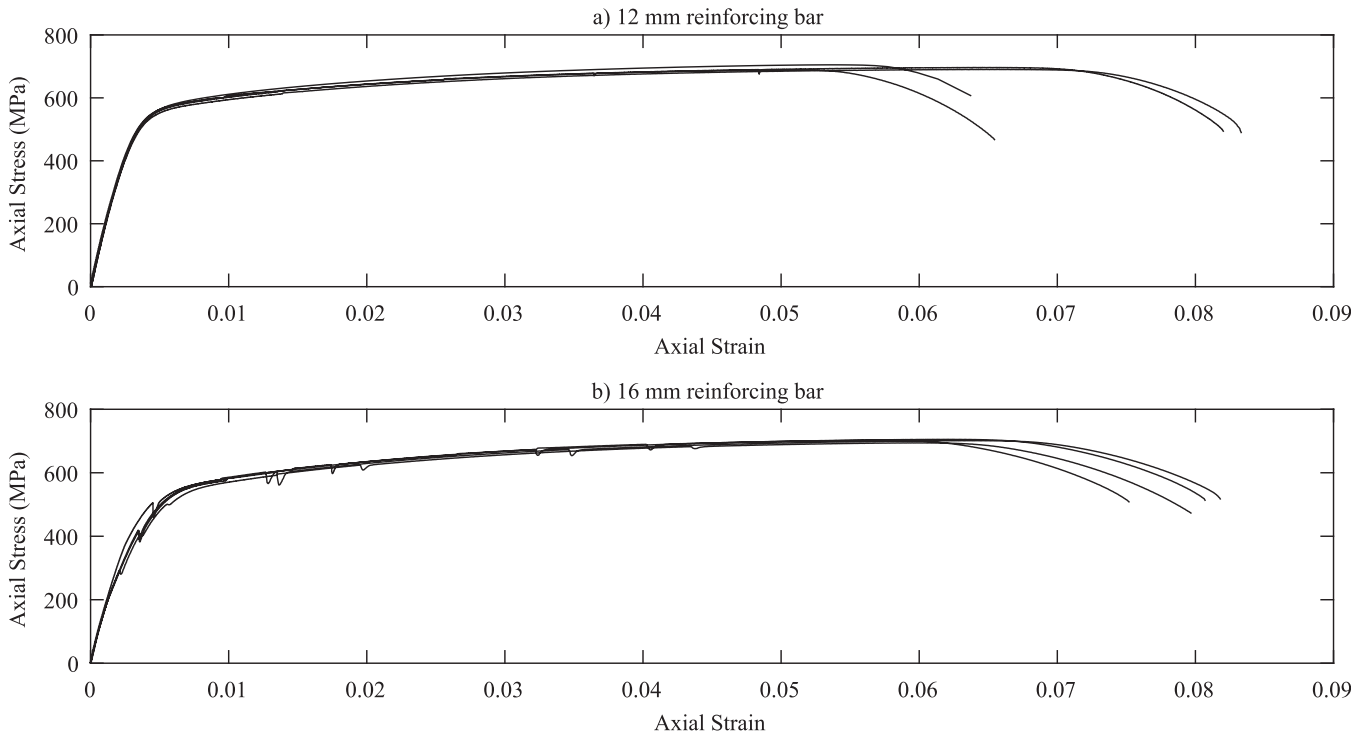
Fig. 6. Stress-strain relationship of steel reinforcement.
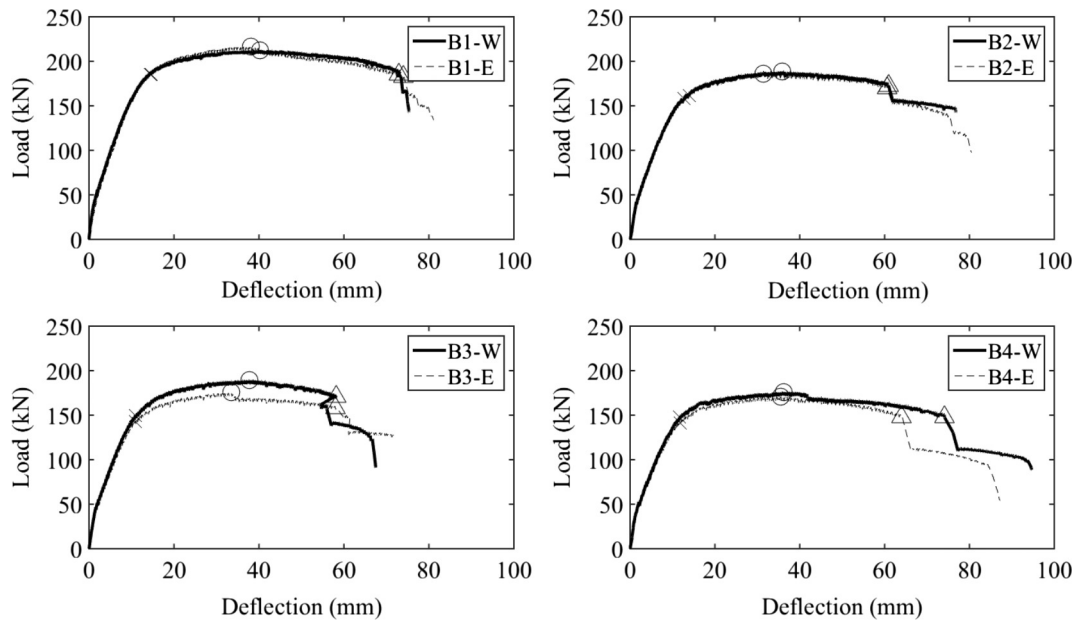
Fig. 7. Load-deflection response of beams.

Fig. 8. Typical beam after failure.
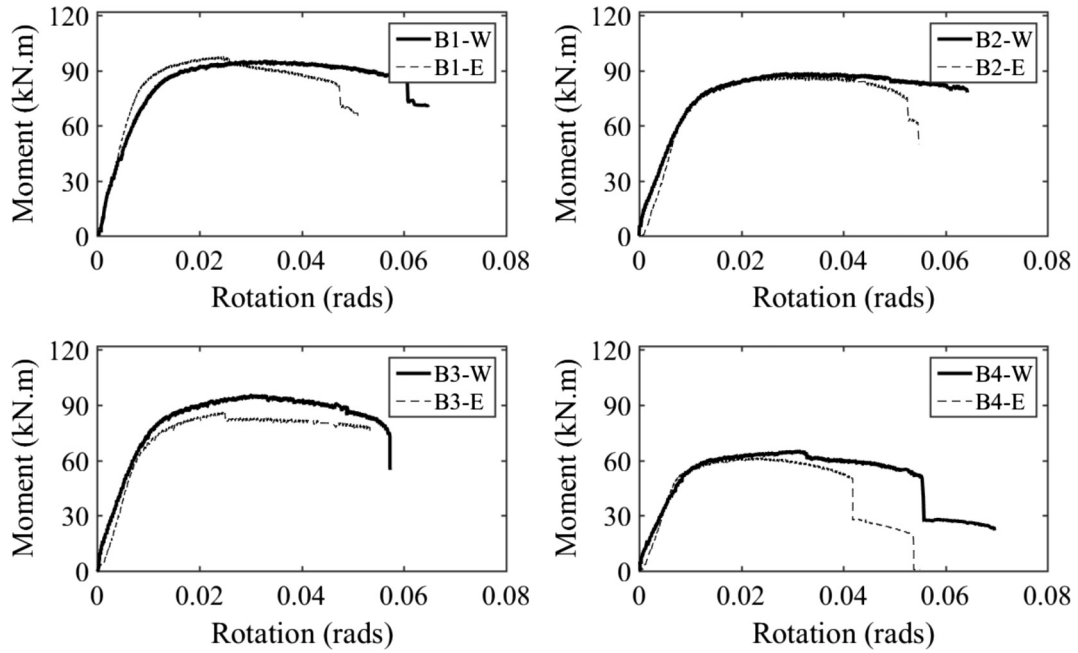
Fig. 9. Moment-rotation relationship.
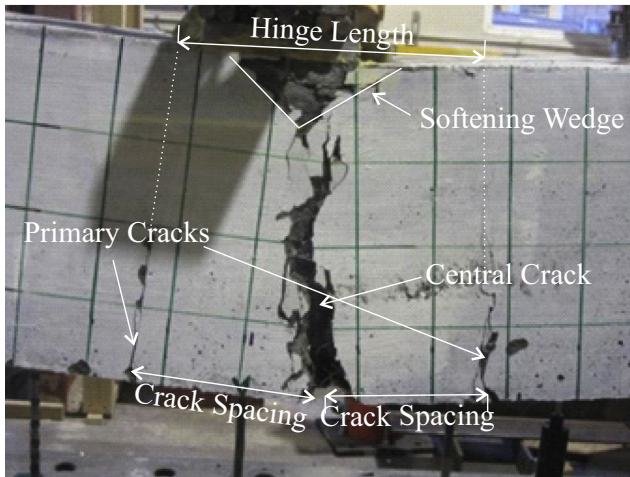
Fig. 10. Typical hinge region at failure.

the load point and the central support. In Fig. 13 the reaction at the centres support versus the applied load is also shown.

5.2. Ductility factor

The ratio of the ultimate to yield deflection, also known as the ductility factor, is often used as a simple measure of energy absorption [6] and is provided for each beam in Table 3. Unlike the behaviour seen in conventional concrete, here it is observed that the ductility factor does vary significantly with the reinforcement ratio. The quantity of the moment redistribution (KMR in Table 2) can also be seen not to be a function of the ductility factor. This contrary to the behaviour observed by do Carmo and Lopes [6], and is likely due to the UHPFRC beams failing by rupture of the tensile reinforcement rather than by compression failure of the softening wedge.

6. Comparison to codes of practice

To investigate the potential to extend existing codified limits on moment redistribution to UHPFRC the experimentally observed moment redistribution is compared to that predicted by the design equations in AS3600-2009 [20], fib Model Code 2010 [9] and ACI 318-14 [2].

In AS3600-2009 [20] permissible moment redistribution, K_{MR} is given by

$$K_{MR} = 0.3; k_u < 0.2 \tag{2}$$

$$K_{MR} = 0.75(0.4 - k_u); 0.2 \le k_u < 0.4 \tag{3}$$

$$K_{MR} = 0; k_u \ge 0.4 \tag{4}$$

and in which the neutral axis parameter k_u is a measure of the ductility of the cross section and is given by

$$k_u = \frac{d_{NA}}{d} \tag{5}$$

where d_{NA} is the neutral axis depth and d is the effective depth of the cross section.

In the fib Model Code 2010 [9] the permissible moment redistribution for concretes with a characteristic compressive strength of greater than 50 MPa is

$$K_{MR} = \min\left(0.46 - 1.25(0.6 + 0.0014\varepsilon_{cu2})k_u, 0.3\right) \tag{6}$$

in which ε_{cu2} is the ultimate strain of the concrete.

Finally according to ACI 318-14 [20], the maximum permissible moment redistribution is

$$K_{MR} = \min(1000\varepsilon_t, 0.2) \tag{7}$$

where ε_t is the tensile strain in the reinforcement at the section redistributing moment.

A standard moment curvature analysis was undertaken as this form of analysis has been assumed to be applicable to fibre reinforced concrete at the ultimate limit [1] and it is an analysis approach most commonly applied in practice.
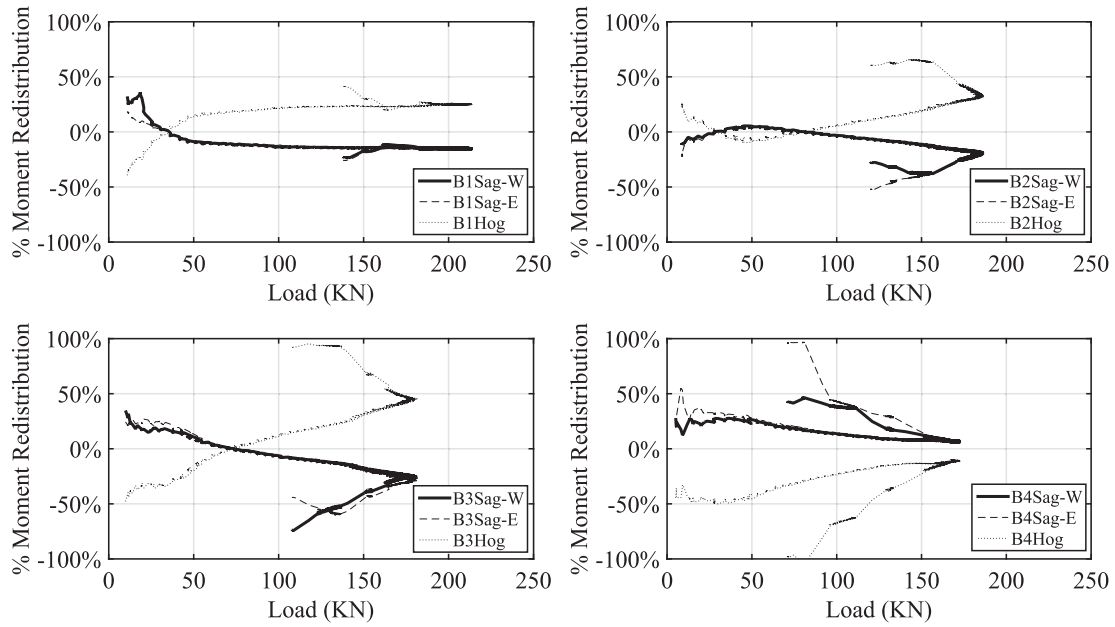
Fig. 11. Moment redistribution at each span.
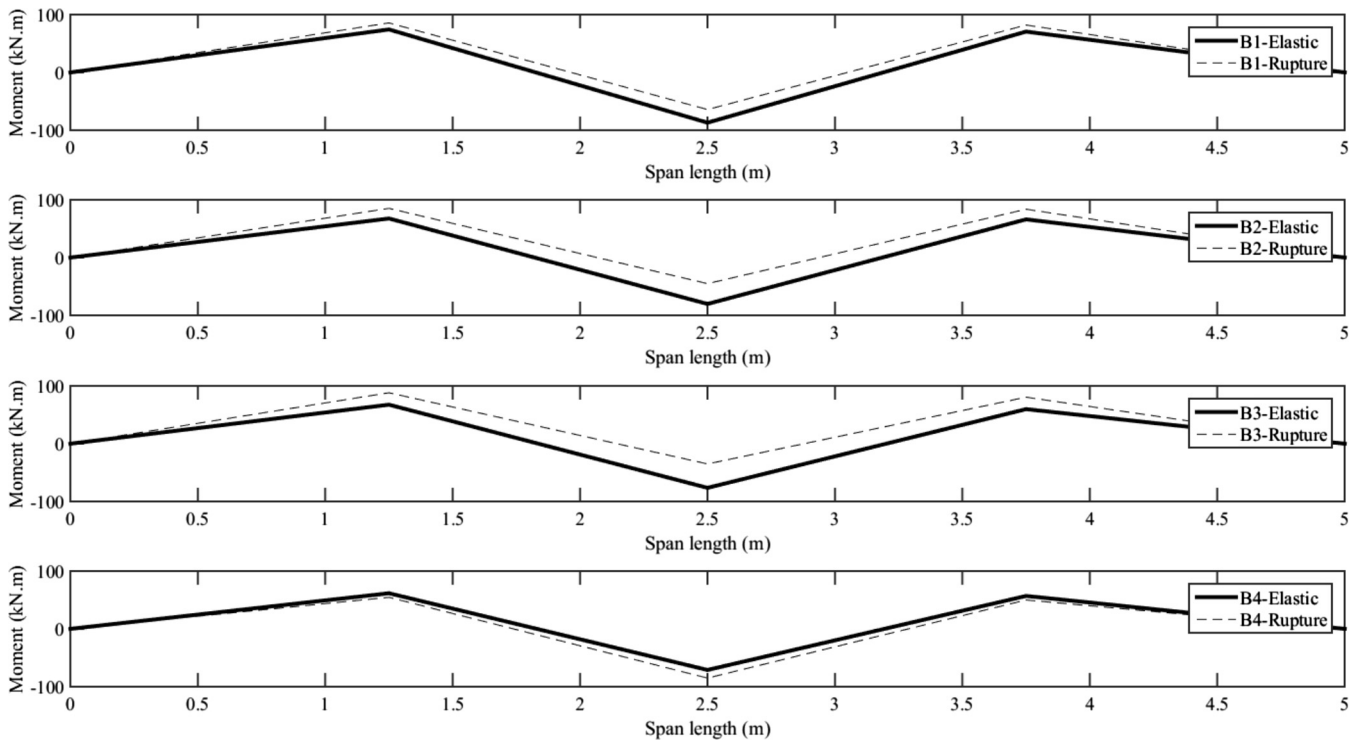
Fig. 12. Comparison of elastic and experimental bending moment diagrams.

For analysis, in Fig. 14a a curvature χ was applied to the cross section and a corresponding neutral axis d_{NA} assumed such that the strain profile is known. From this strain profile the concrete was divided into a series of layers and from the strain the stress was determined using the experimental derived stress-strain curves. Note that the tensile stress-crack width was converted to a stress-strain relationship by assuming a characteristic length equal to the length of the fibres [11]. Applying the assumption of full interaction between the reinforcement and the surrounding concrete and taking the elastic modulus of the reinforcement to

be 200 GPa and the yield stress to be 500 MPa the forces in the reinforcement, P_{rt} and P_{rc} can be determined. Having determined the internal forces the neutral axis is then shifted until equilibrium is achieved. The approach is then repeated for each curvature to generate the full moment curvature relationship for each cross section in Fig. 15, where significant points of interest have been highlighted. These include the curvature at: (i) yielding of the tensile reinforcement; (ii) commencement of crushing of the concrete when the maximum strain in the corresponds to the strain at peak stress in Fig. 3; (iii) an approximation of the end of concrete crush-
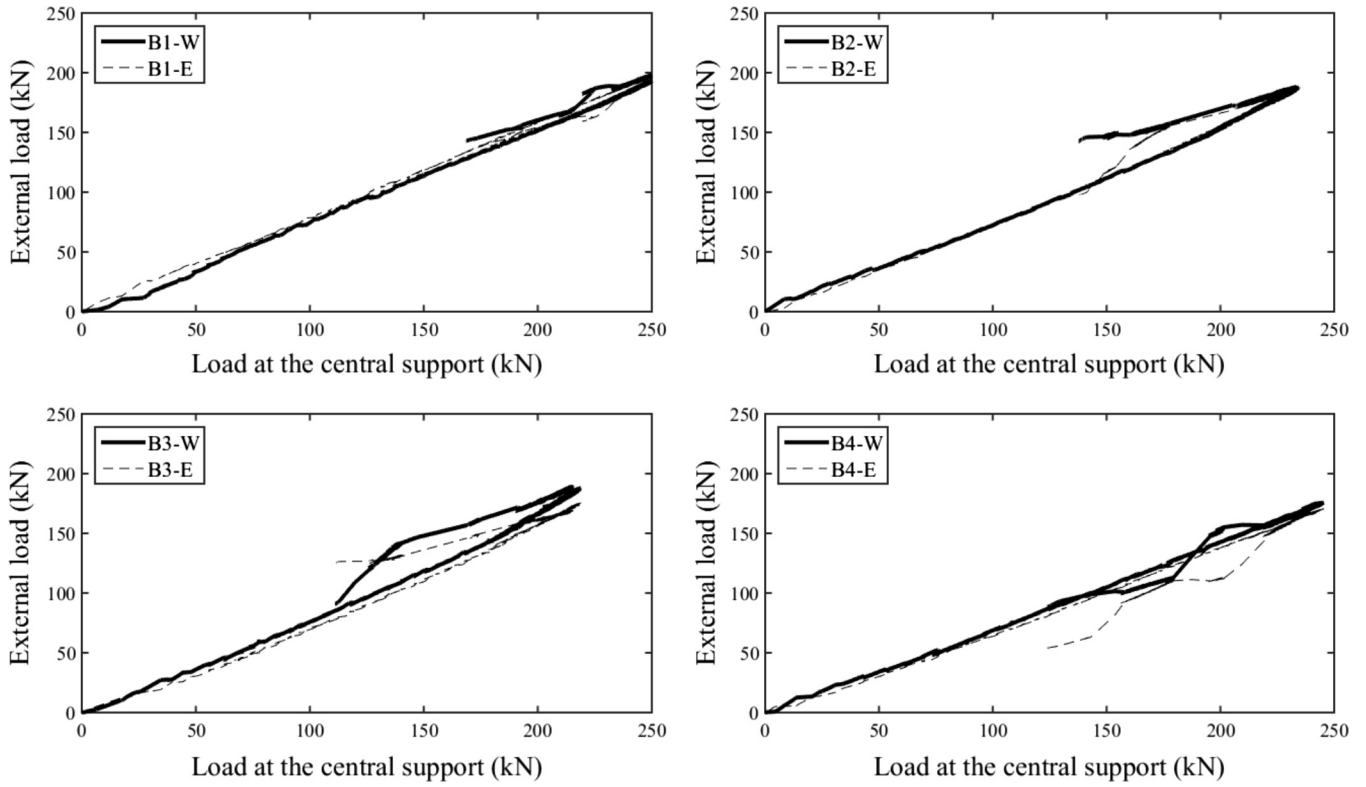
Fig. 13. Comparison of load at central support to the applied external load.

Table 2
Reinforcement details.

Beam	Hogging region				Sagging region			
	Top	Bottom	Tensile reinf. ratio (ρ) (%)	Compressive reinf. ratio (ρ_c) (%)	Top	Bottom	Tensile reinf. ratio (ρ) (%)	Compressive reinf. ratio (ρ_c) (%)
1	2N12 + 2N16	2N12	1.94	0.673	2N12	2N12 + 2N16	1.94	0.673
2	2N12 + 1N16	2N12	1.48	0.673	2N12	2N12 + 2N16	1.94	0.673
3	2N12 + 1N12	2N12	1.28	0.673	2N12	2N12 + 2N16	1.94	0.673
4	2N12 + 2N16	2N12	1.94	0.673	2N12	2N12 + 1N16	1.48	0.673

Table 3
Ductility factors for each beam.

Beam	West			East			Exp. KMR
	Δ_{yield}	$\Delta_{ultimate}$	$\Delta_{ultimate}/\Delta_{yield}$	Δ_{yield}	$\Delta_{ultimate}$	$\Delta_{ultimate}/\Delta_{yield}$	
1	14.5	74.0	5.11	14.6	73.0	4.99	25.0
2	12.7	60.6	4.79	14.0	60.9	4.37	31.8
3	11.0	58.0	5.29	10.9	58.1	5.34	45.3
4	11.8	63.9	5.41	11.7	74.2	6.32	6.7

ing when the maximum strain in the concrete reaches 0.008 which corresponds to the beginning of the residual stress in Fig. 3; and (iv) rupture of the reinforcement. An additional point corresponding to the curvature when the maximum strain in the concrete is 0.003 has been included as this strain condition is commonly used to indicate concrete crushing failure (AS3600-2009; fib Model Code 2010; ACI 318-14).

Based on the results of the moment-curvature analysis the strain in the tensile reinforcement ε_t and the neutral axis depth parameter k_u were determined for each key point and used in conjunction with the code approaches to predict the percentage

moment redistribution at the failure; and the results are summarised numerically in Table 4. This approach was taken as it can be seen in Fig. 3 that the assumption that concrete fails at a strain of 0.003 is not valid for the UHPFRC used in the present study.

From Table 4 it can be seen that for beam 1 AS3600-2009 stipulations yield conservative results, overestimate moment redistribution. ACI 318-2014 and fib Model Code 2010 is conservative for the first three beams which experience moment redistribution from the hogging and sagging regions as are AS3600-2009 for beams 2 and 3. For Beam 4 which experiences moment redistribu-

Slice for sectional analysis
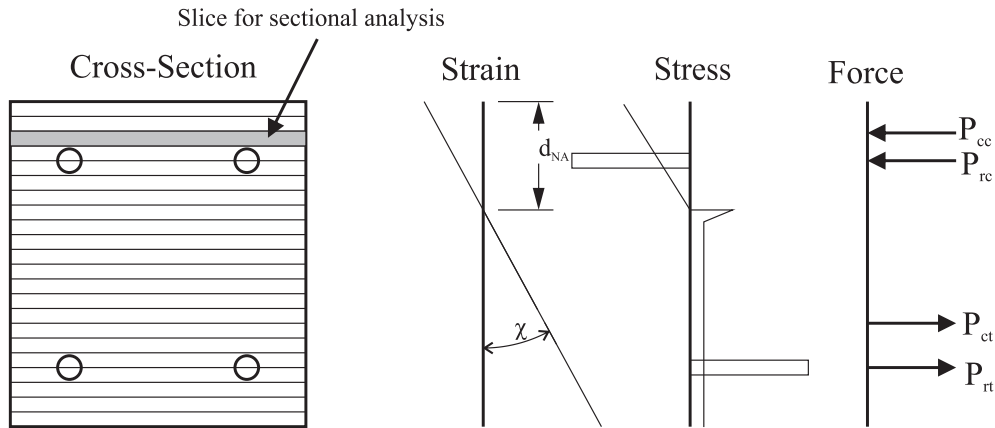
Fig. 14. Illustration of forces and deformations in sectional analysis.

Fig. 15. Moment curvature relationships of cross sections in each beam.

tion from the sagging to the hogging region all three code approaches are very unconservative which suggests that the code approaches can only predict moment redistribution if the moment is distributing away from a support. Further the code approaches

did not show the trend observed experimentally of an increase in moment redistribution as the reinforcement in the hogging region is reduced. It can also be observed that the magnitude of the concrete stain at failure did not significantly influence the predicted

moment redistribution, this is because the reinforcement yielded before the concrete reached its peak stress and hence for all strains investigated the neutral axis and hence k_u remained relatively constant.

7. Conclusion

In this research, an experimental program has been conducted in order to investigate the moment redistribution capacity of reinforced UHPFRC continuous beams as well as the suitability of extending existing code approaches for application to UHPFRC.

The results of the experiments indicate that:

(1) The improved compressive ductility of the concrete introduced by the presence of fibres, including the approximately 25 MPa residual strength, shifted the failure mode of the UHPFRC sections tested from concrete crushing to reinforcement rupture.
(2) Significant redistribution of moments occurs in UHPFRC beams prior to the plastic limit being reached in either the reinforcement or the concrete. This elastic redistribution occurs as a result of the variation in flexural rigidity of the section throughout the span either because of a variation in reinforcement layout or due to cracking.
(3) ACI and FIB reproaches are conservative in all cases where redistribution occurs from the hogging to the sagging region.
(4) No approaches could adequately simulate moment redistribution from the sagging to hogging regions of a beam.
(5) The increased ductility of the concrete was not a significant factor in the analysis approaches as for all limiting strain conditions investigated the neutral axis depth remained relatively constant.

Acknowledgements

References

[1] AFGC (Association Francaise de Genie Civil), Betons fibres a ultra-hautes performances – Recommandations [Ultra High Performance Fibre Reinforced-Concretes – Recommendations], Paris, France, 2013.
[2] ACI Committee, American Concrete Institute, and International Organization for Standardization, Building Code Requirements for Structural Concrete (ACI 318-08) and Commentary, American Concrete Institute, Farmington Hills, MI, 2008.
[3] S.D.P. Benson, B.L. Karihaloo, CARDIFRC – development and mechanical properties: Part 1. Development and workability, Mag. Concr. Res. 57 (6) (2005) 347–352.
[4] G. Chanvillard, S. Rigaud, Complete characterization of tensile properties of Ductal® UHPFRC according to the French recommendations, in: Proceedings of the 4th International RILEM Workshop High Performance Fiber Reinforced Cementitious Composites, 2003, pp. 21–34.
[5] Y. Chen, P. Visintin, D.J. Oehlers, Concrete shear-friction material properties: derivation from actively confined compression cylinder tests, Adv. Struct. Eng. 18 (8) (2015) 1173–1185.
[6] R.N. Do Carmo, S.M. Lopes, Ductility and linear analysis with moment redistribution in reinforced high-strength concrete beams, Can. J. Civ. Eng. 32 (1) (2005) 194–203.
[7] R.N. Do Carmo, S.M. Lopes, Available plastic rotation in continuous high-strength concrete beams, Can. J. Civ. Eng. 35 (10) (2008) 1152–1162.
[8] B.A. Graybeal, Flexural behavior of an ultrahigh-performance concrete I-girder, J. Bridge Eng. 13 (6) (2008) 602–610.
[9] International Federation for Structural Concrete (fib), CEB-FIB Model Code 2010 Final Draft Volume 2, Thomas Thelford, Lausanne, Switzerland, 2010.

Table 4
Comparison of code approaches to experimental moment redistribution.

Beam	Position of Hinge	Exp. KMR	AS3600-2009									ACI 318-14									fib Model Code 2010								
			Crushing		$\varepsilon_t = 0.003$		Rupture		$\varepsilon_t = 0.008$			Crushing		$\varepsilon_t = 0.003$		Rupture		0.008			Crushing		$\varepsilon_t = 0.003$		Rupture		0.008		
			Pred.	Pred./Exp.	Pred.	Pred./Exp.	Pred.	Pred./Exp.	Pred.	Pred./Exp.		Pred.	Pred./Exp.	Pred.	Pred./Exp.	Pred.	Pred./Exp.	Pred.	Pred./Exp.		Pred.	Pred./Exp.	Pred.	Pred./Exp.	Pred.	Pred./Exp.	Pred.	Pred./Exp.
1	Hogging	25	30	1.199	30	1.199	30	(a)	30	(a)		19.7	0.789	14.2	0.568	20	(a)	20	(a)		24.2	0.966	21.6	0.862	24.7	(a)	24.7	(a)
2	Hogging	31.8	30	0.944	30	0.944	30	0.944	30	0.944		18.4	0.577	15.7	0.493	20	0.629	20	0.629		24.5	0.769	23.4	0.737	26.8	0.776	25.3	
3	Hogging	45.3	30	0.662	30	0.662	30	0.662	30	0.662		16.6	0.367	20	0.442	20	0.442	20	(b)		27.5	0.607	28.3	0.625	26.2	0.591	26.2	(b)
4	Sagging	6.7	30	4.448	30	4.448	30	4.448	30	4.448		11.6	1.719	14.6	2.161	20	2.965	20	2.965		24.8	3.671	25.9	3.835	26.2	3.882	26.5	

(a) The cylinder test for this series was stopped at 0.0075 hence a top strain of 0.008 or rupture of the reinforcement could not be achieved in the simulation.
(b) For this test the sectional analysis suggests rupture occurred before a strain of 0.008 was reached.

[10] Japanese Society of Civil Engineers, Concrete Engineering Series 82: Recommendations for Design and Construction of High Performance Fibre Reinforced Cement Composites with Multiple Fine Cracks, JSCE, Tokyo, Japan, 2008.

[11] J. Jungwirth, A. Muttoni, Structural behavior of tension members in Ultra High Performance Concrete, in: Proc., International Symposium on Ultra High Performance Concrete, University of Kassel, Kassel, Germany, 2004, pp. 533–546.

[12] M.R. Moallem, Flexural Redistribution in Ultra-High Performance Concrete Lab Specimens, (Doctoral dissertation), Ohio University, 2010.

[13] A.W. Mohr, Moment Redistribution Behaviour of SFRC Members with Varying Fibre Content (Doctoral dissertation), Stellenbosch University, Stellenbosch, 2012.

[14] D.J. Oehlers, M. Haskett, M.S. Mohamed Ali, M.C. Griffith, Moment redistribution in reinforced concrete beams, Proc. ICE Struct. Build. 136 (3) (2010) 165–176.

[15] T.B. Panagiotakos, M.N. Fardis, Deformations of reinforced concrete members at yielding and ultimate, Struct. J. 98 (2) (2001) 135–148.

[16] T. Paulay, Moment redistribution in continuous beam of earthquake resistant multistory reinforced concrete frames, Bull. N. Z. Natl. Soc. Earthq. Eng. 9 (4) (1976) 205–212.

[17] R.H. Scott, R.T. Whittle, Moment redistribution effects in beams, Mag. Concr. Res. 57 (1) (2005) 9–20.

[18] P. Schumacher, Rotation Capacity of Self-Compacting Steel Fiber Reinforced Concrete (Ph.D. Thesis), TU Delft, Delft, Netherlands, 2006.

[19] M. Singh, A.H. Sheikh, M.M. Ali, P. Visintin, M.C. Griffith, Experimental and numerical study of the flexural behaviour of ultra-high performance fibre reinforced concrete beams, Constr. Build. Mater. 138 (2017) 12–25.

[20] Standards Australia, AS 3600-2009 Concrete Structures, Standards Australia, Strathfield, Australia, 2009.

[21] Standards Australia, AS/NZS 2350.11:2006 – Methods for Testing Portland, Blended and Masonry Cements, Standards Australia, Strathfield, Australia, 2006.

[22] Standards Australia, AS/NZS 2350.13:2006 – Methods for Testing Portland, Blended and Masonry Cements – Determination of Drying Shrinkage of Cement Mortars, Standards Australia, Strathfield, Australia, 2006.

[23] H.R. Sobuz, P. Visintin, M.M. Ali, M. Singh, M.C. Griffith, A.H. Sheikh, Manufacturing ultra-high performance concrete utilising conventional materials and production methods, Constr. Build. Mater. 111 (2016) 251–261.

[24] P. Visintin, D.J. Oehlers, C. Wu, M. Haskett, A mechanics solution for hinges in RC beams with multiple cracks, Eng. Struct. 36 (2012) 61–69.

[25] P. Visintin, D.J. Oehlers, Mechanics-based closed-form solutions for moment redistribution in RC beams, Struct. Concr. 17 (3) (2016) 377–389.

[26] P. Visintin, D.J. Oehlers, Fundamental mechanics that govern the flexural behaviour of reinforced concrete beams with fibre-reinforced concrete, Adv. Struct. Eng. 10 (2017), https://doi.org/10.1177/1369433217739705.

[27] I.H. Yang, C. Joh, B.S. Kim, Structural behavior of ultra high performance concrete beams subjected to bending, Eng. Struct. 32 (11) (2010) 3478–3487.

[28] I.H. Yang, C. Joh, B.S. Kim, Flexural strength of large-scale ultra high performance concrete prestressed T-beams, Can. J. Civ. Eng. 38 (11) (2011) 1185–1195.

LIST OF OTHER PUBLICATIONS DONE DURING THE PERIOD OF PH. D. PROGRAM

Journal papers

1. **Xie, T.,** Elchalakani, M., Karrech, A., Mohamad Ali, M.S., Dong M., Li, G. (2108). Mechanical and Durability Properties of Self-Compacting Concrete with Blended Binders. Computers and Concrete (Accepted).
2. **Xie, T.,** Visintin, P. (2018). A unified approach for mix design of concrete containing supplementary cementitious materials based on reactivity moduli. *Journal of Cleaner Production.*
3. Elchalakani, M., Dong M., Karrech, A., Li, G., Mohamad Ali, M.S., **Xie, T.,** Yang, Bo., (2018) Development of Fly Ash and Slag Based Geopolymer Concrete with Calcium Carbonate or Microsilica. *Journal of Materials in Civil Engineering.* (Accepted).
4. **Xie, T**, Elchalakani, M., Dong M., Karrech, A., Li, G., Mohamad Ali, M.S., (2018) Strength and Durability of Geopolymer Concrete Cured at Ambient Temperature. *KSCE Journal of Civil Engineering.* (Under review).
5. Xu. J, Zhao. X, Yu. Y, Xie. T, Yang. G, Xue. J, (2019) Parametric Sensitivity Analysis and Modelling of Mechanical Properties of Normal- and High-Strength Recycled Aggregate Concrete Using Grey Theory, Multiple Nonlinear Regression and Artificial Neural Networks. Construction and Building Materials, (Under review)
6. Xu. J, Chen. Y, Xie. T, Zhao. X, Xiong. B, Chen, Z(2019) Prediction of Triaxial Behavior of Recycled Aggregate Concrete Using Grey Relational Analysis, Multiple Nonlinear Regression and Artificial Neural Networks Construction and Building Materials, (Under review)

Conference paper:

Xie, T., Fang, C., Mohamad Ali, M.S., Visintin, P., Sheikh, A., (2017). Shrinkage Properties of Ultra-high performance concrete (UHPC): An Experimental Study. In *in Proceedings of 28th Biennial National Conference of the Concrete Institute of Australia 2017,* 2017.

Xie, T., Mohamad Ali, M.S., Visintin, P. (2018). Behavior of Ultra-high Performance Fiber Reinforced Concrete Skew Slab: An Experimental Study. In in Proceedings 3rd RNR International Conference at Mumbai in December 2018